Influence of nano– and microstructural features and defects in fine–grained Ni–Ti on the thermal and mechanical reversibility of the martensitic transformation

Proefschrift voorgelegd tot het behalen van de
graad van doctor in de Wetenschappen, Fysica
aan de Universiteit Antwerpen, te verdedigen door

Saeid Pourbabak

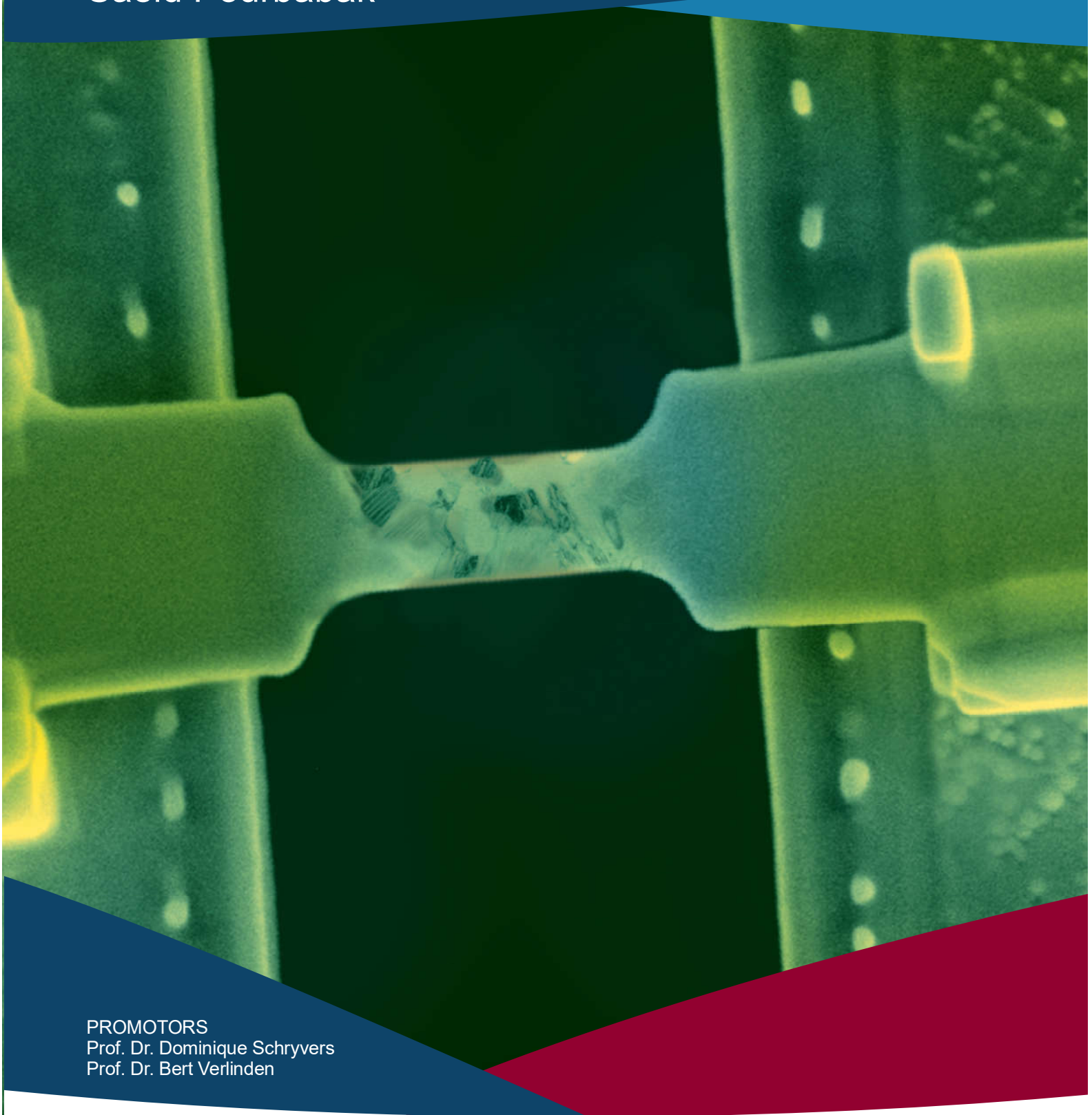

PROMOTORS
Prof. Dr. Dominique Schryvers
Prof. Dr. Bert Verlinden

Faculteit Wetenschappen
Departement Fysica
Antwerpen 2020

Universiteit Antwerpen

Faculteit Ingenieurswetenschappen
Departement Materiaalkunde
Leuven 2020

KU LEUVEN

Faculty of Engineering Science
Department of Materials Engineering (MTM)
Kasteelpark Arenberg 44, bus 2450
B-3001 Heverlee, Belgium
www.mtm.kuleuven.be

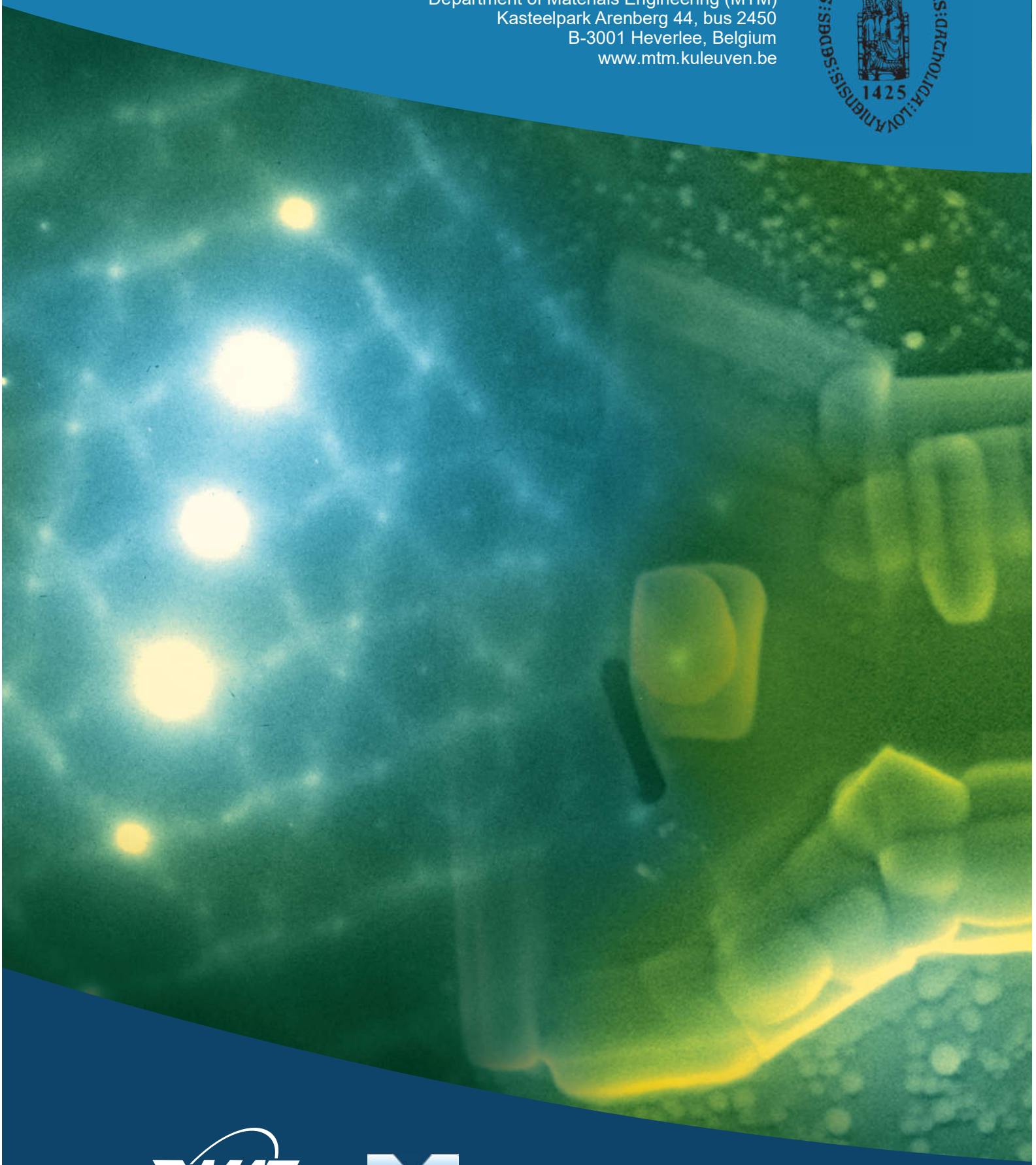

Universiteit Antwerpen

Faculteit Wetenschappen
Departement Fysica

Faculteit Ingenieurswetenschappen
Departement Materiaalkunde

Influence of nano– and microstructural features and defects in fine–grained Ni–Ti on the thermal and mechanical reversibility of the martensitic transformation

Invloed van nano– en microstructurele eigenschappen en defecten in fijnkorrelig Ni–Ti op de thermische en mechanische omkeerbaarheid van de martensitische transformatie

Proefschrift voorgelegd tot het behalen van de graad van
Doctor in de Wetenschappen, Fysica
aan de Universiteit Antwerpen, te verdedigen door

Dissertation presented in partial fulfillment of the requirements for the degree of
Doctor in Engineering Science (PhD): Materials Engineering

Saeid Pourbabak

Promotors:

Prof. Dr. D. Schryvers

Prof. Dr. B. Verlinden

February 2020

Members of the Jury

Chairman

Prof. Dr. M. Milošević, University of Antwerp, Belgium

Promotors

Prof. Dr. D. Schryvers, University of Antwerp, Belgium

Prof. Dr. B. Verlinden, Katholieke Universiteit Leuven, Belgium

Members

Prof. Dr. J. Van Humbeeck, Katholieke Universiteit Leuven, Belgium

Prof. Dr. P. Šittner, Institute of Physics of the Czech Academy of Sciences, Czech Republic

Prof. Dr. W. Wenseleers, University of Antwerp, Belgium

Prof. Dr. X. Wang, Shandong University, China

Contact information

Electron Microscopy for Materials Science
University of Antwerp

Saeid Pourbabak
EMAT – Electron Microscopy for Materials Science
University of Antwerp – Department of Physics
Groenenborgerlaan 171, B–2020 Antwerpen
Belgium
saeid.pourbabak@uantwerpen.be

KU LEUVEN

Saeid Pourbabak
MTM – Department of Materials Engineering
KU Leuven – Faculty of Engineering Science
Kasteelpark Arenberg 44, box 2450, 3001 Leuven
Belgium
saeid.pourbabak@kuleuven.be

Uitgegeven in eigen beheer, Saeid Pourbabak, Kasteelpark Arenberg 44, box 2450, B-3001 Heverlee, Belgium

Contents

Chapter 1:

Introduction

This chapter gives a short introduction on the history and applications of Ni–Ti alloys. It briefly describes the shape memory effect and superelasticity, and at the end, the aim of this work is explained and finally, the layout of the thesis is given.

1.1 Brief history and applications of Ni–Ti alloys

Ni–Ti alloys show shape memory effects (SME) and superelasticity (SE), also called pseudoelasticity, which can be described as the ability of the material to recover from large strains by the change of thermal or mechanical conditions, respectively. The shape memory effect of near equiatomic Ni–Ti alloys was first accidentally discovered in 1963 when Buehler [1] was investigating the property of this alloy in his lab, and during a meeting, a pipe smoking associate applied heat from his pipe lighter to a stretched Ni–Ti strip [2].

In fact, SME was previously discovered in other alloys such as Au–Cd [3] (1932), Cu–Zn [4] (1938) and In–Tl [5] (1954), as well as SE in Cu–Zn (1952) [6,7] and In–Tl (1953) [6,8]. However, such materials have not been applied in devices due to their poor mechanical properties [9]. Ni–Ti alloys, however, became widely used in different sectors soon after the discovery because of their outstanding mechanical properties [10], excellent biocompatibility [11–14], good corrosion resistance [10,15] and ductility [10,16]. Engineers and product developers have considered both the SME and SE property of Ni–Ti alloys in their applications. These days Ni–Ti is known as the most commonly studied [7,17] and used [7,17–19] shape memory alloy (SMA).

The well–documented first large scale commercial application of a Ni–Ti alloy was in 1969 in the joints of hydraulic parts in the Grumman F–14 aircraft [2,20]. Another early usage of Ni–Ti was in orthodontic bridge wires in 1971, which was the first use of the recoverable strain of more than ten times that of stainless steel [2]. The mechanical behaviors of Ni–Ti–based materials closely resemble that of biological tissues such as bone and tendon, as seen from Figure 1–1 [7,21,22], and many other characteristics of Ni–Ti such as the height of the superelastic plateau or the size of the hysteresis loop can be well adjusted to desired values by proper alloying and/or treatments of the Ni–Ti material [7].

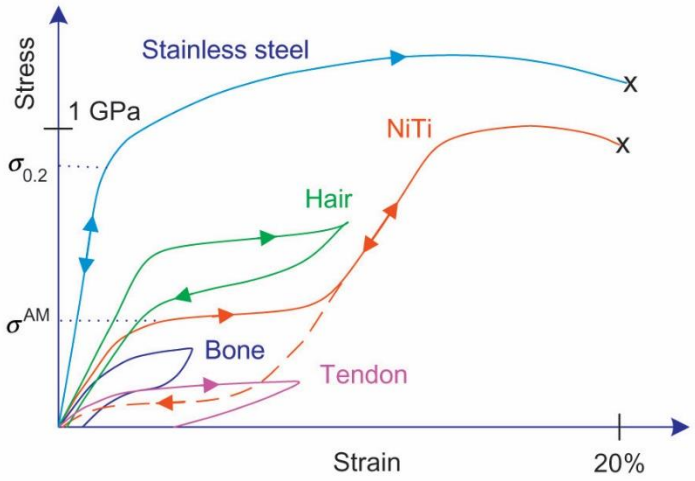

Figure 1–1 Ni–Ti alloy mechanical behavior versus stainless steel and several biomaterials [7].

These excellent mechanical properties of Ni–Ti alloys combined with the good biocompatibility [11–14] have resulted in an expanding interest in the medical industry [12,21,23]. The SME of Ni–Ti is used in bone staple wires used for fixation of fractured bones [24–27] as schematically shown in Figure 1–2(a) and as an example in Figure 1–2(b). Ni–Ti stents, being self–expandable due to the SE properties, are used to treat arterial stenosis (narrowing of the artery). The stent is squeezed into a small diameter delivery system tube and inserted in the human's narrowed lumen where the stent is released and expands the artery, leading to improved blood flow (Figure 1–2(c)) [12].

Superelasticity of Ni–Ti alloys was considered in dentistry for correction of irregular teeth. Very flexible orthodontic braces made of Ni–Ti alloys, shown in Figure 1–2(d), obviates re–applying the wire every time there is movement of the teeth, so that the number of reapplications per patient and treatment time decreases [12,28–30]. Also frames for eyeglasses [31,32], clinical surgical devices such as laparoscopic instruments (Figure 1–2(e)) [21], atrial septal defect occlusion system (ASDOS) to allow nonsurgical repairs of occlusions or holes in the atrial wall of the heart (Figure 1–2(f)) [21,23,33], or Simon vena cave filter (Figure 1–2(g)) which filter rather large embolized blood clots in the vena cave vein [21,23,33], are other medical devices benefitting from the outstanding properties of Ni–Ti.

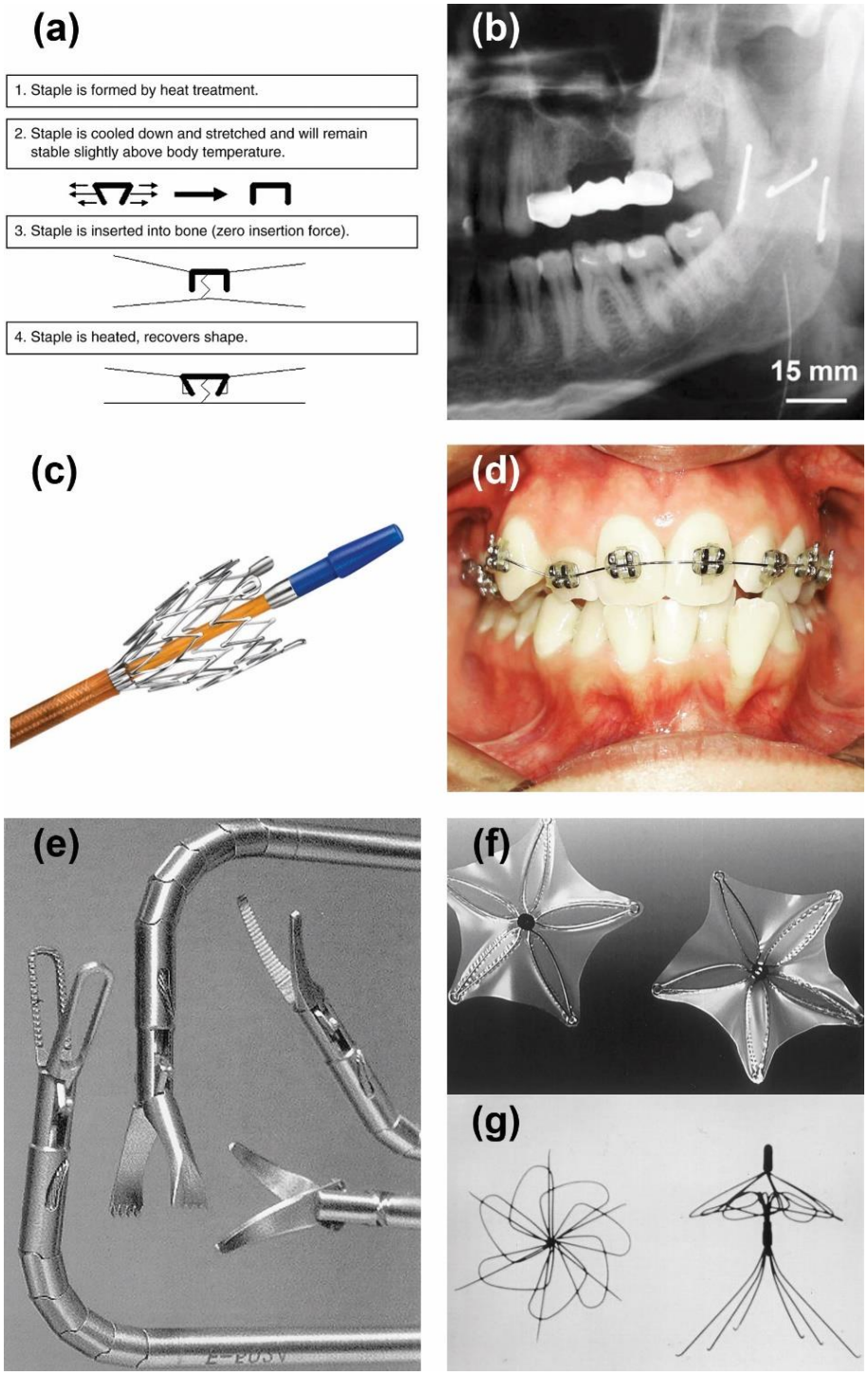

Figure 1–2 (a) Formation, insertion, and compression of Ni–Ti compression staples in the bone [27]; (b) radiogram of joined condyle mandible fracture by Ni–Ti shape memory staples after operation [24]; (c) self–expanding Ni–Ti stent system [34]; (d) orthodontic braces; (e) surgical innovations endoscopic instruments use Ni–Ti rods to actuate scissors, graspers, etc. [21]; (f) atrial septal defect occlusion system allowing nonsurgical repairs of occlusions or holes in the atrial wall of the heart [21]; (g) Simon vena cave filter, filtering large embolized blood clots in the vena cave vein [21].

Ni–Ti alloys have also been successfully used in macro–actuators [35], large variety of size and application of valves [36], robotics [37], automotive [38,39] and aerospace [40,41].

At the micro–size, Ni–Ti is applied in microelectromechanical systems (MEMS) and micro–actuators that produce motion in devices such as micro–valves, –pumps, –switches and –shutters. Ni–Ti alloys are well suited for this purpose, due to their large actuating forces, minimal power consumption and room temperature operational range [10]. Another reason for the special attention on Ni–Ti alloys for MEMS applications is that they can function as sensors and actuators simultaneously [20,42]. One drawback of SMA's in general is a relatively low response time when compared to, e.g., piezoelectric devices [43].

Sputter deposited thin film Ni–Ti layers crystallized after heat treatment and designed by lithographic patterning have been used in MEMS applications as membrane actuator [43–45] and diaphragm [10,43,46] for micro–pumps and valves, an example shown in Figure 1–3(a) [47]. The work density of such thin films exceeds that of any other micro–actuating material [10,43]. A 100 μm thick cold–rolled and laser cutting micro–fabricated Ni–Ti membrane actuator used in micro–valves is shown in Figure 1–3(b) [44,45,48]. Thin films are also used in micro–grippers for grasping and manipulating small or micro–objects with high accuracy in a wide range of applications, such as the assembly in microsystems, endoscopes, for microsurgery, and drug injection micromanipulators for cells [43], an example of which is shown in Figure 1–3(c) [43,49]. The microelectrode with Ni–Ti clipping structure shown in Figure 1–3(d) and (e) can be used for minimal invasive microelectrodes to clip a nerve cord or other living organisms [43,50]. In the micro–tweezer shown in Figure 1–3(f) the Joule heating leads to both martensitic transformation and thermal expansion, leading to move in two perpendicular directions [51]. A micro–wrapper (or micro–cage) made of thin films with overall arms dimension of 100 μm is shown in open (Figure 1–3(g)) and closed (Figure 1–3(h)) condition [51,52]. Ni–Ti thin films are also ideal for applications in micro–sensors due to their sensitivity to environmental changes such as thermal, stress, magnetic or electrical fields [43]. The micro–gripper shown in Figure 1–3(i) made of rolled Ni–Ti sheet employs two actuation units to be heated selectively in order to open and close the gripping jaws with a very short response time [53].

In the SMA actuators the mechanical work is obtained by SME when an electric current flows through the alloy and heats it up to the transformation temperature. As in this method no electric motor is used and an SMA with any shape can play the role of an engine, authors were tempted to extremely downsize the SMA actuators, some even talked about atomic scale [54]. For this purpose,

one should investigate the mechanical properties of the alloy in sub–micron scale and check if our knowledge at the macro–scale is also valid at the micro–scale.

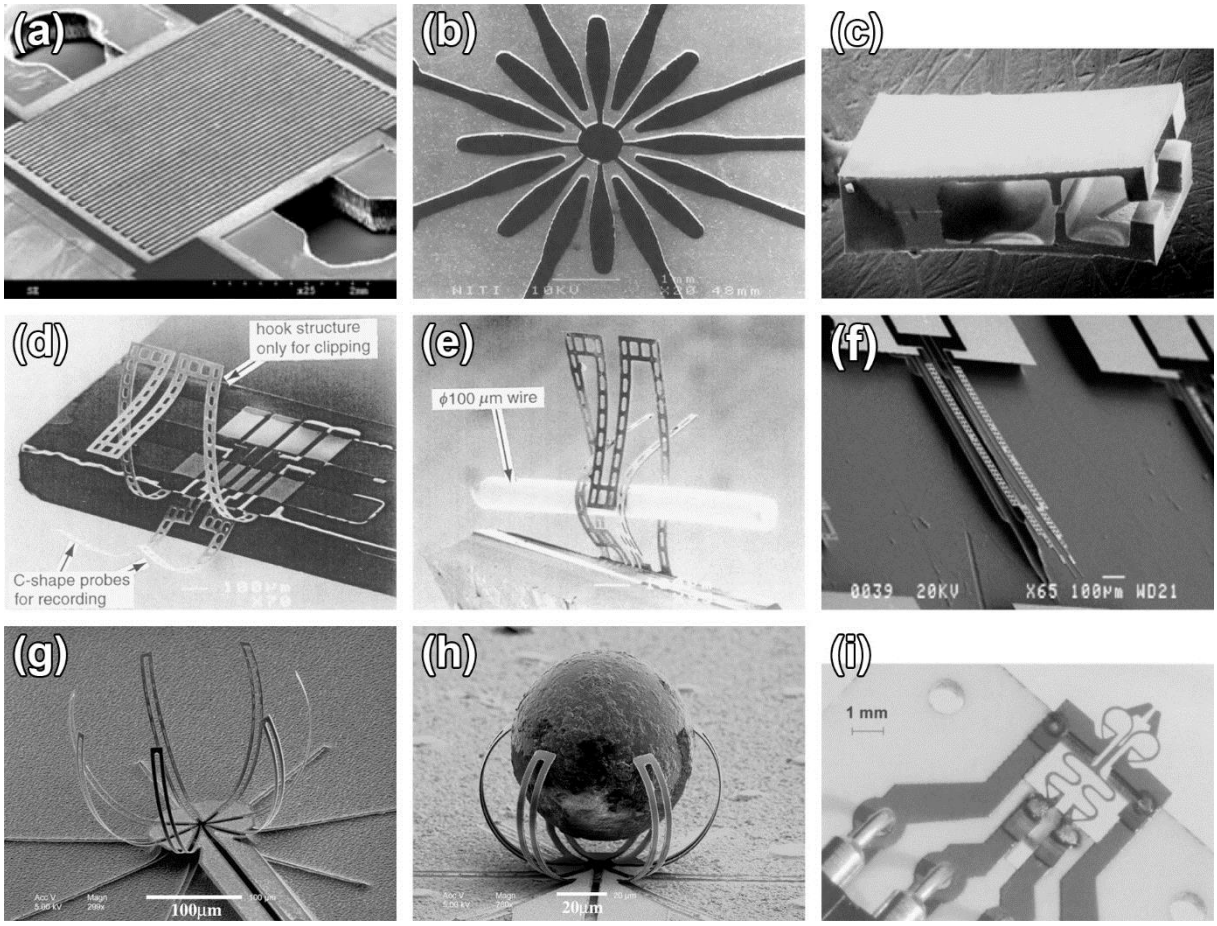

Figure 1–3 (a) Top view of membrane and Ni–Ti electrode in a micro–valve [47]; (b) membrane actuator of a micro–valve consisting of a circular arrangement of double beams [48]; (c) Ni–Ti/Si micro–gripper with cantilever structure with out–of–plane bending mode [43]; (d) & (e) microelectrode with clipping structure designed for nerve clipping [50]; (f) micro–tweezer with both horizontal and vertical movement due to both shape memory and thermal effects [51]; (g) a micro–wrapper or micro–cage with open fingers and (h) with closed fingers grabbing a 50 μm polymer ball [52]; (i) Ni–Ti micro–gripper using two actuation units to quickly respond to the opening/closing signal [53].

1.2 Shape memory effect and superelasticity of Ni–Ti alloys

The shape memory effect refers to the ability of deformed materials to return to their pre–defined shape upon heating. When a shape memory material is deformed up to some extent in a cold temperature, it reclaims its permanent deformation and returns to its original shape upon

heating to a certain characteristic hot temperature. This behavior is known as the one–way shape memory effect. Two–way shape memory effect, on the other hand, is when the material takes two different shapes by heating and cooling above and below specific temperatures. In other words, a one–way SMA can only remember the high temperature shape, while a two–way SMA can remember both high and low temperature shapes. For a material to show two–way shape memory effect normally it requires to undergo a special treatment called "training" [55].

Superelasticity, another property of Ni–Ti alloys, is the ability of the material to be stretched or bent up to large extent and return to its former shape upon releasing the load, without effect on the properties of the material [12]. Elastic strains involved in shape memory alloys are close to two orders of magnitude larger than those of classical engineering materials, e.g., structural steel [6,20]. Superelasticity takes place at higher temperatures compared to those of shape memory effect in a given material.

Both shape memory and superelasticity of Ni–Ti alloys rely on martensitic transformation (MT) [20,56], which will be explained in the Chapter 2.

1.3 Aim and outlines of this PhD thesis

The shape memory and superelasticity effects in Ni–Ti alloys are associated with reversibility of the martensitic transformation. Thus, any irreversible processes occurring during transformation cycles causing a change in the transformation characteristics are of great importance for the practical purposes of the material. One of the phenomena observed in Ni–Ti is the suppression of the MT by thermal cycling [57] and the first objective of this work is to investigate the effect of thermal cycling on the material microstructures using electron microscopy.

The second objective of this work is to investigate the stress–induced martensitic transformation in sub–micron scale samples using in–situ transmission electron microscopy. This is important not only for providing insight in the MT nucleation and propagation, but also since observations during straining can directly be coupled with the mechanical data collected by the in–situ transmission electron microscopy (TEM) straining holder.

As Ni–Ti thin wires are widely applied in micro–actuators [58–60], most of the samples investigated in this work are micro–wires. In order to prepare electron transparent thin specimens for electron microscopy, a method based on conventional twin–jet electropolishing is developed which provides large and clean thin area. An independent chapter is dedicated to this method.

This thesis is organized in seven chapters. After the brief introduction given in the current chapter, a more detailed review of literature related to the present work is given in Chapter 2, including the thermal and stress–induced martensitic transformation, previous works on micro–plasticity induced by MT and thermal cycling, in–situ electron microscopy and electropolishing.

In Chapter 3 the bulk and micro–wire Ni–Ti material used in this work and their thermomechanical history and treatment are presented. Also, the instruments, methods and conditions applied to measure thermal and mechanical properties of the samples are discussed. Moreover, the conventional twin–jet electropolishing specimen preparation method applied for transmission electron microscopy of bulk material and focused ion beam specimen preparation for making in–situ straining specimens are explained. Finally, the Cluster Model which correlates reciprocal space to the real space and which will be applied to interpret diffuse intensities in electron diffraction patterns is introduced.

The specimen preparation technique developed to apply a conventional twin–jet electropolishing apparatus to prepare specimens from micro–wires is presented in Chapter 4 In Chapter 5 the effect of thermal cycling with and without combination with room temperature aging on micron–sized grain bulk material is investigated. In Chapter 6 the question investigated in the former chapter is deepened by using micron– and submicron–sized grain microwires and elevated temperature aging in addition to the room temperature aging.

While the former two chapters focus on thermal effects, in Chapter 7 the focus is on in–situ nano–straining experiments on single crystal and polycrystalline Ni–Ti specimens.

Chapter 2:

Literature review

In this chapter the literature related to this thesis is reviewed. First the Ni–Ti phases appearing in this work and their corresponding crystal structures are introduced. Then the austenite and martensite temperature ranges are discussed and the phase diagram of the material is described. Then the martensitic transformation mechanism which is responsible for the special properties of the material is discussed. It is followed by considering the thermally induced martensitic transformation, including the shape memory effect and differential scanning calorimetry technique. Stress–induced martensitic transformation comes after, focusing on the property of superelasticity and in–situ nano–tensile testing that will be applied in Chapter 7. The influence of precipitates, dislocations and thermal cycling on the martensitic transformation and how it is explained by different authors is also reviewed, which is related to Chapters 5 and 6 of this work.

At the end an overview on the electropolishing procedure and the path from conventional electropolishing to the contemporary twin–jet electropolishing apparatus for TEM specimen preparation is given. This provides a better understanding of the mechanism and development of the technique and is a preface to Chapter 4 in which a technique is developed for thinning undersized samples.

Some materials of this chapter have been published in the following articles:

- Pourbabak, S.; Orekhov, A.; Samaee, V.; Verlinden, B.; Van Humbeeck, J.; Schryvers, D. In-Situ TEM Stress Induced Martensitic Transformation in Ni50.8Ti49.2 Microwires. Shap. Mem. Superelasticity 2019, 5 (2), 154–162. https://doi.org/10.1007/s40830-019-00217-6.
- Pourbabak, S.; Wang, X.; van Dyck, D.; Verlinden, B.; Schryvers, D. Ni Cluster Formation in Low Temperature Annealed Ni50.6Ti49.4. Functional Materials Letters 2017, 10, 1740005. https://doi.org/10.1142/S1793604717400057.

2.1 Phases and crystal structures of Ni–Ti alloys

Ni–Ti can exist in several different phases. In this work we focus only on four most relevant phases for shape memory and superelastic behavior: austenite, R–phase, B19' martensite, and Ni_4Ti_3 precipitates and which are briefly described here. Also, the B19 martensite is shortly introduced. Other existing phases such as Ni_3Ti_2, Ni_3Ti and $NiTi_2$ are out of the scope of this work.

In this work, when the exact composition of the alloy or phase is to be specified, it is presented as subscript (e.g., $Ni_{50.8}Ti_{49.2}$) while Ni–Ti is used as a more general term when no specific composition is meant (although it is, in the framework of shape memory, essentially Ni–rich but still close to the 50/50 equiatomic ratio). When NiTi is used, an exact 50/50 composition is meant.

2.1.1 B2

Close to the equiatomic composition, the high temperature Ni–Ti phase, in the present context referred to as the austenite phase, has the ordered body–centered cubic B2 structure (CsCl), as shown in Figure 2–1(a). As this is the highest symmetry phase in Ni–Ti alloys, other phases with lower symmetries can form in multiple different orientations in reference to the cubic B2 matrix and thus create variants. Since the martensite phases transform from this B2 phase upon cooling, the latter is often also referred to as the parent phase.

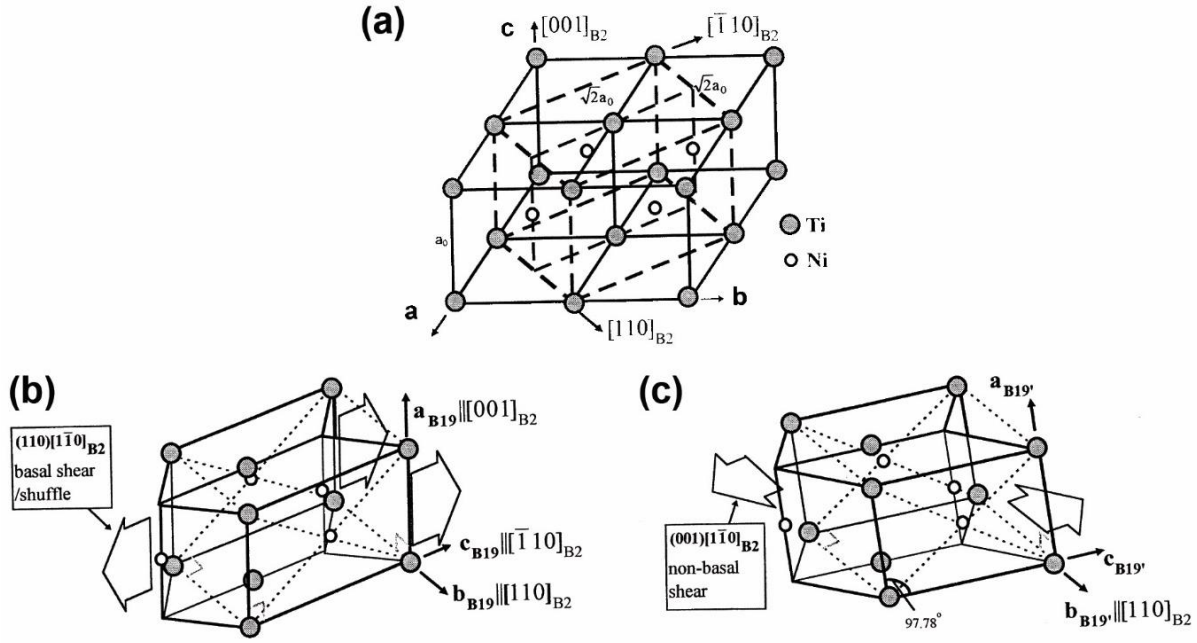

Figure 2–1 (a) The parent B2 phase cells with face–centered tetragonal (FCT) cell outlined and basal planes indicated by dash line; (b) orthorhombic B19 martensite formed by shear/shuffle of the basal plane (110)[1-10]$_{B2}$ direction; (c) monoclinic B19' martensite viewed as a B19 structure sheared by a non–basal (001)[1-10]$_{B2}$ shear [61].

2.1.2 B19′

The low temperature martensite phase has the monoclinic B19' structure, as shown in Figure 2–1(c). This is the phase formed when the first order martensitic transformation occurs in the parent B2, and it allows different twin variants to form. Similar to B2 being referred to as the parent phase, the martensite is often called the product phase.

The transformation from high–symmetry B2 austenite to low symmetry monoclinic martensite state results in 12 variants of martensite. The orientation relation between these variants and the parent phase is listed in Table 2–1.

Table 2–1 Orientation relation between the austenite and martensite [62].

Variants	$[100]_M$	$[010]_M$	$[001]_M$
1	$[100]_{B2}$	$[011]_{B2}$	$[0\bar{1}1]_{B2}$
1'	$[\bar{1}00]_{B2}$	$[0\bar{1}\bar{1}]_{B2}$	$[0\bar{1}1]_{B2}$
2	$[100]_{B2}$	$[0\bar{1}1]_{B2}$	$[0\bar{1}\bar{1}]_{B2}$
2'	$[\bar{1}00]_{B2}$	$[01\bar{1}]_{B2}$	$[0\bar{1}\bar{1}]_{B2}$
3	$[010]_{B2}$	$[101]_{B2}$	$[10\bar{1}]_{B2}$
3'	$[0\bar{1}0]_{B2}$	$[\bar{1}0\bar{1}]_{B2}$	$[10\bar{1}]_{B2}$
4	$[010]_{B2}$	$[10\bar{1}]_{B2}$	$[\bar{1}0\bar{1}]_{B2}$
4'	$[0\bar{1}0]_{B2}$	$[\bar{1}01]_{B2}$	$[\bar{1}0\bar{1}]_{B2}$
5	$[001]_{B2}$	$[110]_{B2}$	$[\bar{1}10]_{B2}$
5'	$[00\bar{1}]_{B2}$	$[\bar{1}\bar{1}0]_{B2}$	$[\bar{1}10]_{B2}$
6	$[001]_{B2}$	$[\bar{1}10]_{B2}$	$[\bar{1}\bar{1}0]_{B2}$
6'	$[00\bar{1}]_{B2}$	$[1\bar{1}0]_{B2}$	$[\bar{1}\bar{1}0]_{B2}$

2.1.3 R–phase

The R–phase in Ni–Ti alloys is an intermediate trigonal phase (as shown in Figure 2–2) between austenite and martensite and its occurrence depends on the exact composition and the thermomechanical history of the alloy. The B2→R transformation competes with the B2→B19' martensitic transformation. If R–phase appears first, the successive transformation occurs such as B2→R→B19', and if B19' transformation occurs first, R–phase transformation is suppressed. For R–phase to form, substitution of Ni by Al or Fe, or coherent Ni_4Ti_3 precipitate formation, or a high density of rearranged dislocations left from cold work are required [56,63,64].

R–phase has four symmetry related variants in the parent B2. The B2→R–phase is a first order diffusionless transformation [65]. R–phase is also associated with a shape memory effect [19,65]

but it is usually not considered as such since it allows a much smaller strain change (0.5%) compared to the MT (5%) [19].

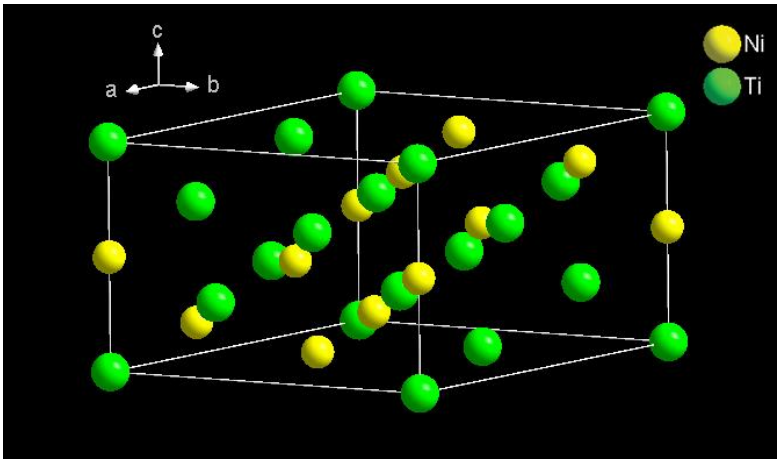

Figure 2–2 Trigonal representation of the R–phase.

2.1.4 B19

Orthorhombic B19 martensite is another intermediate phase which may form in ternary alloys when Ni is substituted by, e.g., Cu. In this case, depending on the ternary element content, the B2 to B19' transformation may occur in two steps: B2→B19 and B19→B19' [56]. In solution–treated binary Ni–Ti alloys, such as those used in the present work, the transformation occurs directly from B2 to B19' and no B19 phase forms [56].

We reserve "martensite" for the B19' phase and "martensitic transformation" for the B2→B19' transformation, and will not refer to B19 any further, since it does not appear in our material.

2.1.5 Ni_4Ti_3 precipitates

Ni_4Ti_3 is a metastable phase which appears as a result of diffusion–controlled precipitation transformation when Ni–rich Ni–Ti is aged at low temperature for short aging times. Ni_4Ti_3 can be described by rhombohedral (eight Ni atoms, six Ti atoms) or hexagonal (24 Ni atoms, 18 Ti atoms) structures, where the latter is often more convenient due to the orientation relation to the parent B2, e.g., $(001)_h$ // $(111)_{B2}$ and $[010]_h$ // $[-2-13]_{B2}$ (index h is standing for hexagonal). Ni_4Ti_3 precipitates are of lenticular shape with the central plane parallel to $\{111\}_{B2}$. The precipitates shrink 2.7% along the $(0001)_h$ habit plane direction and 0.3% along its perpendicular directions relative to the B2 [20]. These precipitates are coherent to the matrix in the early stage of formation. The lattice mismatch between the precipitate and matrix yields a strain field in the matrix around the precipitates which plays an important role in adjusting transformation temperatures and

improving the shape memory characteristics [56]. The precipitates also strengthen the B2 phase and therefore improve the recoverability of the shape memory [20].

In principle eight variants of precipitates in reference to the parent matrix are possible, but since these variants are two by two sharing a same habit plane, only four orientation variants of precipitates occur.

The above mentioned phases together with their corresponding crystal structure information are summarized in Table 2–2 [56,66,67] where the exact cell parameters depend on the specific composition of the alloy [20,67].

Table 2–2 Different phases and corresponding crystal structure of Ni–Ti alloys.

Phase	composition	Space group	Crystal structure	Cell parameters
Austenite	NiTi	$Pm\bar{3}m$	Cubic B2	a = 0.3015 nm
R–phase	NiTi	$P\bar{3}$	Trigonal	a=0.7339 nm c = 0.5284 nm $\gamma = 89°$
Martensite	NiTi	$P2_1/m$	Monoclinic B19'	a =0.2898 nm, b = 0.4108 nm, c = 0.4646 nm, $\beta = 97.78°$
Martensite	NiTi	Pmmb	Orthorhombic B19	a = 0.2881 nm, b = 0.4279 nm, c = 0.4514 nm
precipitate	Ni_4Ti_3	$R\bar{3}$	Rhombohedral	a = 0.670 nm, $\alpha = 113.8°$
			Hexagonal	a = 1.124 nm, c = 0.5077 nm

2.2 Martensite and austenite regime temperature ranges

A typical differential scanning calorimetry (DSC) measurement of a Ni–Ti alloy in the transformation temperature range is shown in Figure 2–3(a). When the sample is cooled down from the austenite B2 parent phase, the MT starts at M_s [68] (MT start temperature), the onset of the MT peak. By further cooling more austenite material transforms into B19' martensite until MT finishes at M_f (MT finish temperature). Upon heating, the martensite phase starts to reverse transform to the austenite phase at A_s (austenite start) and finishes at A_f (austenite finish)

temperature. The M_s, M_f, A_s and A_f temperatures are characteristic temperatures of a single stage Ni–Ti martensitic transformation.

One could also use the electrical resistivity of the material to measure the characteristic temperatures. Figure 2–3(b) is the electrical resistivity versus temperature of Ni–Ti in the transformation temperature range where the electrical resistivity shows a decrease upon cooling in the B2 phase region while an increase of the decreasing rate occurs at the onset of the transformation at M_s [69], due to the crystal structural change. This is an older method and it has the disadvantage that extracting the characteristic temperatures from the curves is not trivial.

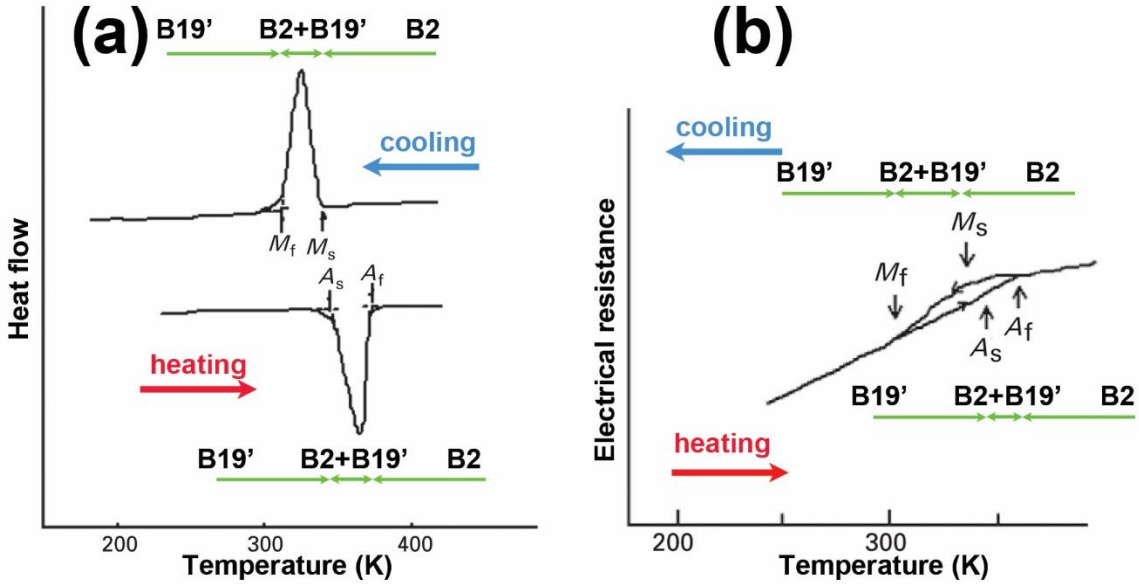

Figure 2–3 (a) DSC curves showing the transformation temperatures of the $Ni_{50}Ti_{50}$ alloy [69]; (b) Electrical resistance versus temperature curve of the same material showing the transformation temperatures [69].

The graphs in Figure 2–3 show that the temperature at which we are looking at a specific sample determines whether it falls in the austenite or martensite regime. In fact the transformation temperatures depend on a number of parameters, including the Ni content, impurity content and thermomechanical history [20,70–72]. Suppliers use these parameters to regulate the transformation temperatures of Ni–Ti alloys for the desired applications anywhere from cryogenic temperatures up to about 100 °C [19]. The main effect is the alloy composition, e.g., increasing the Ni content from 49.4 at.% to 50.4 at.% changes M_s from 57 °C to -30 °C [73]. Figure 2–4 shows the dependency of M_s to the Ni content of the alloy.

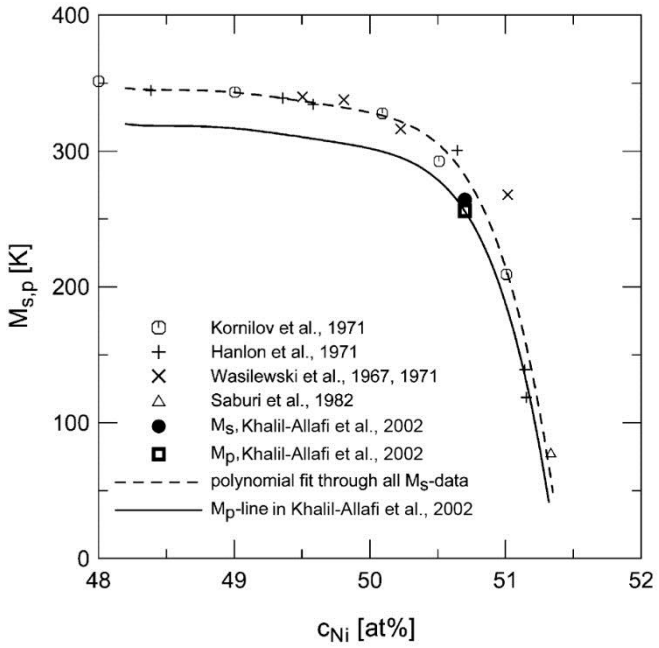

Figure 2–4 M_s versus Ni content experimental data [74].

2.3 Phase diagram

The equilibrium phase diagram of the Ni–Ti system is shown in Figure 2–5. The three equilibrium phases, $NiTi_2$, Ni–Ti and Ni_3Ti locate at 33.3 at.% Ni, near 50 at.% Ni and 75 at.% Ni, respectively [12,69]. The 1090 °C indicated by a dashed line is the order–disorder temperature [56] from which the B2 phase is stable from 49 at% Ni to 57 at% Ni [75]. Upon lowering the temperature, the B2 Ni–Ti phase region narrows down very quickly to a line phase with no solubility below 630 °C [12,69]. Therefore, below this temperature Ni–rich Ni–Ti decomposes upon direct cooling or on aging at a temperature below 630 °C after quenching. The decomposition ultimately leads to stable Ni_3Ti through metastable phases of Ni_4Ti_3 and Ni_3Ti_2. Ni_4Ti_3 which forms in the early stages of aging at low temperatures is the most important phase considering the functionality of Ni–Ti.

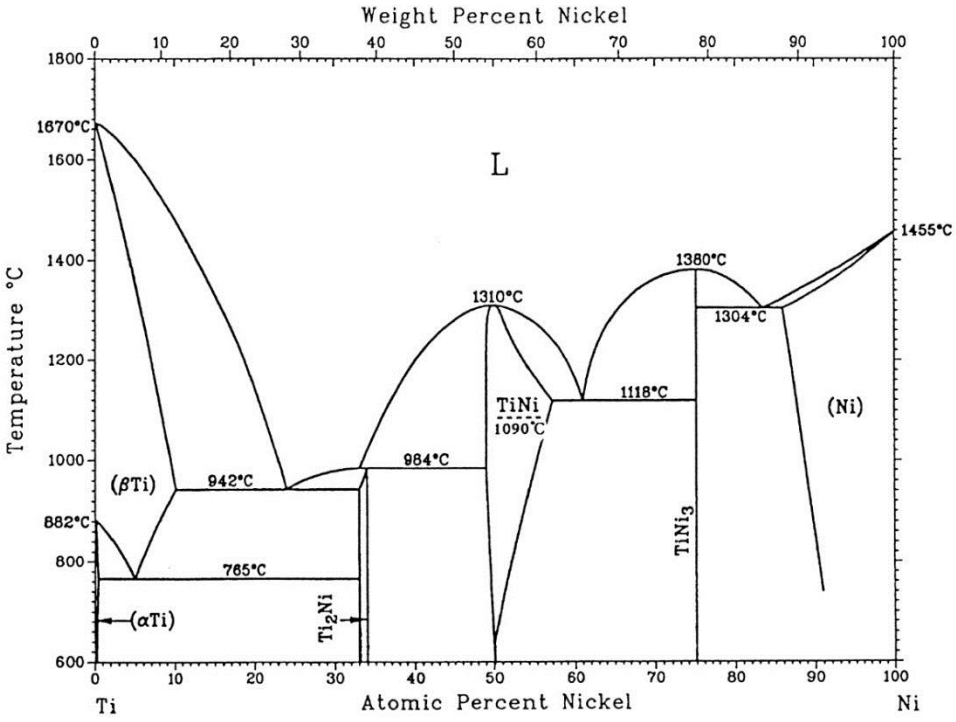

Figure 2–5 Phase diagram of Ni–Ti [61].

2.4 Cold work material and heat treatment

In conventional superelastic Ni–Ti a combination of cold work and subsequent low temperature annealing is employed to improve the characteristics of the material. After cold working material shows a mixture of austenite, amorphous phase, residual martensite and dislocations in the microstructure. Such material exhibits high yield strength, but very low phase transformation temperature and poor superelastic properties since only very low recoverable strain is possible. The characteristic properties are improved by annealing at 400 °C – 500 °C, slightly below the recrystallization temperature which partially removes the lattice defects and internal stress resulting in decreasing the yield stress. The remaining dislocations minimize the plastic accommodation and martensite stabilization via increasing the critical shear stress for dislocation slip [76]. Strengthening in critical shear stress for slip increases the difference in strength between the critical stress for stress–induced martensitic transformation and the macroscopic yield stress of martensite or austenite, yielding an enhancement of the cyclic stability [56,76]. On the other hand, if the material is fully annealed at temperatures of about 600 °C and above, martensite and internal stress gradually disappear, density of defects decreases and size of the recrystallized grains increases as the result of recovery and recrystallization [56]. In general,

superelasticity and shape recovery in solution–treated material takes place only partially due to easy slip deformation [20] in the absence of dislocations. Still, in view of the selected experiments, the present work focuses on recrystallized samples.

2.5 Martensitic transformation

2.5.1 Mechanism

The martensitic transformation is a thermoelastic, diffusionless, first order, solid–to–solid, reversible and shear–like transformation. It can be described as a lattice deformation resulting from shearing and cooperative movement of atoms, rather than their long range diffusional movements [77]. There is a one–to–one lattice correspondence between the lattice points of parent and product phases. As the relationship between neighboring atoms is retained during the MT, the change in the crystal structure can be explained by the deformation of the austenite crystal structure into that of the martensite [77], as schematically is shown in Figure 2–1 (through B19). In Figure 2–1(a) the parent B2 phase cells are shown in which a FCT cell is outlined and the $\{110\}_{B2}$ basal planes are indicated by dashed lines. The B19 martensite structure, Figure 2–1(b), is derived by a basal plane $\{110\}\langle 1\text{-}10\rangle_{B2}$ shear which leads to a more close–packed structure [56]. The B19' martensite, Figure 2–1(c), can be created by an additional monoclinic non–basal shear $\{001\}\langle 1\text{-}10\rangle_{B2}$ distortion.

Although the displacement of each atom is smaller than an interatomic distance, the transformation results in a macroscopic change in shape of the material [20], due to the cooperative movement of atoms, dominated by shear [48]. This macro–scale change can be observed by a simple experiment in which a straight line scratched on the surface of a single crystal austenite changes its direction upon MT. The habit or interface plane between the austenite and martensite should be an invariant plane (undistorted and un–rotated), since it yields the lowest strain energy [77]. This invariant habit plane is formed as a result of invariant plain strain which is a homogeneous distortion in a way that the displacement of any point is in the same direction and proportional to the distance from the habit plane. This plane guarantees the existence of a martensite and austenite compatible interface without large internal strains.

Although the habit plane being an invariant plane results in nearly equal to zero strain energy of the interface between the austenite and martensite phases, during the nucleation and growth of the martensite a large strain occurs due to the different crystal structure of austenite and martensite [78]. In order to reduce the strain and satisfy the invariant plain strain condition, two mechanisms

occur in Ni–Ti. The first mechanism, twinning, is a lattice invariant shear mechanism since it does not change the basic crystal structure of martensite. The second mechanism is self–accommodation [79] of martensite variants by which multiple martensite variants are formed side by side and mutually further reduce the transformation elastic strain energy. As a result, the sample does not experience deformation as a whole and the macroscopic volume change is minimized. The TEM image of a martensite plate and the corresponding selected area electron diffraction (SAED) pattern in Figure 2–6 clearly shows the finely twinned structure of the martensite, in the present case yielding spot splitting and streaking due to non–periodic twin sequences.

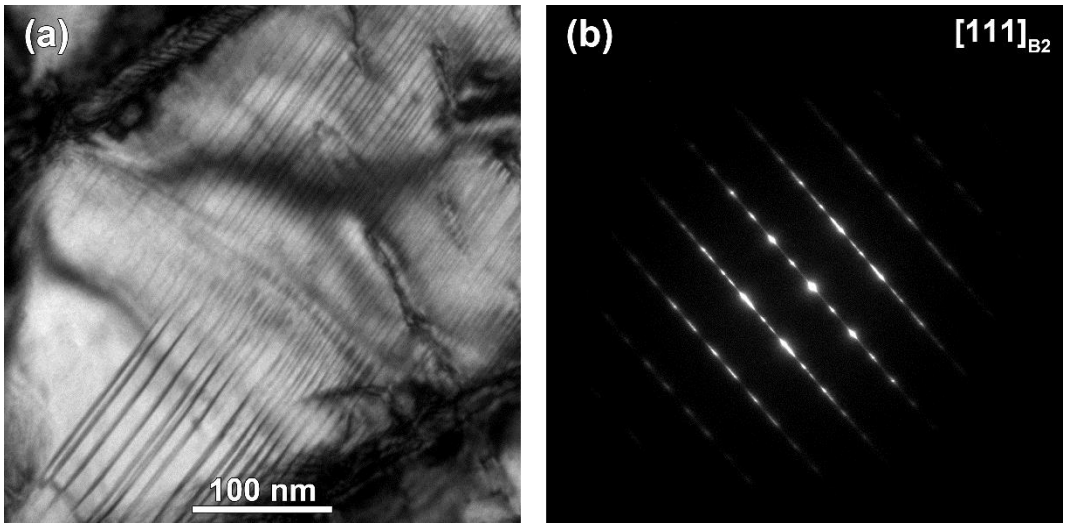

Figure 2–6 (a) TEM image of an internally twinned martensite plate in the B2 background matrix; (b) SAED acquired from the center of the martensite plate with streaks characteristic for non–periodic twins.

MT in Ni–Ti is a thermoelastic transformation, characterized by reversibility and having a small transformation hysteresis compared with non– thermoelastic transformations [61]. In thermoelastic alloys a reversible motion of the martensite plates [61] and austenite–martensite interface is observed during the transformation and the martensite plates shrink and return back completely to the initial austenite phase orientation. In a non–thermoelastic alloy, however, the reverse transformation occurs by nucleation of austenite inside the martensite plates instead of reverting martensite plates back into austenite.

Martensitic transformation can be triggered either thermally or mechanically. In such conditions Ni–Ti B2 austenite transforms into B19' martensite by decreasing temperature or increasing stress, and upon increasing the temperature or unloading, the reverse transformation

takes place. In the following sections these two mechanisms and their role in the functionality of the material are discussed.

2.5.2 Thermally induced martensitic transformation

2.5.2.1 Shape memory effect

Near equiatomic Ni–Ti alloys treated with an appropriate heat treatment exhibit shape memory and superelastic properties originating from the underlying martensitic transformation [20,56].

For the shape memory effect to happen the material must be below A_s at the environment temperature in the initial state. It yields self–accommodating structures formed by all possible, often internally twinned, martensite variants. In the stress–strain–temperature curve of Figure 2–7 this stage is indicated by a, the crossing of the three axes. Then by loading, the twinned martensite elastically deforms up to some extent, point b, after which detwinning of martensite starts. The applied stress promotes the growth of one martensite variant at the expense of the others in order to accommodate the applied stress as best as possible. In this manner the material can accommodate large deformations through martensite detwinning and rearrangement. This process continues until point c where the entire martensite phase is detwinned. If loading continues after this point, the detwinned martensite can still deform elastically up to point d. Upon unloading the material relaxes elastically, but the deformation accommodated by detwinning is retained, point e. Now by heating the sample, the material starts to transform back to austenite, point f, and by reaching A_f temperature, the whole material is back to austenite phase and the original shape of the sample is regained, point g. Now decreasing temperature below M_f to point a and forward MT causes no strain in the material. This is the one–way shape memory effect [20,75]. However, if the self–accommodated martensite variants are permanently favored by forming dislocations or internal stresses, forward MT by decreasing temperature yields large macroscopic strain resulting in shape recovery. This process is called two–way shape memory effect.

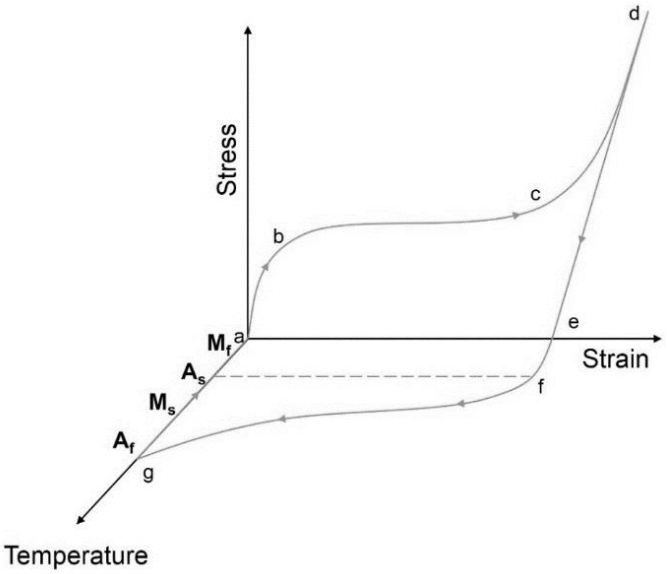

Figure 2–7 Stress–strain–temperature curve of Ni–Ti showing the one–way shape memory effect procedure.

2.5.2.2 Differential scanning calorimetry

Differential scanning calorimetry is a method to measure the total amount of energy released or absorbed by a material during a phase transformation. In this method a few milligrams of material is capsulated in a crucible and undergoes heating and cooling with a constant rate in a certain predefined temperature interval. The heat flow of the material is monitored and compared with that of an empty crucible as the reference and the results are shown in a graph with horizontal axis as temperature (°C) and vertical axis as heat flow normalized by the sample size ($J.s^{-1}.g^{-1}$). In the literature, there is no consistency in the direction of the vertical axis. In this work the exothermic peaks are presented in the positive direction and vice versa. As the MT involves a negative change in chemical enthalpy ΔH, it is seen as an exothermic peak (heat releasing) in the DSC curve during cooling. The reverse MT, on the other hand, appears as an upside–down peak revealing the reaction to be endothermic (heat absorbing).

The martensite peak, as can be seen in Figure 2–3 has a finite width (e.g., M_f – M_s) caused by the resistance (frictional kinetics) of the parent B2 phase to the growth of the product B19' phase [19]. Martensite growth in austenite introduces elastic strains in the surrounding austenite and as a result a larger driving force is required to transform the remaining austenite which lowers the transformation temperature. Therefore, when testing calorimetry of Ni–Ti alloys, a temperature interval including M_f–A_f range should be chosen with some margins to ensure complete forward

and reverse MT. According to ASTM standards for Ni–Ti alloys [80] the minimum temperature should be set at least 30 °C below M_f and the maximum temperature should be at least 30 °C above A_f, and one should hold the system at the minimum and maximum temperatures for a time sufficient for equilibration of the sample with the reference.

Martensitic transformation involves temperature hysteresis (e.g., $A_s - M_f$, although some other definitions were also used by authors), since the monoclinic B19' is not compatible with B2. Therefore, in Ni–Ti internal twinning of martensite occurs in order to generate compatible habit planes between the austenite and martensite which yields plasticity near the interface [19]. The created nucleation energy barrier causes the temperature hysteresis.

In addition to the characteristic temperature for start and finish austenite and martensite, sometimes M_p and A_p (martensite and austenite peak temperature, respectively, also shown by M* and A*) are also used.

Depending on the composition and thermomechanical history of the material, an R–phase peak can appear upon cooling in between the austenite and martensite peaks revealing a two–step transformation of A→R→M in cooling, as shown in Figure 2–8(a). R–phase can return to B2 austenite and show a separate peak during heating only if the cooling is terminated before reaching M_f, i.e., the thermal cycle is incomplete [65,81], an example of which is shown in Figure 2–8(b). Characteristic temperatures of R–phase are defined as R_s and R_f for the transformation start and finish, respectively.

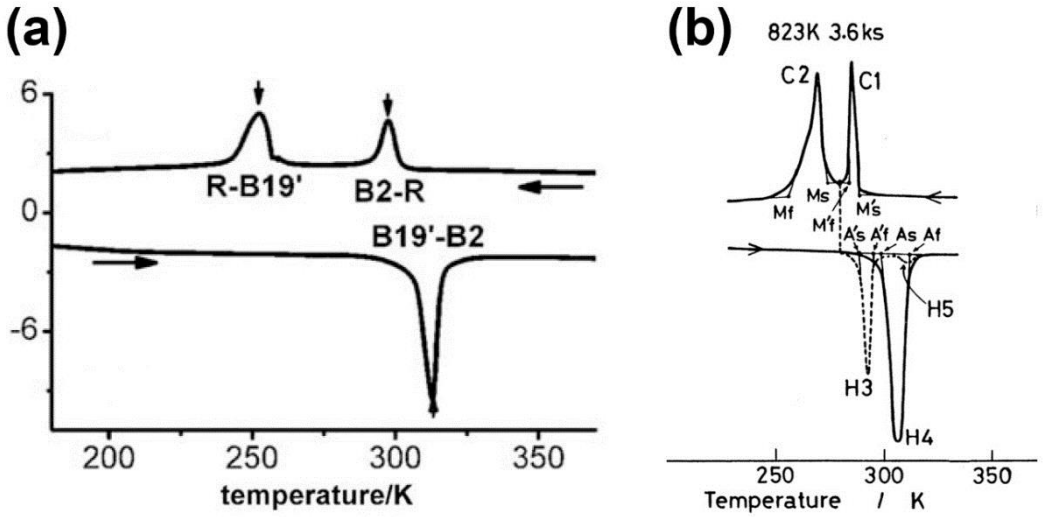

Figure 2–8 (a) DSC curve of a Ni–Ti showing B2→R and R→B19' in the forward and B19'→B2 in the reverse transformation [82]; (b) same peaks as observed in a (C1: B2→R, C2: R→B19' and H4: B19'→B2), plus the dashed H3 peak associated with R→B2 transformation appearing when heating starts at a temperature between C1 and C2 (incomplete cycle) [81].

The R–phase transformation exhibits very small (< 5 °C) temperature hysteresis [35,56,61] which is a quick indication of this transformation. The reason for such small hysteresis is that the R–phase crystal structure is kinematically compatible with that of B2 which implies that the energy stored in the interface due to the lattice mismatch is very small [19].

2.5.3 Stress induced martensitic transformation

2.5.3.1 Superelasticity

Superelasticity requires the material to be in the austenite regime in the environment temperature ($T > A_f$) in the absence of an applied stress. Austenitic Ni–Ti alloys under stress can accommodate large strains, mainly due to the stress–induced martensitic transformation (SIMT) [19]. A schematic superelastic stress–strain curve is shown in Figure 2–9. In such graphs, sometimes three regions are distinguished in the upper part. First, a region of sharp increase of stress versus strain can be recognized between labels a and b in Figure 2–9 and where elastic deformation of the austenite occurs. Second, a plateau region of stable stress exists between labels b and c in Figure 2–9 and where the austenite transforms into martensite. With increasing strain martensite plates grow and more can appear, while some of them coalesce into thicker plates. In this plateau region both austenite and martensite phases co–exist and the martensite variant favored by the tensile direction will be dominant [6,75,83–85]. After the plateau region, between labels c and d in Figure 2–9, the stress again increases with strain, which is related to the linear elastic deformation of the martensite.

When releasing the stress before plastic deformation of the martensite sets in and after a linear martensite elastic relaxation, the material returns to its original condition via the lower part of the curve, again showing a constant stress plateau between e and f where now martensite retransforms into austenite, followed by austenite elastic relaxation between f and a [6,75,84,86–88]. However, dividing such graphs into distinct regions is somewhat misleading since, for example, in between a and b, the slope of the graph can change while at label b the graphs often show a drop in stress before the plateau starts and which is referred to as the "nucleation peak", since the required stress for nucleation of new martensite plates is higher than that for the subsequent propagation and growth of existing plates [89,90].

This phenomenon is called superelasticity. The polycrystalline Ni–Ti alloys can recover strains near to 8% for low cycle use or up to about 2.5% for high cycle use [19].

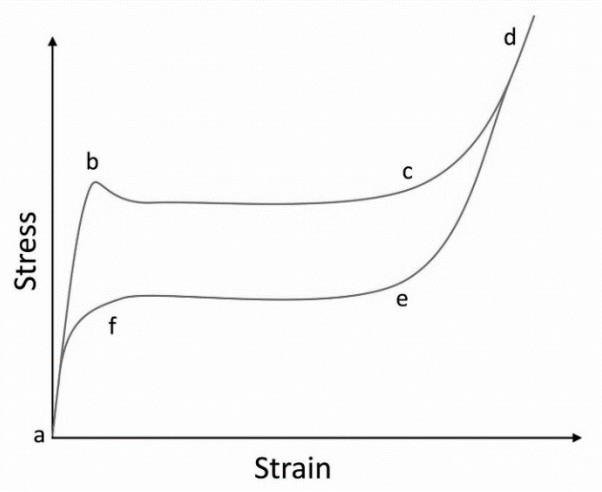

Figure 2–9 Schematic diagram showing the stress–strain curve of superelastic bulk Ni–Ti.

2.5.3.2 In–situ tensile experiment

In–situ straining of thin films [91] or electropolished specimens [92] in a transmission electron microscope, which allows deformation of a specimen while under observation at the microscale, has been developed in the previous century using conventional in–situ strain holders. This technique has been used by several authors to study microstructural features of SIMT in Ni–Ti alloys [93–97]. Xu et al. [93] observed that the initial stress–induced martensite (SIM) laths nucleate preferentially at grain boundaries in $Ni_{51}Ti_{49}$, particularly at triple–points, and the strain arising from the end of a lath induces the martensitic transformation in the adjacent grain when the SIM lath grows and reaches a grain boundary. They found the transformation reversible. Jiang et al. [94] reported nucleation and growing martensite in solution–treated bulk $Ni_{50.6}Ti_{49.4}$ upon loading and corresponding shrinkage by unloading, with the reversibility of the movement of the martensite–austenite interface being dependent on the martensite morphology. Kröger et al. [98] performed in–situ tensile tests on a solution–treated polycrystalline $Ni_{50.7}Ti_{49.3}$ after electropolishing and making a rectangular hole which was sputtered into the thin part of the tensile specimen using the focused ion beam (FIB) technique. They observed that the formation of martensite started at the sharp corner of the rectangular hole acting as a stress raiser as well as the intersection of a grain boundary with the rim of the rectangular hole. They found that the grain boundary can represent an obstacle for the propagation of a martensite/austenite interface and that it can also promote nucleation of martensite. In the work of Tirry et al. [95], the main conclusion for a NiTi polycrystal specimen was the experimental observation of plates of only one variant of martensite and which were reversible upon relaxing. The existence of a compatible

interface between austenite and a single variant of martensite was explained in the framework of non–linear elasticity theory [99] by the assumption of slightly deformed austenite and martensite lattices as a result of the imposed strain. Mao et al. [96] performed in–situ tensile tests on micro–strips of recrystallized cold–rolled $Ni_{50.8}Ti_{49.2}$ with different thicknesses prepared by electropolishing combined with focused ion beam. They found that the transformation occurs first in thicker strips followed by the thinner strips at higher stress and was even completely suppressed in a strip of only 40 nm thick. Pfetzing–Micklich et al. [97] carried out nano–indentation on a solution–treated austenite $Ni_{50.7}Ti_{49.3}$ alloy where stress–induced martensite is thermally stable at room temperature, followed by post–mortem TEM investigation on the FIB lamella prepared from the indented region. Although this is not strictly speaking an in–situ experiment, they identified martensite plates, as confirmed by B19' diffraction spots, as needle like features close to the indent. A subsequent in–situ heating of the specimen yielded the reverse transformation to austenite. Although those experiments allow one to observe the transformation during or after straining, they do not provide mechanical data, e.g., stress–strain curves, correlated to the observed features or mechanisms. The development of novel in–situ TEM straining holders based on MEMS devices and used in the present work allows collecting mechanical data while observing the evolution of the microstructure at the nanoscale and in real time [100], thus providing a more complete and quantitative picture of the behavior of the material under the applied loading conditions.

2.5.4 Martensitic transformation suppression

There are different parameters affecting the MT. In the following sections the effect of Ni_4Ti_3 precipitates, R–phase and dislocations on the martensitic transformation are discussed.

2.5.4.1 Effect of Ni_4Ti_3 precipitates

Aging Ni–rich Ni–Ti alloys in a specific temperature range results in the formation of Ni_4Ti_3 precipitates. The size and density of the precipitates mainly depend on the material composition and aging time: to give an example, aging $Ni_{50.6}Ti_{49.4}$ at 400 °C for 1 h yields a high density of small size precipitates while aging at 500 °C results in a low density of large precipitates, and aging at higher than 600 °C yields no precipitation [56]. The Ni_4Ti_3 precipitates affect the R–phase and MT by two different mechanisms influencing the surrounding matrix: strain fields induced by precipitates and the Ni depletion.

The lenticular–shape Ni_4Ti_3 precipitates are coherent with the austenite matrix in the early stages of formation (below ~ 300 nm diameter [101,102]) which leads to a strain field in the

surrounding matrix [20]. This yields destabilization of B19' due to its large transformation strain while hardly affects the stability of R–phase because of its small transformation strain [64], or even supports it due to the uniformly relaxation of the elastic strain in the matrix near the habit plane of the Ni_4Ti_3 precipitates [103]. Ni depletion from the matrix, on the other hand, leads to the increase of both M_s (Figure 2–4) and R_s [103] temperatures. As the combination of the two effects, R–phase formation is favored, B19' is suppressed and a two stage B2→R→B19' transformation is obtained [64,103].

2.5.4.2 Effect of dislocations

The effect of dislocations on the transformation path can be explained in the same way as the effect of precipitates. A high density of dislocations resists the lattice distortion caused by martensitic transformation, as with precipitates. This resistance is much larger for transformations involving large lattice distortion (e.g., B19') and is very small for transformations involving small lattice distortion (e.g., R–phase). Therefore, introduction of dislocations leads to the same consequence as the formation of fine precipitates which is a change of transformation path from B2→B19' into B2→R→B19' [56,64].

2.5.4.3 Effect of thermal cycling

The influence of thermal cycling on the Ni–Ti transformation characteristics was initially reported as early as 1968 by Wang et al. [70]. They observed irreversibility of electrical resistivity versus temperature path and decreasing of the M_s temperature with increasing number of "incomplete" cycles at and around the MT temperature in a solution–treated $Ni_{51}Ti_{49}$, while "complete" cycles were found to not affect the reversibility of the path. An "incomplete" cycle is a thermal cycle within the temperature range lower than M_s to higher than A_s, but not low (M_f) or high (A_f) enough to transform all material to martensite or austenite, respectively, while in a "complete" cycle the material completely transforms to either of the phases. They attributed the irreversibility of various properties within the critical temperature range to the irreversible shear movement of atoms. At the same time Ball et al. [104] reported formation of high dislocation densities by cycling stress–induced MT in Ni–Ti. Sandrock et al. [72] observed that incomplete thermal cycles cause an increase of dislocation density in a solution–treated $Ni_{50.5}Ti_{49.5}$ and $Ni_{51}Ti_{49}$, which act, as they described, as a form of "cold work". They attributed lowering of M_s to the effect of dislocations as an impediment to further martensite formation resulting in a stabilization effect. Wayman and Cornelis [105] later on noted that MT suppression in a solution–treated NiTi occurs

irrespective of whether the thermal cycles through M_s are complete or incomplete. Figure 2–10(a) shows their results as the electrical resistance versus temperature for a nearly stoichiometric Ni–Ti alloy after 1, 2, 3, 4 and 20 complete thermal cycles [105].

Miyazaki et al. performed a systematic investigation [57] on the effect of thermal cycling on solution–treated $Ni_{49.8}Ti_{50.2}$, $Ni_{50.6}Ti_{49.4}$ and $Ni_{51.6}Ti_{48.4}$ samples which were subjected to various types of thermomechanical treatments. They found that the transformation temperatures remain unchanged after thermal cycling in aged Ni–rich specimens and those annealed at a temperature lower than the recrystallization temperature after cold working, due to the formation of fine precipitates and stabilization of dislocations, respectively. However, M_s of aged Ti–rich specimens (i.e., having no precipitates) and solution–treated samples with various Ni–contents decrease drastically by thermal cycling. They attributed the decrease of M_s to the increase of dislocation density with increasing number of thermal cycles in the solution–treated sample, whose strain fields affect the MT.

In the early studies of the effect of thermal cycles on the MT the electrical resistivity versus temperature curve was used. The electrical resistivity decreases at the direct one–stage B2→B19' MT (e.g., the first cycle in Figure 2–10(a), path 1), while in the two–stage transformation (e.g., the second onwards cycles in Figure 2–10(a), path 2) a peak appears in the resistivity since the R–phase brings about an increase in resistivity [72,106]. During heating no increase in resistivity caused by the appearance of the R–phase is observed [106], as seen in Figure 2–10(b). In the martensite regime an increase in the resistivity is observed by repeating cycles, as seen in the left side of the curves in Figure 2–10(a), which is ascribed to the generation of transformation–induced defects since defects cause scattering of conduction electrons resulting in an increase in resistivity [106].

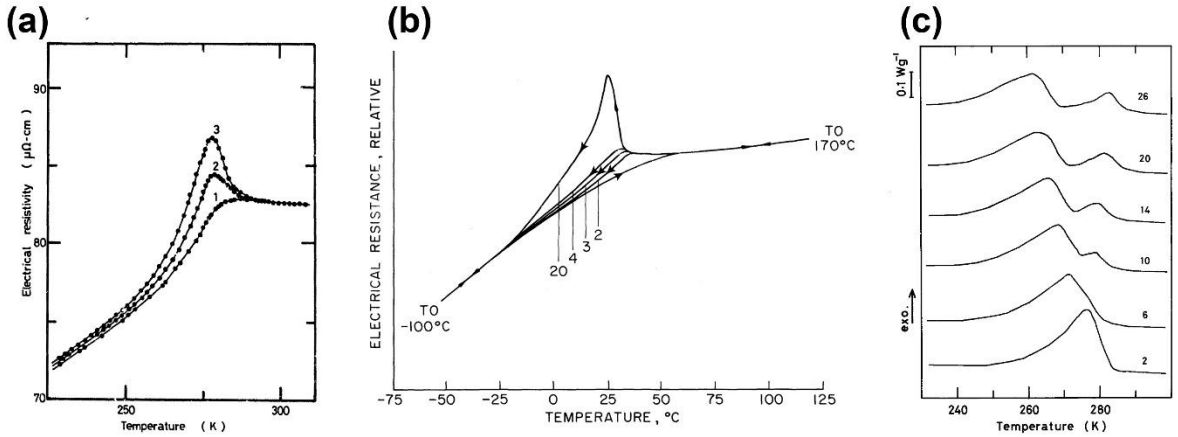

Figure 2–10 (a) Electrical resistivity as a function of temperature for one, two and three cycles only during cooling showing enhancement of the peak in resistivity and the shift in resistivity of the low

temperature phase with increasing thermal cycles [106]; (b) electrical resistance versus temperature for a nearly stoichiometric Ni–Ti alloy after different number of complete thermal cycles [105]; (c) Exothermic DSC curves showing the change of transformation behavior of Ni–Ti during cooling for different number of thermal cycles [107].

While the effect of thermal cycling in the previous studies has been characterized by measuring structure–sensitive properties such as the electrical resistivity, Matsumoto in 1991 [107] studied the transformation behavior of solution–treated NiTi as a continuous change in the transformation against thermal cycles using a differential scanning calorimeter. He observed shifting of the exothermic peak to the low–temperature side with increasing thermal cycles and formation and enhancement of a second peak on the high–temperature side resulting in a two–stage transformation in cooling, as shown in Figure 2–10(c). The endothermic reverse transformation peak remains a one–stage transformation during heating, shifts towards the low temperature and with no R–phase formation. He concluded that the introduction of defects caused by repetition of MT with thermal cycling plays a role in the stabilization of the intermediate (R–) phase which also relates to the transformation mechanism in Ni–Ti.

While earlier authors focused on the role of functional fatigue caused by dislocations formed due to and thus in the temperature range of MT, recent authors investigated the effect of ordering caused either by low temperature aging in the top range of the thermal cycling temperature interval.

In 2010 Wagner et al. [108] carried out DSC test cycling on three solution–treated $Ni_{50.7}Ti_{49.3}$ samples with different maximum temperatures of 150 °C, 200 °C and 250 °C. They reported that shifting MT temperatures towards lower values and also changing from single to a two stage MT occurs faster in experiments with higher DSC maximum temperature. They also observed MT suppression in samples with thermal cycling in a temperature range excluding MT. They concluded that the formation of Ni_4Ti_3 nano–sized precipitates at the top range of the thermal cycling temperature interval has a substantial contribution to the functional degradation of the material.

Kustov et al. [109] performed multiple DSC measurements on some solution–treated $Ni_{50.8}Ti_{49.2}$ alloy and $Ni_{50.6}Ti_{49.4}$ cold drawn wire samples at different days and maintained them at room temperature in between, called room temperature (RT) aging hereafter. They found a remarkable

effect of RT aging in between DSC cycles on the suppression of the MT, and which they also attributed to the formation of nano–sized precipitates due to the RT aging.

Wang et al. [110] systematically investigated the effect of thermal cycling on solution–treated $Ni_{50.6}Ti_{49.4}$ with and without RT aging in between. They designed an experiment with three sets of samples to separate the effect of RT aging and thermal cycling. They found that only RT aging has no effect on the M_s values, while multiple DSC cycles suppress MT, and the suppression becomes even stronger when DSC cycles are combined with RT aging in between.

2.6 Ni_4Ti_3 precipitation at low temperature

Ageing is an effective way to improve the shape memory and mechanical properties of Ni–rich Ni–Ti alloys due to the formation of Ni_4Ti_3 precipitates [111,112]. It is well known that ageing leads to progressive precipitation with increasing ageing time, temperature and Ni content [113]. The effect of intermediate temperature [74,82,114] (400 °C – 500 °C) and low temperature [111,115] (200 °C – 300 °C) ageing on the transformation behavior have been widely investigated before. Ageing at temperatures below 200 °C has been considered too low to cause precipitation, as reported by Kim and Miyazaki [111]. By TEM, they did not observe any precipitates in a $Ni_{50.9}Ti_{49.1}$ sample quenched from 800 °C and aged at 100 °C for 3000 h, and in the sample aged at 200 °C tiny 2 nm – 3 nm precipitates were first observed after 100 h. However, Kompatscher et al. reported that if the sample is quenched from higher temperature, i.e. 1000 °C, small precipitates of size 1 nm can be detected by means of small–angle neutron scattering, even without ageing [116]. Zheng et al. ascribed the suppression of the B2→B19' martensitic transformation in a sample aged below 330 °C to the atomic rearrangement as a precursor phenomenon for precipitation [113].

2.7 Electropolishing technique

2.7.1 Conventional electropolishing

The process of electrolytic polishing (electropolishing) which is the core of the twin–jet electropolishing apparatus was first discovered by Spitalsky in 1910 [117]. He placed silver as anode in an alkaline bath containing silver cyanide, resulting in highly increased lustre material. In 1930 Pierre A. Jacquet [118] developed the method further and systematically studied it for different materials until 1935 when he published his results for electropolishing copper. After elaboration of the basic principles of and procedures for electropolishing by Jacquet an increasing number of studies, publications and applications appeared in this field. Moreover, several lab

instruments for electropolishing were developed such as Micropol and Disa in 1944 and 1949, respectively, by the Danish company Struers.

The electropolishing process takes place by closing the circuit with the metal under consideration as anode together with a cathode in an appropriate electrolyte and right choice of voltage and amperage. An oxidizing solution is used to dissolve the surface of the conductive material. During the process, an electrical voltage establishes at the material–solution interface. Anodic dissolution products react with the electrolyte and form a thin liquid film of high viscosity and high electric resistivity at the metal surface (Figure 2–11(a)), which is the main phenomenon that is causing and regulating the polishing process. A concentration gradient of the film forms from the valleys (low points) to the ridges (high points). Since the film is essentially thinner over the ridges and thicker at the valleys, the resistance to electric current flow is lower over the ridges than in the valleys. Therefore, more current can flow over the ridges yielding faster dissolution process at the ridges, causing leveling of the surface and eliminating the sample roughness caused by previous mechanical polishing (mechanopolishing). An anodically discharged gas, usually oxygen, is also released from the metal surface. The process often requires low temperature electrolytes which reduces current densities and increases polishing layer viscosity, and consequently allows for better control of the polishing rate and quality [119–123].

Electropolishing essentially occurs in two distinct levels: macro–electropolishing or smoothing whereby large scale surface roughness is removed, and micro–electropolishing or brightening in which smaller (< 1 μm) irregularities are removed. In bath electropolishing both processes take place while in jet electropolishing micro–electropolishing is the main process [124].

The electrolyte usually contains two components: an oxidizing agent to oxidize the sample surface, and a depassivator to ensure that a passivating oxide film does not build up and prevent further attack. Sometimes a third component is added to promote the formation of a thick viscous layer on the sample surface [120,125].

If the potential is increased continuously during the process and the stable dissolution current acquired by the surface for each potential is plotted, a current–voltage graph is obtained. As can be seen in the typical example shown in Figure 2–11(b) the current increases initially until reaches a plateau, after which it increases again. In the first region (AB), the surface is etched as a result of regular dissolution of the material in acid and there is hydrogen release in the cathodic domain. In the BC region a slight decrease of the current occurs which is due to the generation of the viscous layer on the anodic surface [126–128]. In the part after the plateau (DE) the viscous layer is

destroyed and bubbles of oxygen begin to develop on the anode surface where pitting will take place causing small holes on the surface. Appropriate electropolishing giving mirror–like surfaces occurs on the central plateau (CD), namely close to the upper third of the plateau [119–121,129–132], where the apparent resistance of the electrolytic cell is the greatest. The plateau is due to the high electrical resistance of the aforementioned viscous film created by dissolution products on the surface of the anode, limiting the current and passivating the metal [119,120,122,126].

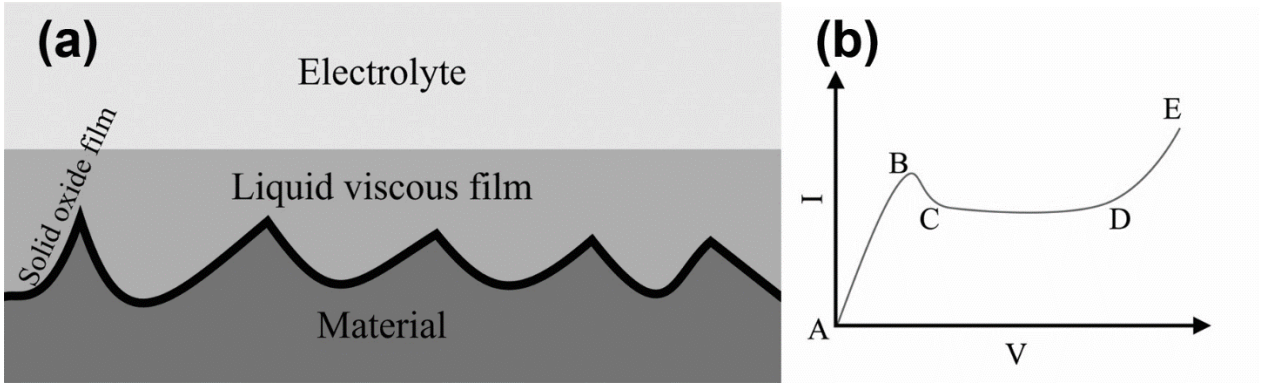

Figure 2–11 (a) Schematic of the material surface during electropolishing; (b) Typical current–potential electropolishing curve showing the plateau for proper polishing.

2.7.2 Electropolishing for TEM specimen preparation

Using electropolishing as a method for TEM specimen preparation was initially proposed by Heidenreich in 1949 [133] in a short section of an article about dynamical theory of electron diffraction in crystals. He developed a so called electro–thinning technique by introducing a Teflon specimen holder. In his original set–up the sample is thinned on one side after which the procedure is stopped and the sample has to be taken out and flipped with the unpolished face out. The polishing is resumed and the sample is carefully observed through a 4× magnifier until the first puncture is seen. Heidenreich applied the technique for aluminum and aluminum–copper, mentioning that the general procedure will likely be the same for any metal or alloy but with the electrolyte and polishing conditions varied for the particular alloy under consideration.

In 1953 Castaing & Laborie [134] resumed the experiments of Heidenreich on aluminum–copper and improved the technique by simultaneous polishing of both sides of the sample and circulating the electrolyte in order to avoid the formation of gas bubbles.

In 1956 Bollmann [135] insulated the edges of the chrome–nickel–steel sample with varnish and used two pointed cathodes to polish both sides of the sample at the same time. He did the

preparation in two steps in which the cathodes were placed at two different distances from the sample yielding two holes with a large thin area in between. The Bollmann technique later lead to another electropolishing method called window technique [129,136].

In 1961 Strutt [137] used a microscope focused on the sample base while illuminating the sample from the other side by a point–source light and when a tiny speck of light appears through the sample, the current is instantly stopped. In the same year Riesz & Bjorling [138] developed an automatic detection and stop system, yielding larger thin areas. By this time various attempts were made to further improve the technique and instrumentation[139–145], e.g., by the introduction of a P.T.F.E. holder (Dewey & Lewis [146]) and double jet polisher (Hugo and Phillips [145]).

In 1966 Schoone & Fischione [147] introduced a specimen holder with basically the same principles as the P.T.F.E. holder and a polishing unit with an automatic shutoff system. The unit utilizes a submerged double jet simultaneously polishing the sample from both sides, and a photocell and Light Wires for automatically stopping the polishing current the instant perforation occurs. This device called "Automatic Twin–Jet electropolisher Model 110" is the first commercial twin–jet electropolisher for TEM specimen preparation.

In 1971 the Danish company Struers brought Tenupol on the market for TEM specimens thinning. In this first model the sample is illuminated from one side and observed from the other side with a magnifier. A photocell provided as extra equipment could be installed in front of the magnifier to automatically stop the polishing. Tenupol, in contrast with Fischione unit is a non–submerged jet equipment. The setup could also be used for pre–thinning of the sample with maximum diameter of 21 mm and thickness of 1 mm by changing the nozzle from 1 mm to 2.5 mm and the specimen holder from 2.3/3 mm to 10 mm.

2.7.3 Contemporary electropolishing apparatus

A contemporary electropolishing apparatus consists of a sample holder, an electrolyte tank, an electropolishing cell and a control unit to adjust the electropolishing parameters.

The flow rate setting determines the strength of the jets and the photo sensitivity gives some control on the size of the hole. Both parameters have arbitrary units indicated on the setup and proper settings are to be found by experience. The flow rate should not be too strong, otherwise etching by direct dissolution occurs due to prevention of formation of the viscous layer [121,147], and also the thin specimen edge risks distortion [147,148]. A too weak flow rate causes surface contamination due to the redeposition of material [147]. The current displayed on the device is to

be adjusted by the potential, ideally to obtain the CD plateau range of Figure 2–11(b). A too low voltage results in inhomogeneous etching while a too high voltage causes banana shape holes on the edges with no thin surroundings.

A schematic of a twin–jet electropolishing unit is shown in Figure 2–12. When inserting the holder, the electrical connection between the sample and the polishing circuit is automatically established and in which the sample act as the anode (positive) and the two nozzles as the cathode (negative). Nozzles are centered on both sides of the specimen with a symmetrical jet force in order not to deform the thin edges of the specimen [121]. Upon starting the machine, a pump runs to supply the two horizontal jets of electrolyte ejecting to both surfaces of the sample. This causes simultaneously material removal from both sides of the 3 mm disk and formation of two dissolution basins [121]. The basins meet in the middle of the sample thickness, far from any damage caused by previous surface mechanopolishing [149]. As soon as the sample perforates, the electrolyte flow and potential are cut off immediately and the procedure terminates automatically through an infra–red or light detector system. The holder and the sample should be taken out as quickly as possible and subsequently rinsed into the same pure solvent (such as pure ethanol or methanol) several times in order to stop residual polishing of the surface of the material [150]. A successfully electropolished specimen usually has bright and shiny basins on both sides [149].

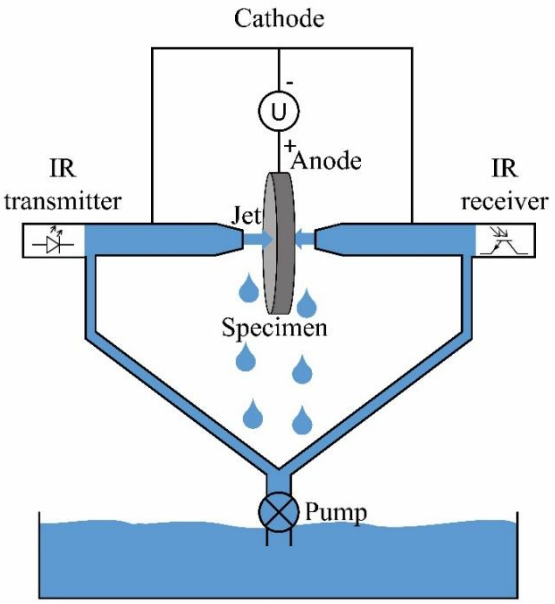

Figure 2–12 Schematic of a twin–jet electropolishing unit.

2.7.4 Side effects of electropolishing

When using electropolishing, one should be aware of effects of the procedure on the material. The first effect to consider is due to a change in temperature. Electropolishing for most of the materials should be done at lower than room temperature with a cooled electrolyte. On the other hand, the flowing current through the small and thin sample heats up the latter [121,151].

Preferential dissolution for multiphase materials and/or those containing precipitates or segregations is another issue [121,152] which is caused by the different electrochemical potential of each phase. It can yield selective thinning of precipitates in the case of Ni_4Ti_3 in a Ni–Ti matrix [153]. This effect may also cause loosening or falling precipitates, failing the electropolishing process.

As electropolishing removes the uppermost layers of the surface, the surface is stress relieved and possesses no cold–worked structure resulting from mechanical grinding [119,122,154]. For the same reason, electropolishing has a detrimental effect on the fatigue properties [154]. Electropolishing decreases fatigue strength of electropolished specimens due to removal of, or inability to produce, compressive stress in metal surfaces. In this way electropolishing is comparable in effect to a stress–relieving anneal [122].

Surface contamination may occur in electropolished specimens due to oxidation [121,134,139] or redeposition [152] which may cause enrichment of one or more elements of the sample material on the surface [121,134,155]. The oxide layer is very thin, 1 nm – 2 nm [121] and does not cause a significant inconvenience for the microscopy and interpretations [139]. However, it can be removed by slight ion milling [156], if needed. A too low electrolyte jet strength escalates redeposition [157].

2.7.5 Electropolishing of Ni–Ti

Electropolishing of bulk Ni–Ti for TEM specimen preparation has been widely and commonly applied since 1971 [72,158]. Authors have used different electrolytes and settings, as listed in Table 2–3, which can be summarized as the following three most common options, each with its own pro's and cons:

1. Mixture of ~ 20% sulfuric acid and ~ 80% methanol is best for materials close to equiatomic Ni–Ti, but in case of existence of Ni_4Ti_3 precipitates, the latter are preferentially thinned [153].

2. Mixture of ~ 93% acetic acid and ~ 7% perchloric acid gives poorer results overall, but shows no preferential etching between possible precipitates and matrix [159].
3. Mixture of ~ 30% nitric acid and ~ 70% methanol, which should be used with awareness at the recommended working temperature (~ -30 °C) Ni–Ti with higher Ni–content might undergo a MT during polishing.

Table 2–3 Electrolytes used for Ni–Ti TEM specimen preparation twin–jet electropolishing together with data given in the corresponding references. The component amount is in volume percent.

Methanol	Ethanol	Sulfuric acid	Nitric acid	Acetic acid	Perchloric acid	Butoxy-ethanol	$C_4H_{10}O$	V (V)	I (mA)	T (°C)	Ref	remarks
80		20						21		9	[95]	
80		20						9	20		[160]	
80		20						19.5		20	[161]	
80		20						20		7	[153]	
80		20								0	[150]	
80		20						45		0–8	[162]	
83		17						17			[163]	
83		17						18		20	[164]	
83		17									[165]	
75			25							-30	[166]	
75			25					15		-22	[167]	
75			25							-30	[168]	
75			25					12		-15	[169]	Flow Rate 4
70			30							-30	[96]	
70			30					10		-30	[170]	
66			33					10		-20	[171]	
				93	7					6	[159]	
				95	5			19.5		18	[98]	
				90	10					23	[172]	
83						7		80		-60	[169]	+ 9g LiCl + 19g $Mg(ClO_4)_2$, Flow Rate 8
60					6		34				[173]	
	95				5			35		-15	[174]	
		7		93				20		7	[175]	

Chapter 3:

Materials and methods

In this chapter the materials investigated, the instruments employed and the methods applied through this work are described. First the Ni–Ti materials under investigation in this thesis are introduced. Then heat treatment procedure of materials using a vertical furnace is discussed. It is followed by explaining the thermal and mechanical tests by DSC and dynamic mechanical analysis (DMA) machines, respectively. After that the main two conventional TEM specimen preparation methods applied in this work, electropolishing and FIB lift–out, are introduced.

In the TEM section the two imaging and diffraction modes are discussed. Then automated crystallographic orientation mapping (ACOM)–TEM is explained after which the Picoindentor holder used in the nano–mechanical tests is introduced. Then two thickness measurement techniques, convergent beam electron diffraction (CBED) and electron energy loss spectroscopy (EELS) are considered and finally the chapter is concluded by describing the Cluster Model used to interpret the diffuse intensity present in the acquired diffraction patterns.

Some of the material of this chapter have been published in the following articles:

- Pourbabak, S.; Orekhov, A.; Samaee, V.; Verlinden, B.; Van Humbeeck, J.; Schryvers, D. In-Situ TEM Stress Induced Martensitic Transformation in Ni50.8Ti49.2 Microwires. Shap. Mem. Superelasticity 2019, 5 (2), 154–162. https://doi.org/10.1007/s40830-019-00217-6.
- Pourbabak, S.; Wang, X.; van Dyck, D.; Verlinden, B.; Schryvers, D. Ni Cluster Formation in Low Temperature Annealed Ni50.6Ti49.4. Functional Materials Letters 2017, 10, 1740005. https://doi.org/10.1142/S1793604717400057.

3.1 Bulk and micro–wire materials

The micro–wire used in the Chapters 4, 6 and 7 is a 46.3% cold drawn $Ni_{50.8}Ti_{49.2}$ (nominal composition) wire with a diameter of 150 μm which was heat treated depending on each specific experimental requirement, presented in the corresponding sections.

The bulk material used in the experiments discussed in Chapter 5 is a $Ni_{50.6}Ti_{49.4}$ alloy (nominal composition) in the form of discs of ~ 3.7 mm diameter and ~ 0.7 mm thickness.

3.2 Materials heat treatment

A vertical furnace shown in Figure 3–1 was used for the material heat treatments in this work. It consists of a vertical cylinder surrounded by heating elements and two thermocouples to measure the temperature of the elements (set) and the sample (real). Before introducing the sample, the furnace was flushed by argon gas which continued to flow after inserting the sample to carry out heat treatment under inert atmosphere.

The sample was hanged in the furnace when the set temperature is stably reached. Due to the small size and weight of the micro–wires, the wire was wound around an iron strip of the size 10.0 cm × 2.0 cm × 0.3 cm before being hanged in the furnace. When the heat treatment was finished, the sample was released by turning a handle at the top of the furnace, the sample fell and, after breaking a thin aluminum foil blocking the bottom of the furnace, was drown in a bucket containing room temperature water.

As introducing the sample causes a drop in the furnace temperature, the initial temperature of the furnace was adjusted to some degrees above the desired temperature (the temperature difference of about 15 °C was previously found by trial and error) and after hanging the sample the temperature was readjusted to the aimed temperature. In this way the time to temperature equilibrium is minimized.

In order to meaningfully compare and interpret the results of this work, the material used in each set of experiments was taken from a single heat treatment so that even small possible differences resulting from different runs at different times is avoided.

Figure 3–1 The vertical furnace used for heat treatment.

3.3 Thermal and mechanical measurements

3.3.1 DSC thermal analysis

A METTLER TOLEDO differential scanning calorimeter (Figure 3–2(a) and (b)) equipped with a mechanical cooling system was used to measure the characteristic MT temperatures of the materials. The weight of the material (~ 15 mg for micro–wires) was measured with a Mettler Toledo AE 240 Analytical Balance (Figure 3–2(c)) with 0.01 mg readability and ± 0.03 mg linearity [176]. The material is to be put into a 6.7 mm diameter aluminum pan and closed with the corresponding aluminum lid. While bulk samples fit into the aluminum pans, wires have to be chopped into lengths of ~ 5 mm. The wire pieces were placed side by side in the pan, as shown in (Figure 3–2(d)), in order to obtain maximum thermal contact between the sample and bottom of the pan and consequently to the DSC thermal sensor [19]. A typical fixed [19,80] cooling/heating rate of 10 °C/min was applied for all measurements with three minutes as an isothermal segment at two ends of the temperature interval to thermally equilibrate the sample and reference [80]

before the next segment of the measurement is performed, as seen in the temperature–time graph of one DSC cycle in Figure 3–2(e).

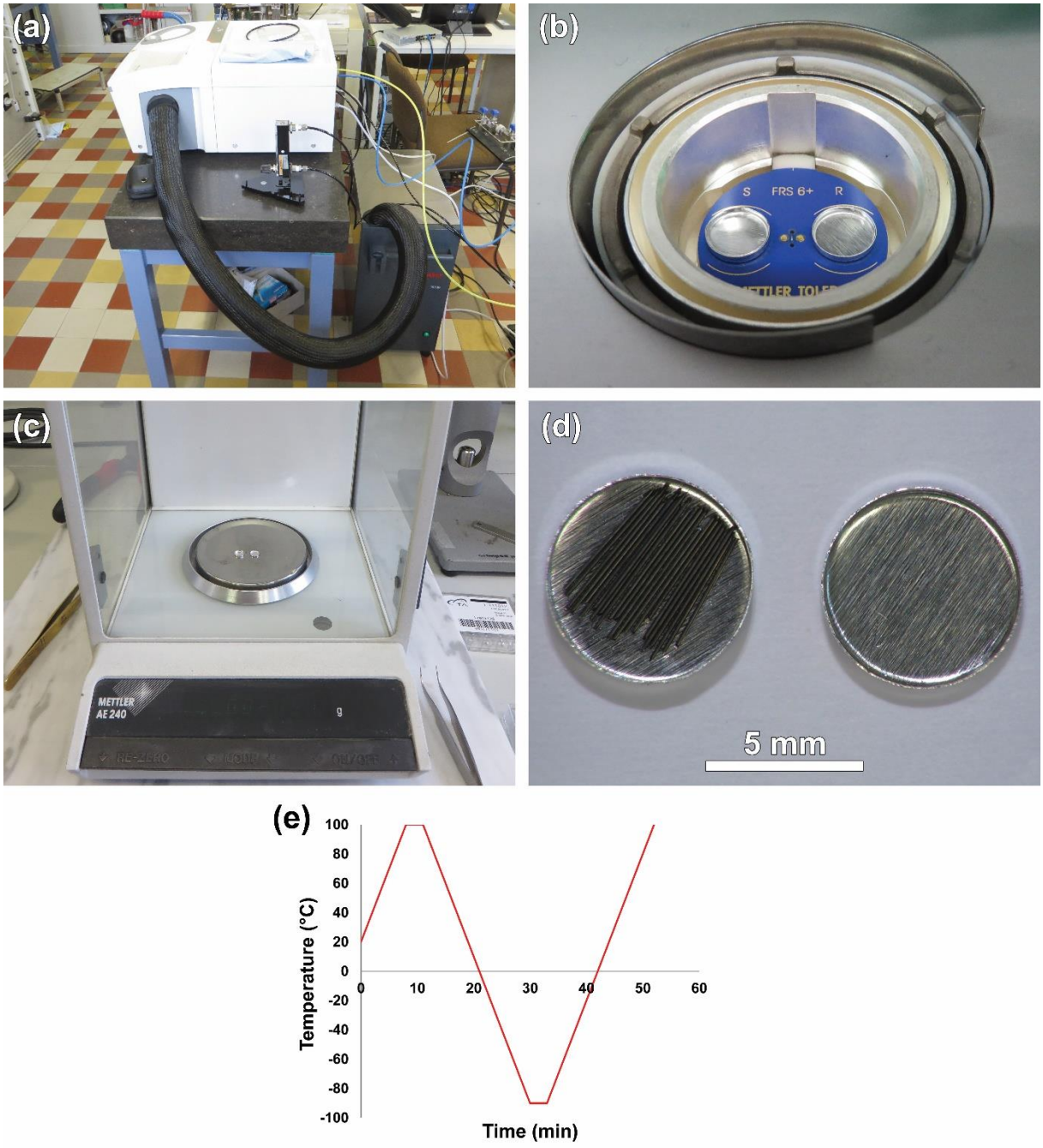

Figure 3–2 (a) METTLER TOLEDO DSC machine; (b) chamber of the DSC machine with a pan containing a sample on the sample sensor (S, left) and an empty pan on the reference (R, right) sensor; (c) Mettler Toledo AE 240 Analytical Balance; (d) aluminum pan containing chopped wire and the lid; (e) temperature–time graph of a DSC cycle with 10 °C/min cooling or heating rate and three minutes isothermal segment between each two consecutive ramps.

The METTLER TOLEDO STARe Evaluation Software was used to analyze the DSC results. The M_p temperature was found using the MinMax function of the software in the specified frame (Figure 3–3(a)) while the M_s and M_f temperatures were extracted by intersecting a tangent line to the steepest sides of the peak with the corresponding baseline [19], as seen in Figure 3–3(b). One can expect some uncertainty involved in this procedure due to the bell–like shape of the enthalpy peak and the chosen tangent and baseline. Also other parameters such as the precision of the measured weight of the material, the quality of the thermal contact between the sample crucibles and the sensor of the DSC machine, etc. may cause some uncertainty. In order to quantify this, M_s and M_p of 10 samples with the same heat treatment are measured yielding a respective uncertainty of 0.1 °C and 0.2 °C obtained as standard error.

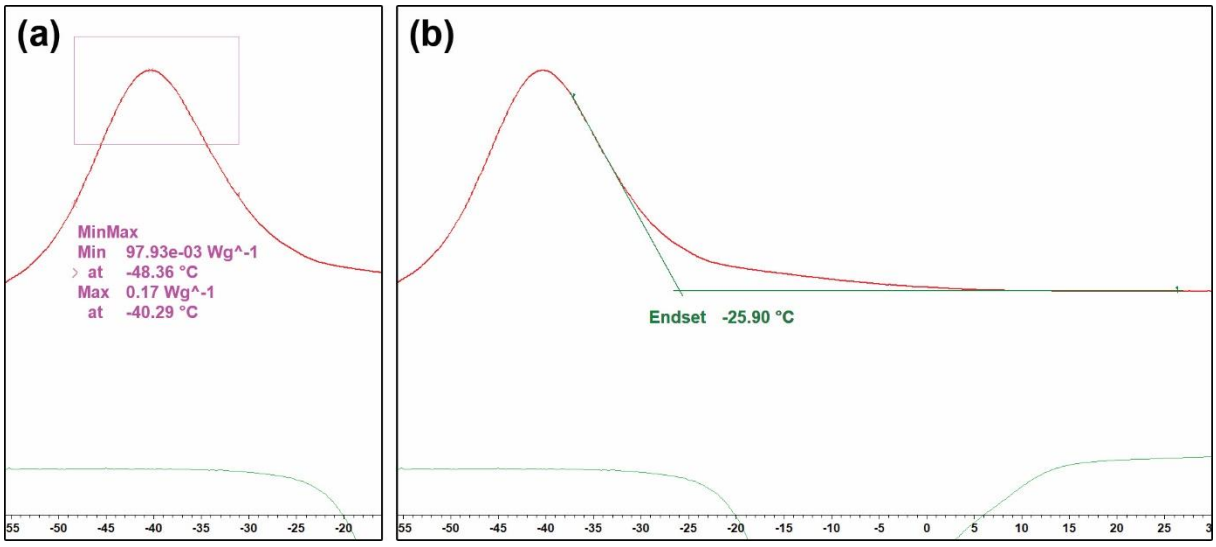

Figure 3–3 METTLER TOLEDO STARe Evaluation Software screenshot indicating (a) the frame for finding M_p and (b) the tangent lines for determining M_s of a typical DSC cycle.

3.3.2 DMA macro–mechanical measurements

A Q800 dynamic mechanical analysis machine shown in Figure 3–4(a) was employed to carry out tensile tests on the micro–wire and to obtain the macroscopic stress–strain curves. A ~ 10 mm ± 1 mm wire was clamped to the top and bottom grips, as can be seen in Figure 3–4(b), and strained with a constant strain rate of ~ 10^{-4}/s [177] at room temperature. The values of stress and strain are obtained from the machine after the experiment has ended.

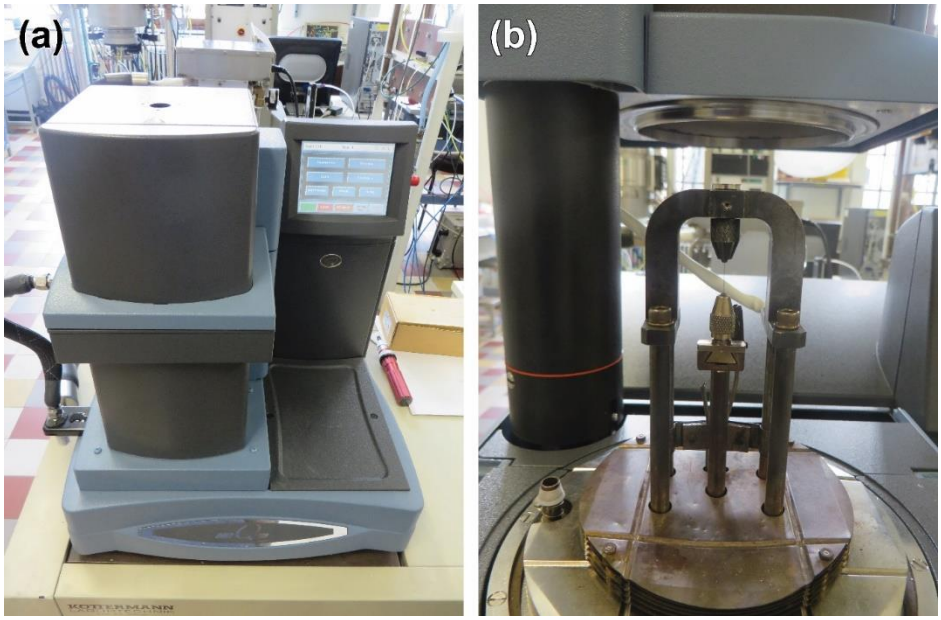

Figure 3–4 (a) Q800 DMA machine with closed chamber (left) and the control panel (right); (b) 150 μm micro–wire clamped by the grips inside the chamber.

3.4 TEM sample preparation

3.4.1 Electropolishing sample preparation

For conventional twin–jet electropolishing of bulk material the sample was sliced, grinded, cut and mechanically polished (mechanopolished) into the form of discs with 3 mm diameter and about 120 μm – 150 μm thickness. A spark erosion machine was used for the cutting of the 3 mm disk in order to avoid inducing mechanical stress during punching.

A Struers TenuPol apparatus (Figure 3–5) was used for the electropolishing. From the parameters and settings to be determined, the voltage, the electrolyte composition and electrolyte temperature depend on the sample material [123,147,150]. An electrolyte mixture of 80% methanol and 20% sulfuric acid was chosen from the electrolytes listed in Table 2–3 due to the ideal thinning of the Ni–Ti B2 matrix and also the fact that its working temperature (~ 0 °C) is fairly above the MT temperature range (M_s < -20 °C) of the materials used in this work. This guarantees maintaining the austenite phase during the sample preparation.

The voltage was set to ~ 18 V resulting in ~ 0.13 A current. The flow rate setting on the machine was set to ~ 5 and the photo sensitivity to ~ 8, both parameters having arbitrary units indicated on the setup.

Figure 3–5 The Struers TenuPol apparatus used in this work (control panel, electropolishing cell and tank, and the cooling system).

This conventional electropolishing method using commercially available setups was employed for bulk material. In Chapter 4 an in–house method developed to electropolish micro–wires will be introduced.

3.4.2 In–situ tensile test specimen preparation

In–situ nano–tensile testing of micro–wires requires a sequence of dedicated specimen preparation procedures to obtain the needed sample shape. First the wire is embedded in EPO–TEK 353ND [178] epoxy resin as a surrounding and supporting medium and is heated up to 120 °C for 5 min to cure the resin, as shown in Figure 3–6(a). Then the hardened resin embedding the wire is polished using a MultiPrep polishing system and a tripod polisher under an angle of ~ 10 ° with respect to the central axis of the wire. As a result a large elliptic cross–section of the wire is obtained, as can be seen in Figure 3–6(b). Fine grain diamond film discs (particles down to 0.5 micron diameter) were used to polish the wire in order to obtain a smooth surface and minimize any defects induced in the material by the polishing. In order to prevent charge accumulation on the non–conductive resin surface during the ensuing FIB procedures, a ~ 3 nm thick layer of carbon was deposited on the resin surface.

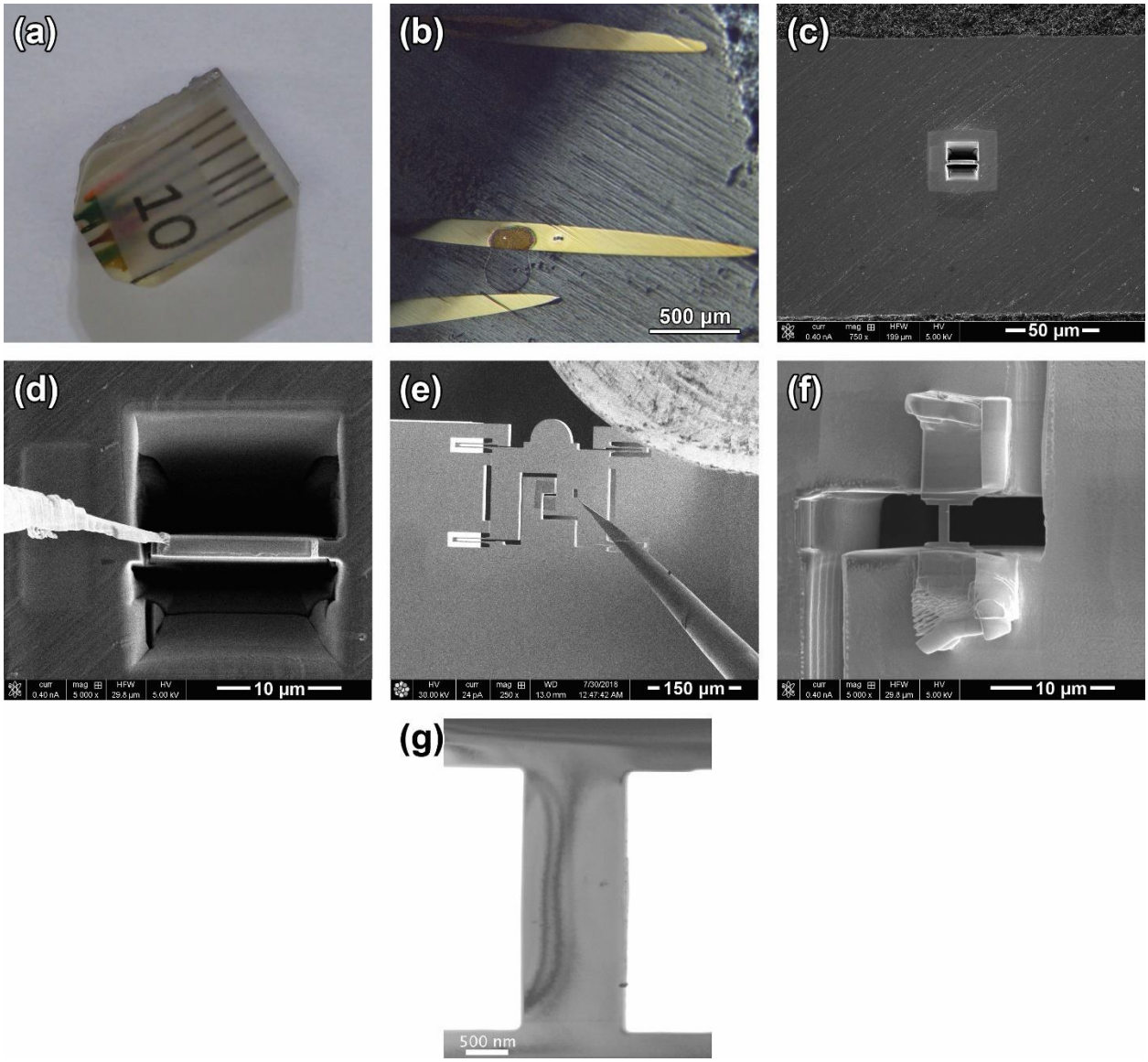

Figure 3–6 (a) Light optical microscope (LOM) image of some micro–wires embedded in resin; (b) LOM image of the polished wires revealing an elliptical cross–section; (c) scanning electron microscopy (SEM) image of the cross–section of a wire (horizontal) with a specimen cut parallel to the wire; (d) SEM image of the specimen attached to the FIB omni–probe ready for the last cut and being lift–out; (e) SEM image of the specimen being placed on the PTP gap; (f) SEM image of the specimen fixed on the PTP gap by Pt deposition and cut in the dog–bone shape; (g) TEM image of the specimen when mounted on the PicoIndenter holder and just before tensile test.

A dual–beam focused ion beam scanning electron microscopy system of an xT Nova Nanolab 200 FEI was used to cut the in–situ specimen from the above obtained sample, Figure 3–6(c), and detach it from the sample by lift–out, an intermediate step which is shown in Figure 3–6(d). The lifted specimen is then mounted on a MEMS push–to–pull (PTP) chip described in § 3.5.4.2, as shown in Figure 3–6(e), and fixed from two ends on the 2.5 µm gap between the fixed and mobile

parts by Pt deposition. Then the specimen is thinned to the final desired thickness and cut in a dog–bone shape perpendicular to the gap edges, as shown in Figure 3–6(f). FIB induced defects could be reduced by avoiding to expose the specimen while mounting on the PTP and careful thinning with low voltage in the last steps. Figure 3–6(g) shows a TEM image of the specimen when the PTP chip is mounted on the holder and is ready for the tensile test. (Details on the working principle of the holder are given in § 3.5.4).

3.5 Transmission electron microscopy

A transmission electron microscope operates with the same principles as a light optical microscope, with a fundamental difference that in a TEM an electron beam plays the role of imaging probe instead of light. Consequently, the illumination, magnification, projection and detection systems in a TEM are designed to function with an electron beam as the probe: the specimen must be electron transparent, the electron beam pathway from the electron source all way down to the detector, called column, must be vacuum and electromagnetic fields will act as lenses. The reason why a TEM provides a higher resolution than a light optical microscope is that the wavelength of the accelerated electron which, according to the Rayleigh criterion, defines the resolution of the instrument is considerably smaller than that of visual light.

A diagram of a conventional TEM is shown in Figure 3–7 which from top to bottom consists of: an electron gun which generates an electron beam at a high accelerating voltage, condenser lenses which condense the electron beam on the specimen, the electron transparent specimen, the objective lens which collects the transmitted electrons from the specimen and forms a pattern of reciprocal space in the back focal plane and an image of the specimen in the first image plane, and the projection lens which projects the image plane (in image mode) or back focal plane (in diffraction mode) of the objective lens on the florescent viewing screen or the charge–coupled device (CCD) camera which is the last element at the bottom of the column. In different heights of the column several apertures are introduced to the microscope such as a condenser aperture (to control the beam intensity and reduce the aberration), objective aperture (to acquire bright field (BF)– and dark field (DF)–TEM) and selected area (SA) aperture to define the area of which the diffraction pattern is acquired.

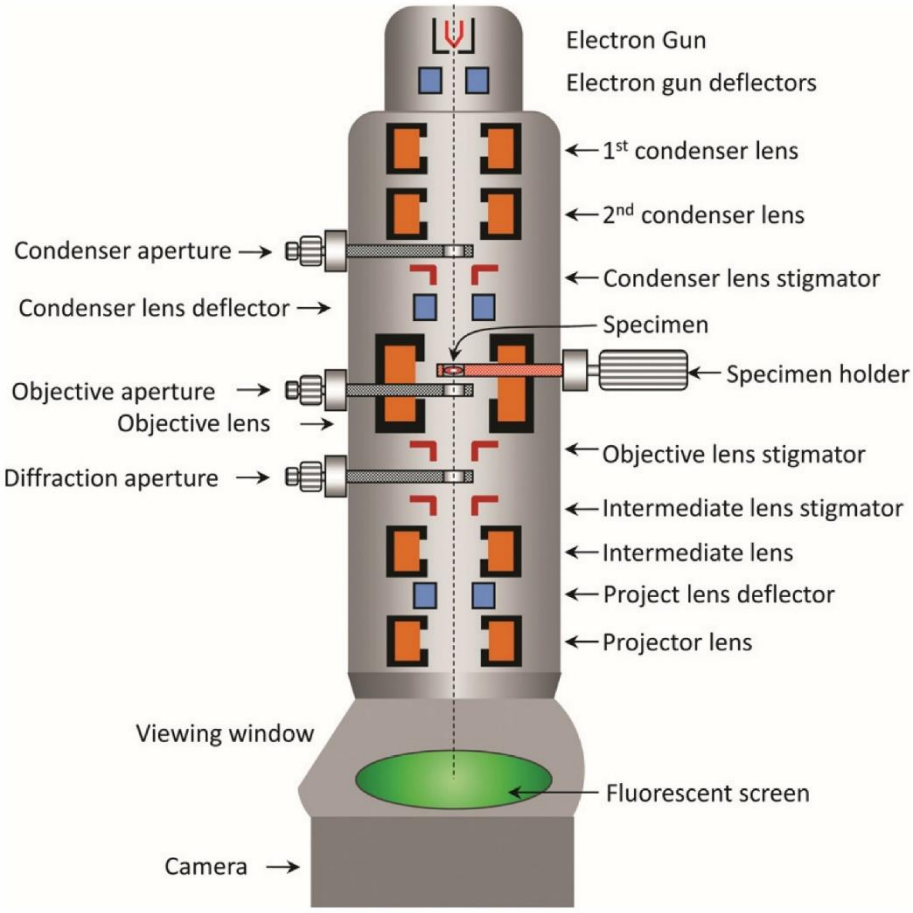

Figure 3–7 Schematic drawing of a TEM with the main stages [179].

A TEM is not only a high magnification and resolution microscope to visually observe the material microstructures, but also a powerful characterization instrument thanks to the electron diffraction mode and several other analytical side equipment. Contemporary TEM instruments have several different modes of operation, a few of which are used in this work and discussed in the following sections such as diffraction mode, imaging mode and automated crystallographic orientation mapping.

3.5.1 Electron diffraction

Electron diffraction (ED) is a powerful microscopy mode which allows very localized investigation of the crystallographic nature of the specimen. This includes whether the material is crystalline or amorphous, the crystallographic characteristics such as crystal orientation, symmetry, lattice parameter, etc. (for crystalline material), whether the material is single crystal or polycrystalline, what are the grain orientations (for polycrystalline material), whether the material

is single–phase or multi– phase, what are the orientation and symmetry relations of the phases (for multi–phase materials), etc. [180].

ED is formed due to the interaction of the electron beam with the atomic planes of the material and the constructive and destructive interference of the diffracted beams caused by their phase difference. In Figure 3–8(a) the geometry of diffraction of two parallel rays with two planes of atoms with distance d and viewed under an angle θ is shown. The difference in path length of the two rays is $2d \sin\theta$ and the wave interference is constructive when this difference in path length is equal to an integer multiple of the wavelength λ, which is called the Bragg condition:

$$2d \sin\theta = n\lambda \tag{3.1}$$

When the Bragg condition is satisfied, this yields the formation of rods in reciprocal space. Those reciprocal rods that touch the Ewald sphere, an imaginary sphere with the radius inversely proportional to the wavelength of the electron beam and touching the reciprocal plane at its origin, appear as spots in the diffraction pattern, which is shown schematically in Figure 3–8(b) and (c).

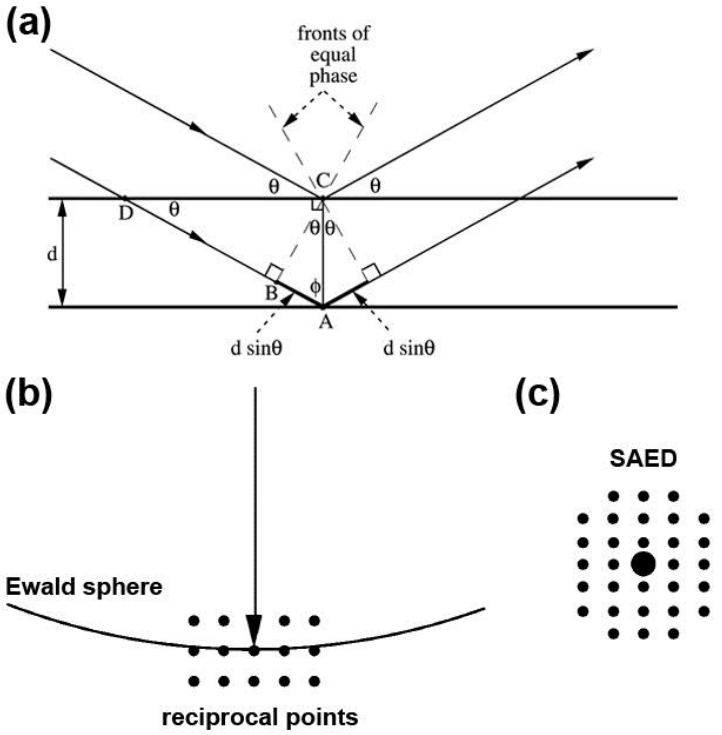

Figure 3–8 (a) Interference of a wave scattered from two planes of atoms with distance d; (b) a cut of the Ewald sphere touching a reciprocal plane and (c) the resulting selected area electron diffraction pattern [181].

In order to exclusively obtain ED from a small area of the material, e.g., a single grain, precipitate, etc., a selected area aperture with different size can be inserted to restrict the area of which the ED is acquired. The obtained ED is called a selected area electron diffraction pattern, an example of which is shown in Figure 3–9(a). The central spot in the SAED results from the non–diffracted electrons passing through the specimen while any other spot is formed by and represents a family of atomic planes for which the incident beam satisfies the Bragg law. Therefore, the lattice parameters and symmetry present in the specimen crystal are reflected in the SAED in terms of, respectively, the distance between the central spot and diffracted spots and the angles between the diffracted spots. Since the SAED is a cross–section of the reciprocal space, distances in the SAED are inversely proportional to the corresponding interplanar distances in the crystal in real space.

As one can switch between the ED and image mode by just pushing a button on the microscope, ED is an easy and quick way to obtain crystallographic information of small area of the specimen and relate these to the features observed in the image mode.

Structure factor calculation for body–centered cubic (BCC) structures shows that the corresponding SAED spots with indices h+k+l=2n+1 are extinct [181]. In Figure 3–9(b) a simulated ED for Fe BCC is shown in which between each two visible spots in the horizontal direction one spot (outlined by $\times$) is extinct. In Ni–Ti with ordered B2 CsCl structure, however, odd values of h+k+l are also present due to the different atomic scattering factor of Ni and Ti, but weaker than the even values [71]. This can be observed in the simulated ED of the Ni–Ti in the Figure 3–9(c).

3.5.1.1 Diffuse intensity in SAED

In some diffraction patterns a diffuse intensity can be observed in the area between the Bragg spots, as seen in Figure 3–9(d). In a perfect crystal the incident electrons end up either in the central or diffracted spots. Therefore, any intensity away from the Bragg spots includes information about additional structural configurations in the material. For example, an amorphous region will yield diffuse rings with a diameter corresponding to the average interatomic distance in the amorphous material [182]. In the present work, the diffuse intensities investigated have particular geometric configurations that can be interpreted as originating from particular clusters inside the perfect crystal, as further explained in Chapter 5.

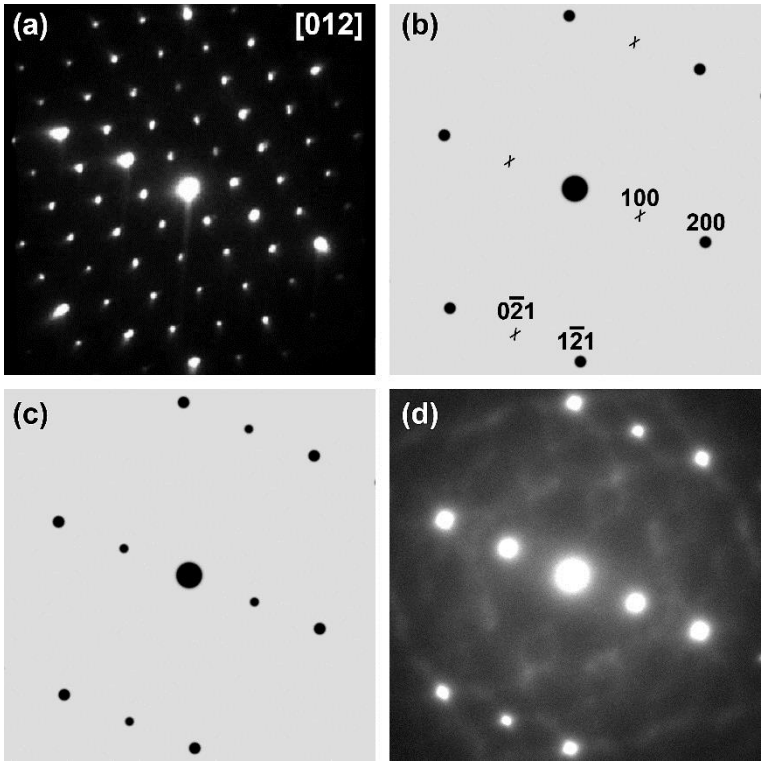

Figure 3–9 (a) $[012]_{B2}$ ED of Ni–Ti (main spots) and Ni_4Ti_3 precipitates (superspots) [175]; (b) simulated ED of $[012]_{BCC}$ of Fe having extinct spots; (c) simulated $[012]_{B2}$ ED of Ni–Ti with no extinct spots due to the B2 ordering; (d) $[012]_{B2}$ ED of Ni–Ti revealing diffuse intensity between the spots.

Diffuse intensity is usually very weak and not trivial to record on a CCD. In order to properly record diffuse intensity the ED must be exactly focused [183] and –if possible– acquired by a large SA aperture. The exposure time should be chosen short enough not to over–expose and damage the CCD. The beam stopper can be inserted in order to block the central (and maybe neighboring) spots and allow longer exposure time. Another possibility (applied in Chapter 6) is to acquire several images and overlap them afterwards. This approach is more effective than just increasing the exposure time due to the noise reduction achieved by overlapping.

While the obtained SAEDs were directly used for quantification, the presented SAEDs –including those shown in this thesis– have been rescaled in intensity to be properly seen in the print.

3.5.1.2 Focusing SAED patterns

SAED should ideally be acquired when the incident beam to the specimen is parallel so that the objective lens makes the pattern of reciprocal space in the back focal plane from where the

diffraction lens projects it onto the viewing screen. Since both condenser and diffraction lenses are involved in the formation of the final image, one could have one of those lenses defocused and compensate its effect with the other lens and still obtain a "focused" diffraction on the screen. In this case, however, the incident beam is not parallel and the pattern of reciprocal space is below or above the back focal plane, the SAED is slightly rotated and the camera length shown on the microscope is incorrect (so it cannot be used to accurately determine interplanar spacing of crystals using the distance of the diffraction spots).

In order to have the SAED in focus one should thus ensure that the reciprocal pattern is formed on the back focal plane. The image of an objective aperture can be used for this purpose since the latter is located in the back focal plane. After inserting the objective aperture, the diffraction lens (focus) knob should be used to carefully make the edge of the objective aperture sharp, i.e., in focus. In this way the diffraction lens is properly focused and now the condenser lens (intensity) knob should be used to focus the diffraction pattern [184].

3.5.1.3 Image and diffraction orientation relation

In TEM the Lorentz force causes the electrons in a helical path around the optical axis. Any change in the excitation of lenses such as an intermediate lens used to switch between the diffraction and image mode yields a rotation around the optical axis. Therefore, the TEM image and the ED pattern of a specimen are often rotated with respect to each other by a finite angle depending on the used magnification and camera length. So if the ED is employed to find the in–plane crystallographic orientation of a TEM image, e.g., for the in–situ tensile tests, this image–diffraction orientation relation is required to properly assign the specimen crystallographic orientation. For this purpose the "shadow image" which contains both the diffraction and image information can be used. When an ED pattern is focused in the back focal plane, the pattern is spot with no image information. However, if the ED is defocused, the diffraction spots expand into discs showing a small image from the area from where the diffraction information is originating. The central spot shows the bright field image and each diffracted spot contains the corresponding dark field image.

Now one can easily find the orientation relation between the image and the diffraction pattern, as shown in Figure 3–10. The shadow image can also be used in order to track a desired grain or particle and correct for the sideways movement when tilting in the diffraction mode [185,186].

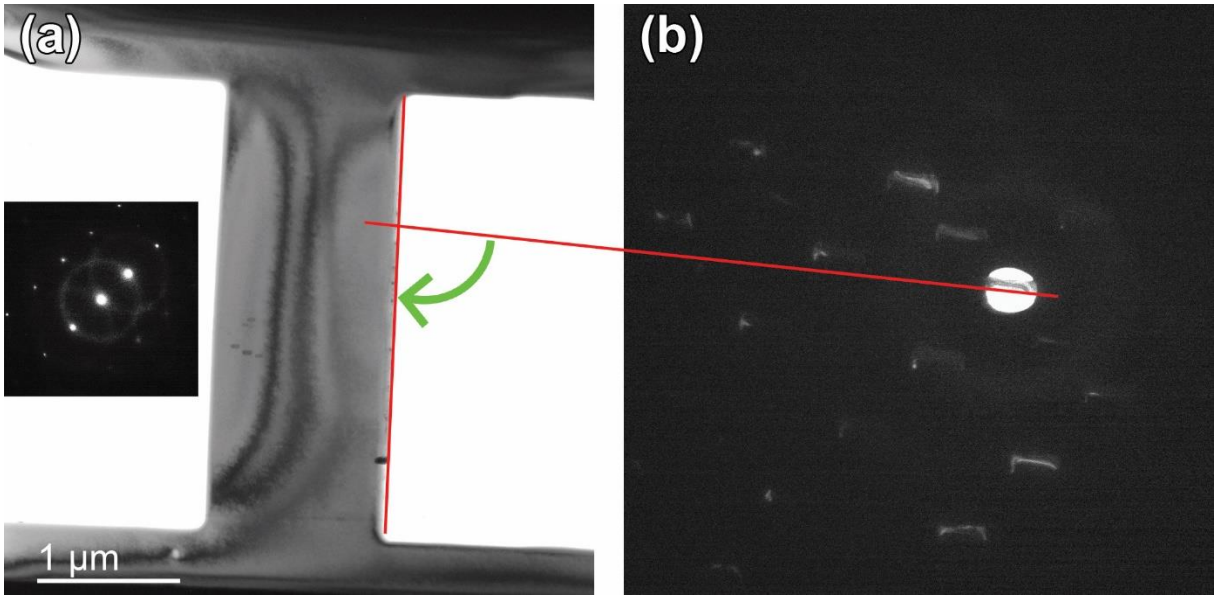

Figure 3–10 (a) BF–TEM image of a tensile test specimen with SAED as inset; (b) defocused SAED showing shadow image of the specimen and revealing the angle under which the SAED inset should be rotated in order to match the image mode.

3.5.2 Bright field TEM Imaging

A TEM is in image mode when the projection lens projects the image plane of the objective lens on the viewing screen. BF–TEM is the image mode in which most images presented in this work are acquired. In this method the objective aperture is inserted in the back focal plane of the objective lens allowing only the transmitted beam to pass and contribute to the image formation. As the diffracted beams are excluded from a BF–TEM image, the areas from which beams are diffracted (being in Bragg condition) show up as dark contrast in the image. This contrast will change when the specimen orientation in the microscope is changed. The absorption of electrons in thicker areas of the specimen is another source of contrast in the BF–TEM images, but depends much less on specimen orientation.

3.5.3 ACOM–TEM

While SAED is acquired over a "large" area of the specimen and thus often yields averaged information, if ED is collected using a small probe it allows local analysis of structure and orientation. This is the core idea of ACOM–TEM [187,188] in which a nano–beam diffraction scanning is performed over a rectangular mesh pattern and collecting very local ED data. By matching the acquired ED with software generated ED patterns the crystal phase and orientation of each scanning point is found and used to draw a phase and/or orientation map.

This method is the TEM analogy of EBSD in SEM. The nano–size probe and scanning mesh allows crystallographic orientation identification with sizes down to a few nanometers. Moreover, acquiring large numbers of ED patterns provides enough data for statistical analysis. Also, precession of the incident beam can be used to minimize the dynamical effects in the diffraction [189].

3.5.4 In–situ nano–tensile tests

The in–situ nano–tensile tests presented in Chapter 7 of this thesis were performed using a Hysitron PI 95 TEM Picoindenter and a Push–to–Pull MEMS device, both from Bruker Inc. and which are described in this section.

3.5.4.1 Nano–tensile test TEM holder

The Hysitron PI 95 TEM Picoindenter holder is equipped with a quantitative indenter which is precisely controlled by the data acquisition computer through a control unit. The system provides time, displacement and force data while the in–situ nano–mechanical test is being performed and live observed. During the test also the TEM CCD screen is grabbed by the integrated video interface and synced with the collected quantitative mechanical data. The holder is shown in Figure 3–11 with an enlarged inset showing the PTP device installed on the holder.

The tip positioning and mechanical testing is controlled in three different scales. First, the rough positioning in mm scale is done by turning the fully mechanical three–axis positioner knobs (golden wheel at the left of the holder in Figure 3–11) by hand under the light optical microscope and afterwards at low magnification TEM (from millimeters to few micrometers distance between the indenter and the tip of the PTP chip). In the second step a 3D piezoelectric actuator controlled by the software is used for fine positioning and approaching the tip of the indenter (from a few micrometers distance till touching). In the third step by starting the test, the transducer for electrostatic actuation and capacitive displacement sensing for acquiring quantitative mechanical data is activated by the software. The transducer has a capacitive displacement sensor for acquiring quantitative nanoscale mechanical data. The holder is single tilt and has two control modes, displacement and load control. The maximum force is 1 mN (with 0.2 μN noise floor) and maximum displacement is 1 μm (1 nm noise floor) [190].

Figure 3–11 A Hysitron PI 95 TEM Picoindenter with PTP device installed.

3.5.4.2 Push–to–pull MEMS device

The PTP chip designed by Bruker to work with the PI 95 PicoIndenter holder is a device that converts the compressive (push) force provided by the holder into a tensile (pull) force [100,191,192]. This is possible due to the special design of the PTP wafer, shown in Figure 3–12(a), consisting of a fixed (blue shaded) and a mobile (pink shaded) part connected by four identical spring–like silicon pieces, as indicated in the figure. Now by applying a compressive force on the mobile part of the PTP device (push arrow in Figure 3–12(a)), the gap's width between the fixed and mobile part of the device extends and induces a tensile force on the specimen. Figure 3–12(b) is the enlargement of the red square in Figure 3–12(a) showing the edges of the gap and the specimen in between.

The force applied on the mobile part of the device by the PicoIndenter holder acts on both specimen and the PTP springs. So one can write:

$$F_H = F_S + F_{PTP} \tag{3.2}$$

in which F_H is the load measured by the holder and F_S and F_{PTP} are the force applied on the specimen and PTP springs, respectively. If Δl is the elongation of the specimen due to pulling and K_{PTP} is the PTP springs stiffness, 15 N/m in this work (value provided by the company), then the PTP force is:

$$F_{PTP} = K_{PTP}.\Delta l \tag{3.3}$$

which yields the force applied on the specimen using equation 3.2.

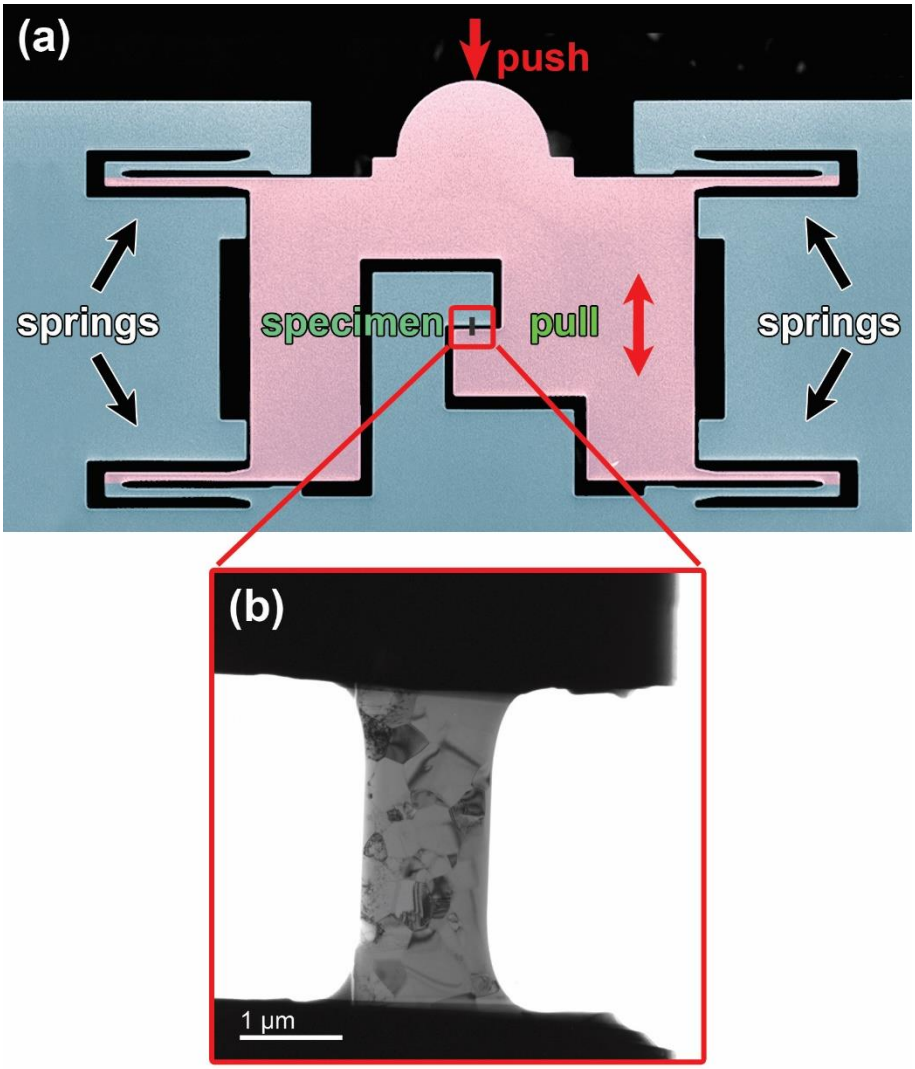

Figure 3–12 (a) SEM image of a PTP chip revealing four springs, fixed and mobile parts overlaid with blue and pink colors, respectively, and where the specimen is mounted between the two parts framed by the red square; (b) TEM image of the specimen and the PTP edges, enlargement of the red square in (a).

3.5.5 TEM specimen thickness measurements

For proper interpretation of the various results in this work, it is important to have some information on the thickness of the specimens. This is of importance for the in–situ nano–tensile tests in order to investigate the effect of specimen thickness on the transformation, and in the thermal cycled specimens since the observed diffuse intensity is strongly thickness dependent. In this work two specimen thickness measurement methods were applied. For the investigations of the nano– and microstructures of thermally cycled specimens the CBED method was used since the TEM experiments were also primarily performed in reciprocal space, so no back and forth

switching between different microscope modes was required. The tensile test specimens were measured by EELS, since the corresponding holder did not allow double tilt to get to the specific orientations required for CBED.

One should be aware of the validity of any thickness measurements over a finite area of a non–homogeneous thickness specimen. In electropolished specimens due to the wedge shape of the thin area, presenting one value as the thickness of an area selected by the SA aperture is of limited precision. In such cases the thickness of the center of the area is measured.

3.5.5.1 Convergent beam electron diffraction

CBED requires inserting no apertures and is simply obtained by converging the electron beam on the specimen. Unlike SAED in which a parallel beam illuminates a micron–scale area of the specimen (e.g., a disk of 0.2 μm – 16 μm SA aperture size for the TEM employed in this work), a condensed beam with a diameter of a few nm in size is required for CBED.

Using CBED is the oldest specimen thickness measurement technique [193] and yet provides accurate results. Across a CBED disk a range of diffraction conditions (range of deviation vectors $\boldsymbol{s}$) exists. Being in two–beam conditions, $s = 0$ in the center of the disc and non–zero anywhere else on the disc. These variations of $\boldsymbol{s}$ yield oscillations of intensity in the discs which can be used to quantify the specimen thickness [181]. For this, one requires to insert the largest condenser aperture which is still small enough to return a non–overlapping CBED disc (Kossel–Mollenstedt) pattern. A reflection (best to be in the 7 1/nm – 1.3 1/nm range [193]) should be chosen as the second spot together with the central spot. As the measured thickness is the specimen thickness in the beam direction and not the true thickness, the reflection should also be chosen where the orientation of the specimen is close to the one desired for the following main experiment. The CBED acquisition should be quick due to the rapid contamination build up caused by the focused beam.

A CBED of Ni–Ti having 000 and 121 spots in two–beam conditions is shown in Figure 3–13. $2\theta_d$ is the separation of the 000 and the hkl disc and $\Delta\theta_i$ the distance between each dark fringe and the central bright fringe where $s = 0$. The deviation of the i^{th} fringe (i being an integer) is found by the equation:

$$s_i = \lambda \frac{\Delta\theta_i}{2\theta_d d^2} \tag{3.4}$$

in which λ is the electron wavelength and d is the hkl interplanar spacing. Now the thickness t is found by:

$$\frac{1}{t^2} = \frac{1}{\xi_g^2 n_k^2} + \frac{s_i^2}{n_k^2} \tag{3.5}$$

in which ξ_g is the extinction distance and n_k is an integer equal to i or different from i by a constant integer. Plotting $\frac{s_i^2}{n_k^2}$ versus $\frac{1}{n_k^2}$ gives $\frac{1}{t^2}$ by the intercept on the y axis and $\frac{1}{\xi^2}$ as the slope. This is done by guessing different sequences of integer values of n_k (e.g., 1,2,3,… or 2,3,4,.. etc.) until $\frac{s_i^2}{n_k^2}$ versus $\frac{1}{n_k^2}$ plot becomes a straight line [181,193–195].

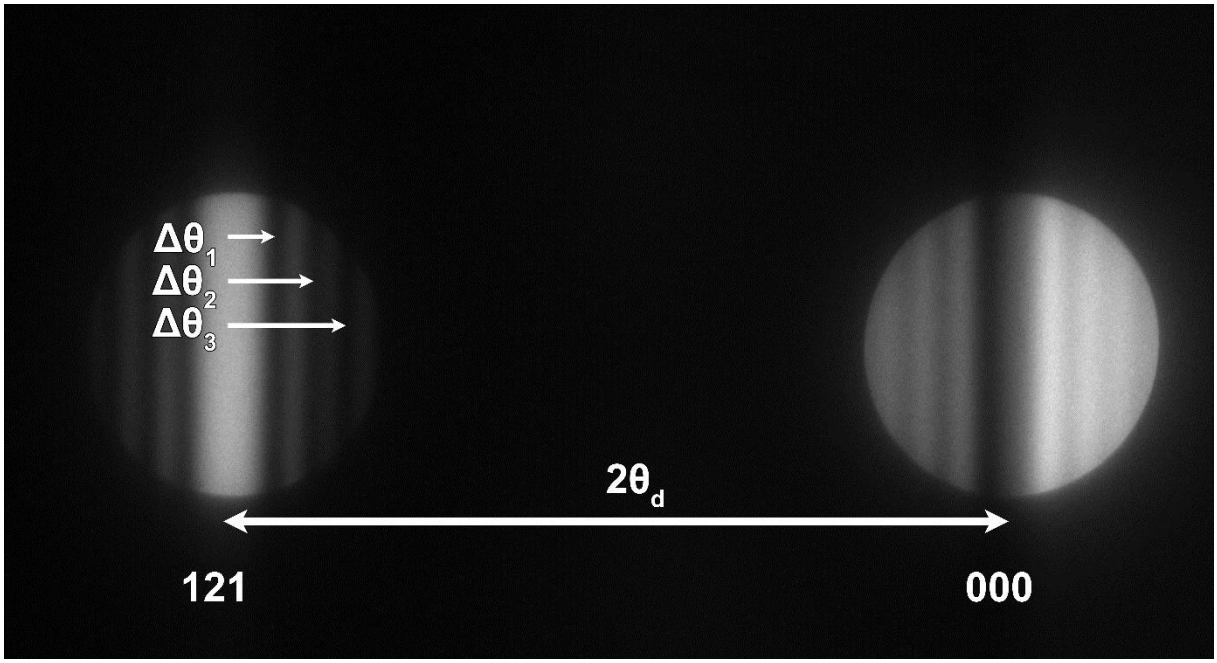

Figure 3–13 CBED of Ni–Ti in two–beam conditions showing the central and 121_{B2} disks and the required measures.

3.5.5.2 EELS

When the electron beam exposes the specimen in a TEM some electrons interact with the specimen atoms and loose a fraction of their energy (inelastically scattered electrons) while the rest leave the specimen with the same energy (un– or elastically scattered electrons). The inelastically scattered electrons contain information about the chemical and structural properties of the specimen. In EELS mode the energy of the electrons passing through the specimen is measured with an electron spectrometer.

As a thicker specimen yields more electron–specimen interactions, the ratio of the number of elastic and inelastic electrons can be used as a measure of the specimen thickness. This is done by the integration of the area under the zero–loss peak (I_0) and that of the total spectrum (I_t), as shown in Figure 3–14. The thickness is then calculated by the so called log–ratio formula:

$$t = \lambda \, ln(\frac{I_t}{I_0}) \tag{3.6}$$

in which t is the thickness and λ the total inelastic mean free path in the specific material [196,197].

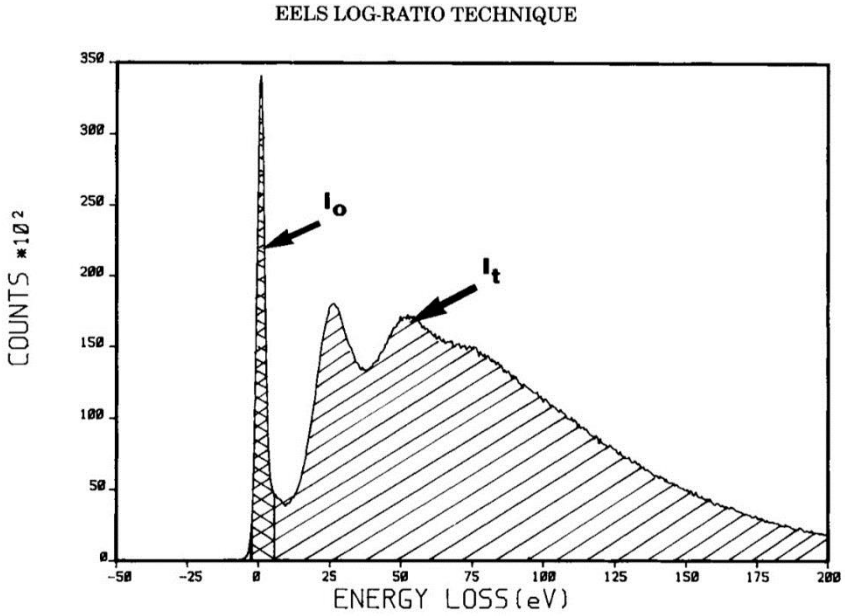

Figure 3–14 EELS of carbon film showing the area under the zero–loss peak (I_0) and the total area under the full spectrum (I_t) [197].

3.6 Cluster Model

If a second phase is present as a superstructure in a given material it leads to the formation of superspots in the SAED. However, if the superstructure is not fully ordered, diffuse scattering rather than sharp spots in between the Bragg spots will be observed. In order to find the structural configurations underlying the diffuse intensities in the SAEDs, the Cluster Model [198–201], which assigns reciprocal diffuse intensity to micro–domains in real space, is used. In this section, first the kinematical diffuse intensity amplitude is derived. Then it is applied for a binary system, after which the periodicity of the diffuse intensity is used to obtain the ordering relation.

We start from a specimen extending in the x–y directions of the Cartesian coordinates system. The incident electron beam with wave vector $\boldsymbol{k}_i$ coming along the z axis hits the specimen. $\boldsymbol{k}$, a general vector in reciprocal space can be written as:

$$\boldsymbol{k} = \boldsymbol{k}_d - \boldsymbol{k}_i \tag{3.7}$$

in which $\boldsymbol{k}_d$ is the wave vector of a diffracted beam. Now if $\boldsymbol{g}$ is the diffraction vector of the reflecting lattice planes lying in the x–y plane, $\boldsymbol{k}$ can also be written as the deviation $\boldsymbol{s}$ from $\boldsymbol{g}$:

$$\boldsymbol{k} = \boldsymbol{g} + \boldsymbol{s} \tag{3.8}$$

The structure factor of a perfect crystal unit cell is defined as:

$$F^{(0)}(\boldsymbol{g}) = \sum_j f_j \, e^{2\pi i \boldsymbol{g}.\boldsymbol{r}_j} \tag{3.9}$$

in which f_j is the atomic scattering factor of the atom at position $\boldsymbol{r}_j$ and the summation is over lattice sites j in the unit cell. The kinematical diffraction amplitude in case of local variation of the structure is:

$$A(\boldsymbol{k}) = \sum_i F_i \, (\boldsymbol{g}) e^{2\pi i \boldsymbol{k}.\boldsymbol{r}_i} \tag{3.10}$$

where $\boldsymbol{i}$ runs over all lattice vectors $\boldsymbol{r}_i$ of the positions of the unit cells and F_i is the structure factor of the unit cell at $\boldsymbol{r}_i$ position.

If N is the number of unit cells, the average structure factor can be introduced as:

$$\langle F(\boldsymbol{g}) \rangle = \frac{1}{N} \sum_i F_i(\boldsymbol{g}) \tag{3.11}$$

The deviation of the local structure factor $F_i(\boldsymbol{g})$ from the average structure factor $\langle F(\boldsymbol{g}) \rangle$ is found as:

$$\Delta F_i(\boldsymbol{g}) = F_i(\boldsymbol{g}) - \langle F(\boldsymbol{g}) \rangle \tag{3.12}$$

By substitution of $F_i(\boldsymbol{g})$ obtained from equation 3.12 in equation 3.10, the kinematical diffraction amplitude $A(\boldsymbol{k})$ can be rewritten as:

$$A(\boldsymbol{k}) = \langle F(\boldsymbol{g}) \rangle \sum_i e^{2\pi i \boldsymbol{k}.\boldsymbol{r}_i} + \sum_i \Delta F_i(\boldsymbol{k}) \, e^{2\pi i \boldsymbol{k}.\boldsymbol{r}_i} \tag{3.13}$$

The first term yields sharp Bragg reflections at $\boldsymbol{k} = \boldsymbol{g}$.

The second term describes the diffuse intensity which vanishes for $\boldsymbol{k} = \boldsymbol{g}$, because per definition:

$$\sum_i \Delta F_i(\boldsymbol{g}) = 0 \tag{3.14}$$

Now the total diffracted intensity $I(\boldsymbol{k})$ can be split into two distinct terms, the Bragg reflection $I^{(B)}(\boldsymbol{g})$ and the diffuse diffraction $I^{(D)}(\boldsymbol{k})$:

$$I(\boldsymbol{k}) = I^{(B)}(\boldsymbol{g}) + I^{(D)}(\boldsymbol{k}) \tag{3.15}$$

We focus on the second term in which we are interested. The intensity of the diffuse diffraction $I^{(D)}(\boldsymbol{k})$ can be calculated as the square of the absolute of the second term of equation 3.13:

$$I^{(D)}(\boldsymbol{k}) = \sum_{i,j} \Delta F_i(\boldsymbol{k}) \Delta F_j^*(\boldsymbol{k}) e^{2\pi i \boldsymbol{k}.(\boldsymbol{r}_i - \boldsymbol{r}_j)} \tag{3.16}$$

which by changing the index of the summation becomes:

$$I^{(D)}(\boldsymbol{k}) = \sum_k e^{2\pi i \boldsymbol{k}.\boldsymbol{r}_k} \sum_j \Delta F_j^*(\boldsymbol{k}) \Delta F_{j+k}(\boldsymbol{k}) \tag{3.17}$$

Now these mathematical derivations are applied to the Ni–Ti system.

In a binary system of Ni and Ti atoms with their atomic fraction of m_{Ni} and m_{Ti}, respectively, in such a way that:

$$m_{Ni} + m_{Ti} = 1 \tag{3.18}$$

and $f_{Ni}(\boldsymbol{k})$ and $f_{Ti}(\boldsymbol{k})$ as scattering factors for Ni and Ti, respectively, the average structure factor (equation 3.11) is found to be:

$$\langle F(\boldsymbol{k}) \rangle = m_{Ni} f_{Ni}(\boldsymbol{k}) + m_{Ti} f_{Ti}(\boldsymbol{k}) \tag{3.19}$$

and since

$$F_i(\boldsymbol{k}) = \begin{cases} f_{Ni} & Ni \text{ on position } i \\ f_{Ti} & Ti \text{ on position } i \end{cases} \tag{3.20}$$

the deviation of the local structure factor from the average structure factor, $\Delta F_i(\boldsymbol{k})$ (equation 3.12) can be obtained as:

$$\Delta F_i(\boldsymbol{k}) = \begin{cases} m_{Ti}[f_{Ni}(\boldsymbol{k}) - f_{Ti}(\boldsymbol{k})] & Ni \text{ on position } i \\ -m_{Ni}[f_{Ni}(\boldsymbol{k}) - f_{Ti}(\boldsymbol{k})] & Ti \text{ on position } i \end{cases} \tag{3.21}$$

which by using the Flinn site occupation operator σ_i defined as follows:

$$\sigma_i = \begin{cases} m_{Ti} & Ni\ on\ position\ i \\ -m_{Ni} & Ti\ on\ position\ i \end{cases} \tag{3.22}$$

can be simplified to:

$$\Delta F_i(\boldsymbol{k}) = \sigma_i[f_{Ni}(\boldsymbol{k}) - f_{Ti}(\boldsymbol{k})] \tag{3.23}$$

Now using the second term of equation 3.13, the diffuse scattering amplitude $A^{(D)}(\boldsymbol{k})$ can be written as:

$$A^{(D)}(\boldsymbol{k}) = [f_{Ni}(\boldsymbol{k}) - f_{Ti}(\boldsymbol{k})] \sum_i \sigma_i\, e^{2\pi i \boldsymbol{k}.\boldsymbol{r}_i} \tag{3.24}$$

and the obtained equation can be normalized to:

$$\hat{A}^{(D)}(\boldsymbol{k}) = \frac{A^{(D)}(\boldsymbol{k})}{f_{Ni}(\boldsymbol{k}) - f_{Ti}(\boldsymbol{k})} = \sum_i \sigma_i\, e^{2\pi i \boldsymbol{k}.\boldsymbol{r}_i} \tag{3.25}$$

Now the geometrical information about the occupancy of the sites in the σ_i is completely separated from the physical information of the atoms in $f_{Ni}(\boldsymbol{k}) - f_{Ti}(\boldsymbol{k})$.

The normalized diffuse intensity is stated as:

$$\hat{I}^{(D)}(\boldsymbol{k}) = \sum_{i,j} \sigma_i \sigma_j e^{2\pi i \boldsymbol{k}.(\boldsymbol{r}_i - \boldsymbol{r}_j)} \tag{3.26}$$

$$= \sum_k e^{2\pi i \boldsymbol{k}.\boldsymbol{r}_k} \sum_j \sigma_j \sigma_{j+k} \tag{3.27}$$

The Warren–Cowley short–range order α_k is defined as:

$$\alpha_k = \alpha_{\boldsymbol{r}_k} = \frac{\langle \sigma_j \sigma_{j+k} \rangle}{m_{Ni} m_{Ti}} = \frac{1}{N} \frac{1}{m_{Ni} m_{Ti}} \sum_j \sigma_j \sigma_{j+k} \tag{3.28}$$

which helps to write equation 3.27 as:

$$\hat{I}^{(D)}(\boldsymbol{k}) = N m_{Ni} m_{Ti} \sum_k \alpha_k e^{2\pi i \boldsymbol{k}.\boldsymbol{r}_k} \tag{3.29}$$

If the diffuse intensity is concentrated near a periodical locus, like a surface or a curve, real space information from the locus of the reciprocal diffuse intensity can be derived. If the locus has the translational symmetry of the reciprocal lattice, it can be presented by the following Fourier series:

$$l(\boldsymbol{k}) = \sum_{k} \omega_k e^{2\pi i \boldsymbol{k}.\boldsymbol{r}_k} = 0 \tag{3.30}$$

If all diffuse intensity is concentrated on the locus $l(\boldsymbol{k})$, the following identity holds:

$$\hat{A}^{(D)}(\boldsymbol{k}).\, l(\boldsymbol{k}) = 0 \qquad for\ all\ \boldsymbol{k} \tag{3.31}$$

Substitution of equation 3.25 and equation 3.30 into equation 3.31 leads to:

$$\sum_{i,k} \sigma_i \omega_k e^{2\pi i \boldsymbol{k}.(\boldsymbol{r}_i - \boldsymbol{r}_k)} = 0 \qquad for\ all\ \boldsymbol{k} \tag{3.32}$$

and thus

$$\sum_{j} e^{2\pi i \boldsymbol{k}.\boldsymbol{r}_j} \left[\sum_{k} \omega_k \sigma_{j+k}\right] = 0 \qquad for\ all\ \boldsymbol{k} \tag{3.33}$$

which results in:

$$\sum_{k} \omega_k \sigma_{j+k} = 0 \qquad for\ all\ \boldsymbol{k} \tag{3.34}$$

which is a linear relation between the Flynn operators and referred to as the ordering relation.

If coefficients ω_k can be determined from the experimental diffuse intensity, the linear relation identifies the lattice sites with the same composition in the cluster via σ [182,202].

Chapter 4:

Twin–jet electropolishing for TEM specimen preparation of Ni–Ti micro–wires

In this chapter a method developed to use a conventional electropolishing apparatus to prepare TEM specimens from micro–size wires is presented.

4.1 Introduction

The necessity for this work became apparent during transmission electron microscopy (TEM) investigations of Ni nano–clusters in $Ni_{50.8}Ti_{49.2}$ micro–wires with a diameter of 150 μm, which will be presented in Chapter 6. Due to the small diameter of the wire, cross–sectional FIB specimen preparation seemed to be the most appropriate thinning procedure. However, FIB induced damage severely hampers a proper interpretation of the intended high resolution images needed to investigate the expected nano–precipitates. Moreover, the 5×10 μm^2 dimensions of a typical FIB specimen do not allow proper statistical investigations when looking for averaged diffraction data. Therefore, the use of conventional electropolishing for obtaining thin TEM specimens was reconsidered.

Twin–jet electropolishing is one of the cheapest, fastest and cleanest methods to prepare TEM specimens from bulk electrically conductive materials such as metals and alloys. In this method the material is electrochemically removed from both sides of a mechanically thinned disc of, e.g., 3 mm diameter and 100 μm – 150 μm thick, until sample perforation occurs. The surroundings of the small perforation are sufficiently thin for TEM. The achieved specimen is free of mechanical or ion damage, typically shows large regions of electron transparent material, is easy to handle due to the rigid rim which supports and protects the thin area in the center and requires no grid support to be mounted on the TEM holder [133,144]. Also heating of the specimen by the electron beam during TEM investigations remains limited since the heat generated in the thin region is rapidly dissipated by the rather thick surroundings [203]. Electropolishing is specifically appropriate for (inter)metallic samples, since these materials are too soft for crushing and easily damaged by ion milling [153]. However, the conventional twin–jet electropolishing apparatuses are designed for bulk material, namely discs of 3 mm or 2.3 mm diameter and can normally not be applied for specimens of smaller size such as micro–wires. In Figure 4–1 the small diameter of the micro–wire under consideration can visually be compared with the perforation size of a typical 3 mm electropolished specimen.

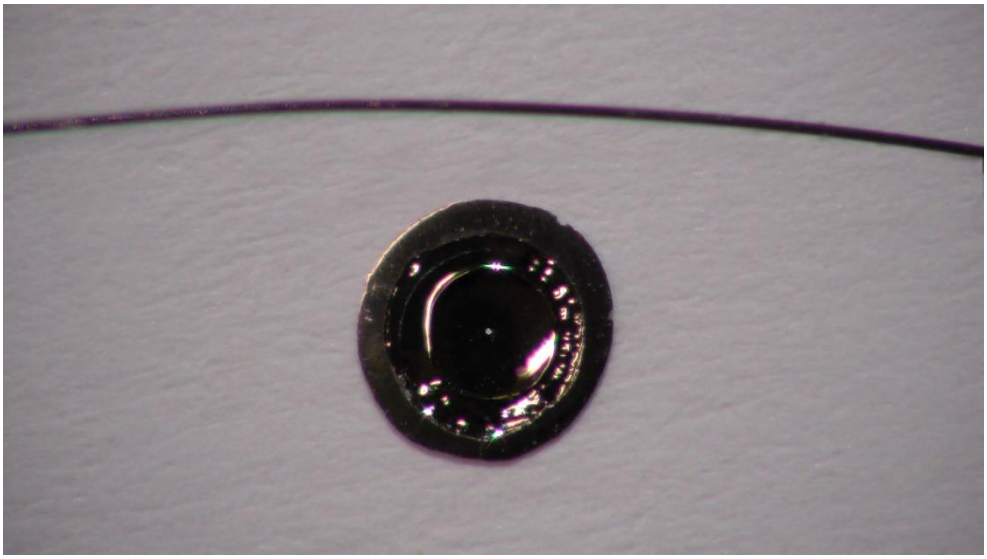

Figure 4–1 Comparing perforation size of a 3mm disc electropolished specimen and diameter of a 150 μm Ni–Ti wire.

Very few studies have been performed on TEM specimen electropolishing of samples smaller than the conventional 3 mm or 2.3 mm discs. Stickler & Engle [204] electropolished 1 mm diameter wires of tungsten and bismuth telluride in a two–step procedure. The first step, indentation on the specimen (dimpling), is performed with a vertical gravity fed electrolyte machine using a 0.01mm nozzle with a platinum wire as cathode, as shown in Figure 4–2(a). In the second step final electropolishing is performed in an electrolyte bath equipped with a light source and a light microscope to detect the first break–through of the indentation, as presented diagrammatically in Figure 4–2(b). The perforation occurs on the region thinned in the first step. This method cannot be used for wires smaller than 1 mm, such as the 150 μm wires in this work.

Kestel [205] introduced three methods for TEM electropolishing of undersized samples. In the first method, plating or coating the wire with a metal to increase its diameter to 3 mm, a 120 μm stainless steel wire is plated with nickel, after which it is sectioned and grinded to the desired size disc. Then it is electropolished. If the hole is at the interface of wire and plating, it is masked with lacquer, covering all but the wire center. After electropolishing again, a second perforation, this time on the wire will appear, as shown in Figure 4–2(c).

As a second approach, an arbitrary shaped sample of the size of 1.5 mm × 2 mm is placed on a 3 mm standard copper disc with a 1 mm hole in the center, as shown in Figure 4–2(d). The sample is fixed and coated with lacquer on all but the center of the sample and is then electropolished.

The third method introduced by Kestel [205] is embedding the sample in molten metal. As shown in Figure 4–2(e) a 250 μm thoriated tungsten wire is embedded into molten gold and electropolished.

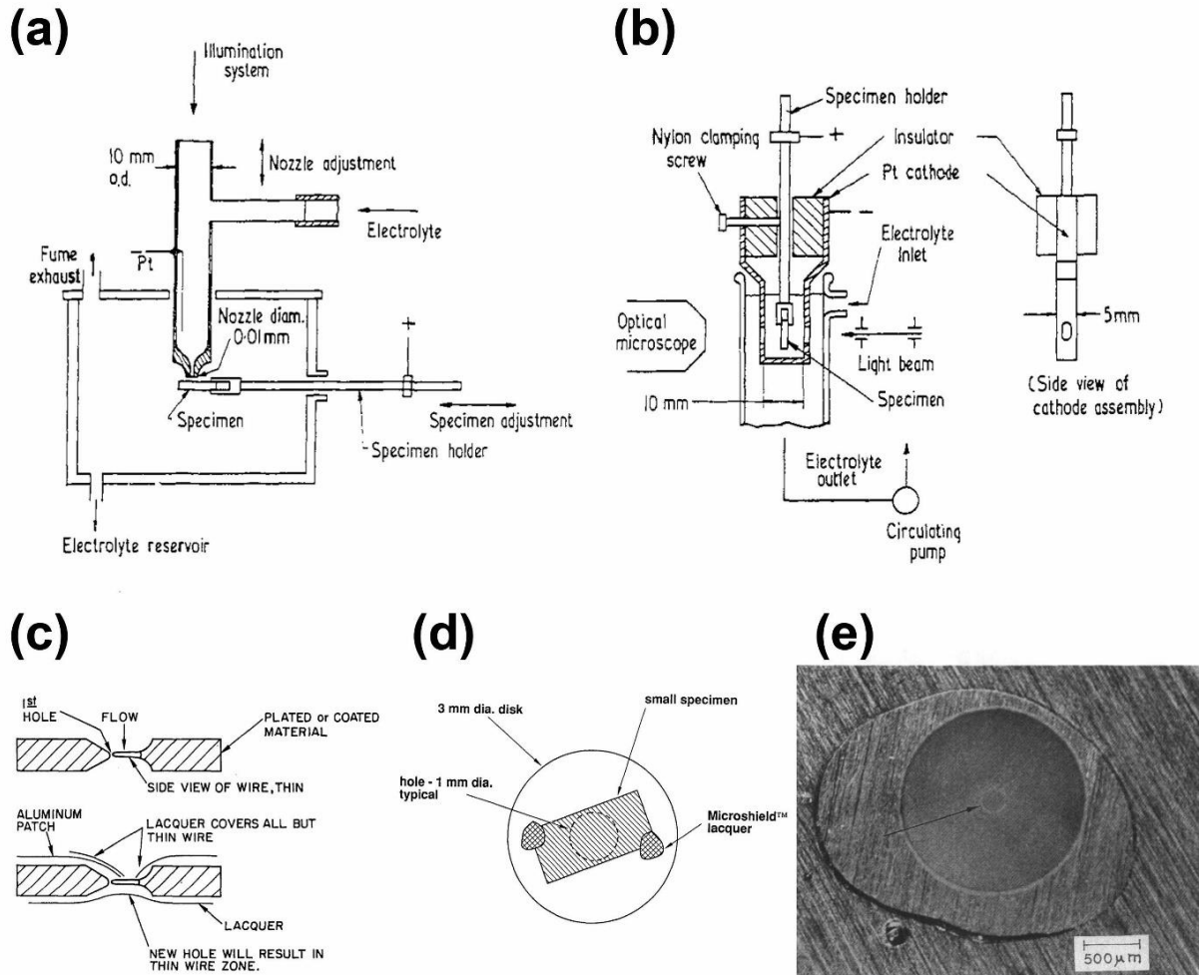

Figure 4–2 (a) dimpling and (b) electropolishing of 1 mm diameter wire [204]; (c) plating stainless steel wire with nickel; (d) sandwiching the sample between two copper discs with a hole and (e) embedding a thoriated tungsten wire into molten gold, followed by electropolishing [205].

The idea of enlarging the sample to a 3 mm size was retained in the present work, but due to the further reduction of the size of the original material, an alternative approach had to be introduced which also has the advantage of not manipulating the specimen by high temperature or contaminating with other metals, as is unavoidable in the Kestel procedure. Only a commercial twin–jet electropolishing apparatus and some other available lab setups and materials are needed to apply this new method.

4.2 Experimental procedure

The main idea is to embed the micro–wire under consideration in a medium in a way that the obtained complex fits into the clamping holder of a twin–jet electropolishing unit, which means having a disc shape of 3 mm diameter and ~ 150 μm thickness, and the wire is exposed on both sides of the embedding disc so that it can be reached by the electrolyte during the electropolishing process.

To be applicable for this purpose the embedding medium should have the following properties:

1. Being adhesive, so that it can embed the wire, and being hard enough after hardening, so that it can endure the mechanical stress during mechanopolishing without cracking and detaching from the wire.
2. Resistant to the applied electropolishing electrolyte (acids + alcohols), e.g., sulfuric acid and methanol which are used in this work.
3. Resistant to acetone, which is used to remove the glue from the medium in the mechanopolishing procedure.
4. Being electrically conductive to establish electrical contact between the embedded wire and the electropolisher holder.
5. Being non–transparent, so that it can block the light–photocell path in the unit and allow the use of the automated stop mechanism of the setup.

Epoxy resins are found to match the three first conditions since they suffer least from chemical attack and show true adherence to the sample, especially metals [206]. They induce no chemical reaction with the material and cause no contamination on the material surface. However, epoxy resins with no filler are generally semitransparent and non–conductive, so some kind of filler needs to be used in order to match conditions 4 and 5.

Electrically conductive epoxies that are non–transparent due to a filler are commercially available, however, the vast majority of these are silver–filled, some other copper–, nickel– and gold–filled, which all dissolve in the sulfuric acid mixture under the present electropolishing conditions [207–209]. Very few epoxy resins with graphite as filler and which do not react with acids exist. However, they all share the disadvantage of having a resistivity of orders of magnitude higher than that of the metal–filled resins, which hampers electropolishing. For example, the volume resistivity of the graphite–filled EPO–TEK 377H [210] epoxy resin is more than 400 Ω.cm,

while that of the silver–filled EPO–TEK H20E [211] is less than 0.0004 Ω.cm. Due to this reason, placing the wire perpendicular to the disc surface, as shown in Figure 4–3(a), and relying on the resin conductivity to make electrical contact between the wire and the platinum strip of the holder does not lead to proper electropolishing, but partial etching instead. In Figure 4–4 an example of such an experiment with graphite–filled EPO–TEK 377H is shown under a light optical microscope (Figure 4–4(a)) and BF–TEM (Figure 4–4(b) and (c)). It can be seen from the SAED in Figure 4–4(d) that some electron transparent regions are indeed obtained, but the specimen thickness is not uniform and the surface is rough (due to partial etching). These results confirm that the perpendicular method can be successful if a high conductive epoxy resin is applied. This approach is needed when the cross–section TEM view of an, e.g., textured wire is desired.

In order to avoid this conflict of needed properties for the embedding medium, the electrical contact can be obtained by embedding the wire in the resin parallel to the surface of the 3 mm disc (Figure 4–3(b)) and ensuring direct electrical contact between the wire and the metallic strip of the holder. The length of the wire was thus chosen large enough to reach the platinum of the electropolisher holder from one (or both) sides of the strip hole, as shown in Figure 4–3(c), ensuring electrical contact between the sample and the system while the strip also acts as a heat sink minimizing sample heating during polishing. This method provides a plan–view of the wire sample.

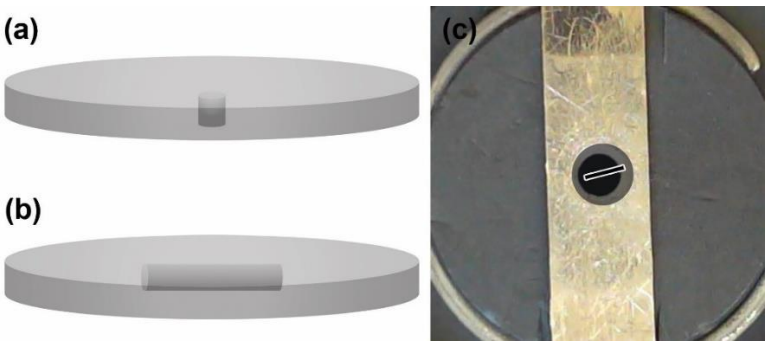

Figure 4–3 Wire piece embedded (a) perpendicular and (b) parallel to the disc surface; (c) schematic of a resin disc embedding a 1.9 mm long wire piece overlaid on a platinum hole of a Tenupol holder, connecting to the platinum on the right side.

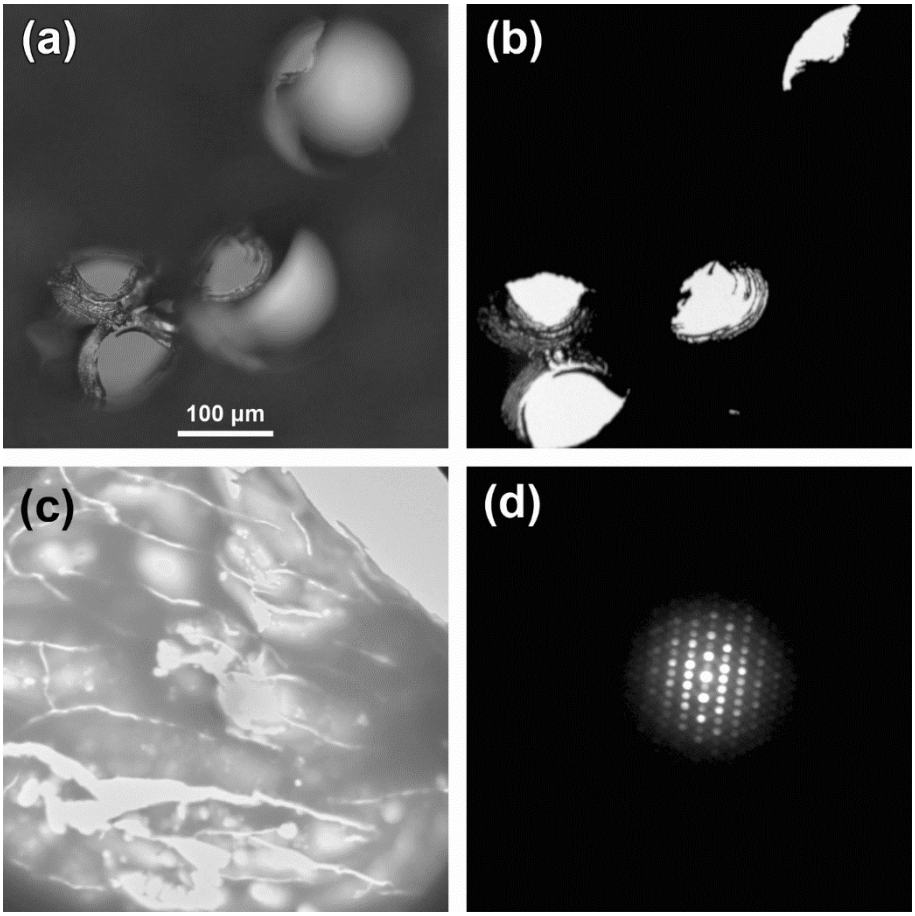

Figure 4–4 (a) Low magnification light optical microscope and (b) BF–TEM image of three perpendicularly embedded electropolished micro–wires; (c) higher magnification BF–TEM image of the edge of one of the wires showing non–uniform thinning; (d) SAED of the same region revealing electron transparency.

In the present work an EPO–TEK 353ND [178] epoxy resin was used which is transparent when liquid and becomes amber to dark red after curing. Therefore, complete non–transparency was achieved by adding 10 wt.% graphite powder with particle size of ~ 5 μm to the resin. This amount of graphite makes the resin non–transparent but has no effect on the electrical conductivity. Mixing the epoxy, the hardener and graphite powder should be done gently to avoid forming tiny bubbles. In case of micro–bubbles formation in the resin, vacuum degassing or centrifuge should be carried out to eliminate minute air bubbles and prevent the appearance of holes in the final polished resin disc.

The standard Tenupol holders for 3 and 2.3 mm samples have a platinum strip hole of diameter 2.6 and 2.1 mm, respectively. The latter was used for this work since it allows the use of shorter wires. Since it is sufficient for the wire to be in contact with the platinum strip only on one side,

there is no need for the wire to be longer than 2.1 mm. It only needs to be placed in the resin disc in such a way that when mounting in the electropolisher holder

1. The wire is connected to at least one side of the strip hole
2. The wire reaches the center of the hole where the electrolyte jet is most active
3. The resin disc completely blocks the holder hole, as shown in Figure 4–3(c).

The wires were chopped into a length of ~ 2 mm and placed on a microscope glass slide wrapped in Teflon tape which eases detaching the resin after hardening, as shown in Figure 4–5(a). A drop of resin mixture was placed on each wire piece using a needle, as seen in Figure 4–5(b). The resin drop should be big enough to make a hemisphere with a diameter of appr. 3 mm, completely covering the wire, as schematically shown in Figure 4–5(c). Due to the still viscous nature of the resin some resin will flow underneath the wire, but most of the resin will form the hemisphere above the wire. The resin was then left to harden at room temperature which took about 4 days. In case the sample is not affected at elevated temperature, the resin can be heated up to speed up hardening according to the resin technical data sheet, e.g. 10 minutes at 100 °C. An image of hardened hemisphere resins is shown in Figure 4–5(d).

The hardness of the resin was checked by scratching the surface with a sharp needle. Then it was mechanopolished from both sides until a disc of ~ 100 μm thickness was obtained with the wire surface appearing from both sides of the disc. To this purpose the resin embedding the wires was fixed on a microscope slide to be held and handled easily using Crystalbond™ 821–3 adhesive which melts at ~ 120 °C, requiring a few seconds heating at each attaching or detaching step. Polishing should start from coarse to soft paper, each step removing the plastically deformed or structurally altered layers induced by the previous polishing step. As a rule of thumb, polishing with abrasive papers can produce a depth of damage to the material up to three times the size of the abrasive particles [121]. The polishing steps should be carried out in a way that after the last polishing the sample is slightly thicker than twice the damage penetration depth of the last polishing step so that the central part of the material is unaffected [212]. After achieving the final thickness the disc should be rinsed in acetone to completely remove the remaining adhesive. An image of some mechanopolished discs is shown in Figure 4–5(e).

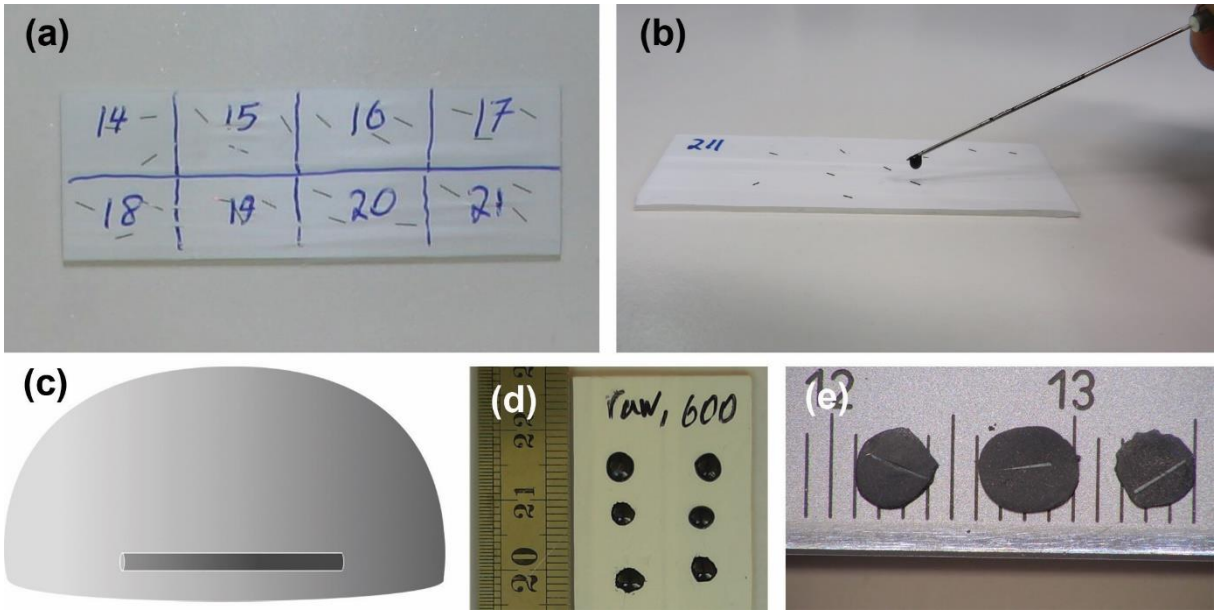

Figure 4–5 (a) Chopped wires of different samples on a Teflon covered microscope slide; (b) putting a drop of resin on each piece of wire using a needle; (c) schematic of the wire embedded into a hemisphere resin; (d) hardened hemisphere resin containing single wire pieces; (e) mechanopolished discs.

As from this point the resin disc embedding the wire should be handled gently since it is fragile. When possible, using a vacuum pickup tool instead of tweezers is recommended for picking up the disc.

If the resin disc is larger than 3 mm, it should be resized to fit into the TEM holder. To this purpose the resin disc perimeter was cut using a scalpel. In order to minimize the risk of breaking the resin disk or detaching the wire from it, cutting should be done by pressing a curved scalpel down from one side of the resin disc to another with a rolling movement over the curved edge of the blade, instead of pulling the blade in a horizontal direction, or landing it in the vertical direction, as shown in Figure 4–6(a). A resin disc before cutting and another after proper cutting are shown in Figure 4–6(b).

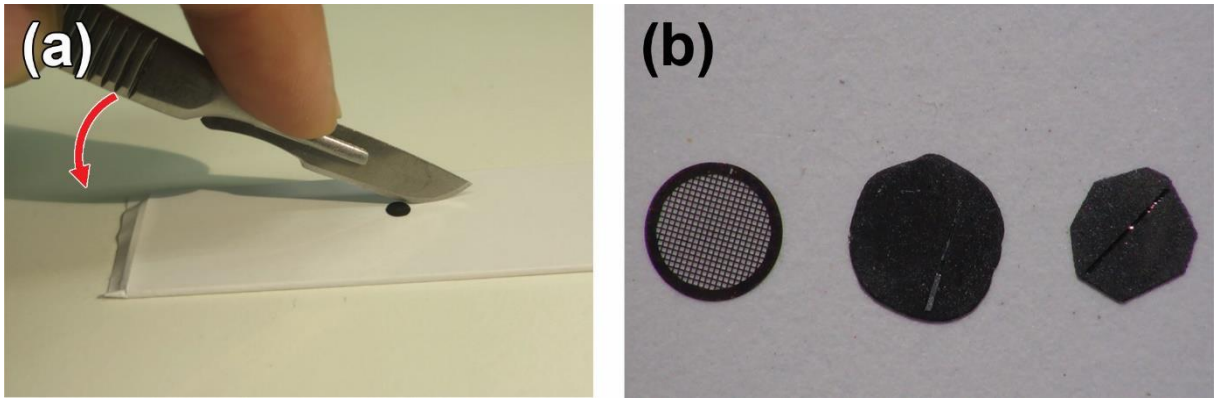

Figure 4–6 (a) Cutting the resin disc from one side to another by using the curved blade of a scalpel (see arrow); (b) Left to right, a 3 mm cupper grid as reference size, a resin disc larger than 3 mm diameter and another resin disc after being cut.

The disc was mounted into the twin–jet electropolisher holder in the way that the wire connects to the edge of the hole of the platinum strip of the holder, as was shown in Figure 4–3(c). The holder is then inserted into the electropolisher, settings of the machine are set equal to those of the respective bulk material, and the electropolishing procedure can be started. In the present case the mixture of 80% methanol and 20% sulfuric acid operating at 18 V, 0.13 A and 0 °C was used.

Voltage and current indicators of the electropolisher control unit give information about the process and whether or not electropolishing is occurring. When both potential and current are non–zero, electropolishing occurs. If the potential is non–zero and the current is zero, the electrical contact between the wire sample and the apparatus is not established [150]. If both potential and current are zero, this is an indication that the auto–stop has been triggered even before electropolishing starts. This might happen for the present resin embedded wire samples due to the semi–transparency of the thin filled resin. In bulk Ni–Ti the material completely blocks the light source–photocell path and photosensitivity determines the perforation size. In the resin embedded wire disc, however, the graphite–filled resin can transmit some light when thinned to around 100 μm. Therefore, the light received by the photocell is a combination of wire perforation and transmitted light through the resin. As the resin disc thickness and graphite content or distribution might be slightly different from one sample to another, the photosensitivity should be adjusted as follows: it is set to 8, as for bulk material. If the current and potential are both zero, which means the auto–stop mechanism is activated, photosensitivity is set to zero and the start button is pushed again. Then the photosensitivity is increased until the auto–stop is triggered due to the semi–transparency of the resin, so the photosensitivity number in which the auto–stop is activated is found. Then electropolishing is restarted with the photosensitivity set to a number ~ 0.5–1 lower

than the triggering number. With judicious adjustments of the photosensitivity a successful electropolished specimen can be obtained and the procedure has a success yield of around 90%.

The achieved specimen is examined after rinsing and drying. As the wire is already thinned, even if the resin breaks at this step, the specimen can still be used, as shown in Figure 4–7.

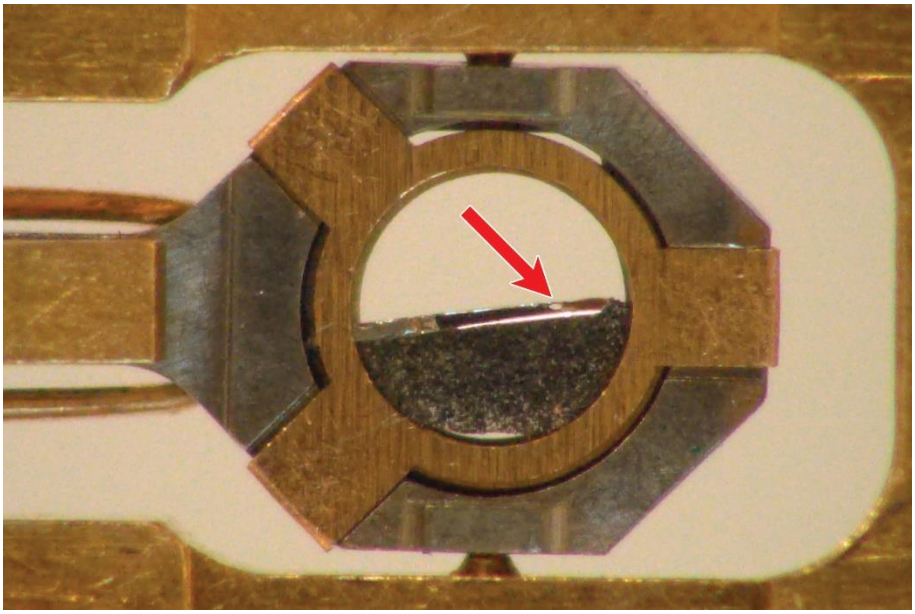

Figure 4–7 A specimen with the resin half–disc broken and detached from the wire after cutting and electropolishing, but still usable when mounted in a TEM holder. The perforation is indicated by an arrow.

When mounting the specimen in the TEM holder the wire should be in contact with the holder to avoid charge accumulation on the specimen. In case this is not possible due to size limitations of the wire, a 5 nm carbon layer can be deposited on the surface of the resin.

4.3 Results

A light optical microscope image of a Ni–Ti micro–wire TEM specimen obtained by the above method is shown in Figure 4–8(a). In this image the perforation in the center of the wire is clearly seen. The corresponding low magnification scanning transmission electron microscopy (LM–STEM) image is shown in Figure 4–8(b). A higher magnification BF–TEM image is presented in Figure 4–8(c) together with an SAED pattern as inset. In Figure 4–8(d) a high resolution (HR)–STEM image along the $\langle 111 \rangle_{B2}$ direction is presented. The BF TEM image, the diffraction pattern as well as the HR–STEM showing atomic resolution clearly indicate the local

quality of the thinning procedure, with the LM–STEM image revealing a successful thinning around the entire hole.

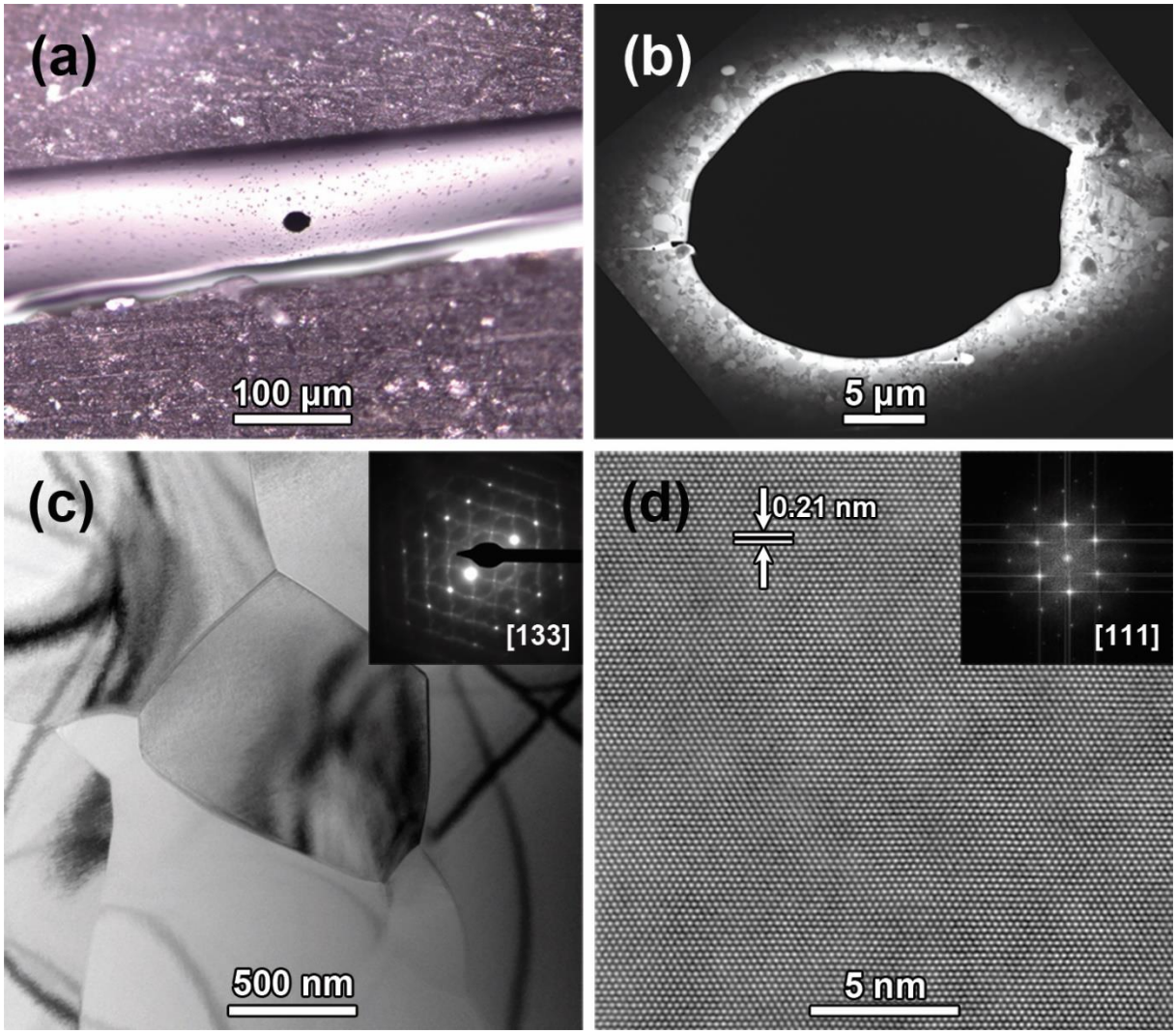

Figure 4–8 (a) LOM image of the specimen after electropolishing showing the perforation in the wire; (b) LM–STEM image of the specimen shown in a; (c) a BF–TEM image of some grains of the wire together with the SAED pattern (inset); (d) HR–STEM image with the corresponding fast Fourier transformation (inset).

In another specimen three elongated holes appeared along the wire, providing thin areas between the holes in addition to the surroundings. A LM–STEM image of the region between two holes is shown in Figure 4–9(a). In Figure 4–9(b) an annular dark field (ADF) image of the rectangle indicated in Figure 4–9(a) is shown with the corresponding EELS thickness map in Figure 4–9(c). The thickness map shows that the specimen reaches about 20 nm – 25 nm thickness in the thinnest region. It also reveals that a 2 µm – 3 µm wide band with a thickness lower than

50 nm surrounds the holes and becomes up to 5 µm wide between the holes, yielding in total much larger thinned areas than with conventional FIB specimens.

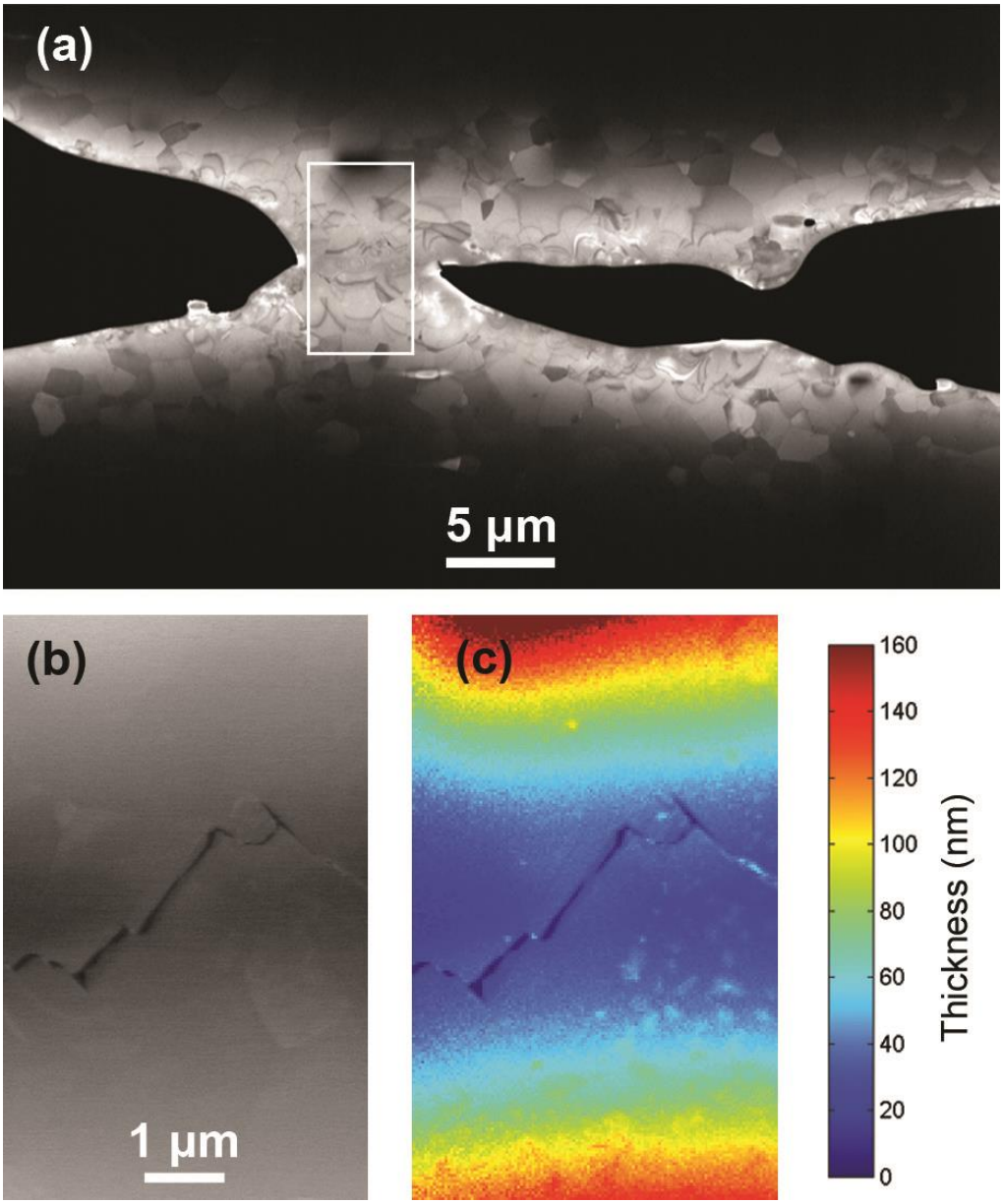

Figure 4–9 (a) LM–STEM image of a specimen where two lateral elongated holes meet; (b) higher magnification ADF image of the region indicated in (a), showing a crack in the middle, and (c) EELS color coded thickness map of (b) in nanometer.

4.4 Conclusions

A novel method to prepare TEM specimens from micro–size thin wires is introduced which can be used with instrumentation available in most electron microscopy labs. The wire is enlarged in size by embedding into a graphite filled resin medium after which it is treated as bulk material

and electropolished by a conventional twin–jet electropolishing apparatus. The result is a well–polished specimen without radiation damage and large electron transparent areas and with a success rate similar to that of bulk material. This method is used to prepare TEM specimens from micro–wires in Chapter 6.

Chapter 5:

Effect of room temperature aging combined with DSC cycling on micron grain size bulk $Ni_{50.6}Ti_{49.4}$

In this chapter the effect of thermal cycling induced by DSC measurements on bulk $Ni_{50.6}Ti_{49.4}$ material with and without room temperature aging in between cycles is investigated.

This chapter is based on the following paper:

- Pourbabak, S.; Wang, X.; van Dyck, D.; Verlinden, B.; Schryvers, D. Ni Cluster Formation in Low Temperature Annealed $Ni_{50.6}Ti_{49.4}$. Functional Materials Letters 2017, 10, 1740005. https://doi.org/10.1142/S1793604717400057.

5.1 Introduction

It is known that thermal cycling, including those occurring during DSC measurements, suppresses the martensitic transformation, i.e. lowers M_s. As explained in § 2.5.4, this is classically attributed to the micro–plasticity introduced by thermally induced martensite transformation which causes formation of dislocations whose strain fields affect the martensitic transformation [57]. Recently nano–scale Ni_4Ti_3 precipitates formation at the high range of the DSC temperature interval is also considered as an additional factor to suppress martensitic transformation [108,109]. In this chapter different microscopy techniques are applied to investigate the effect of thermal cycling on the micron grain size bulk Ni–Ti, with and without room temperature aging in between.

5.2 Experimental Procedure

5.2.1 Sample treatment

A $Ni_{50.6}Ti_{49.4}$ alloy was annealed at 1000 °C for two hours followed by room temperature water quenching. The quenched samples were subjected to three different procedures:

- Protocol A, nine samples: DSC cycling was done on one sample immediately after quenching, the remaining eight samples were aged at RT respectively for 1, 2, 4, 8, 15, 30, 60 and 90 days, always followed by a DSC cycle. All samples were again aged at RT afterwards. For later reference the samples are labeled with A followed by the day of the test, e.g., A0, A1, A2, etc. The aging and DSC diagram of the A30 sample is shown in Figure 5–1(a), as an example.
- Protocol B, one sample: nine consecutive DSC cycles were performed on one sample immediately after quenching and followed by aging for one year at RT afterwards, as diagrammatically shown Figure 5–1(b). This sample is called B.
- Protocol C, one sample: The sample was measured by DSC cycling immediately after quenching and aged at RT afterwards, interrupted by single DSC cycles performed at 1, 2, 4, 8, 15, 30, 60 and 120 days after quenching, as schematically shown in Figure 5–1(c). This sample will be referred to as C.

The DSC measurements were performed between -150 °C and +25 °C in a TA Q2000 calorimeter with a cooling/heating rate of 10 °C min^{-1}.

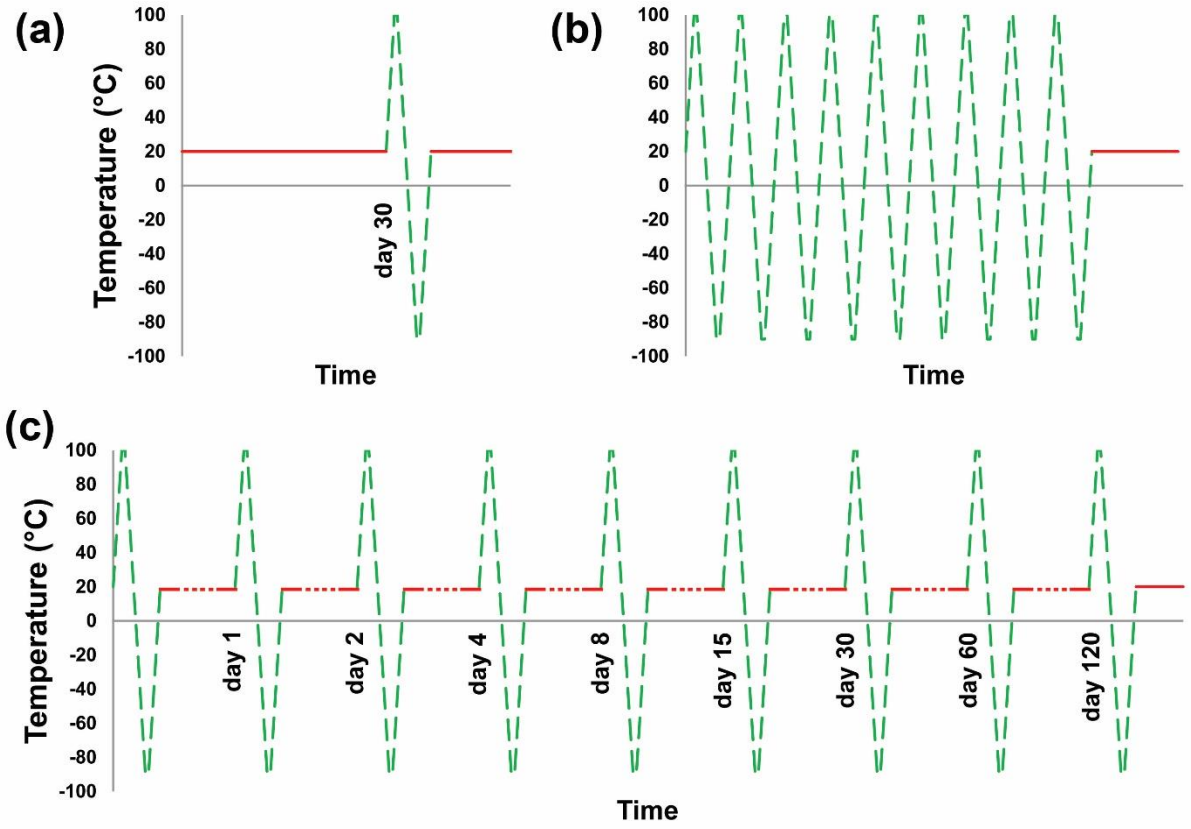

Figure 5–1 Diagram of aging (red) and DSC measurement (green) of (a) A30, (b) B, and (c) C sample.

The M_s values versus aging time for samples A and C are compared in Figure 5–2(a). M_s of samples A varies between -23 °C and -19 °C, and does not seem to be affected by aging [213]. M_s of sample C decreases from -23 °C for the measurement just after quenching to -40 °C after 120 days.

M_s values versus number of thermal cycles for samples B and C are shown in Figure 5–2(b). M_s of the sample with only consecutive thermal cycling, B, lowers from -21 °C to -27 °C, but the decreasing is much less intense than that of the combined aging–cycling treatment, C.

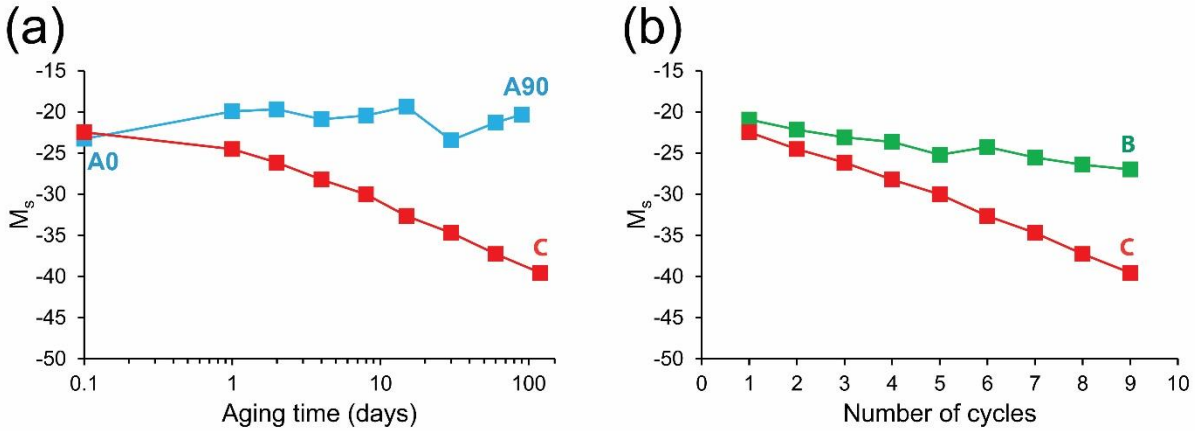

Figure 5–2 (a) M_s comparison between A samples only aged at RT and C sample aged at RT combined with DSC cycling; (b) M_s comparison between B sample with consecutive DSC cycling and C sample aged at RT combined with DSC cycling.

5.2.2 TEM investigation

Samples A0, A90, B and C from the aforementioned procedures were selected for the TEM investigation. Moreover, a sample with no DSC tests but only aged at RT after annealing at 1000 °C was used as reference, called REF hereafter. The corresponding M_s points of samples A0 and A90 are indicated on Figure 5–2(a). Sample B produces all points of the upper (green) curve in Figure 5–2(b) and all points of the lower (red) graphs in Figure 5–2(a) and (b) are obtained from sample C. Sample REF had no DSC cycle and appears in none of the graphs.

TEM specimens were made of the selected samples by electropolishing, as explained in § 3.4.13.4. The obtained electron transparent specimens were used to acquire tilt series of SAED patterns using a Philips CM 20 TEM to study the reciprocal space in three dimensions. High resolution (HR)–TEM and dedicated SAED patterns were acquired in some different high– and low–index zones aiming for further quantification on a FEI Tecnai G2 instrument running at 200 kV. In order to achieve comparable quantitative data some considerations were taken into account: CBED, explained in § 3.5.5.1 was applied to measure the specimen thickness which allowed to use a consistent thickness of 120 nm ± 20 nm for all acquisitions. Microscope settings such as beam spotsize, condenser and objective lenses excitation, condenser and selected area apertures and camera length were kept unchanged. Also, camera settings (exposure time) and calibration (gain and bias corrections) were consistent for the whole procedure. In parallel, the data collection feature of TOPSPIN strain mapping in TEM was employed to scan a rectangular

region of the specimen with the nano–probe and acquire very local electron diffraction from an infinitesimal volume of the material.

Also, high–angle annular dark field (HAADF)–STEM on a FEI Titan 50–80 instrument operating at 300 kV was used to exploit the Z–contrast ability of the technique.

5.3 Results

Figure 5–3(a) shows a bright field TEM image of the REF sample in which clearly no fully formed precipitates can be seen. Accordingly, the SAED pattern of the zone $[012]_{B2}$ shown in Figure 5–3(b) does not represent any of the characteristic superspots of Ni_4Ti_3 precipitates along $\langle 123 \rangle^*$. However, it does reveal a clear structured pattern of diffuse intensity. By tilting the specimen it is found that similar diffuse intensity patterns also exist in zones in which no Ni_4Ti_3 superspots are expected in specimens with fully grown precipitates, such as $[122]_{B2}$ shown in Figure 5–3(c). The main properties of the diffuse intensities observed in different zone axes are as follows:

1. They are more pronounced in high–index zones and less visible in low–index zones.
2. They are arranged around specific geometrical loci.
3. In the 2D SAED patterns they generally appear as line shapes.
4. They reveal a periodical character.

Contrary to the clear structural diffuse intensity found in reciprocal space, which indicates the existence of some kind of short range order in the lattice, HR–TEM images taken along various zones do not reveal any useful information. In Figure 5–3(d) an example along the $\langle 111 \rangle_{B2}$ direction is shown which does reveal some contrast variation in the resolved atom columns. However, these contrast variations strongly depend on the used imaging focus and are thus not very reliable to be used as guidance for any possible structural feature, although they have been shown to provide some guidance in order–disorder transformations [214,215].

The HAADF–STEM image acquired along the same $\langle 111 \rangle_{B2}$ and shown in Figure 5–3(e) is more stable against focal changes and is expected to reveal differences in the intensity of atom columns due to Z–contrast, in case changes in atom occupation along the columns exist [216]. In the perfect austenite B2 matrix the $\langle 111 \rangle_{B2}$ atom columns consist of alternating Ni and Ti atoms, so all dots in the HAADF–STEM image should have the same intensity, and since in the hexagonal Ni_4Ti_3 precipitates 1 out of 7 $\langle 001 \rangle_H$ // $\langle 111 \rangle_{B2}$ columns of atoms is pure Ni, in case of existence of some Ni_4Ti_3 precursors, i.e., increased Ni occupation along some $\langle 001 \rangle_H$ // $\langle 111 \rangle_{B2}$ columns for a

precipitate with the central plane perpendicular to the viewing direction, one might expect to see some variation in the HAADF–STEM intensities. However, although a variation in intensity of the column dots is indeed visible, the measured intensity differences run up to about 8% while MULTEM [217] simulations indicate that a precursor of, e.g., 7 unit cells (i.e., 15 Ni atoms in a $\langle 111 \rangle_{B2}$ row) in a 50 unit cell thick specimen yields an intensity increment of only 2%, due to the close atomic number of Ni and Ti. Thus, the observed difference in the HAADF–STEM intensity of atomic columns cannot be attributed to the presence of a precursor. Moreover, aside from some minor shifts due to the use of STEM, no coordinated atom shifts, which might indicate a precursor to a displacive transformation, can be observed in this image.

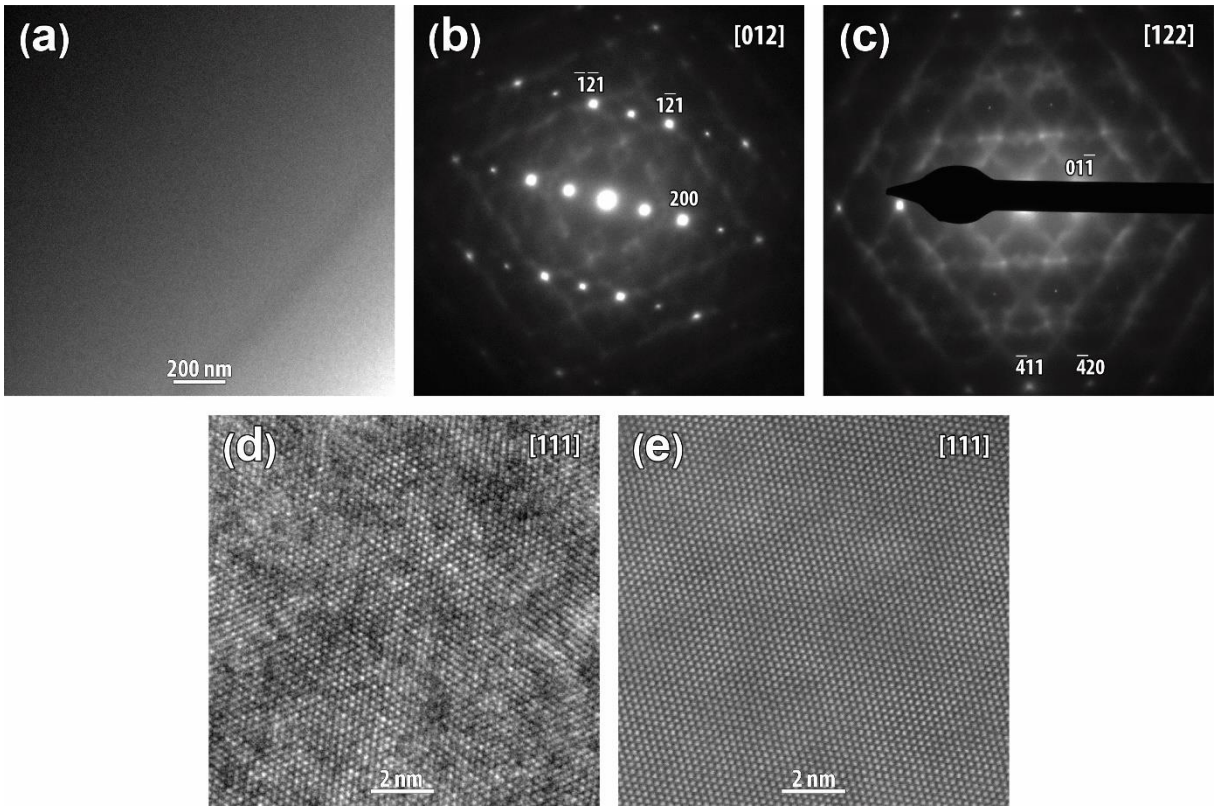

Figure 5–3 REF sample (a) Bright field showing no full grown precipitates; (b) $[012]_{B2}$ SAED pattern revealing no Ni_4Ti_3 superspots; (c) $[122]_{B2}$ SAED pattern representing structural diffuse intensity; (d) HR–TEM and (e) HAADF–STEM along $[111]_{B2}$ revealing atomic resolution with no meaningful correlation between atomic column intensity and corresponding Ni content.

In order to check whether the observed diffuse intensity in SAEDs is caused by averaging over the rather large area of the 3.8 μm diameter disc of the specimen selected by the SA aperture, or it is also present when the data is collected from a much smaller region, nano–probe electron diffraction scanning was acquired on a grid of 100 nm ×150 nm rectangle with 5 nm mesh distances

and a probe size of ~ 3 nm, resulting in 600 nano–probe electron diffraction patterns, three of which are presented in Figure 5–4. The results show that similar diffuse intensity, in shape and strength, is present in each and every diffraction pattern acquired from a volume more than six orders of magnitude smaller than that of SAEDs. It reveals that the origin of diffuse intensities is homogenously spread all over the sample and in any small volume of the material.

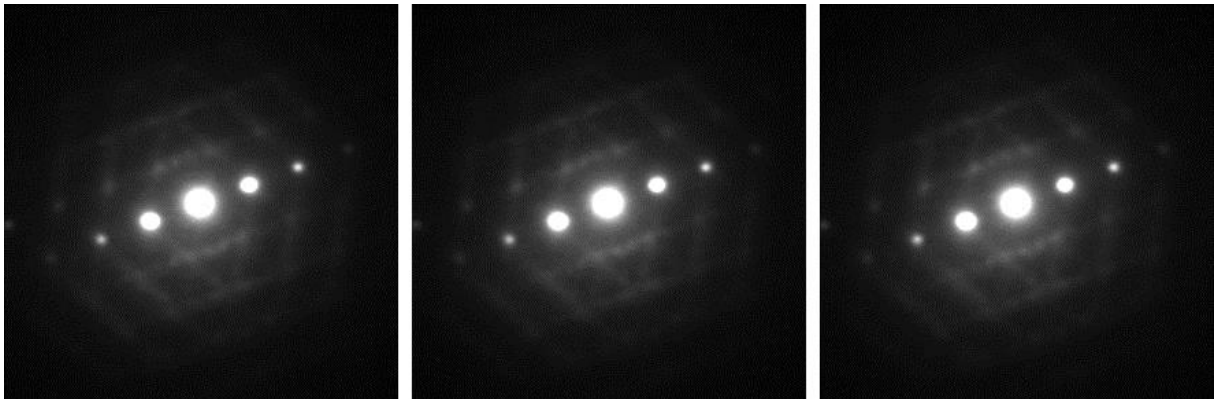

Figure 5–4 Nano–probe electron diffraction acquired from three neighboring regions at 5 nm distance on the scanning mesh.

A tilt series of regular SAED patterns was acquired to obtain a 3D view of the diffuse intensity in reciprocal space, an example of which is shown in Figure 5–5 for the REF sample. In this 90 °C tilting the reciprocal space between $[011]_{B2}$ and $[100]_{B2}$ through $[111]_{B2}$ is covered. The angle between two consecutive images was one degree when close to perfect zones where patterns change quickly and two degree when far from perfect zones. This shows that the diffuse streaks observed in each diffraction pattern, to a first approximation, are created by the intersection of diffuse 2D $\{111\}^*_{B2}$ sheets with the observing plane. All four equivalent $\{111\}^*_{B2}$ families of parallel planes exist with only even values of h,k,l occurring.

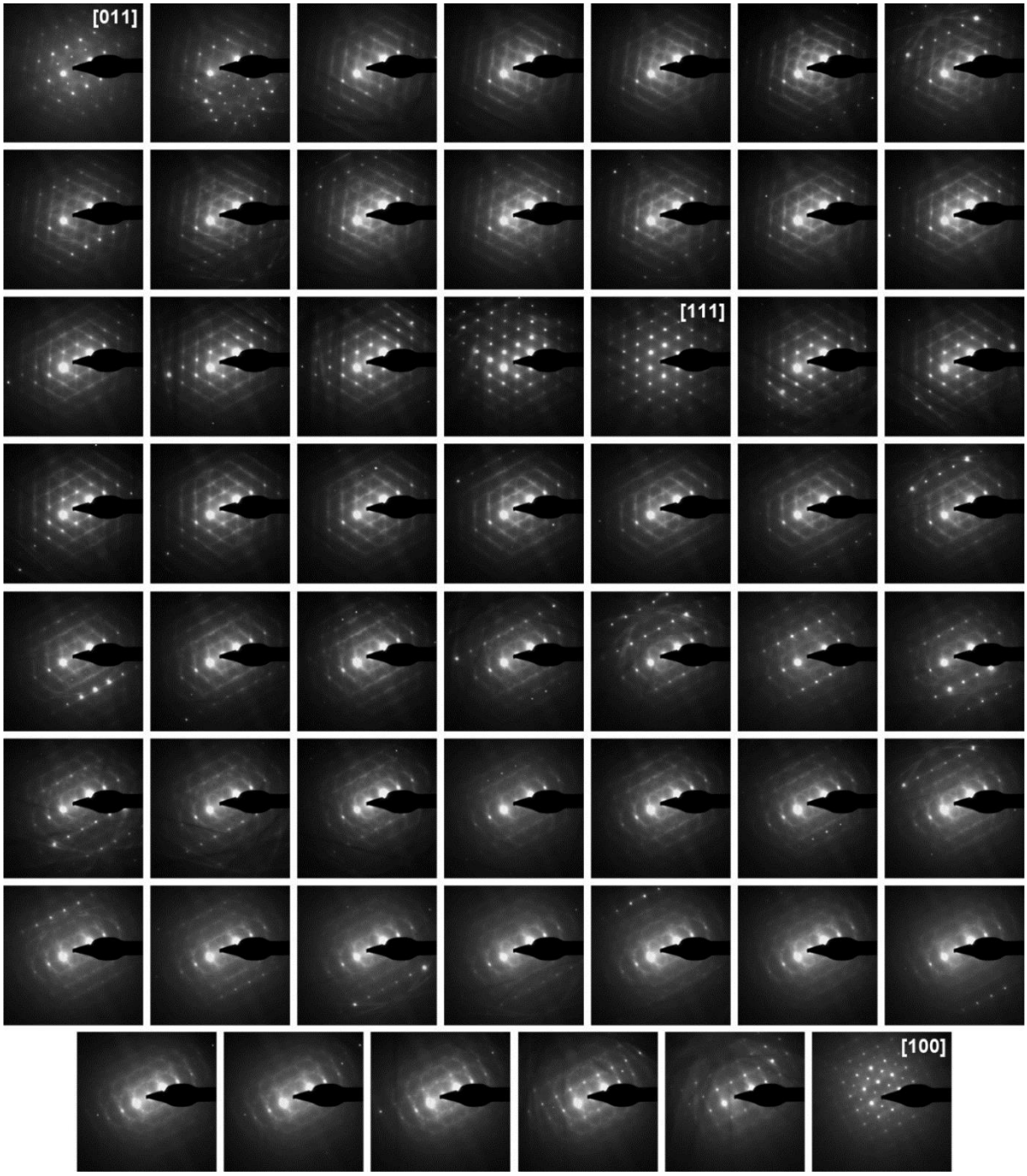

Figure 5–5 Tilt series of REF sample acquired from [110] to [111] through [001] at every one or two degree.

There are two exceptions for the above statements, both concerning the absence of specific traces of $(111)^*$ planes. In Figure 5–6 the loci of intersections of $\{111\}^*_{B2}$ planes with the $(012)^*_{B2}$ plane are schematically plotted. The dashed red streaks are obviously absent in Figure 5–3(b). This phenomenon, where the traces of one or two $\{111\}^*_{B2}$ families are absent, is observed in all

diffraction patterns of the series. Investigating the properties of the invisible traces reveals that diffuse planes with angles smaller than about 48° with the viewing plane cannot be seen in the diffraction pattern. In the above example the angle of the green streaks is 75°, while that of the dashed red streaks is 39°. The same phenomenon was observed by Baba–Kishi et al. in PZT ceramics, while they found 67° as the critical angle [218]. It is still unclear whether this is related to the relative orientation of these families of $\{111\}^*_{B2}$ planes to the selected zone or whether there is a structural origin. The reason for the absence of the dotted yellow streaks, belonging to the same family as the visible green streaks, will be explained in the following section.

SAED patterns of all five samples were obtained using the same experimental conditions as explained before. The respective patterns for the $[112]_{B2}$ zone axis are presented in Figure 5–7. A slight difference in the intensity and distribution of the diffuse intensities can already be distinguished by eye. In order to allow quantitative comparison between the samples, a rectangle region of the patterns as shown in Figure 5–7(a) was selected to achieve an averaged line profile. In this region three diffuse planes cross each other and the spot–like intensity enhancements correspond to the intersection of the Ewald sphere with the intersection line of two such diffuse planes, as schematically shown in Figure 5–8.

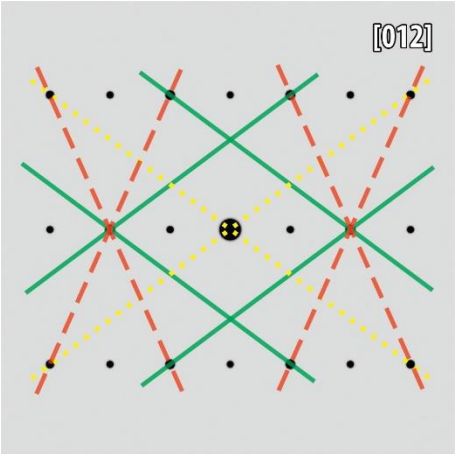

Figure 5–6 Intersection traces of $(012)^*$ and $\{111\}^*$ planes.

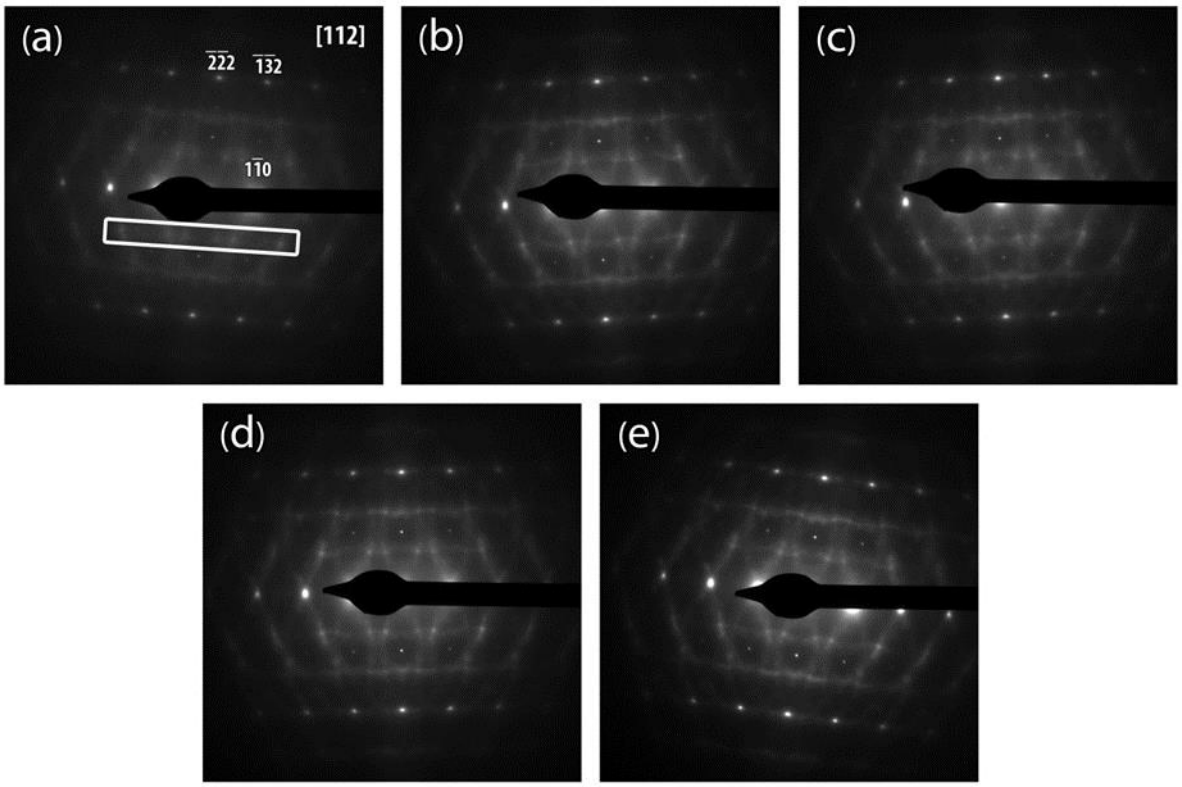

Figure 5–7 (a) to (e), $[112]_{B2}$ SAED of samples REF, A0, A90, B and C, respectively. The rectangle shown in (a) indicates the area over which the averaging is performed.

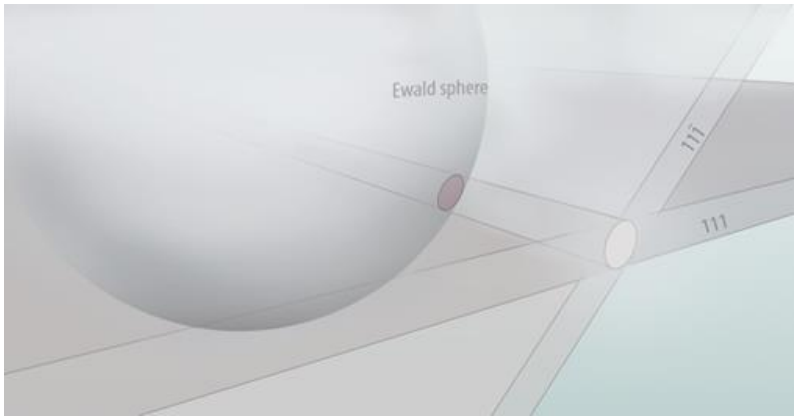

Figure 5–8 Schematic of the cross–section of the Ewald sphere with two {111}* diffuse planes, yielding a diffuse spot in the diffraction pattern.

The rectangular profiles obtained from all SAEDs are plotted in Figure 5–9. The lowest (yellow) trace belongs to sample REF with no DSC cycling. Samples A0 (light blue) and A90 (dark blue) mostly show a very similar intensity distribution. This is also true for remaining B (green) and C (red) samples when compared with one another. Each peak is fitted with a Gaussian function to

determine the top or bottom value. The diffuse intensity factor (DIF) is then defined as the difference of the averaged four maxima and minimum of the averaged line profile of each sample compared with that of the REF sample and presented in %:

$$DIF = \frac{\overline{Max} - min}{\overline{Max}_{REF} - min_{REF}} \times 100$$

Although a certain difference in sample foil thickness cannot be avoided (CBED measures yield an uncertainty of ~ 20 nm for the foil thickness) and which is expected to be the origin of the slight differences in absolute intensity of the Bragg reflections between each pattern, and also each SAED might be slightly deviated from the perfect zone axis which is the reason for non–perfectly symmetric peaks (best seen in the green graph), this type of relative measure uses an internal reference for each pattern so the results can be properly compared between patterns. The results are presented in Table 5–1 and Figure 5–10. Although the standard errors of some of the DIF values overlap, the trend of an increasing intensity of the diffuse spots with increasing treatment times at those very low temperatures is clear.

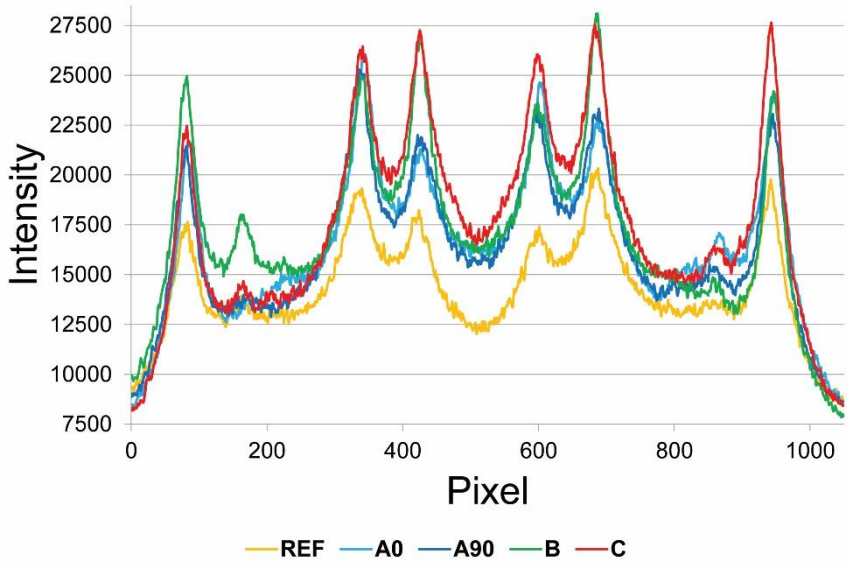

Figure 5–9 Rectangular averaged profiles of the same region in the $[112]_{B2}$ SAED patterns of all five samples.

Table 5–1 Statistical data of Figure 5–7 (standard errors for the maximum average are calculated and their average percentage error is also used for the minimum intensity)

Sample	Max avg.	min	Max avg. - min	DIF
REF	18410±680	12340±390	6070±780	100±18
A0	23180±990	16110±510	7070±1110	116±24
A90	23020±680	15580±490	7450±840	123±21
B	25260±930	16330±510	8930±1060	147±26
C	26250±290	16940±530	9300±610	153±22

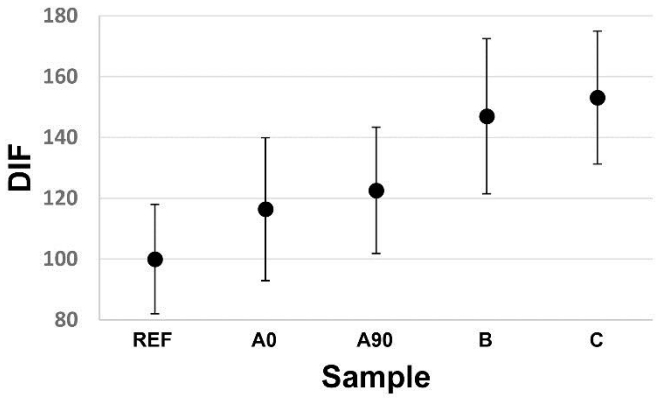

Figure 5–10 Trend of increasing intensity of the diffuse spots in comparison with the relative measure in sample REF.

5.4 Discussion

The Cluster model introduced in § 3.6 was used to interpret the acquired SAEDs. The fact that the observed diffuse intensities are arranged around specific geometrical loci allows to analytically solve the diffuse scattering amplitude equation. Therefore, ordering relation, equation 3.34, can be applied for analyzing the results.

As the diffuse intensities are located on equivalent $\{111\}^*_{B2}$ planes in the reciprocal space, they satisfy the requirements of equation 3.30. So, the mathematical equation of the planes can be found as:

$$e^{2\pi i \boldsymbol{g}.\boldsymbol{r}} = 1 \tag{5.1}$$

in which $\boldsymbol{r} = (111)$. This can be written as:

$$l(\boldsymbol{g}) = e^{2\pi i \boldsymbol{g}.\boldsymbol{r}} - 1 = 0 \tag{5.2}$$

As four families of (111) planes exist, each has a mathematical function of the form $l(\boldsymbol{g}) = 0$. The product of those functions should satisfy:

$$l_1(\boldsymbol{g}).l_2(\boldsymbol{g}).l_3(\boldsymbol{g}).l_4(\boldsymbol{g}) = 0 \tag{5.3}$$

which requires at least one of four functions to be zero. Thus, it is enough to study each relation independently, and the clusters have to obey any of the relations.

The equation 5.2 is of the form of equation 3.30, in which $\boldsymbol{r}_k$ is the vector of the cluster and $\omega_{\boldsymbol{k}}$ is the coefficient. Thus, the cluster relation in real space will be of the form of the ordering relation, equation 3.34:

$$\sum_k \omega_k \sigma_{j+k} = 0 \qquad for\ all\ \boldsymbol{k} \tag{5.4}$$

Equating equation 3.30 with $e^{2\pi i \boldsymbol{g}.\boldsymbol{r}} - 1$ and considering even (hhh)* planes gives:

$$\sum_k \omega_k e^{2\pi i \boldsymbol{k}.\boldsymbol{r}_k} = e^{2\pi i \boldsymbol{g}.\boldsymbol{r}} - 1 \ \Rightarrow\ \omega_1 = -1, \qquad \boldsymbol{r}_1 = [000] \tag{5.5}$$

$$\omega_2 = +1, \qquad \boldsymbol{r}_2 = [½½½] \tag{5.6}$$

As a result

$$\sigma_1 - \sigma_2 = 0 \quad \Rightarrow \quad \sigma_1 = \sigma_2 \tag{5.7}$$

Obtaining $\sigma_1 = \sigma_2$, r_1=[000] and r_2=[½½½] means that atoms occupying [000] and [½½½] positions are of the same kind, and since the alloy is slightly Ni–rich, having Ni in both sites is more favorable. In other words, the diffuse {111}* planes correspond with clusters of the form of pure Ni strings oriented along all four equivalent $\langle 111 \rangle_{B2}$ directions. These can easily be produced by replacing a single Ti atom by a single Ni atom, as this immediately induces three consecutive Ni atoms in all four $\langle 111 \rangle_{B2}$ directions. Figure 5–11(a) shows a 3×3×3 B2 supercell with three Ti to Ni atom replacements resulting in a cluster of seven Ni atoms long along the $\langle 111 \rangle_{B2}$ direction and indicated by a red bar. As mentioned before, as far as the ordering is concerned, the Ni_4Ti_3 precipitates can be distinguished from the B2 structure since 1 out of 7 $[111]_{B2}$ columns consists of pure Ni, as shown in Figure 5–11(b). This matches well with the above clusters since these clusters in the quenched samples can be considered as early stages of some columns of the Ni_4Ti_3 precipitates which normally start appearing upon annealing. Having Ni atoms with the periodicity of $½\langle 111 \rangle_{B2}$ also matches the $2\{111\}^*_{B2}$ periodicity of diffuse intensities in reciprocal space. The length of the clusters will inversely correspond with the width of the diffuse $\{111\}^*$ planes in reciprocal space and as long as the clusters do not get ordered (e.g., in an arrangement resembling the Ni_4Ti_3 structure) no intensity enhancement in the form of superspots will exist inside the diffuse planes.

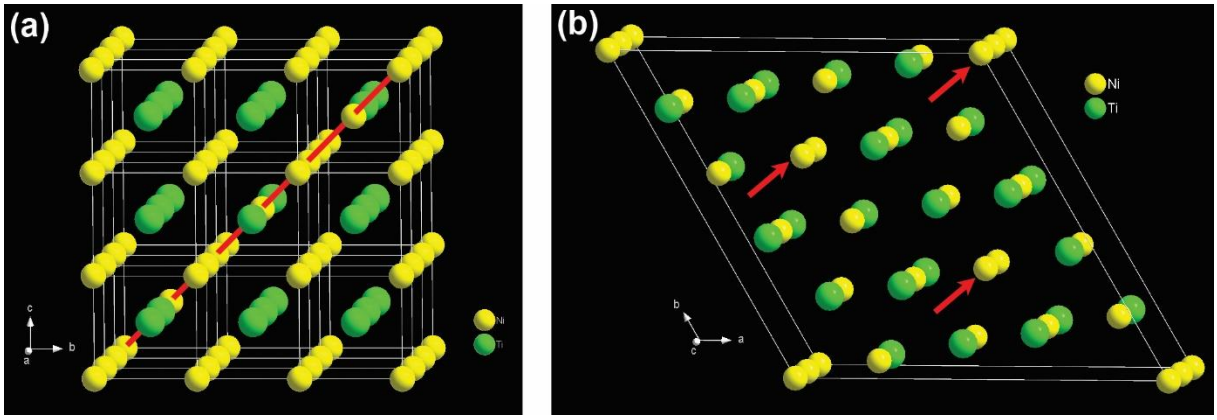

Figure 5–11 (a) A 3×3×3 B2 supercell containing a Ni cluster of seven atoms along the $\langle 111 \rangle_{B2}$ direction; (b) a Ni_4Ti_3 hexagonal unit cell with 18 columns of alternative Ni and Ti atoms and three columns of Ni atoms (indicated by red arrows) along the $\langle 001 \rangle_H$ // $\langle 111 \rangle_{B2}$ direction.

The missing dotted yellow streaks in Figure 5–6 belong to the same family as the visible green streaks but pass through the central spot. This phenomenon was previously observed in Ti–Nb and explained by Sass [219]. The reason is that the scattering phase term is not changed by an atom shift normal to the reciprocal lattice vector. As the reciprocal lattice vector is passing through 000 and the atom columns are in the [111] direction, the scattering phase is the same before and after the formation of clusters and as a result a $\langle 111 \rangle_{B2}$ cluster in the B2 structure will not produce a {111} plane of diffuse intensity passing through 000.

It should be mentioned that earlier investigations have related part of similar diffuse intensity patterns to precursors of the *displacive* R–phase, omega or martensitic transformation[220–222], be it in Ti–rich systems with other or additional chemical elements (Ti–Ni–Fe, Ti–Pd–Fe, Ti–Nb, …). Although also in our patterns faint diffuse intensities could be recognized in, e.g., the $[111]_{B2}$ zone and resembling the onset of the R–phase superspots, the present explanation includes the full 3D shape of the diffuse intensity loci containing diffuse intensities not expected for the displacive precursors. Moreover, an increasing number of DSC cycles increases the diffuse intensities, while M_s decreases further below room temperature. Since the TEM in the present work is always performed at room temperature, this means we are looking at a situation farther away from the transformation temperature and so any displacive precursors would be expected to become weaker rather than stronger. Also, no signature of any displacive nature was observed in the HAADF–STEM images, as seen in Figure 5–3(e). It can of course not be excluded that part of the diffuse intensity is still originating from some displacive precursors.

Analyzing the data presented above in view of the proposed short range order mechanism could possibly help explaining the effect of the DSC cycling on M_s. Sample REF has the weakest concentration of diffuse intensity, which can be ascribed to very short clusters. The diffuse intensity is slightly more concentrated in samples A0 and A90, which both had only one DSC cycle but at different times during processing. The M_s of these two samples are also quite similar. The concentration of diffuse intensity is more pronounced in samples B and C which had several DSC cycles. Sharper and more focused diffuse intensities in these cases can be explained by more concentrated diffuse $\{111\}^*$ planes which leads to sharper cross–sections and thus stronger diffuse spots, e.g., as those highlighted in Figure 5–8. Such concentration of diffuse intensity can be related to the elongation of clusters which implies some short range diffusion or re–ordering of atoms during thermal cycling. However, since the cycling for the present samples was performed between -150 °C and +25 °C, very little thermal energy is provided. Still, with a transformation front moving across the system, sufficient energy could be available on a local scale to move a single atom from one lattice site to the next [223]. Since all of these samples still reveal strong diffuse intensity in the $[112]_{B2}$ zone in which no Ni_4Ti_3 superspots exist, no ordering into nano–precipitates is expected as yet, which is confirmed by the fact that no structural features can be recognized in the HR–TEM or HAADF–STEM images. The effect of short pure Ni strings on the decrease of M_s will be discussed in the next chapter.

5.5 Conclusions

The effect of low temperature thermal cycling combined with room temperature aging on the M_s of some $Ni_{50.6}Ti_{49.4}$ samples was investigated. Strong structured diffuse intensities condensed in periodic loci were observed in SAED. The cluster model was used to interpret the results which reveals the existence of micro–domains in the form of clusters of pure Ni atoms along $\langle 111 \rangle_{B2}$ directions. Quantitative comparison between samples with and without a DSC cycle reveals that the more DSC cycles a sample has received, the more condensed the diffuse intensity which is expected to be caused by longer Ni clusters. The required energy for atom diffusion on a local scale may be provided by the transformation front moving across the system during the DSC cycling.

Chapter 6:

Effect of different parameters of DSC cycling on the phase transformation temperatures of micron and submicron grain size $Ni_{50.8}Ti_{49.2}$ micro–wire

In this chapter the effect of thermal cycling induced by DSC measurements on $Ni_{50.8}Ti_{49.2}$ micro–wires with micron and submicron grain size with and without room and elevated temperature aging in between cycles is investigated. Moreover, the effect of different DSC temperature intervals is elaborated. TEM was employed in order to study the microstructural alteration of the material and find the origin of the change of martensitic transformation characteristics.

6.1 Introduction

The shape memory alloys used in engineering applications often undergo cyclic shape recovery during either strain or thermal cycling. While the martensitic transformation responsible for the functionality of these materials should ideally [224] and theoretically [225] be reversible, in reality it shows some irreversibility mainly observed as changing transformation temperatures [57], changing amount of recoverable deformation, and changing amount of transformed martensite [109]. As SMAs devices require stable recovery with no degradation caused by metallurgical alteration, understanding the nature and origin of MT suppression as a result of thermal cycling is necessary to effectively apply such SMA.

As mentioned in § 2.4, for conventional SMAs to perform efficiently the material needs to be annealed below the recrystallization temperature. However, in order to obtain a useful orientation for SAED from a single grain in the present work, the grain size of the material should be large enough. Therefore, in this work, where the aim is on understanding the fundamental influence of the short range order, the material is annealed above the recrystallization temperature.

6.2 Experimental procedure

Two sets of experiments with different objectives have been performed, each involving several samples which are labeled with letters and numbers depending on their heat treatments and thermal cycling conditions. A 46.3% cold drawn $Ni_{50.8}Ti_{49.2}$ wire with a diameter of 150 μm was recrystallized by annealing for 20 minutes at two different temperatures of 575 °C and 600 °C followed by room temperature water quenching which resulted in submicron– and micron–size grains, respectively. The samples originated from these two treatments were labeled starting with S (for small) or L (for large) grain size hereafter, and used as initial material for two different sets of experiments.

The objective of the first set of experiments is to investigate how the effect of thermal cycling on the MT is influenced by parameters such as including aging between the DSC cycles, the temperature of aging between the cycles, number of cycles and sample grain size. 30 samples with different treatments schematically demonstrated in Figure 6–1(a) were involved in these experiments. Some S and L samples were subjected to three different DSC cycling procedures as described in the following, and aged at room temperature (labeled with R) or at elevated temperature of 100 °C (labeled with E) between the DSC tests, as schematically shown in Figure 6–1(b). The three DSC cycles procedures are as follows:

A: six samples each undergoing one DSC cycle at respectively day 0, 2, 8, 30, 90, 120 after annealing. These samples are labeled as SRA, SEA, LRA and LEA followed by the number of the day, e.g., SEA30 for a small grain sample aged at elevated temperature until day 30 when the DSC test was performed, etc. In case of the E samples the elevated temperature aging was stopped after the DSC test. The aging and DSC cycling diagram of L(S)RA30 and L(S)EA30 samples are shown in Figure 6–2(a) and (b), respectively.

B: one sample undergoing 10 consecutive DSC cycles at the day of annealing, (R or E is not applicable for this procedure, since the sample was not aged between the cycles), resulting in samples labeled as LB and SB, the diagram of which is shown in Figure 6–2(c).

C: one sample undergoing 10 DSC cycles at days 0, 1, 2, 4, 8, 15, 30, 60, 90, 120 after annealing, resulting in SRC, SEC, LRC and LEC samples. Elevated temperature aging was stopped after day 120 for the E samples. The aging and DSC diagram of the L(S)RC and L(S)EC samples are demonstrated in Figure 6–2(d) and (e), respectively.

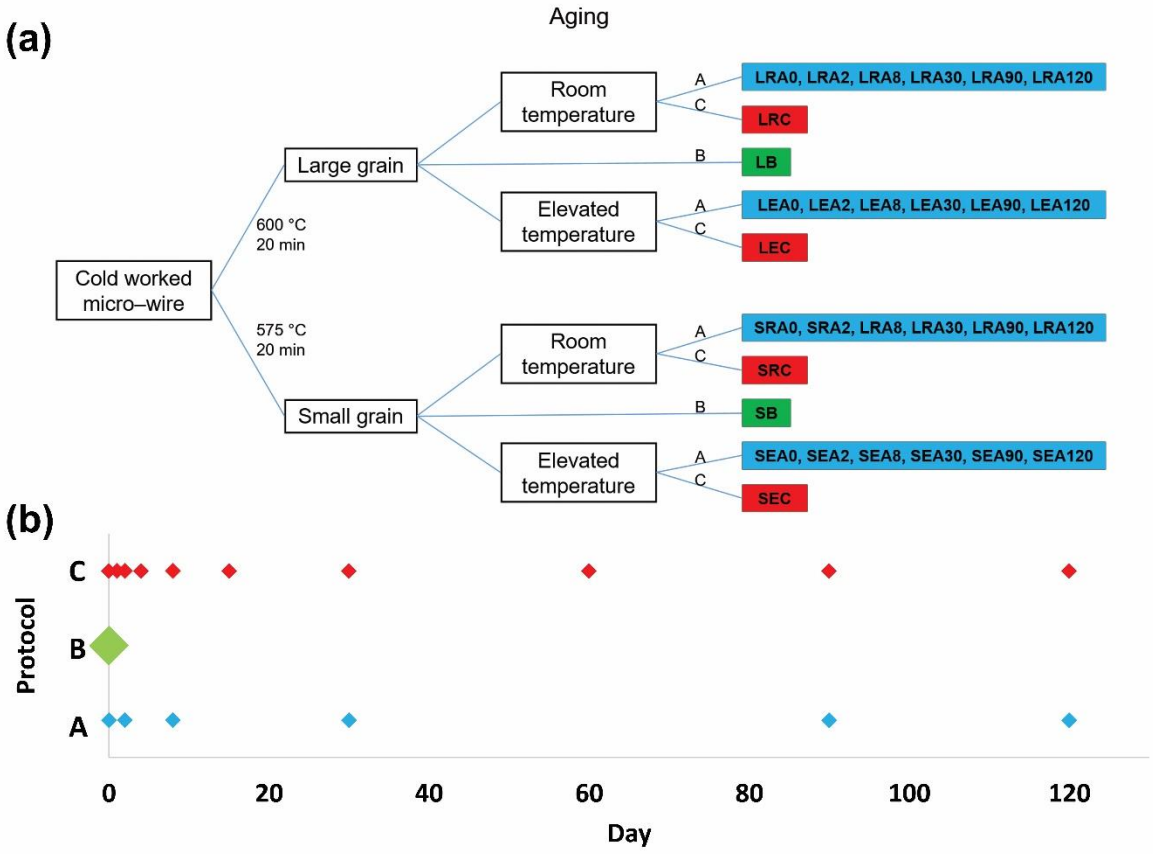

Figure 6–1 First set of experiments, (a) flowchart of heat treatments, aging and three different DSC procedures; (b) DSC timetable of protocols A (six samples, each one cycle at six different days), B (one sample, 10 cycles at day 0) and C (one sample, 10 cycles at 10 different days).

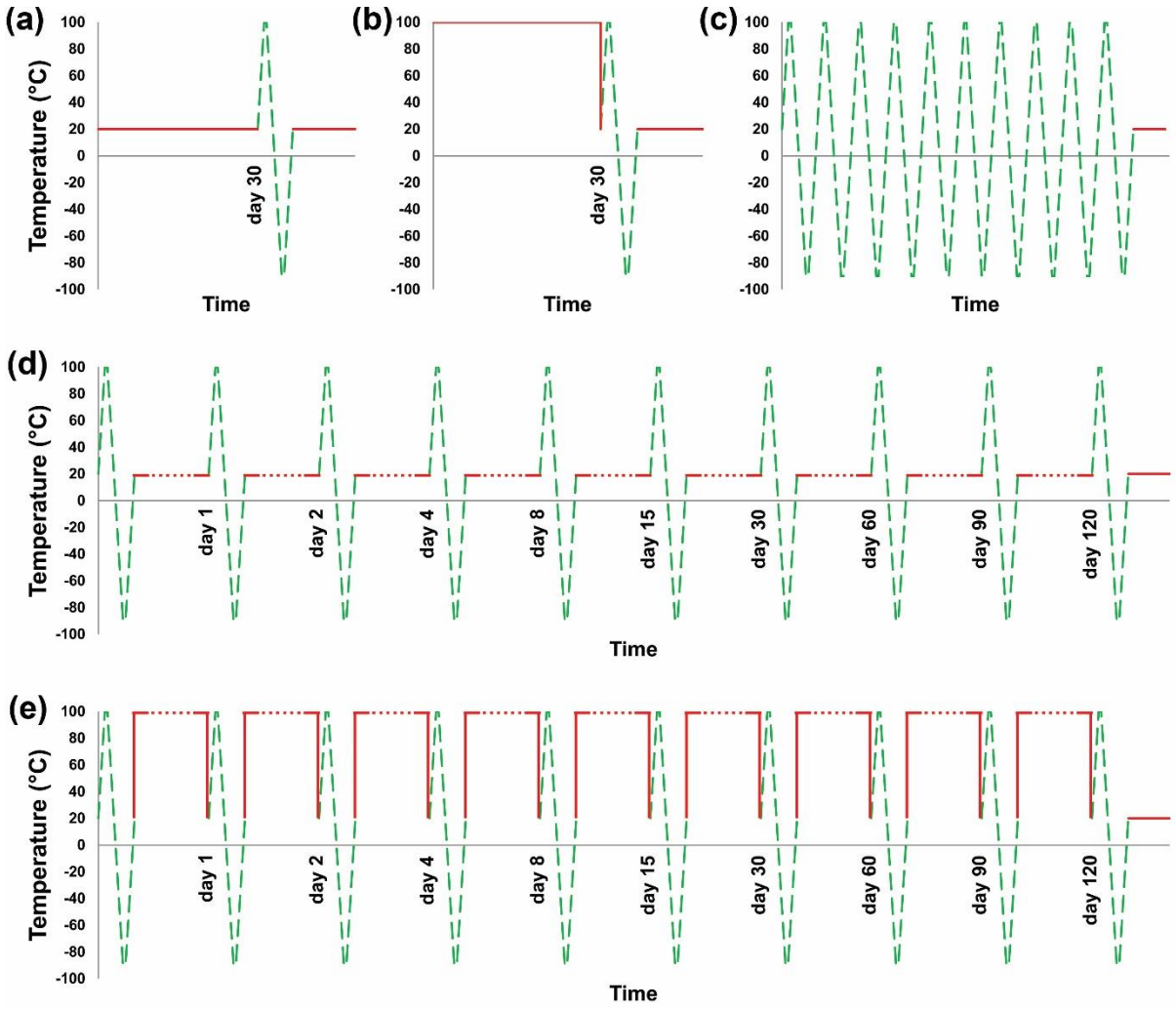

Figure 6–2 diagram of aging (red) and DSC measurement (green) of (a) L(S)RA30, (b) L(S)EA30, (c) L(S)B, (d) L(S)RC and (e) L(S)EC.

The timetable of DSC measurements for the A, B and C procedures is shown in Figure 6–1(b), in which A markers refer to different samples while C markers belong to a single sample. Comparing results of B and C will show the effect of room temperature aging between the cycles, while comparing A and C is to reveal the effect of the number of cycles. The L and S comparison is to show the effect of grain size and the R and E comparison will reveal the effect of aging temperature between the cycles. For all the above mentioned DSC tests a temperature range of (-90, +100) °C was used which guarantees full forward and reverse MT.

The second set of experiments was designed in a way to separate the effect of the bottom range of the DSC cycling temperature interval (including MT) and the top range of the DSC cycling temperature interval (excluding MT). In order to do so, the DSC measurement of the L sample,

shown in Figure 6–3 was used to find the transformation temperature ranges and to determine the experimental conditions.

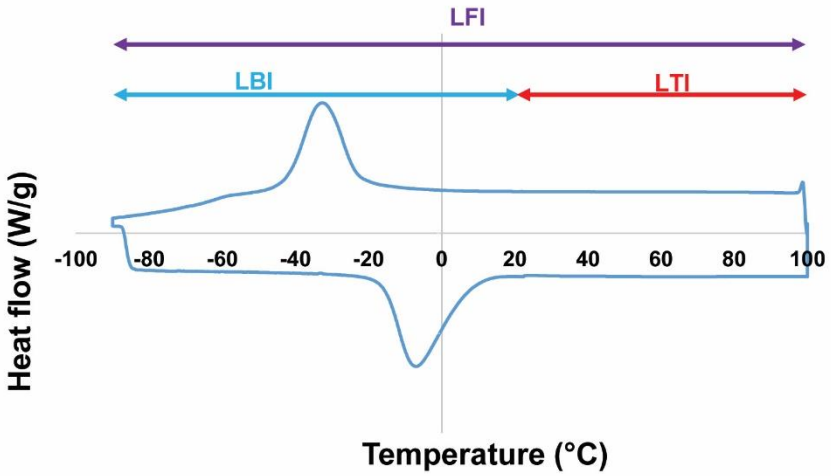

Figure 6–3 DSC curve of the L sample with the LBI, LTI and LFI temperature ranges indicated.

Three experiments were performed starting with an L sample, an initial (-90, +100) °C DSC measurement, and a package of 11 DSC cycles to be repeated 10 times. The first 10 cycles of each package cover the following temperature intervals:

- (-90, +20) °C for a sample labeled as LBI (large grain bottom interval), as shown with red solid line in Figure 6–4(a), which only includes the MT temperature range
- (+20, +100) °C for LTI (large grain top interval) sample, as shown with red solid line in Figure 6–4(b), covering only the top range of the DSC cycling temperature interval, excluding MT
- (-90, +100) °C for LFI (large grain full interval) sample, as presented with red solid line in Figure 6–4(c), including both MT and the top range of the DSC cycling temperature interval

Each package completes with a (-90, +100) °C DSC measurement, shown with green dashed line in Figure 6–4(a)–(c). In fact, the first 10 cycles of each package are meant as the actual treatment on that specific sample, while the 11th cycle is to measure the effect of that treatment.

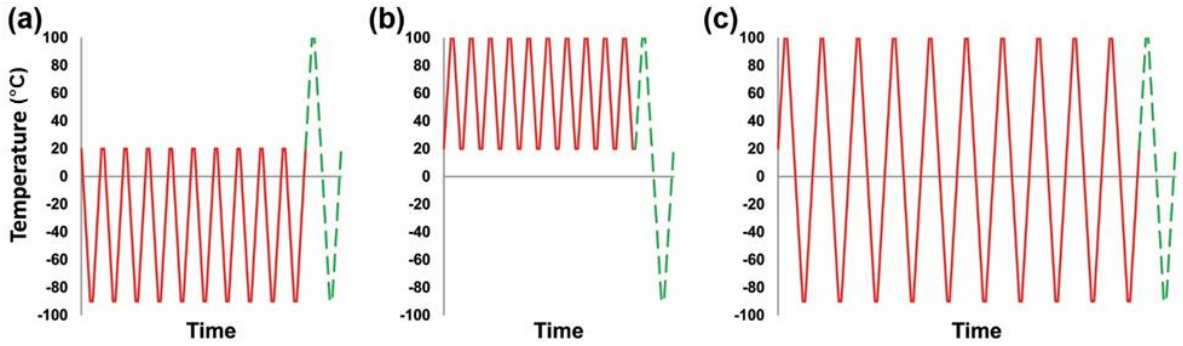

Figure 6–4 DSC temperature intervals (red) of the second set of experiments consisting of 10 times DSC cycles of (a) LBI (-90, +20) °C; (b) LTI (+20, +100) °C and (c) LFI (-90, +100) °C. All three procedures are followed by a (-90, +100) °C cycle (green and dashed) which is considered for measurements.

The method explained in Chapter 5 was used to prepare TEM specimens by electropolishing microwires. BF–TEM and SAED patterns were acquired to investigate the microstructural changes of the material in image and diffraction mode, respectively. In order to obtain meaningful comparison of quantitative data for SAEDs, the electron beam illumination (all lenses excitation, condenser and selected area apertures), specimen thickness, and imaging conditions (exposure time and camera calibration) were kept consistent for the whole procedure. CBED was used to measure the thickness of the sample and to select consistent areas for all SAEDs. As the diffuse intensity is very weak and a large selected area aperture could not be used due to the small grain size in the present samples, for each SAEDs 10 images were acquired and superimposed in order to improve the signal–to–noise ratio.

6.3 Results

DSC results of the first set of experiments for large grain samples are summarized in Figure 6–5. Samples belonging to A, B and C procedures are represented by triangles, squares and circles, respectively, and RT and ET aging are shown by solid and dashed lines, respectively. In Figure 6–5(a) M_s versus number of cycles is presented while Figure 6–5(b) shows M_s versus the day of the experiment after quenching. Each of eight A samples undergoes only one DSC cycle at a specific day, so they appear only in the graph with the day of the experiment, Figure 6–5(b). The opposite holds for B sample which undergoes multiple DSC tests at the day of quenching, so it appears only in the graph involving the number of cycles, Figure 6–5(a). Sample C undergoes

repeated DSC tests at different days, so it appears in both graphs and can be compared with samples A and B. The obtained results are analyzed in the following three sections.

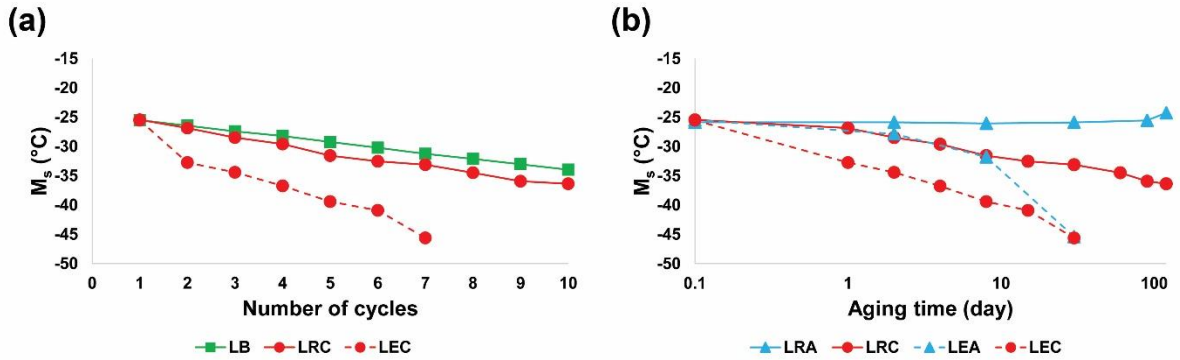

Figure 6–5 (a) M_s versus number of cycles for LB, LRC and LEC samples; (b) M_s versus aging time for LRA, LRC, LEA and LEC samples. M_s of LEC and LEA samples for some high number of DSC cycles could not be found due to the weak MT peak as a result of strong MT suppression.

6.3.1 Effect of including RT aging between DSC cycles

The large grain sample DSC tested at different days and kept at RT in between, LRC curve in Figure 6–5(a) and (b), resembling the condition of the material in typical applications, shows a nearly linear decrease of M_s by 1.2 °C ± 0.2 °C per DSC cycle. There are two parameters that may play a role in this behavior: repeated DSC tests on the sample and the time gap between the day of quenching and each DSC measurement, RT "aging". In order to separate these two effects, LB and LRA tests were designed in the way that in each of them the sample is only affected by one of these conditions. LRA results obtained from *different* large grain samples each DSC tested at different days (i.e., no repeating cycles on a single sample, only time gap difference) are presented in Figure 6–5(b). Apart from small fluctuations the graph shows no decrease but instead even a slight increase of M_s towards the long aging times. This shows that RT aging alone will not suppress MT.

LB, which is a large grain sample 10 times DSC cycled continuously at the day of quenching (only repeating, no time gap), on the other hand, shows a linear decrease of M_s by 1.0 °C ± 0.1 °C per DSC cycle, as can be seen in Figure 6–5(a). These LB results reveal that the accumulative effect of DSC cycles on the sample is responsible for the MT suppression. Moreover, comparing LB and LRC shows that this effect is enhanced if the sample is aged at RT between the DSC measurements.

In Figure 6–6 $[112]_{B2}$ SAEDs of different samples are shown. Figure 6–6(a) belongs to the original sample, REF, with no thermal cycles and Figure 6–6(b)–(c) represent LRA8 and LRC, respectively. The difference in strength and spread of the diffuse intensity in the different SAEDs

due to the improvement of ordering by formation of Ni clusters can already be seen by eye. In order to obtain quantitative comparison between the observed diffuse intensities, the rectangle shown in Figure 6–6(a) where three families of diffuse planes cross each other and produce intensity maxima and minima was selected to find the averaged line profile as an internal reference, similar to the procedure presented in Chapter 5. In the current series of experiments, however, a self–written Matlab code was used to automatically select the region of interest from the SAED pattern, calculate the averaged profile, fit the Gaussian curve to the local extrema and calculate the DIF value introduced in Chapter 5. A screenshot of the Matlab code output is shown in Figure 6–7 and the obtained DIF values of Figure 6–6 are demonstrated in Figure 6–8.

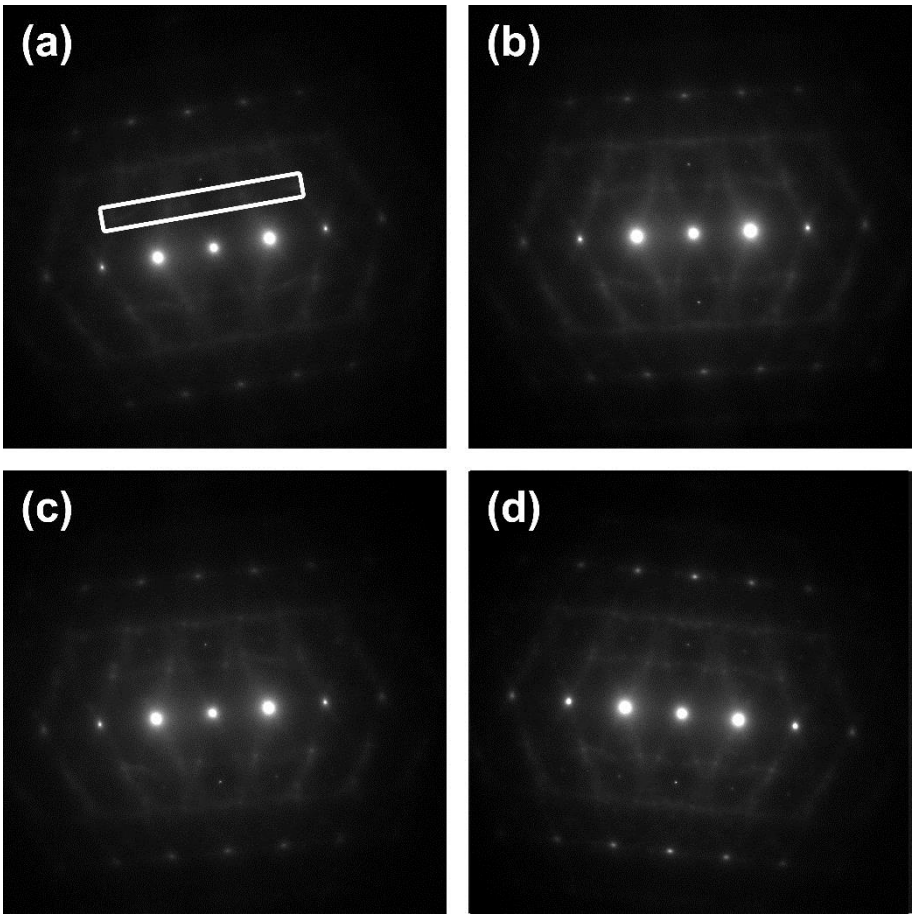

Figure 6–6 $[112]_{B2}$ SAED patterns of the samples (a) REF, (b) LRA8, (c) LRC and (d) LEC.

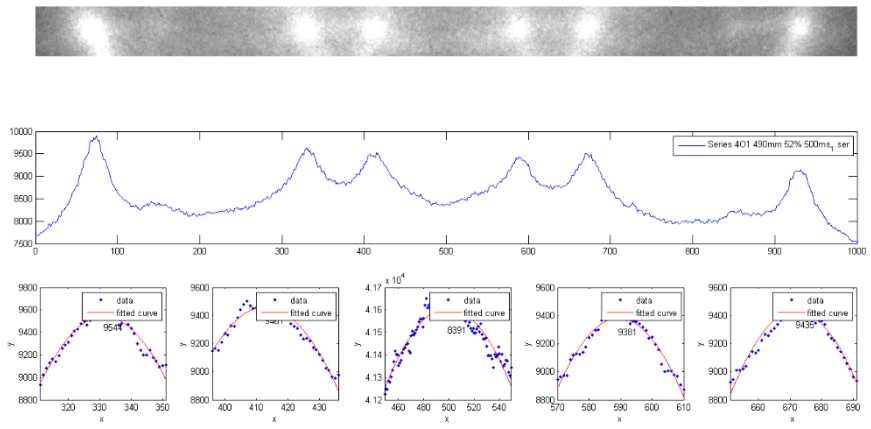

Figure 6–7 Screenshot of the Matlab code showing the region of interest from the SAED, the average profile and Gaussian curves fitted to the peaks.

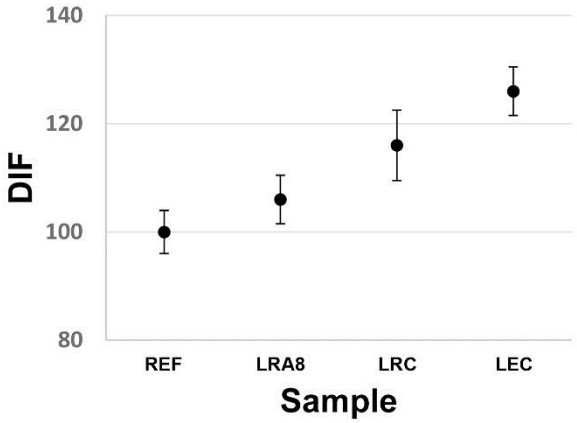

Figure 6–8 DIF values of LRA8, LRC and LEC samples.

6.3.2 Effect of aging at 100 °C between DSC cycles

Enhancement of MT suppression by RT aging between DSC cycles raises the question of what if the aging temperature is slightly higher than RT, but not high enough to get close to the Ni_4Ti_3 precipitation range of about 350 °C – 400 °C? To answer this question, a large grain sample was DSC tested similar to the LRC sample but aged at an elevated temperature of 100 °C in between. The M_s results in Figure 6–5(a) and (b) labeled as LEC show severe suppression of MT (about 20 degrees after 7 cycles), and the DSC curves shown in Figure 6–9 reveal the following behavior: By increasing the number of DSC cycles and aging prolongation the high B2→B19' peak (LEC0) splits into two peaks revealing a B2→R and R→B19' two-stage process, the former propagating towards

higher temperatures and increases in peak height while the latter shifts towards the lower temperature and spreads out and nearly becomes invisible. A similar process happens in the reverse transformation, however, the peak separation in the reverse transformation only occurs after more cycles and is less pronounced.

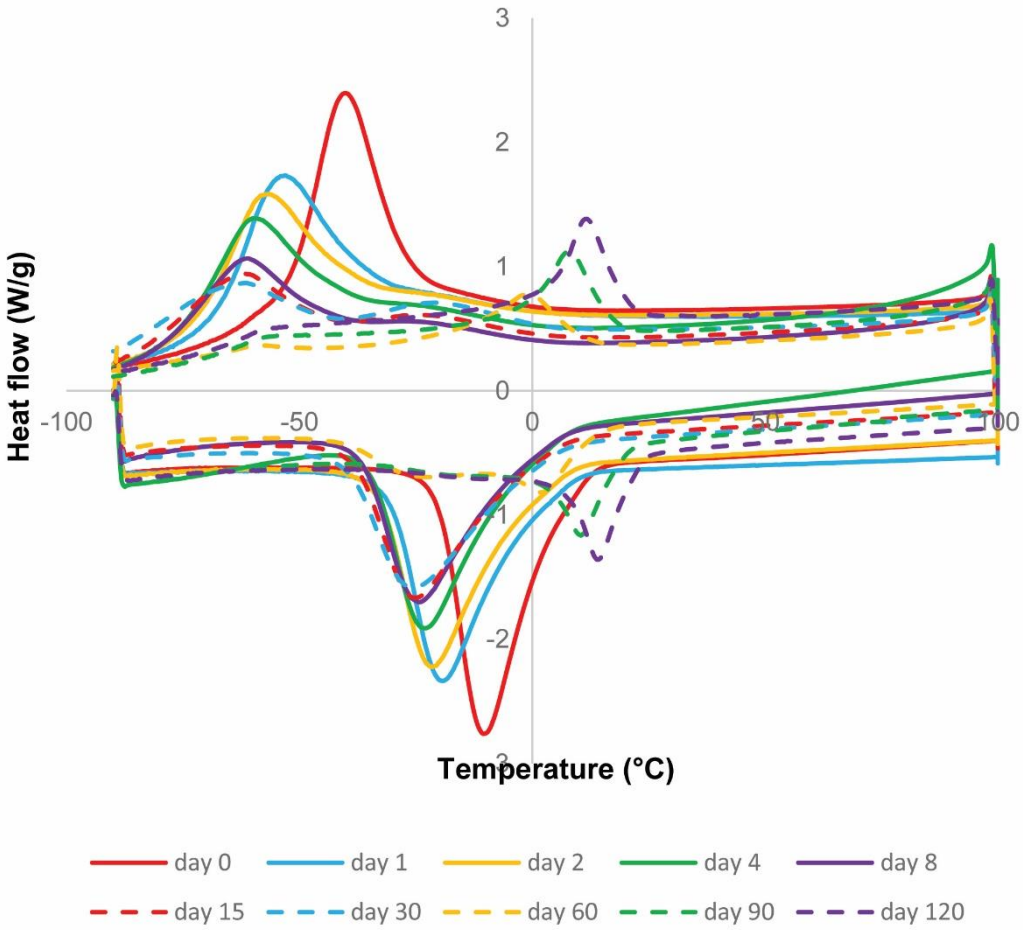

Figure 6–9 DSC results of the LEC sample tested at different days and aged at 100 °C in between.

LEA experiments were also performed on samples kept at 100 °C and DSC tested only once at different days after quenching. The results presented in Figure 6–5(b) show a slighter decrease of M_s compared to that of LEC, showing DSC cycling combined with elevated temperature aging in between to be the strongest MT suppression procedure. These experiments show that drastic changes in material behavior may occur at temperatures that are normally considered too low to induce any effect on the structure or behavior of the material.

Figure 6–6(d) shows the $[112]_{B2}$ SAED of the LEC sample, of which the DIF is plotted in Figure 6–8.

6.3.3 Effect of grain size

In order to study the effect of grain size, the aforementioned procedures were also performed on small grain samples, S. The results presented in Figure 6–10(a) and (b) show a similar trend as that of the L samples, but different in numbers.

Comparing the first cycle in Figure 6–5 and Figure 6–10 shows that the S sample reveals an initial M_s of ~ -21 °C which is slightly higher than that of L sample, ~ -25 °C. However, M_p of both samples is ~ -41 °C.

Comparing the full graphs it can be concluded that the grain size has a clear effect on the changes of the MT temperatures when retaining the same external variations. For the present small grain sample M_s decreases by 0.7 °C ± 0.1 °C per DSC cycle for SB sample, an effect which is about 30% smaller than for the larger grain sample LB. The SRC sample shows a decrease of 1.0 °C ± 0.2 °C per DSC cycle, an effect about 15% smaller than in the LRC sample. SRA, however, shows a slight increase. Comparing the S results with those of corresponding L samples thus show slighter MT suppression in the small grain samples.

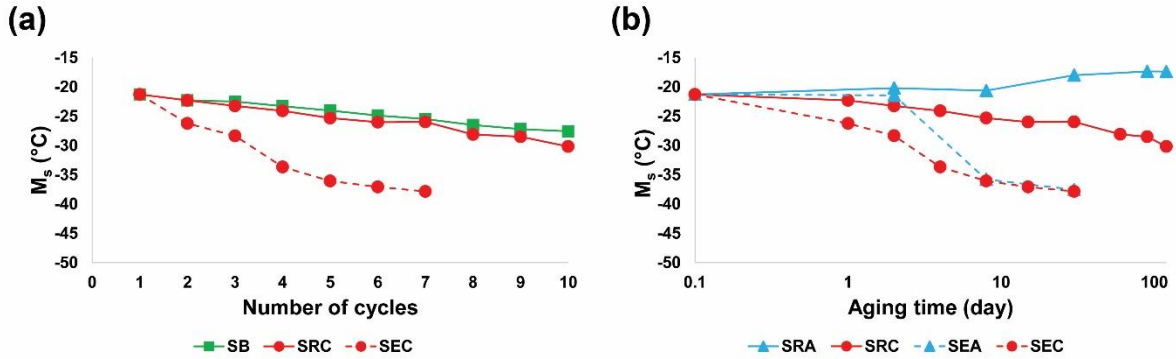

Figure 6–10 M_s versus number of cycles for SB, SRC and SEC samples; (b) M_s versus aging time for SRA, SRC, SEA and SEC samples. M_s of SEC and SEA samples for some of the higher number of DSC cycles cannot be found due to the weak MT peak as a result of the strong MT suppression.

No SAED from the small grain samples were acquired since the diffuse intensity obtained from a small enough selected area aperture to cover only one grain, necessary to fix the orientation as in Figure 6–5, was too weak to yield meaningful results.

6.3.4 Effect of the temperature interval of DSC cycling

The so far presented DSC results of which the thermal cycling effect was investigated were all performed in the (-90, +100) °C temperature interval. In the second set of experiments, three

different DSC temperature intervals, schematically shown in Figure 6–3, were chosen to study the effect of the thermal cycling temperature interval on the MT.

Figure 6–11 shows M_s versus the number of DSC cycles for the LBI, LTI and LFI experiments. The full LFI test that includes both the MT and top temperature range shows the most abrupt decrease of M_s values. LBI including only the MT temperature range has a smaller effect and LTI covering only the top temperature range reveals the least effect on M_s. In these three samples M_s suppression between two consecutive points is caused by the 10 treatment cycles (red line in Figure 6–4) and one measurement cycle (green dashed line in Figure 6–4) all combined. In order to determine the effect of the measurement cycles, REF sample with 11 consecutive measurement cycles is presented. Therefore, the net effect of treatment cycles in different temperature intervals of LBI, LTI and LFI samples is the difference of those curves with the REF curve.

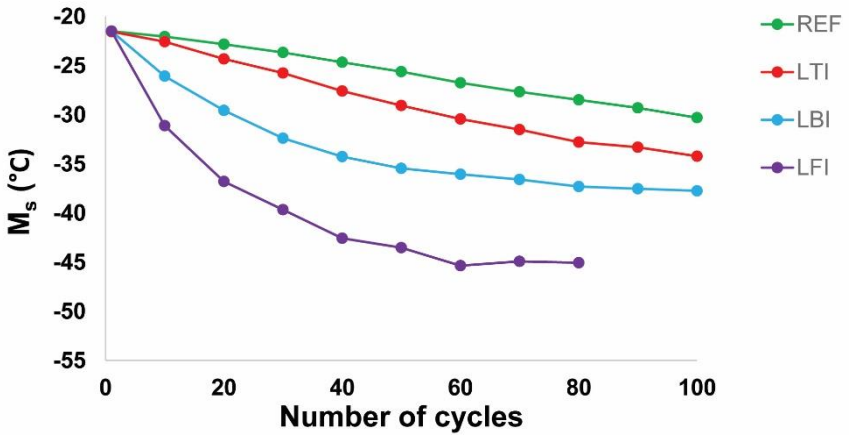

Figure 6–11 M_s versus number of DSC cycles for the LBI, LTI, LFI and REF samples. M_s of LFI sample for some high number of DSC cycles cannot be found due to the weak MT peak as a result of strong MT suppression.

Figure 6–12 shows $[112]_{B2}$ SAED patterns of the REF, LTI and LFI samples, respectively, and obtained at the end of the series (unfortunately, no good samples could be produced from the LBI batch). The corresponding DIF values are presented in Figure 6–13.

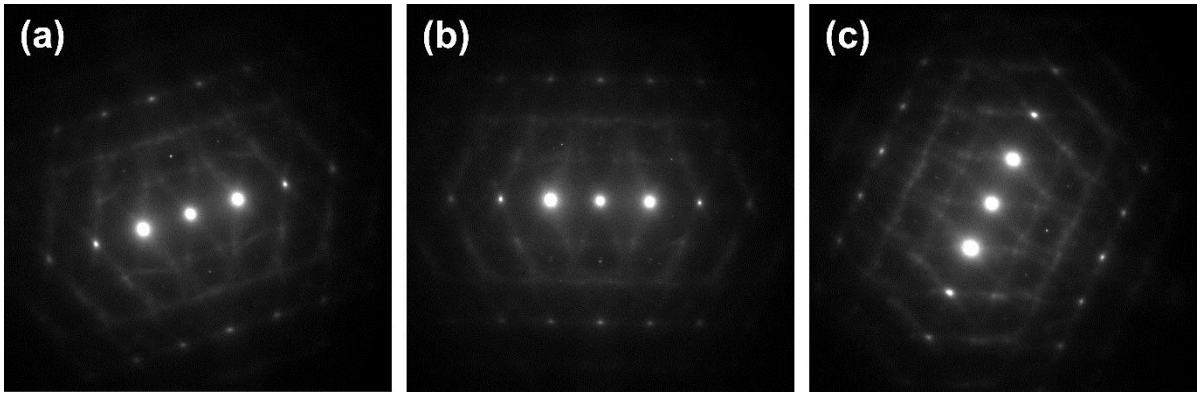

Figure 6–12 $[112]_{B2}$ SAED patterns of (a) REF (b) LTI and (d) LFI samples.

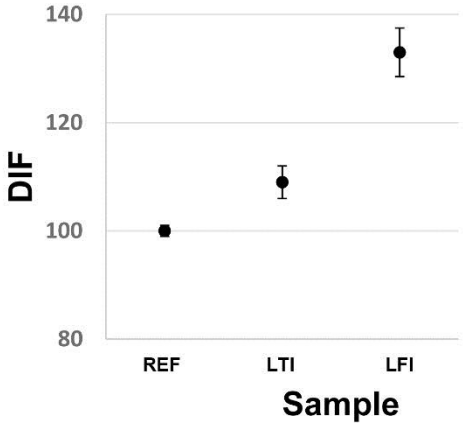

Figure 6–13 DIF of LTI and LFI samples.

6.4 Discussion

The DSC results of the first set of experiments confirm the results obtained for bulk material in Chapter 5. Enhancement of ordering due to repetitive thermal cycling is concluded from the evolution of the diffuse intensity from the more homogeneous and spread intensity of the reference sample to a sharper and more localized intensity in the cycled samples and which is linked to the formation of the Ni_4Ti_3 precursors. The change of DIF parameter for each sample is in line with the decrease of M_s for that sample.

There are three parameters that are known for affecting MT as a result of thermal cycling. The first parameter is the strain field induced by the coherent Ni_4Ti_3 precipitates (suppressive), as explained in § 2.5.4.1. The second one is the local decreasing of Ni content in the matrix by Ni depletion caused by formation of Ni_4Ti_3 precipitates (supportive), as described in § 2.5.4.1 and Figure 2–4. The third parameter is dislocation formation due to the MT in the former cycles

(suppressive), as was explained in § 2.5.4.2. Which and how strong these parameters play a role in the MT changes depends on each specific experiment.

The decrease of M_s in the repeatedly cycled samples occurs in spite of the depletion of Ni in the matrix due to the formation of Ni_4Ti_3 precursors which is expected to promote MT. In order to understand this, one should consider the size of "precursor" and "matrix" in this scheme. Although there is no direct measurement of the dimension of the clusters, their size could not be larger than a few atoms, since they were not detected by TEM or STEM imaging and produce no super–spots in the SAED patterns. In other words, such small clusters will not deplete the matrix from Ni content at a large scale, as was also concluded from Figure 5–4 where diffuse intensity was present in every diffraction pattern recorded from a nm area of the sample acquired by nano–probe scanning on a large area of the sample. A simple calculation based on the composition of the material shows that if the Ni needles are of 7 atoms length (three Ti to Ni replacements), on average each cube of the size of about 6×6×6 unit cells contains such a cluster. The size of the cube will be about 7×7×7 and 8×8×8 unit cells for a Ni cluster of 13 and 17 Ni atoms length, respectively. So even if the Ni clusters are as large as 13 atoms length, in each about 2 nm^3 of the material one such cluster can be found, which, taking a TEM sample thickness of a few tens of nm into account, explains the observed diffuse intensity in the nano–probe mode. This shows that Ni depletion due to the formation of such small clusters will not provide large equiatomic matrix volumes with higher M_s than that of the Ni–rich material. As the equiatomic matrix should be sufficiently larger to play a role in the transformation dynamics (e.g., mean interparticle spacing should be larger than 200 nm (650 unit cells) to cause a change from a two–step to a three–step martensitic transformations on cooling [226]), the Ni depletion due to the Ni clustering at this scale cannot be expected to have an effect on MT.

The well–known dislocation formation due to the MT can cause the MT suppression, but it cannot explain the enhancement of the systematic diffuse intensity at well–defined geometric loci in between the reciprocal spots. Moreover, it cannot explain the stronger MT suppression of the LTI sample where there is no MT during the cycling and thus also no introduced dislocations (Figure 6–11). In Ni_4Ti_3 precipitates the $\{111\}_{B2}$ planes collapse and a strain field develops surrounding the precipitates, allowing the R–phase to form first and thus decreasing M_s. The reordering in those Ni_4Ti_3 precipitates is obtained by replacing, in an ordered fashion, some Ti atoms by Ni atoms in the B2 structure. Since the latter has an ordered bcc CsCl structure, this automatically yields pure Ni atom rows in the $\langle 111\rangle_{B2}$ direction (which becomes the $[001]_{4:3}$

direction in the precipitates, hexagonal description). $\langle 111 \rangle_{B2}$ Ni needles responsible for the observed diffuse intensity can thus be considered as an early stage of the Ni_4Ti_3 precipitates. The systematic replacement of Ti atoms with smaller Ni atoms forming pure Ni needles is expected to induce smaller but similar kind of strain fields as the full–grown precipitates, thus yielding a similar but smaller effect on M_s. The $\langle 111 \rangle_{B2}$ Ni needles will eventually line up to form the Ni_4Ti_3 precipitates and are oriented in the direction perpendicular to the central plane of those precipitates which is also the direction of the largest induced strain field.

The smaller effect of full thermal cycling on the S samples can be explained by the fact that the mobile dislocations created during MT can be easier absorbed at the grain boundaries compared with in the L samples, which reduces the MT suppression by the dislocations. On the other hand, upon full annealing Ni_4Ti_3 precipitates are much smaller and denser in the vicinity of the grain boundaries rather than in the grain interior [114]. This implies that in the S samples the cluster evolution will be more complete than in L samples, which should increase the share of MT suppression by Ni clusters compared with that of dislocations. In this case, the lowered influence of the dislocations in the S sample takes the upper hand.

The LTI and LFI results of the second set of experiments confirm the work of Wagner et al. [108], while LBI was not covered in their work. One should note that the maxima of the DSC temperature interval in their work were 150 °C, 200 °C and 250 °C (for a material with $M_f \approx$ -30 °C and $A_f \approx$ +30 °C), which enhances the formation of Ni_4Ti_3 precursors at those maximum temperatures. However, the DSC temperature interval maximum in the present work is 100 °C, which still improves ordering as seen from the DSC and DIF results. This shows that for short–range ordering to improve one does not need to go to a temperature far above A_f, (~ 120 °C – 220 °C above A_f in Wagner's work) but that this can already occur at lower temperatures (~ 80 °C above A_f in the present work). More importantly, the observation of increasing of DIF with decreasing M_s for the bulk material with a DSC temperature interval maximum of 25 °C (in Chapter 5) reveals that the MT itself has its own effect on the enhancement of ordering. One mechanism that could play a role is the shuffling of atoms when the martensite front moves back and forth in the matrix which could enhance the local replacement of individual Ti atoms by Ni atoms yielding short $\langle 111 \rangle_{B2}$ Ni clusters precursing the formation of Ni_4Ti_3 precipitates at higher temperatures.

6.5 Conclusion

From the two sets of experiments the following conclusions were drawn. In samples annealed above the recrystallization temperature, yielding large enough grains to acquire meaningful SAEDs, consecutive thermal cycling not exceeding temperatures above 100 °C suppresses MT. The suppression enhances when the DSC cycling is combined with RT aging and becomes even stronger when the aging is performed at elevated temperature of 100 °C. M_s measurements show that aging at RT alone has no significant effect on the MT. Aging at elevated temperatures of 100 °C alone, however, suppresses the MT. Comparing DSC results of large and small grain samples shows that the effect of room and elevated temperature aging is stronger in large grain samples than in small grain samples. SAED patterns show an increase of Ni clustering in line with decreasing M_s. Since due to the small size of these Ni clusters there is no precipitate–free matrix with lower Ni content, martensite nucleation is not supported but instead suppressed due to the strain field induced in the matrix by the Ni clusters. It is suggested that the smaller size of Ni atoms compared to that of Ti atoms induces strain into the matrix surrounding the $\langle 111 \rangle_{B2}$ Ni clusters promoting R–phase and suppressing MT.

MT included, high temperature included and full range temperature DSC cycling were performed to separate the effect of MT and high temperature range of DSC cycling. High temperature included cycling suppresses MT by enhancement of ordering due to the high temperature range, while MT included cycles suppress MT by enhancement of ordering due to the MT and also strain field of the introduced dislocations. The full range temperature DSC cycling shows the most MT suppression due to the combination of all aforementioned reasons.

Chapter 7:

In–situ TEM stress–induced martensitic transformation in $Ni_{50.8}Ti_{49.2}$ micro–wires

In this chapter stress–induced martensitic transformation in sub–micron size Ni–rich Ni–Ti specimens is investigated using in–situ transmission electron microscopy tensile straining.

This chapter is based on the following publication:

- Pourbabak, S.; Orekhov, A.; Samaee, V.; Verlinden, B.; Van Humbeeck, J.; Schryvers, D. In-Situ TEM Stress Induced Martensitic Transformation in Ni50.8Ti49.2 Microwires. Shap. Mem. Superelasticity 2019, 5 (2), 154–162. https://doi.org/10.1007/s40830-019-00217-6.

7.1 Introduction

As described in § 2.5.2 and 2.5.3 a martensitic transformation can either be induced thermally or mechanically. The L micro–wire with micro–sized grains of which the thermal characteristics have been investigated in Chapter 6, together with a micro–wire with much larger grain size are chosen for macro– and micro–size tensile straining tests to develop a full picture of the properties of this material. As mentioned in § 2.4, conventional SMAs are annealed below the recrystallization temperature [227] in order to maintain the MT stress lower than that of plastic deformation. However, the very small grains and also presence of dislocations in such materials complicate proper imaging in TEM tensile tests and prevent single crystal tensile examination. Therefore, the tensile test specimens were obtained from recrystallized material with larger grains and less dislocations.

Although stress–induced martensitic transformations have been well studied [6,86,89,228,229] and utilized [12,75,230] at macro–scale, not many quantitative investigations have been performed at the nano–scale, partly due to technical restrictions. Such studies are, however, essential in order to apply Ni–Ti alloys in micro–mechanical devices. Although the previous in–situ experiments discussed in § 2.5.3.2 provide some insight on the martensitic transformation and behavior of the material, they usually lack quantification and mechanical data linked to the TEM observations. The micro– and nano–scale of the present observations enables us to better understand the underlying structural mechanisms that play their part in the overall mechanical response to deformation of Ni-Ti polycrystals. Translating these observations to the macroscopic behavior is, however, beyond the scope of this work.

The results of a series of in–situ experimental investigations of the SIMT in single crystal and polycrystalline Ni–Ti material are given in this chapter. The experiments were performed at room temperature and the CCD images were continuously captured by the integrated video interface during the experiments and synced with the collected quantitative mechanical data of the holder, enabling dedicated post processing of the results and coupling the micro–structural observations directly to quantitative stress–strain curves. In all cases the starting material is in the austenite phase at room temperature which implies that the observed and induced transformations yield superelasticity at the macro–scale.

7.2 Experimental procedure

The $Ni_{50.8}Ti_{49.2}$ wire with 150 μm diameter introduced in § 3.1 was heat treated at the two following conditions (each used separately):

1. 600 °C for 20 min yielding sub–micron–sized grains (up to ~ 1.5 μm)
2. 800 °C for 30 min yielding micro–sized grains (up to ~ 30 μm)

and followed by room temperature water quenching to prevent precipitation.

The key parameters of the martensitic transformation and the status of the material at room temperature, at which the mechanical tests are performed, were investigated using DSC measurements by METTLER TOLEDO. Also, tensile tests were carried out on the micro–wire to obtain the macroscopic parameters and stress–strain curves.

Dog–bone shaped specimens with lateral sizes of ~ 0.7 μm – 1.5 μm × 2 μm – 3 μm were cut from the wires and mounted on a PTP device using FIB, as was described in § 3.4.2. The specimens obtained from the large grain size sample (i.e., annealing at 800 °C) were cut from grain interiors resulting in single crystal specimens for the in–situ experiment, while those obtained from the small grain size sample (i.e., annealing at 600 °C) contain multiple grains of different sizes.

Before the mechanical tests EELS was performed on each specimen to measure the thickness [197]. The nano–mechanical tests were performed using the Bruker PI95 PicoIndenter holder in a FEI Osiris instrument running at 200 kV. The in–situ tensile experiments were carried out in the displacement control mode [88,177]. As the gauge length was slightly different from one specimen to another (2000 nm – 3000 nm), the displacement rate was proportionally chosen as 0.2–0.3 nm/s depending on each specimen length, in order to achieve a common strain rate of 10^{-4}/s [177] for all tests and to obtain comparable results. The holder provides the quantitative load–displacement data while at the same time a real time movie of the experiment can be obtained under bright field conditions using the microscope CCD camera; most images shown in this work are snapshots from these videos. Since the development of the micro–structural changes occurs at relatively high speed, i.e., often from one frame to the next, and a continuous BF–TEM video was also required for post analysis displacement measurements, no live diffraction data could be obtained during these running in–situ experiments. Still, some selected area electron diffraction data was obtained at the start and finish of particular cycles. The interpretation of the images obtained during the in–situ experiments is thus solely based on the BF contrast, which in some cases is not fully conclusive, in part also since only one tilt axis is available and no tilting can be performed during

the in–situ experiment because of risks of instabilities affecting the deformation control. On one occasion (Specimen Single3) the experiment was stopped after the appearance of the first martensite plates (which means that at that moment the displacement was kept constant), in an attempt to obtain diffraction data from an intermediate situation. Unfortunately, the transformation did not stop and the specimen fractured shortly after, so no further data could be gathered this way.

Due to the probable influence of thermal drift on the displacement data obtained from the instrument, the real displacement of the specimens was obtained by image displacement tracking of the deformation movies and accordingly strain amounts were obtained by dividing the raw displacement data by the initial length of the specimen [191]. The load data obtained from the instrument is a combination of the PTP device springs and the force applied on the tensile specimen. Knowing the device spring constant, the force on the specimen can be calculated thus yielding the stress by dividing by the specimen cross–section [100,191,192].

Nanomegas® ACOM–TEM [231] was performed in a FEI Tecnai instrument running at 200 kV on one of the polycrystalline specimens to investigate its texture.

In total three single crystal and three polycrystalline specimens with different thicknesses were investigated. They are referred to as Single1–Single3 and Poly1–Poly3 hereafter. One polycrystalline specimen (Poly3) was chosen perpendicular to the wire direction while the other specimens were taken along the central axis of the wire.

7.3 Results

The A_f temperature of the large and small grain size material was measured by DSC and in all cases found to be ~10 °C, which means that the material is in the austenite phase at room temperature, at which all tensile experiments are performed. This is confirmed by TEM observations and SAED patterns before each test. Also, no precipitates were found by TEM in any of the specimens, confirming the rapid quench.

7.3.1 Single crystal

The uniaxial stress–strain curve of the original 150 μm wire annealed at 800 °C for 30 minutes and of which the PTP single crystal specimens have been taken is shown in Figure 7–1. In this graph the stress plateau starts at ~ 0.9% strain with a drop in the beginning and ends at ~ 7.3% strain, where the martensite elastic deformation starts. The drops observed on the stress plateau

are due to the transformation of some martensite laths which causes temporary relaxation and decreases the stress. The height of the stress plateau is ~ 380 MPa and the Young's modulus is ~ 53 GPa.

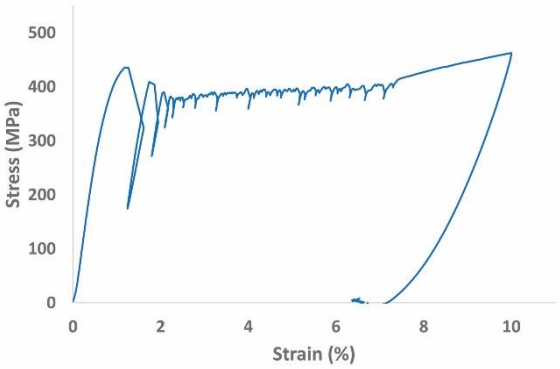

Figure 7–1 Stress–strain curve of the 150 μm wire annealed at 800 °C for 30 minutes, from which the single crystal PTP specimens were taken.

7.3.1.1 Specimen Single1, along the wire, 105 nm thick

Figure 7–2(a) represents the in–situ stress–strain curve of the single crystal specimen cut along the wire and having a thickness of 105 nm ± 11 nm as measured by EELS. The normal to the specimen is close to the $[011]_{B2}$ direction and the pulling direction is close to $[-11-1]_{B2}$ (Figure 7–2(b)), confirming the $\langle 111\rangle_{B2}$ texture of a drawn wire [54,232].

Halfway the region of sharp increase of stress versus strain, at appr. 1.8% strain, the slope of the curve slightly decreases and the remaining stress increase is followed by a stress drop, similar as in the bulk material [89,233]. The stress plateau, apart from some small fluctuations, remains horizontal up to ~ 12% strain where the specimen fractures. The height of the plateau is ~ 2.0 GPa and the Young's modulus, obtained from the slope of the curve in the austenite elastic deformation between 0 and 0.6% strain (in order to avoid any contribution from the first transforming parts and also used for all following cases), is found to be ~ 78 GPa. The TEM video of the experiment together with the synced stress–strain curve can be seen using the Figure 7–2(c) QR code or this link in the digital version of the thesis.

Figure 7–2(d) – (f) show bright field TEM images of the single crystal specimen at different moments of the tensile test, indicated by red arrows in Figure 7–2(a). From the corresponding TEM video, the first visible signs of the martensitic transformation occur at ~ 2.2% strain (white arrow in Figure 7–2(a)) with the appearance of a dark region on the bottom–right side with

internal plate–like contrast. A short moment later a single needle appears in the top–right corner in Figure 7–2(d), corresponding to point d on the curve, which is at the end of the elastic regime. The latter reveals typical twin variant black/white contrast surrounded by interface contrast separating the plate from the austenite matrix, as seen in the zoom of Figure 7–2(d). Upon increasing the strain, more dark parallel plates again clearly resembling martensite micro–structure nucleate and grow in different regions of the specimen, as can be seen in Figure 7–2(e), some now showing a different variant orientation from those nucleated before as judged from the main direction of the plates and interfaces.

Since no in–situ diffraction data could be collected from the specimen in Figure 7–2, it is unclear whether the major B/W plate–like contrast reveals twinned martensite or single variant plates (dark) with remaining austenite (bright, as in Figure 7–2(d)) in between, as seen in earlier qualitative in–situ work [95]. In the latter case, the slight diffraction contrast changes in the bright areas in between the dark plates could be due to small rotations of the austenite lattice. In all cases, the transformation nucleates from one edge of the specimen after which it rapidly propagates to the other side of the specimen or the boundary with other martensite variants. In the zoom from the center of the specimen in Figure 7–2(e) finer plates can be observed, indicating that already at this early stage martensite appears over the entire length of the gauge. By further pulling the specimen, the contrast of several martensite plates changes and neighboring plates seem to coalesce, from which an intermediate stage is shown in Figure 7–2(f), and plastic deformation occurs within the already existing martensite by (de)twinning and/or dislocation slip, explaining the change in diffraction contrast. In case austenite is still present, as mentioned above, these contrast changes could indicate further stress-induced transformation into martensite or newly formed twinned austenite grains, as observed by Šittner et al. [234].

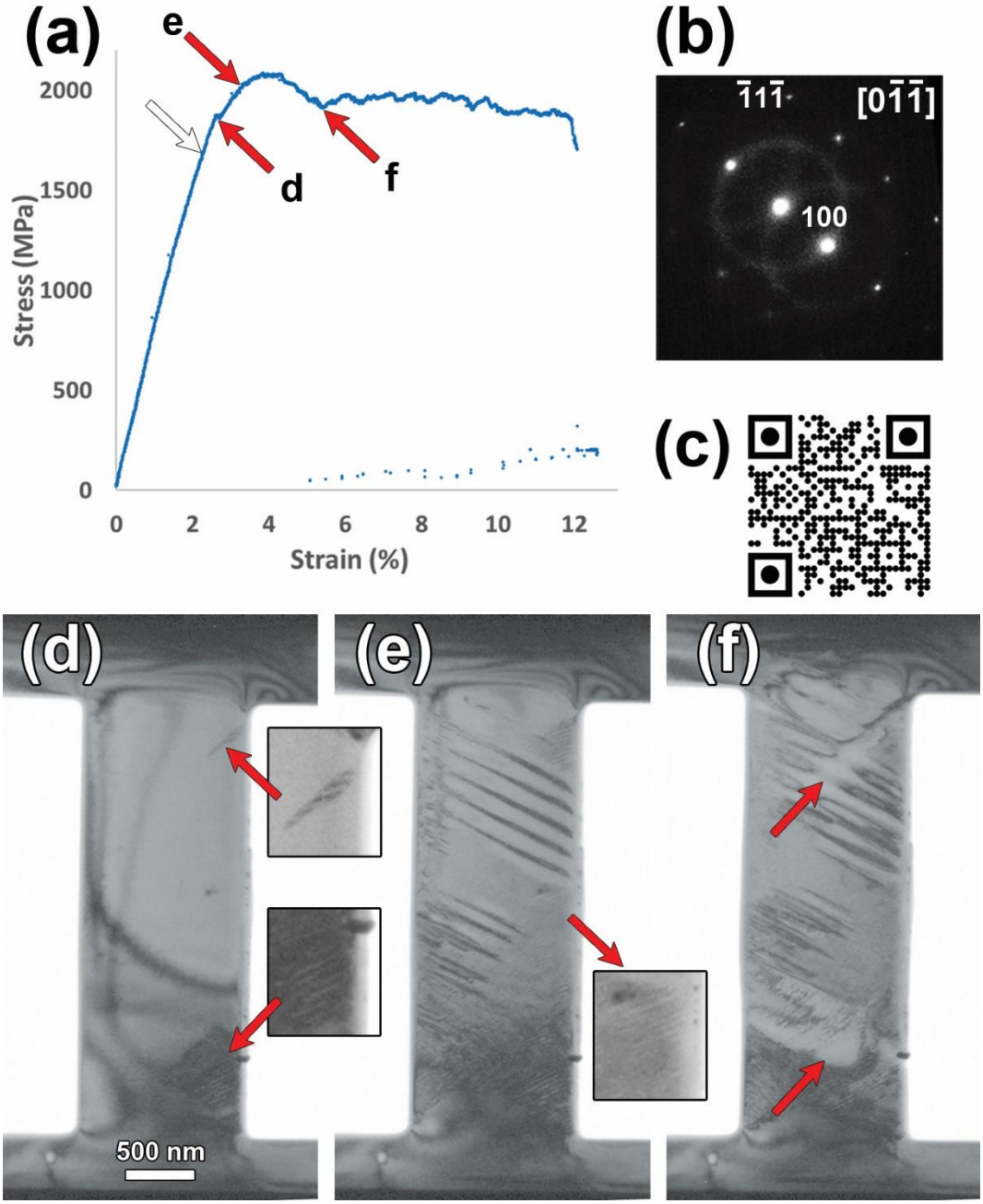

Figure 7–2 (a) Stress–strain curve of the PTP single crystal specimen, (b) SAED pattern of the specimen revealing a close to $[-11-1]_{B2}$ pulling direction, (c) QR code of the corresponding experiment video (https://www.youtube.com/watch?v=1dRp-V0AWi8), (d) – (f) different stages of the tensile test obtained as snapshots from the video and corresponding to the points indicated on the stress–strain curve of (a).

7.3.1.2 Specimen Single2, along the wire, 230 nm thick

This specimen was severely beam damaged during the FIB procedure and was also quite thick, thus did not provide proper images from the beginning of the experiment, as seen from

Figure 7–3(a). Yet, some mechanical data and diffraction patterns could be obtained. The specimen was cut along the wire and had a thickness of 230 nm ± 23 nm.

The stress–strain curve of this test is shown in Figure 7–3(b). At a strain of ~ 1.1% the curve slightly bends down, and first parallel dark laths characteristic for martensite plates start to develop at ~ 1.7% in different locations of the specimen, but are rather hard to see beyond the dislocations induced by FIB. Two main variants of martensite can be recognized in Figure 7–3(c) (indicated by dashes on either side), the snapshot taken from the indicated moment in Figure 7–3(b).

The specimen fractured at a strain of about 2.8% which is very low compared to other specimens. This is due to the strength–degrading surface defects introduced by high–energy Ga ions during the FIB process which promote plasticity on the specimen surface. Bei et al. found [235] that the shear stress of Mo micro–pillars produced by etching away the matrix, is much higher than when produced by FIB, which they attribute to the surface FIB damage. Also Lee et al. [236] found that FIB irradiation significantly reduces the yield strength of pristine Au micro–particles. The fracture interface, as seen in Figure 7–3(d), is parallel to one of the martensite variants. Due to the very early fracture of the specimen, it is not certain that the small period before fracture in which the increase of stress is interrupted should be interpreted as the start of stress plateau. Figure 7–3(e) is the QR code linked to the video of this experiment which also can be found in this link in the digital version of the thesis. The Young's modulus was found to be ~ 81 GPa.

The SAED provided in Figure 7–3(f) shows the $\langle 011 \rangle_{B2}$ orientation for the specimen surface and a $\langle 111 \rangle_{B2}$ as pulling direction, similar to the case of the Single1 specimen.

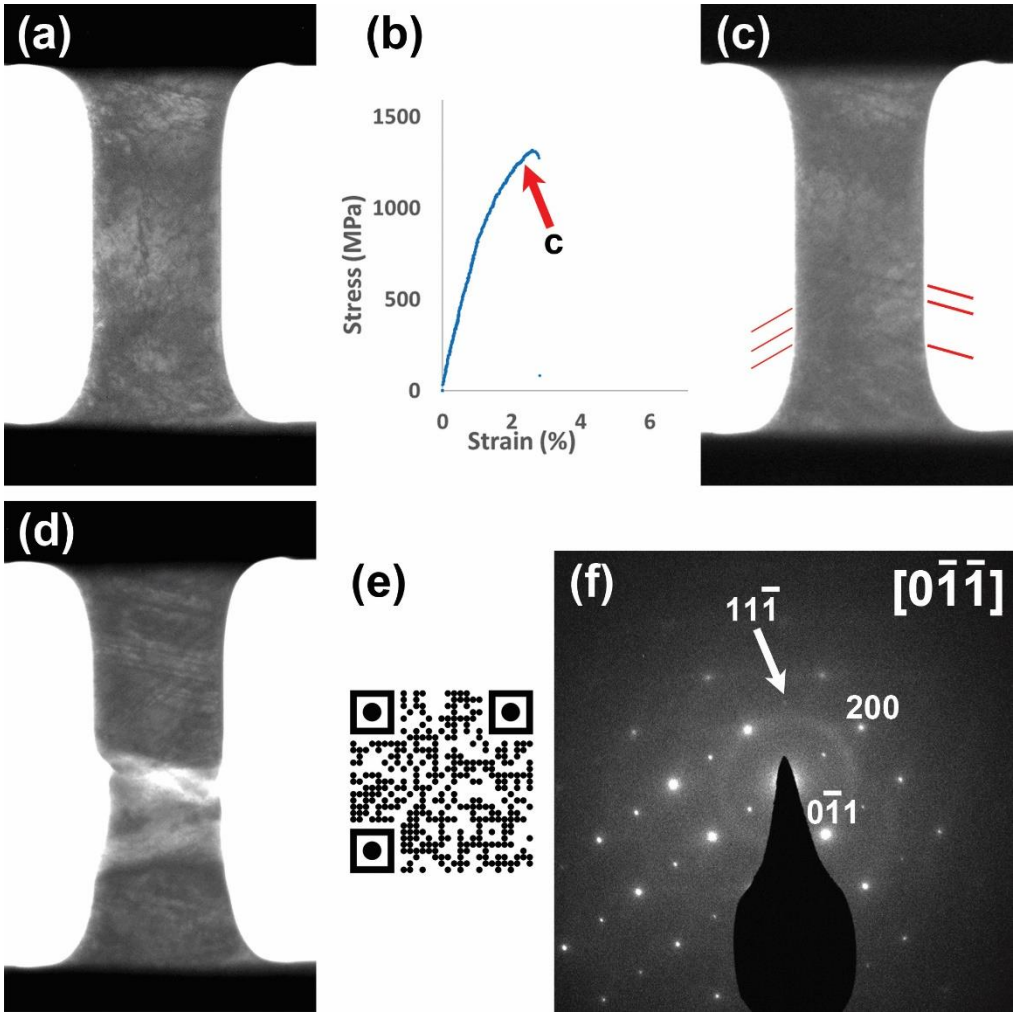

Figure 7–3 (a) BF–TEM image of the specimen before pulling, (b) stress–strain curve, (c) image from the moment indicated on the stress–strain curve with dashes indicating the two appearing variants, (d) specimen after fracture along one of the variants, (e) QR code of the video experiment (https://www.youtube.com/watch?v=DuwBjbCT-yU), (f) SAED pattern revealing $\langle 111 \rangle_{B2}$ to be the pulling direction.

7.3.1.3 Specimen Single3, along the wire, 200 nm thick

A third single crystal specimen was prepared for tensile testing, this time with the intention to obtain diffraction data during the experiment where the specimen was under strain, in order to investigate the nature and micro–structure of the transformed region. The specimen was cut along the wire and has a thickness of 200 nm ± 20 nm. The BF–TEM image and its corresponding SAED are presented in Figure 7–4(a) and (b), respectively. The specimen had a surface orientation of $\langle 011 \rangle_{B2}$ and pulling direction $\langle 211 \rangle_{B2}$.

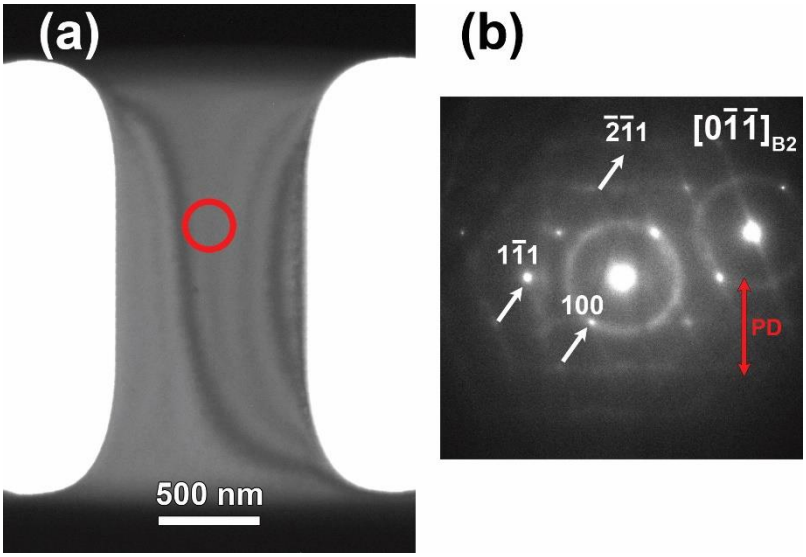

Figure 7–4 (a) BF–TEM image of the specimen before tensile test conforming single crystal, (b) SAED pattern of the indicated region revealing $\langle 011 \rangle_{B2}$ as surface orientation and $\langle 211 \rangle_{B2}$ as pulling direction.

The experiment was set as before, but straining was stopped at about 2.1% strain, the moment the first martensite plates appeared. This was done by pausing the in–situ straining which keeps the displacement fixed. The BF–TEM image just after pausing is presented in Figure 7–5(a), showing two different variants of martensite growing at the extremes of the transformed region but also in the central area of the specimen where austenite is still present. Despite pausing the pulling, transformation continued to proceed in the specimen, while attempting to record diffraction data. Figure 7–5(b) is the BF–TEM image of the moment of recording of Figure 7–5(c) SAED at about 4% strain and from the indicated area. The SAED clearly shows the martensite character of the appearing plates in nearly the entire specimen and also reveals some R–phase reflections.

Figure 7–5(c) was the first and last achieved diffraction pattern, since the specimen fractured shortly after that at about 5% strain along one of the martensite variants, since pausing the pulling did not stop the transformation. The TEM video can be seen using the QR code provided in Figure 7–5(d) or in this link in the digital version of the thesis. Although the TEM recording was interrupted by going to diffraction mode, the provided video is not edited in order to show the real sequence of events and experiment, as well as the moment of fracture.

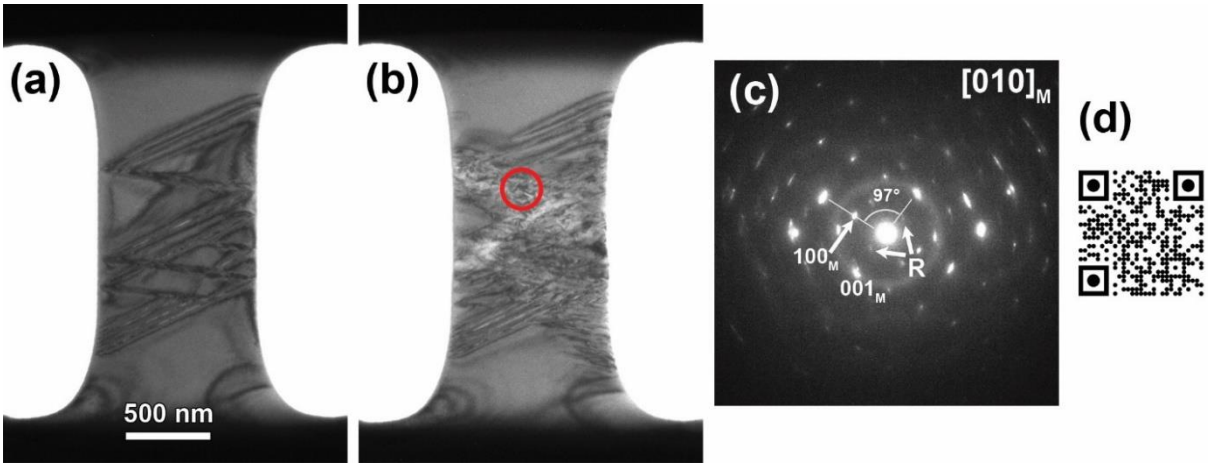

Figure 7–5 (a) BF–TEM image taken immediately after martensite appearance and pausing the pulling, showing two variants of martensite, (b) BF–TEM image at about 4% strain, (c) SAED of the indicated area of b revealing $[010]_M$ and some additional R–phase reflections, (d) QR code of the TEM video of the experiment (https://www.youtube.com/watch?v=ueM88hc2OGo).

A BF–TEM image of the fractured specimen is shown in Figure 7–6(a) SAED patterns taken from indicated regions show large single variants of retained martensite close to the fracture, while those of areas far from the fracture reveal the B2 structure. In Figure 7–6(b) a DF–TEM image of the indicated spot from the B19' phase is presented, revealing that specific variant of the residual martensite in the upper and lower part with bright contrast and showing a curved but well delineated interface with the B2 austenite, especially in the top part.

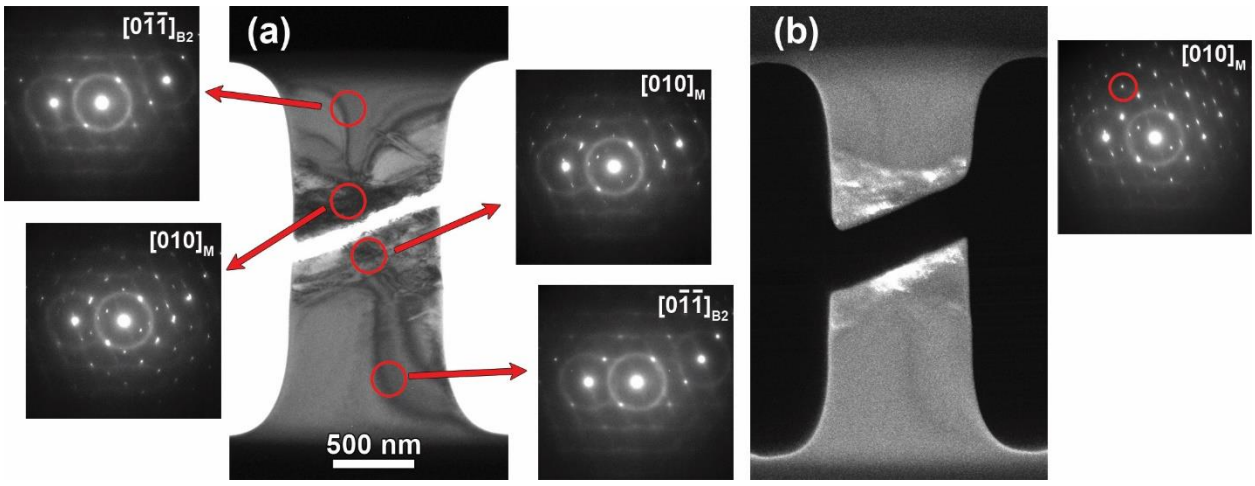

Figure 7–6 (a) BF of the specimen after fracture with four SAED patterns from indicated regions, showing retransformation to austenite at the upper and lower parts of the specimen, while retaining martensite around the fractured area; (b) DF image of the specimen using one of the martensite diffraction spots (red circle in SAED), revealing retained martensite close to the fracture edges.

The trace of the fracture plane is along the $[2\text{-}11]_{B2}$ direction, as seen from the simulated SAED of the $[0\text{-}1\text{-}1]_{B2}$ zone overlaid with the fractured specimen image in Figure 7–7(a). From the lack of thickness fringes in the contrast of the edge of the fracture it can be assumed that the fracture's cross–section is almost perpendicular to the specimen top surface. Assuming this and knowing the specimen's zone axis and fracture trace direction, the fracture cross–section is found to be along a $(\text{-}1\text{-}11)_{B2}$ plane, which is confirmed by the stereographic projection shown in Figure 7–7(b). In this image the $(\text{-}1\text{-}11)_{B2}$ plane (red straight line, indicated by arrows) matches the direction of the crack, while the expected slip planes [237] of $(011)_{B2}$ (green) and $(100)_{B2}$ (blue) do not. From the SAED in Figure 7–7(c) which belongs to the upper fraction and is an overlapping of B2 and B19' spots (Figure 7–7(d)), the austenite–martensite orientation relation is found to be close to $[010]_{B19'}//[0\text{-}1\text{-}1]_{B2}$, $(001)_{B19'}//(100)_{B2}$ with some deviations due to strain. Using these relations, the directional orientation relation is found to be $[100]_{B19'}//[0\text{-}11]_{B2}$, $[101]_{B19'}//[1\text{-}11]_{B2}$ and $[010]_{B19'}//[0\text{-}1\text{-}1]_{B2}$, as confirmed by Figure 7–7(e) and (f) in which the directions are, respectively, shown in black, green and purple, the latter being normal to the page. Assuming that the common plane between martensite and austenite is perpendicular to the specimen surface, the right part of the austenite–martensite interface in the top half of the fractured sample is found to be $(20\text{-}1)_{B19'}//(\text{-}1\text{-}11)_{B2}$, as shown in red in Figure 7–7(e) and (f), and which is parallel to the fracture surface. In the left part of this half, the interface is along $(20\text{-}3)_{B19'}//(\text{-}3\text{-}11)_{B2}$ plane, shown in blue in Figure 7–7(e) and (f), but parallel with the second variant also observed in Figure 7–5 (a). This implies that the observed crystallographic relationship does not comply with one of those expected for the thermoelastic transformation (see Table 2–1), which could be the effect of the influence of external stress.

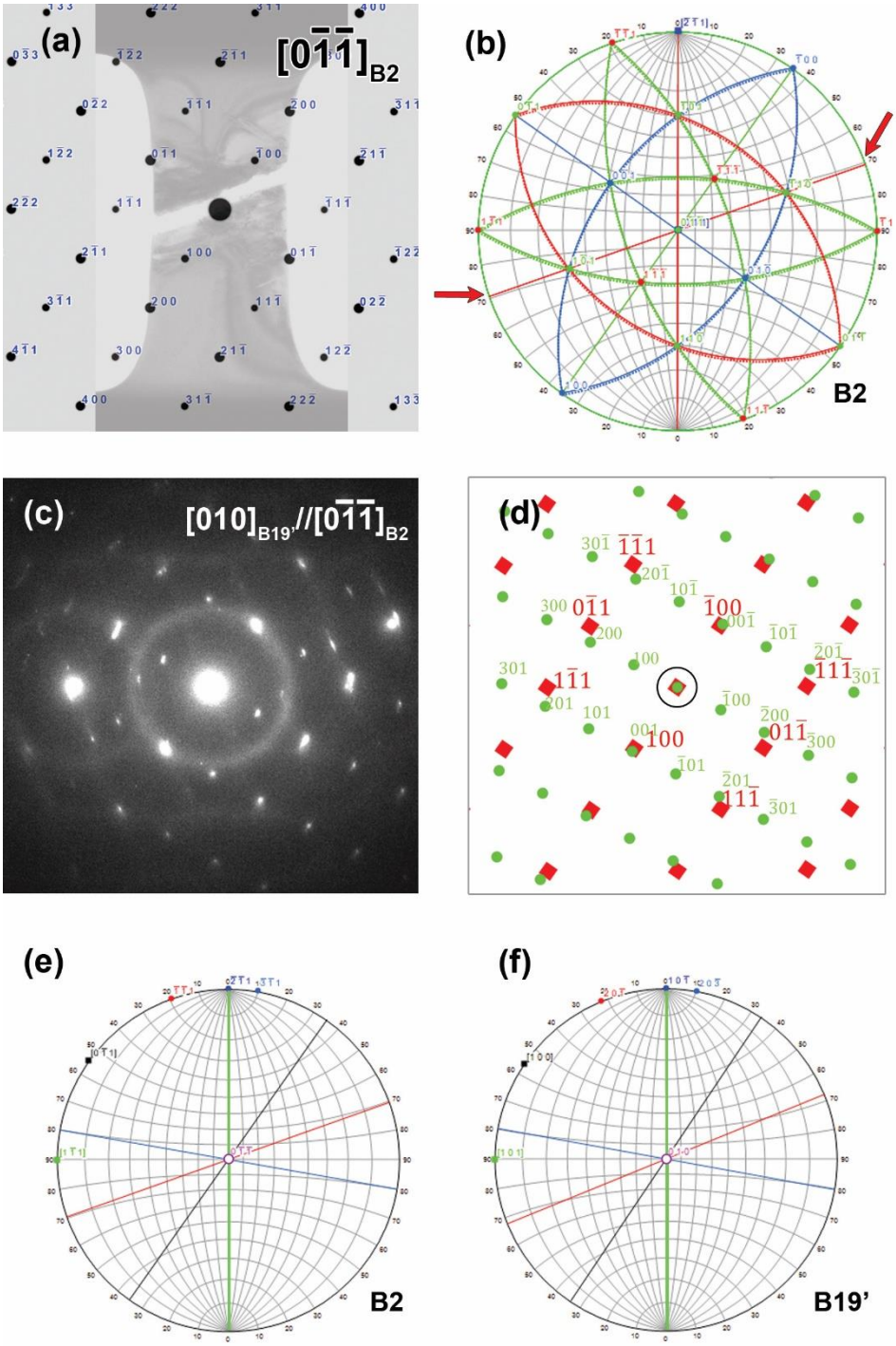

Figure 7–7 (a) The fractured specimen overlapped with the simulated $[011]_{B2}$ SAED pattern showing the pulling and fracture directions; (b) stereographic projection of $[011]_{B2}$ zone and three different planes of which only one ($(\bar{1}\bar{1}1)_{B2}$) matches the fracture direction; (c) SAED of the top part of the fractured specimen revealing overlapping of B2 and B19' spots; (d) simulated SAED of austenite (red square) and martensite (green circle) spots; (e)–(f) stereographic projection of B2 and B19' revealing the orientation relation to be $[100]_{B19'}//[0\bar{1}1]_{B2}$ (black), $[101]_{B19'}//[1\bar{1}1]_{B2}$ (green) and $[010]_{B19'}//[0\bar{1}\bar{1}]_{B2}$ (purple) and the austenit–martensite interface planes as $(20\bar{1})_{B19'}//(\bar{1}\bar{1}1)_{B2}$ (red) and $(20\bar{3})_{B19'}//(\bar{3}\bar{1}1)_{B2}$ (blue).

Figure 7–8(a) shows the stress–strain curve of specimen Single3. The first martensite plates appear at about 2.1% strain at the onset of the stress plateau, which is unique for this specimen. At about 3.1% (arrow in Figure 7–8(a)) a big part of the specimen (seen as clear contrast change in the center of the specimen when comparing Figure 7–8(b) and (c)) transforms into martensite, which causes an abrupt drop in the curve, and also partially retransforms the martensite into austenite in some regions (e.g., top–left and bottom–center indicated by two circles in Figure 7–8(c)) due to a spontaneous decrease of the tension (cf. drops shown in Figure 7–8(a)). Finally, the specimen fractured at about 5%.

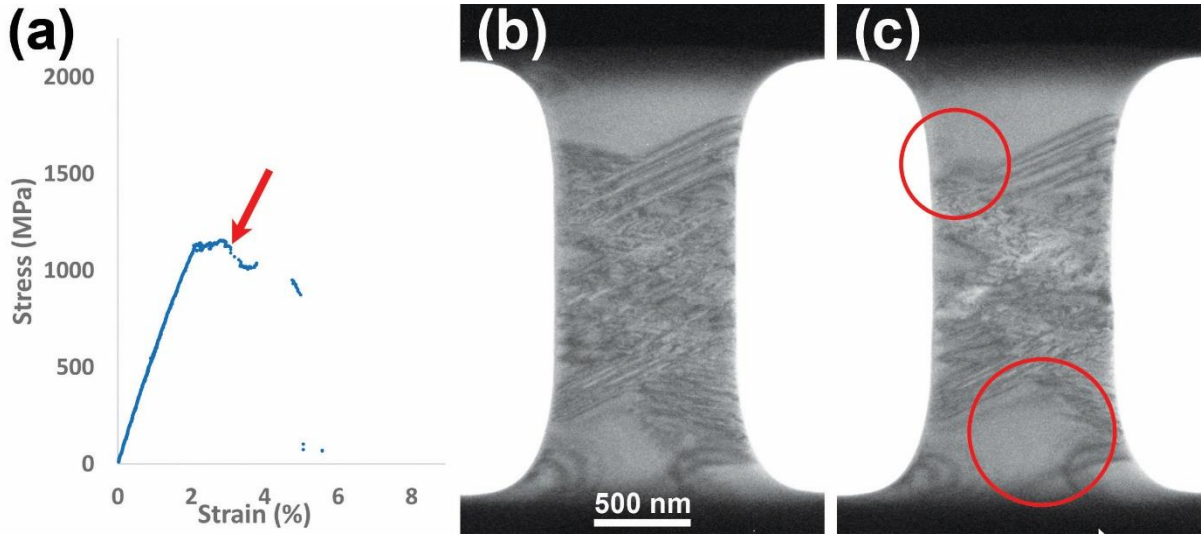

Figure 7–8 (a) Stress–strain curve of the Single3 specimen. (b) and (c): Snap–shots at and immediately after the arrow in (a) showing large martensite varaints and retransformation in the top–left and bottom–center encircled areas in (c).

The Young's modulus is about 60 GPa and the height of the plateau about 1.1 GPa. The missing parts of the curve correspond to the moments that the TEM video recording was interrupted by diffraction acquisition so that no proper values for displacement could be measured.

7.3.2 Polycrystalline specimens

The stress–strain curve of the 150 μm wire annealed at 600 °C from which the following three nano–sized grain PTP specimens were cut is shown in Figure 7–9. In this graph the plateau starts at ~ 0.9% strain with a small stress drop in the beginning and ends at ~ 9.2% strain, where martensite elastic deformation starts. The height of the stress plateau is ~ 390 MPa and the measured Young's modulus is ~ 57 GPa.

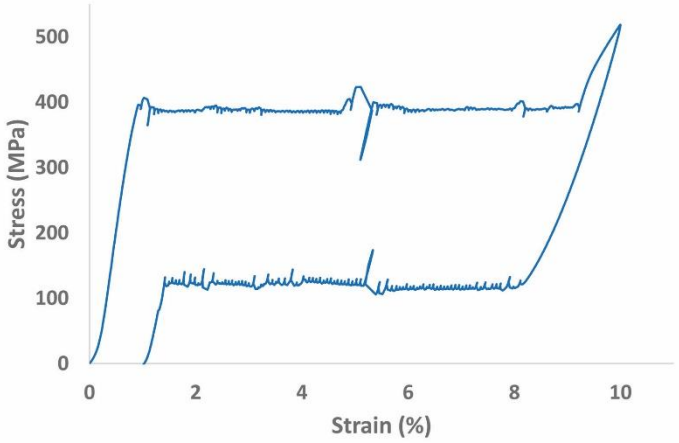

Figure 7–9 Stress–strain curve of the 150 μm wire annealed at 600 °C for 20 minutes, from which the polycrystalline PTP specimens were taken.

7.3.2.1 Specimen Poly1, along the wire, 210nm thick

Shorter annealing time at lower temperature yields the formation of smaller grains which allows for multiple grains in the PTP specimen. Figure 7–10(a) is a BF–TEM image of such a specimen cut along the wire axis and with a thickness of 210 nm ± 21 nm, revealing grains of 100 nm – 500 nm size. In order to examine the texture of the specimen ACOM–TEM was performed. The orientation map Figure 7–10(b) of this first polycrystalline specimen, further referred to as Poly1, shows the preferential orientation of several grains to be $\langle 111 \rangle_{B2}$ perpendicular to the surface (normal direction ND). The inverse pole figure (IPF) maps in Figure 7–10(c) further reveal $\langle 101 \rangle_{B2}$ to be along the pulling direction (PD) of the specimen and with a prominent transverse direction (TD) of $\langle 112 \rangle_{B2}$. Here it should be noted that this particular texture is not necessarily representative for the entire wire, as it was shown by, e.g., Laplanche et al. [232] and Gall et al. [238] that drawn Ni–Ti wires after recrystallization exhibit a strong $\langle 111 \rangle_{B2}$ fiber texture along the wire axis, which apparently is not the case for the region where this particular specimen of $2 \times 0.7\ \mu m^2$ was cut.

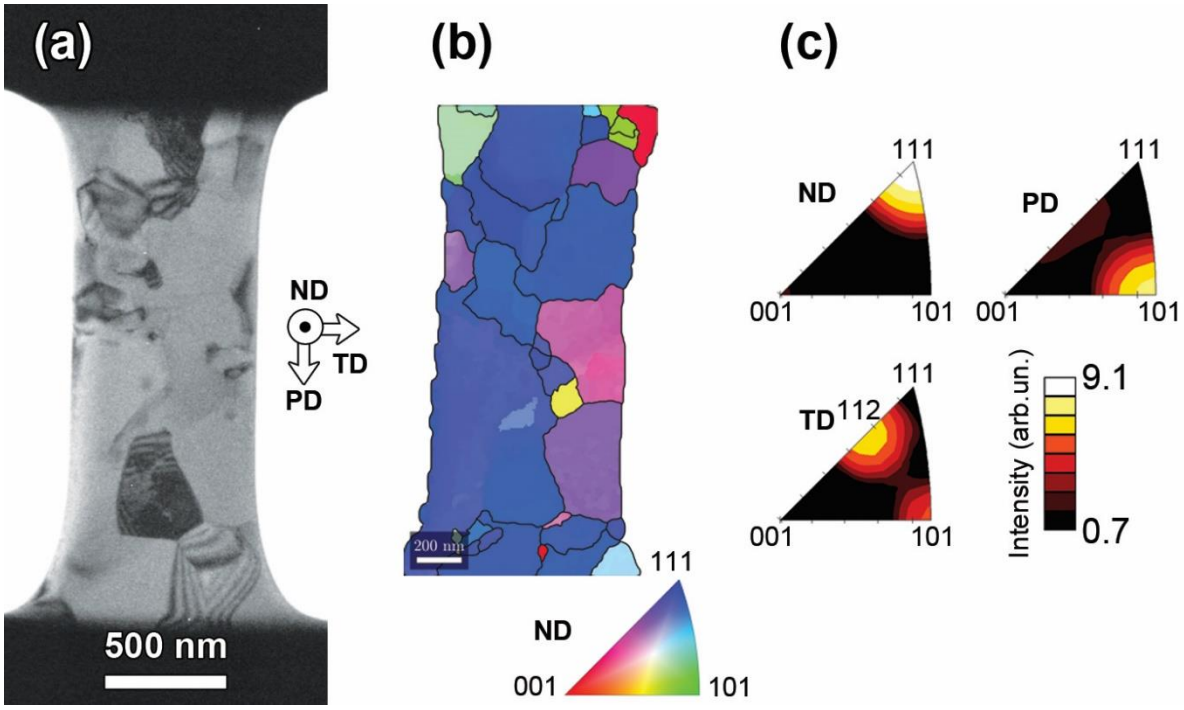

Figure 7–10 (a) BF–TEM image and (b) ACOM–TEM of the Poly1 specimen, (c) IPF maps showing strong preferential orientation of $[110]_{B2}$ along the length of the specimen, i.e., the pulling direction.

Figure 7–11(a) shows the stress–strain curve of the Poly1 specimen. The first transformation occurs at ~ 0.9% and the specimen exhibits elastic deformation of austenite up to ~ 1.8% strain, where the stress plateau starts. Transformation continues to happen in different grains on the stress plateau, however, some grains did not seem to transform even at ~ 8.2% strain where the pulling was stopped, as can be seen in the video linked to the Figure 7–11(b) QR code or in this link in the digital version of the thesis. Figure 7–11(c) is taken from the indicated moment on the curve and shows some transformed grains (red solid arrows) while some other grains are still in the austenite phase (hollow arrows). The height of the stress plateau is about 1.1 GPa and the Young's modulus ~ 76 GPa.

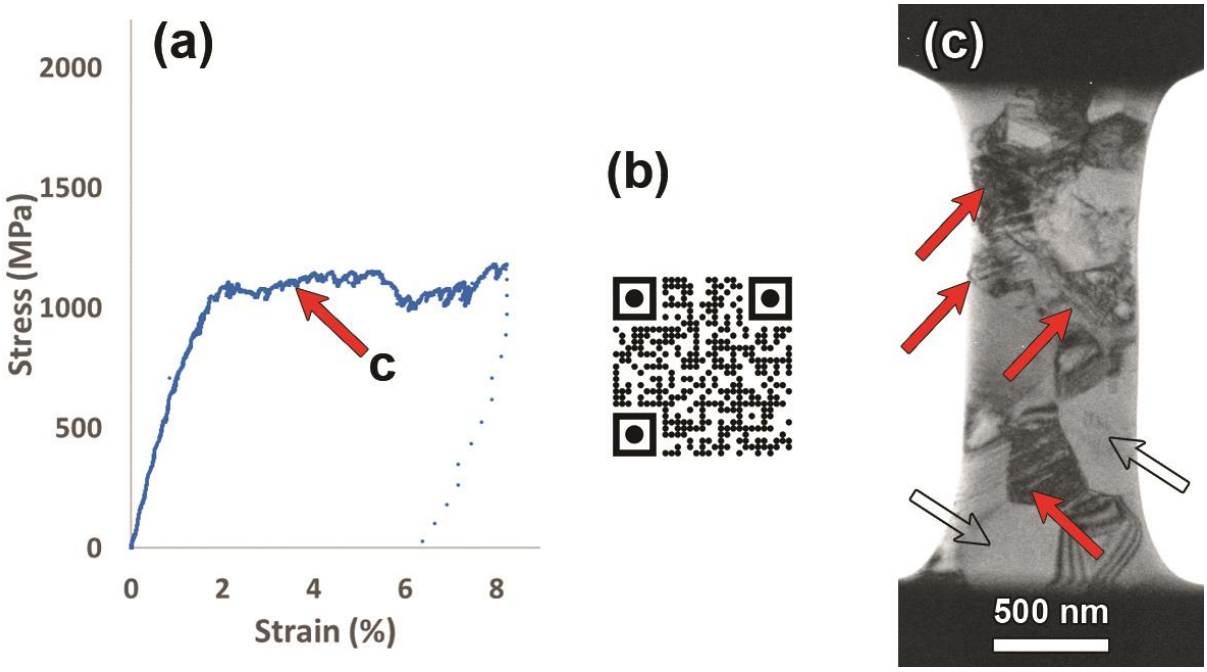

Figure 7–11 (a) Stress–strain curve with an arrow indicating the moment that the image in c is taken, (b) QR code of the TEM video (https://www.youtube.com/watch?v=RgWkbNv0zxo), (c) BF–TEM image showing transformed (red arrow) and non–transformed (white arrows) grains.

7.3.2.2 Specimen Poly2, along the wire, 220 nm thick

A second experiment was performed on a specimen with thickness of 220 nm ± 22 nm, referred to as Poly2 and cut from the same region of the same wire and again along the wire axis. This specimen has a similar $\langle 111 \rangle_{B2}$ ND texture as Poly1, but an average $\langle 211 \rangle_{B2}$ pulling direction, as concluded from the overall SAED pattern in Figure 7–12(a), and shows the stress–strain curve in Figure 7–12(b). The first transformation occurred at 0.6% strain in a 300 nm diameter grain, shown in Figure 7–12(c), which is clearly not the largest grain in the view. The austenite was elastically deformed up to ~ 1.5% strain where the stress plateau with a small stress drop in the beginning started. At this point a sharp martensite plate appeared on the top–left side of the specimen, quickly followed by an inclined and localized deformation band in the center of the specimen, as indicated by arrows in Figure 7–13(a). The latter propagated sideways towards upper and lower parts of the specimen and while some extra martensite plates appeared in adjacent grains, the deformation in this band continued to increase, indicating a Lüders-band like behavior [239]. The transformation continued up to 17.2% deformation, where the pulling was stopped and the specimen was released. At this stage, all but the lower and upper shoulder of the specimen have been transformed into martensite. The height of the plateau is ~ 1.0 GPa and the Young's modulus is ~ 69 GPa.

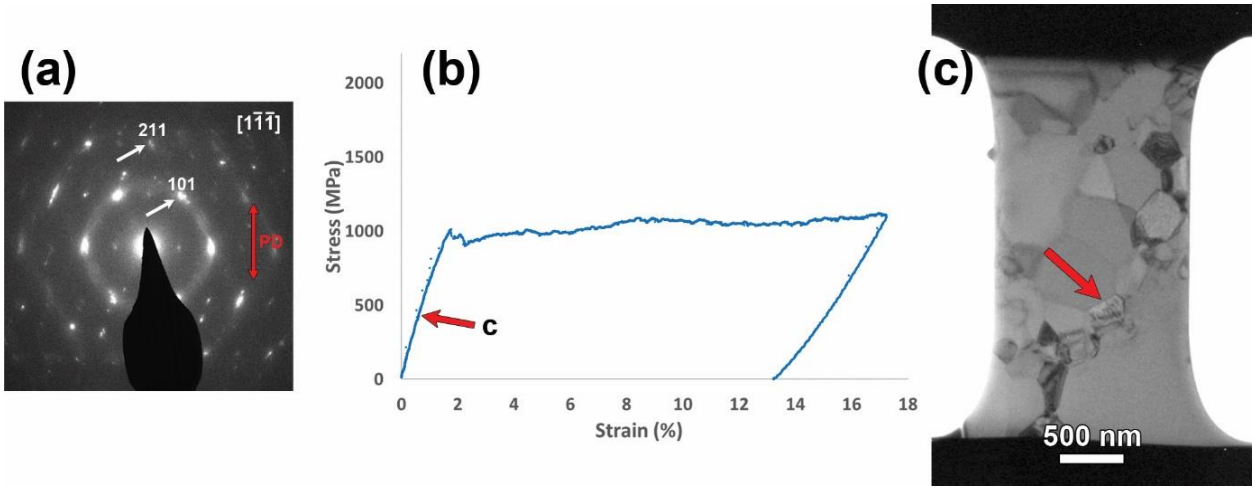

Figure 7–12 (a) SAED pattern of the entire Poly2 specimen revealing $[-111]_{B2}$ to be the most prominent normal to the specimen and an approximate $[211]_{B2}$ the PD for the majority of grains. (b) Stress–strain curve of the specimen and (c) the first transformation occurring in the indicated grain.

Figure 7–13(b) presents the BF–TEM image of the specimen after release, showing some austenite recovery at the wider top and bottom shoulders of the specimen, seen as a return to a larger area with lower contrast, and with the central part retaining the stronger martensite contrast which confirms the remaining strain of about 13% after unloading. In the video linked to the QR code of Figure 7–13(c) or in this link in the digital version of the thesis it can be seen that nearly halfway the plateau the specimen starts to show necking so that all strain becomes localized in this area finally yielding plastically deformed martensite, explaining the retained martensite after release.

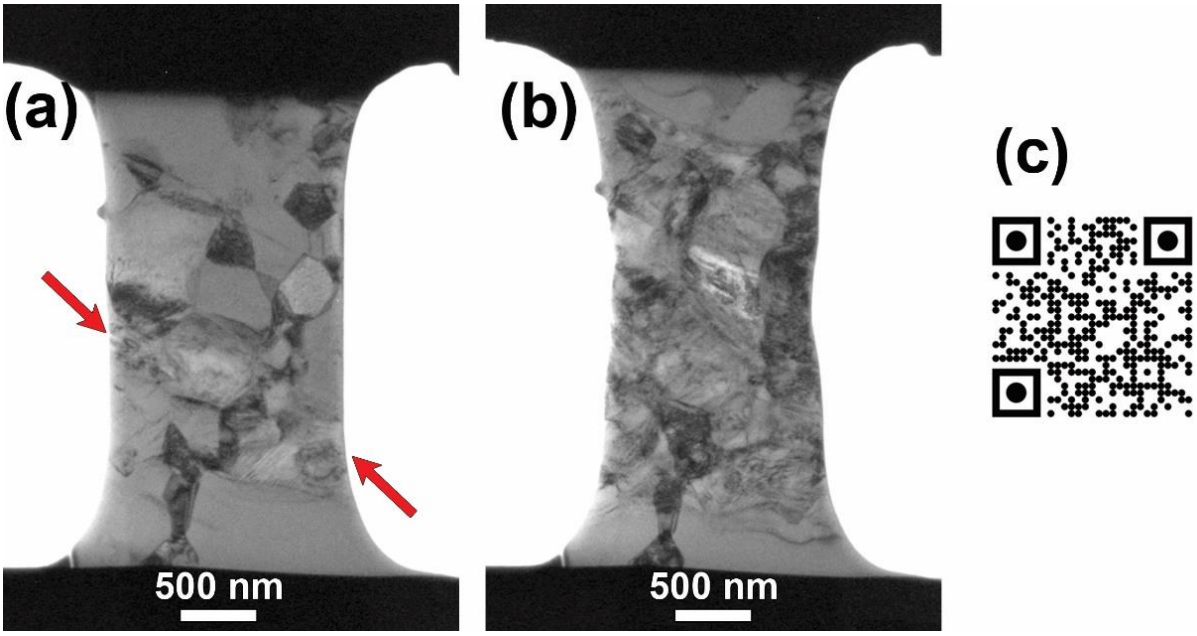

Figure 7–13 (a) The specimen where the Lüders–like band indicated by arrows forms upon the stress drop in the beginning of the plateau (b) The specimen released after the tensile test, (c) QR code of the Poly2 TEM video (https://www.youtube.com/watch?v=7Dm9_BFDHgE).

7.3.2.3 Specimen Poly3, perpendicular to wire, 160 nm thick

The stress–strain curve of the third nano–sized grain specimen with thickness 160 nm ± 16 nm, further referred to as Poly3, and cut perpendicular to the axis of the wire annealed at 600 °C is shown in Figure 7–14(a). The first transformation starts at ~ 0.7% strain. In Figure 7–14(b) a BF–TEM image of some fully transformed grains is presented. When a martensite plate reaches the opposite side of the grain, transformation nucleates from the other side of the grain boundary and propagates in the neighboring grain, as shown by arrows in the enlarged image of Figure 7–14(c), and is also seen in the TEM video linked to the Figure 7–14(d) QR code or in this link in the digital version of the thesis. The plateau of the curve starts at ~ 2.5% strain and continues to ~ 3.7% where the pulling was stopped. After releasing the load, most martensite transformed back to austenite, as seen in Figure 7–14(e). The height of the stress plateau is about 1.3 GPa and the Young's modulus is ~ 70 GPa.

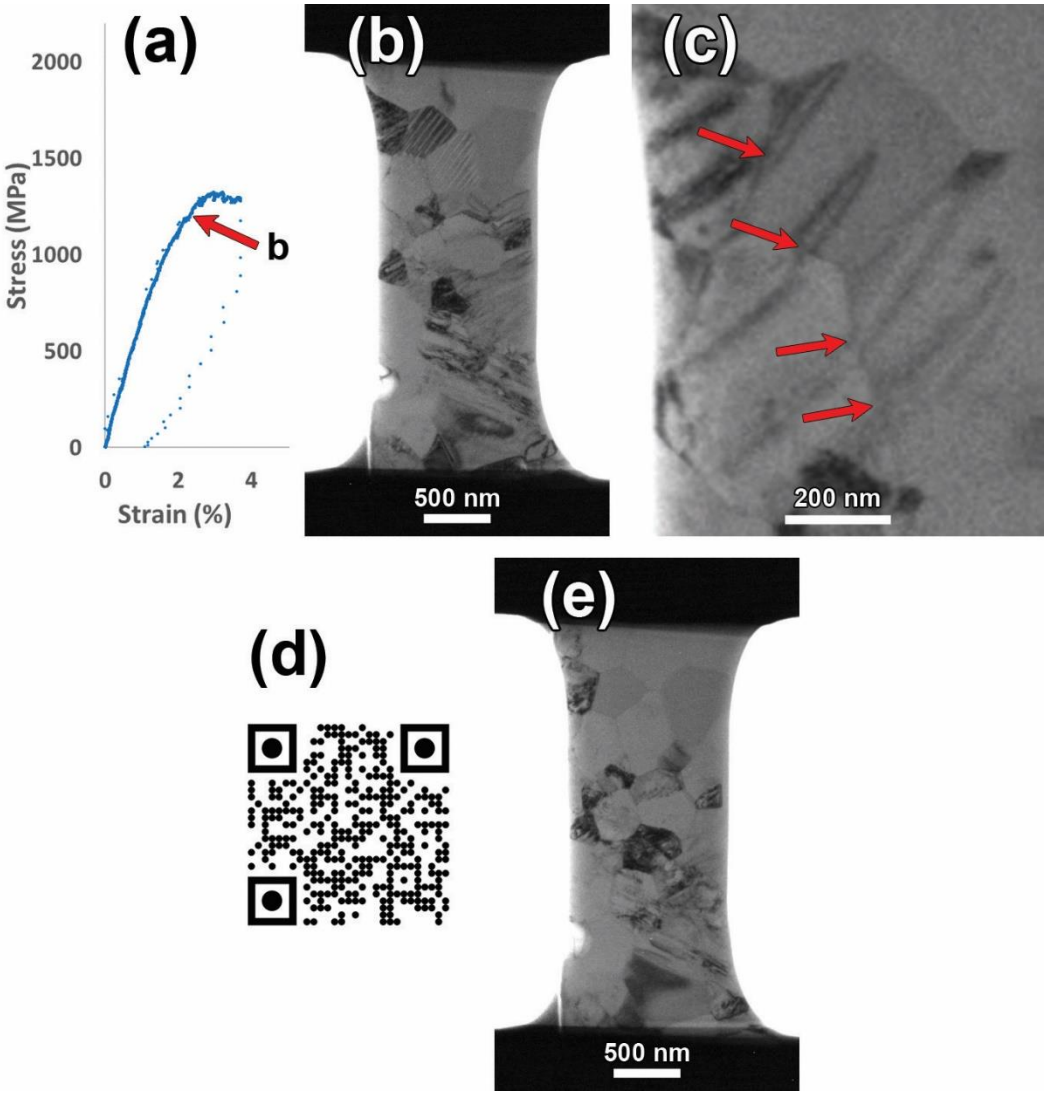

Figure 7–14 (a) Stress–strain curve of a PTP test on a polycrystalline specimen cut perpendicular to the wire axis. (b) BF–TEM image showing several grains transformed into martensite, (c) martensite plates nucleating where an earlier plate in the neighboring grain hits the grain boundary, (d) QR code of the TEM video (https://www.youtube.com/watch?v=23xWCTabhEE) and (e) partial recovery to austenite after releasing the stress.

7.4 Discussion

The results of the different measurements from the six different specimens are combined in Table 7–1, together with those of the original micro–wires. At first sight, the stress–strain curves of the six nano–sized specimens resemble the part between labels a and c of the bulk curve shown in Figure 2–9 in § 2.5.3.1. They start with a sharp increase of stress during the elastic regime of the austenite. Somewhere along this line, the slope starts to decrease when the first martensite plates appear and in the beginning of the stress plateau a stress drop is observed due to the diminishing

of the required stress subsequent propagation and growth of existing plates. This feature is stronger in the single crystal specimen, which could be related to the fact that in this specimen no new plates seem to nucleate after this nucleation peak while for the polycrystalline specimens some grains only transform after the plateau has already started. Depending on the specimen conditions, severe strains can be developed with a maximum of 17% found in one of the polycrystalline specimens. The nano–mechanical test stress–strain curves do not show the start of elastic transformation of the martensite after the plateau, which possibly corresponds with the fact that in all cases some austenite is still present in the specimen, be it sometimes only at the upper and lower ends where the specimen base becomes wider and the stress decreases.

Table 7–1 Measures of the examined PTP specimens and the original micro–wires. Errors of the Young's modulus were found by calculating standard error for linear regression of each curve between 0 and 0.6% strain, and that of the plateau height were found by standard error of the stress value in the plateau interval.

Single/ poly/ micro–wire	Thickness	Specimen–wire orientation	Pulling direction (PD)	Surface orientation (ND)	Grain size	Young's modulus (GPa)	Plateau height (GPa)
Large grain micro–wire	150 μm	–	–	–	~20–30 μm	52.5 ± 0.5	0.38 ± 0.02
Single1	105 ± 11 nm	parallel	⟨111⟩	⟨011⟩	–	77.9 ± 0.2	1.96 ± 0.05
Single2	230 ± 23 nm	parallel	⟨111⟩	⟨011⟩	–	80.8 ± 0.4	–
Single3	200 ± 20 nm	parallel	⟨211⟩	⟨011⟩	–	59.7 ± 0.1	1.10 ± 0.05
Small grain micro–wire	150 μm	–	–	–	~0.1–1 μm	57.1 ± 0.3	0.39 ± 0.01
Poly1	210 ± 21 nm	parallel	⟨011⟩	⟨111⟩	100–500 nm	76.1 ± 0.3	1.08 ± 0.04
Poly2	220 ± 22 nm	parallel	⟨211⟩	⟨111⟩	120–950 nm	68.5 ± 0.6	1.04 ± 0.05
Poly3	160 ± 16 nm	normal	–	–	120–650 nm	69.6 ± 0.1	1.29 ± 0.02

Except for the Single3 specimen, in all of the above examples the Young's modulus for the austenite phase, as determined from the slope of the linear elastic part at the onset of the stress–strain curves, is close to the averaged literature value of ~ 70 GPa [240], confirming the accuracy of the quantitative data of the MEMS device. In the case of the single crystal specimen where the pulling direction was along a $\langle 111 \rangle_{B2}$ direction, the measured value is between 78 and 81 GPa. All polycrystalline specimens have lower values for the Young's modulus confirming that the $\langle 111 \rangle_{B2}$ direction is a stiff direction [240,241]. The Young's moduli of the treated micro–wires are lower than for the single crystal specimen, which can be understood since some grains will not have a $\langle 111 \rangle_{B2}$ stiff direction along the pulling direction. However, the micro–wire values are also

lower than those measured for the polycrystalline PTP specimens, which could be due to the initiation of the stress–induced transformation in the region between labels a and b in Figure 2–9 where the slope is measured without exactly knowing where the martensite starts [240]. Since the start of the transformation induces a lowering in slope, also the averaged measured Young's modulus will be smaller.

The height of the obtained stress plateaus shows considerable difference for the various samples and specimens investigated. When comparing the 3 in–situ polycrystalline TEM specimens an increase of the stress plateau with decreasing specimen thickness is seen. This is also the case comparing 2 single crystal (Single1 & 3) specimens that show the stress plateau, as shown in the graph of Figure 7–15. This confirms the in–situ work by Mao et al. [96] who also found an increase in the needed stress with decreasing specimen thickness to transform small strips of Ni–Ti. They attribute this "size effect" to the increasing influence of non–transforming surface layers with decreasing thickness of the specimen, including a Ga^+ impregnated layer caused by FIB and a natural oxide layer, which also enriches Ni in the matrix and thus further suppresses the martensitic transformation. Since also in our case especially the edges of the specimens are often seen as the nucleation points of the transformation, such surface effects could indeed play an important role. On the other hand, also for thermally induced martensite a decreasing grain size lowers the martensite start temperature [167] so the nano–scale dimensions of the thickness of the specimens should also be considered.

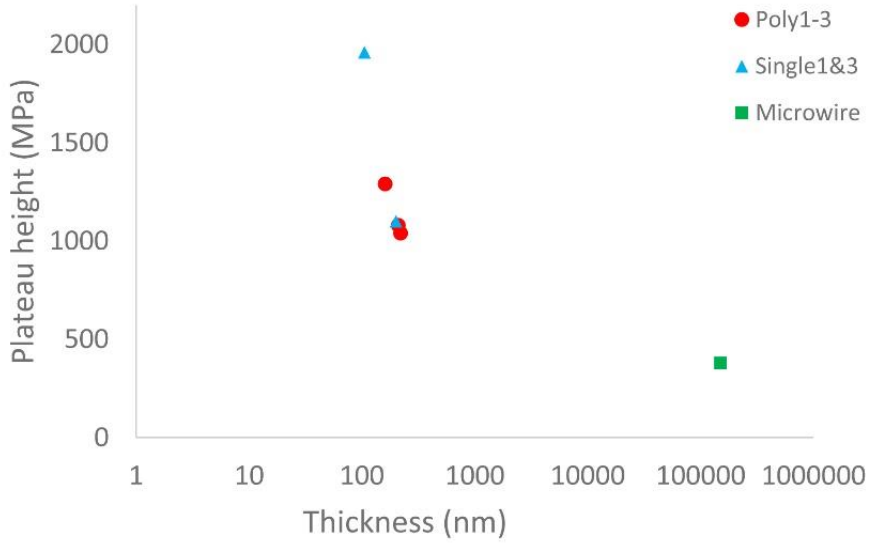

Figure 7–15 Plateau height of the stress–strain curves versus thickness (log–scale) of five different TEM specimens as well as the micro–wire.

In the Poly2 specimen a Lüders–like band forms at the beginning of the stress plateau causing a drop in the stress. Lüders–like bands form when grains in the high strain region fully transform to martensite with mutually compatible shear while the grains in the low strain regions remain mostly austenite [239]. It is a localized deformation behavior via propagation of shear bands suggesting the heterogeneity of the martensitic transformation. Although the macroscopic observation of Lüders–like band has been reported in Ni–Ti by a number of research groups [88,177,242–244], this is the first in–situ TEM observation of this phenomenon.

For all specimens, together with elastic deformation of austenite, some martensitic transformation occurs well before reaching the plateau. The transformation accelerates in the beginning of the plateau, where parallel plates of martensite form next to each other, whether it is in the single crystal specimen or in certain grains of a polycrystalline specimen. In the single crystal specimen, many plates very rapidly after nucleation reach the opposite side of the specimen, while in the polycrystalline specimen the grain boundaries form obstacles and some austenite grains need a much higher applied strain to show any sign of transforming to martensite. In many cases, new plates nucleate at sites on grain boundaries where the earlier martensite plates grown in the neighboring grain have ended, confirming the observations of Xu et al. [93]. The plates in the top–left area of the Single1 specimen are further apart than those in the bottom–left and central parts. This can be due to the local width of the austenite area, which is larger on the top since the central and bottom areas are limited by the earlier appearing variant in the bottom–right corner, and the need to balance the elastic strain energy of the austenite/martensite transformation with the surface energy of a single plate [245–248]. By increasing the load, the martensite plates broaden and seem to merge, which can be associated or with detwinning or reorientation of martensite or with final transformation of any remaining austenite, favoring those variants that best accommodate the external stress and result in single variant parts of the martensite. (in the single crystal specimen this is seen in Figure 7–2(f) (Single1), in Figure 7–16 an example in the polycrystalline specimen (Poly1) is shown) However, without any in–situ SAED support, the exact micro–structure of the strong changes in contrast cannot be concluded.

Plastic deformation observed in the specimen Single1 martensite or austenite by (de)twinning and/or dislocation slip may result in permanent deformation and suppression of the recoverability of transformation strains in tensile tests [234,249,250].

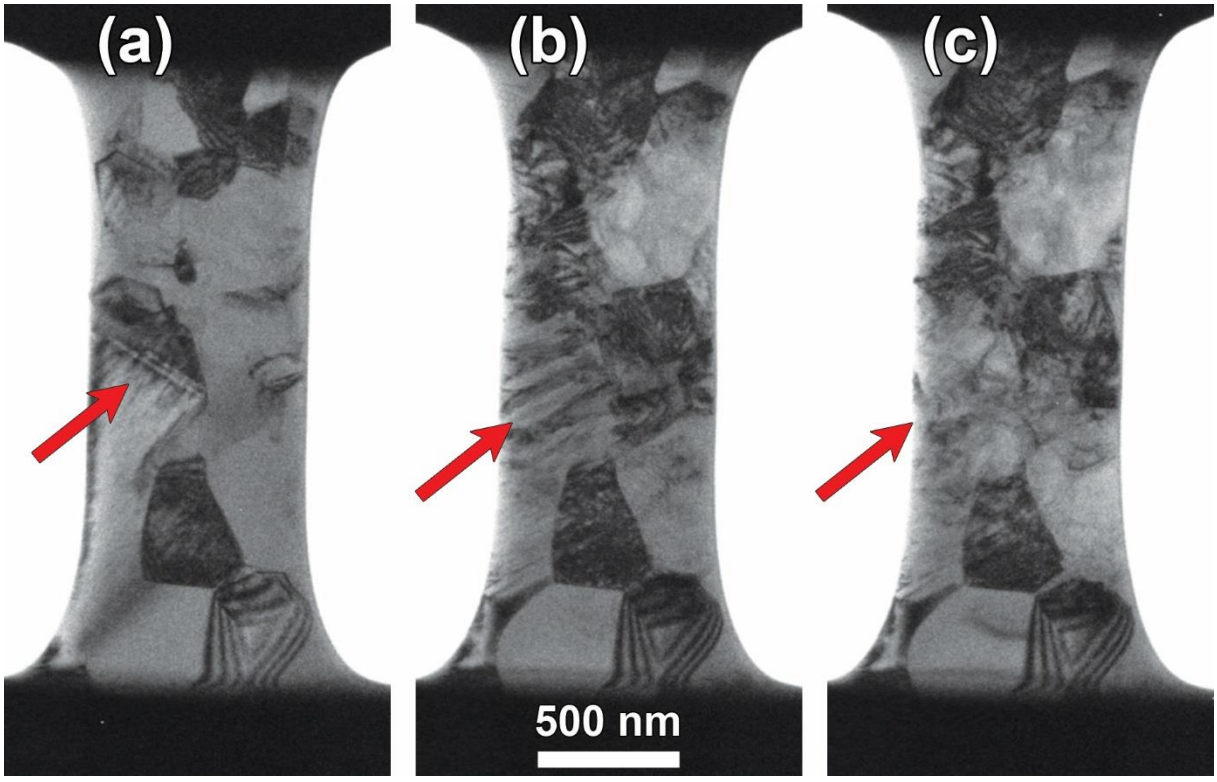

Figure 7–16 (a) The first martensite plate appears in a grain, (b) another martensite variant grows in the grain, (c) martensite plate contrast disappears which is an indication of transforming the grain into a single variant of martensite.

7.5 Conclusions

In–situ TEM tensile tests on nano–scale single crystals and polycrystalline Ni–Ti specimens have been performed. The formation of stress–induced martensite is followed and stress–strain curves are plotted based on the mechanical data. The stress plateau height increases by decreasing specimen thickness but remains independent of the grain size since the latter is, on average, larger than the specimen thickness. In all cases the martensitic transformation starts well before the plateau is reached and results in a slight decrease of the slope of the initial sharp increase of the stress–strain curves. When measuring the Young's modulus from the slope before the martensite nucleates, values around 70 GPa are found. Martensite transformation starts at edges of the specimen for the single crystal and on the edges and grain boundaries for the polycrystalline specimen. When a martensite plate reaches a grain boundary in the polycrystalline specimen, it initiates the transformation in the neighboring grain at the other side of the grain boundary. After releasing the load some residual martensite remains in the specimen, the amount depending on the totally induced strain and indicating the existence of induced plasticity in the martensite at

large strains. Formation of a localized deformation Lüders–like band was observed in one of the polycrystalline specimens.

Summary

The main properties of Ni–Ti alloys, i.e., shape memory and superelasticity, are used in engineering applications usually through a cyclic shape recovery during thermal or strain cycling, respectively. As these properties originate from the martensitic transformation, the functional stability of the material depends on the reversibility of this martensitic transformation. Therefore, the reversibility of MT for Ni–Ti material under thermal cycling was investigated for bulk and micro–wire Ni–Ti.

After introducing the material and used techniques, in Chapter 5 the effect of low temperature thermal cycling combined with room temperature aging on the M_s of some recrystallized $Ni_{50.6}Ti_{49.4}$ samples was studied. While no apparent effect was observed in TEM image mode using different techniques, strong structured diffuse intensities condensed in specific periodic loci were observed in SAED. The cluster model was used to interpret these results which revealed the formation of micro–domains in the shape of needle clusters of pure Ni atoms along $\langle 111 \rangle_{B2}$ directions. Quantitative comparison between samples with and without a DSC cycle revealed that the more DSC cycles a sample has received, the more condensed the diffuse intensity becomes which is expected to be caused by longer Ni clusters and enhancement of short–range ordering. The required energy for atom diffusion on a local scale may be provided by the transformation front moving across the system during the DSC cycling.

A similar procedure was followed in Chapter 6 for recrystallized Ni–Ti micro–wires, this time with changing some parameters such as grain size, aging temperature and DSC temperature interval. It was found that consecutive thermal cycling suppresses MT, the suppression enhances when the DSC cycling is combined with RT aging and becomes even stronger when the aging is performed at elevated temperature of 100 °C. However, RT aging alone did not show a significant effect on the MT. Aging at elevated temperatures of 100 °C alone, however, suppresses the MT.

Comparing DSC results of large and small grain samples shows that the effect of room and elevated temperature aging is stronger in large grain samples than in small grain samples. SAED patterns show an increase of Ni clustering in line with decreasing M_s. Since due to the small size of these Ni clusters there is no precipitate–free matrix with lower Ni content, martensite nucleation is not supported but instead suppressed due to the strain field induced in the matrix by the Ni clusters.

In order to investigate the aforementioned micro–wires using TEM, a novel method was introduced in Chapter 4 to use a conventional twin–jet electropolishing apparatus for thin wires. In this method the wire is embedded in a graphite filled epoxy resin medium which after hardening is mechanopolished so that both sides of the wire a free from resin. The obtained complex is then inserted into the electropolishing holder and undergoes the conventional polishing process. The method provides damage–free specimens with large electron transparent areas.

Chapter 7 focuses on in–situ TEM tensile tests on nano–scale single crystals and polycrystalline Ni–Ti specimens, obtained from recrystallized material. The formation of stress–induced martensite was observed and stress–strain curves were plotted based on the obtained mechanical data. The stress plateau height shows an increase by decreasing specimen thickness but remains independent of the grain size since the latter is, on average, larger than the specimen thickness. In all cases the martensitic transformation starts well before the stress–strain plateau is reached and results in a slight decrease of the slope of the stress–strain curves. Young's modulus before the martensite nucleates was found to be around 70 GPa. Martensitic transformation starts at edges of the specimen for the single crystal and on the edges and grain boundaries for the polycrystalline specimen. When a martensite plate approaches a grain boundary in the polycrystalline specimen, it provokes the transformation in the neighboring grain at the other side of the grain boundary. After releasing the load, depending on the totally induced strain, some residual martensite remains in the specimen indicating the existence of induced plasticity in the martensite at large strains. In–situ TEM observation of the formation and propagation of a Lüders–like band is reported for the first time.

Samenvatting

Vormgeheugen en superelasticiteit zijn de belangrijkste eigenschappen van Ni–Ti–legeringen voor technische toepassingen. Deze eigenschappen spelen een belangrijke rol tijdens het cyclisch vormherstel bij thermische of stress geïnduceerde cycli. Aangezien deze eigenschappen voortkomen uit een martensitische transformatie, hangt de functionele stabiliteit van het materiaal af van de omkeerbaarheid van deze transformatie. Daarom werd de omkeerbaarheid van martensitische transformatie voor zowel bulk als microdraad Ni–Ti–materialen onder thermische cycli onderzocht.

Na de introductie van het materiaal en de gebruikte technieken, werd in hoofdstuk 5 het effect van thermische cycli bij lage temperatuur in combinatie met de veroudering bij kamertemperatuur op de M_S van sommige $Ni_{50.6}Ti_{49.4}$–stalen bestudeerd. Hoewel er via verschillende TEM technieken geen duidelijk effect werd waargenomen, werden toch sterk gestructureerde diffuse intensiteiten gevonden op specifieke periodieke locaties in de diffractiepatronen. Toepassing van het Cluster–model toonde aan dat deze intensiteiten correleren met de vorming van microdomeinen van naaldvormige clusters van zuivere Ni–atomen langs $\langle 111 \rangle_{B2}$–richtingen. Kwantitatieve vergelijking tussen stalen met en zonder een DSC cyclus toonde dat meer DSC–cycli leiden tot een versterking van de diffuse intensiteit wat, naar verwachting, wordt veroorzaakt door langere Ni–clusters en een verhoogde ordening. De vereiste energie voor atoomdiffusie op lokale schaal kan worden geleverd door het transformatiefront dat zich door het systeem verplaatst tijdens de DSC–cyclus.

Een vergelijkbare procedure werd gevolgd in hoofdstuk 6 voor microdraad Ni–Ti, waarbij enkele parameters werden gevarieerd zoals korrelgrootte, verouderingstemperatuur en het DSC temperatuurinterval. Het bleek dat opeenvolgende thermische cycli MT onderdrukken, verder treedt er meer onderdrukking op wanneer de DSC–cycli worden gecombineerd met veroudering bij kamertemperatuur en dit effect wordt extra versterkt bij veroudering bij een verhoogde temperatuur van 100 °C. Veroudering bij kamertemperatuur alleen toonde echter geen significant

effect op de MT, terwijl veroudering bij een verhoogde temperatuur van 100 °C MT wel onderdrukt. Vergelijking van DSC–resultaten van stalen met verschillende korrelgrootte toont aan dat het effect van veroudering bij kamertemperatuur en verhoogde temperatuur sterker is bij grote dan bij kleine korrelgrootte. SAED diffractiepatronen tonen een toename van Ni–clustering met afnemende M_s. Wegens de kleine omvang van deze Ni–clusters is de matrix, met een lager Ni–gehalte, niet precipitaatvrij, daardoor wordt martensietnucleatie onderdrukt als gevolg van een spanningsveld dat door de Ni–clusters in de matrix wordt geïnduceerd.

Om de bovengenoemde microdraden met behulp van TEM te onderzoeken, werd in hoofdstuk 4 een nieuwe methode geïntroduceerd om een conventionele twin–jet elektropolijstmachine te gebruiken voor dunne draden. Bij deze methode wordt de draad ingebed in een met grafiet gevuld epoxyhars dat na uitharding mechanisch wordt gepolijst zodat beide zijden van de draad vrij zijn van hars. Het verkregen staal wordt vervolgens in een elektropolijsthouder geplaatst en ondergaat het conventionele polijstproces. Op deze manier werden stalen vrij van schade en met grote elektronen–transparante gebieden verkregen.

In Hoofdstuk 7 werden in–situ TEM–trektesten op zowel afzonderlijke nanoschaal monokristallen als polykristallijne Ni–Ti–stalen onderzocht. De vorming van stress geïnduceerde martensiet werd waargenomen en spanning–rekdiagrammen die werden uitgezet op basis van de verkregen mechanische gegevens. Een toename van de hoogte van het spanningsplateau werd waargenomen bij afname van de monsterdikte, onafhankelijk van de korrelgrootte, aangezien deze gemiddeld groter is dan de dikte van het staal. In alle analyses werd genoteerd dat de martensitische transformatie start voordat het spanning–rekplateau bereikt wordt wat opgemerkt wordt door een lichte afname van de helling van de spanning–rekcurves. De Young–modulus voor de martensitische nucleatie was ongeveer 70 GPa. Martensitische transformatie begint bij randen van de monokristallijne stalen en bij de randen en korrelgrenzen voor polykristallijne stalen. Wanneer een martensietplaat een korrelgrens in een polykristallijne staal nadert, veroorzaakt dit de transformatie in de naburige korrel aan de andere kant van de korrelgrens. Na het vrijgeven van de spanning en afhankelijk van de totaal geïnduceerde spanning, blijft er wat martensiet in het staal achter, wat wijst op het bestaan van geïnduceerde plasticiteit in het martensiet bij grote spanningen. In–situ TEM–observatie van de vorming en verspreiding van een Lüders–achtige band werd voor het eerst gerapporteerd.

Bibliography

[1] Buehler, W. J., Gilfrich, J. V., and Wiley, R. C. "Effect of Low-Temperature Phase Changes on the Mechanical Properties of Alloys near Composition TiNi." *Journal of Applied Physics*, Vol. 34, No. 5, 1963, pp. 1475–1477. doi:10.1063/1.1729603.

[2] Kauffman, G. B., and Mayo, I. "The Story of Nitinol: The Serendipitous Discovery of the Memory Metal and Its Applications." *The Chemical Educator*, Vol. 2, No. 2, 1997, pp. 1–21. doi:10.1007/s00897970111a.

[3] Ölander, A. "An Electrochemical Investigation of Solid Cadmium-Gold Alloys." *Journal of the American Chemical Society*, Vol. 54, No. 10, 1932, pp. 3819–3833. doi:10.1021/ja01349a004.

[4] Greninger, A. B., and Mooradian, V. G. "Strain Transformation in Metastable Beta Copper-Zinc and Beta Copper-Tin Alloys." *Trans. AIME*, Vol. 128, 1938, pp. 337–368.

[5] S. Basinski, Z., and Christian, J. W. "Crystallography of Deformation by Twin Boundary Movements in Indium-Thallium Alloys." *Acta Metallurgica*, Vol. 2, No. 1, 1954, pp. 101–116. doi:10.1016/0001-6160(54)90100-5.

[6] Otsuka, K., Wayman, C. M., Nakai, K., Sakamoto, H., and Shimizu, K. "Superelasticity Effects and Stress-Induced Martensitic Transformations in Cu-Al-Ni Alloys." *Acta Metallurgica*, Vol. 24, No. 3, 1976, pp. 207–226. doi:10.1016/0001-6160(76)90071-7.

[7] Ziolkowski, A. *Pseudoelasticity of Shape Memory Alloys, Theory and Experimental Studies*. 2015.

[8] Burkart, M. W., and Read, T. A. "Diffusionless Phase Change in the Indium-Thallium System." Vol. 197, 1953, pp. 1516–1524.

[9] Mohd Jani, J., Leary, M., Subic, A., and Gibson, M. A. "A Review of Shape Memory Alloy Research, Applications and Opportunities." *Materials & Design (1980-2015)*, Vol. 56, 2014, pp. 1078–1113. doi:10.1016/j.matdes.2013.11.084.

[10] Wolf, R. H., and Heuer, A. H. "TiNi (Shape Memory) Films on Silicon for MEMS Applications." *Journal of Microelectromechanical Systems*, Vol. 4, No. 4, 1995, pp. 206–212. doi:10.1109/84.475547.

[11] Ryhänen, J., Niemi, E., Serlo, W., Niemelä, E., Sandvik, P., Pernu, H., and Salo, T. "Biocompatibility of Nickel-Titanium Shape Memory Metal and Its Corrosion Behavior in Human Cell Cultures." *Journal of Biomedical Materials Research*, Vol. 35, No. 4, 1997, pp. 451–457.

[12] Yamauchi, K., Ohkata, I., Tsuchiya, K., and Miyazaki, S., Eds. *Shape Memory and Superelastic Alloys*. Woodhead Publishing, 2011.

[13] Shabalovskaya, S. A. "Surface, Corrosion and Biocompatibility Aspects of Nitinol as an Implant Material." *Bio-Medical Materials and Engineering*, Vol. 12, No. 1, 2002, pp. 69–109.

[14] Es-Souni, M., Es-Souni, M., and Fischer-Brandies, H. “Assessing the Biocompatibility of NiTi Shape Memory Alloys Used for Medical Applications.” *Analytical and Bioanalytical Chemistry*, Vol. 381, No. 3, 2005, pp. 557–567. doi:10.1007/s00216-004-2888-3.

[15] Buehler, W. J., and Wang, F. E. “A Summary of Recent Research on the Nitinol Alloys and Their Potential Application in Ocean Engineering.” *Ocean Engineering*, Vol. 1, No. 1, 1968, pp. 105–120. doi:10.1016/0029-8018(68)90019-X.

[16] Miyazaki, S., Kohiyama, Y., Otsuka, K., and Duerig, T. W. Effects of Several Factors on the Ductility of the Ti-Ni Alloy. *Materials Science Forum*. https://www.scientific.net/MSF.56-58.765. Accessed Mar. 26, 2019.

[17] Elahinia, M. H., Hashemi, M., Tabesh, M., and Bhaduri, S. B. “Manufacturing and Processing of NiTi Implants: A Review.” *Progress in Materials Science*, Vol. 57, No. 5, 2012, pp. 911–946. doi:10.1016/j.pmatsci.2011.11.001.

[18] Miyazaki, S., Ohmi, Y., Otsuka, K., and Suzuki, Y. “Characteristics of Deformation and Transformation Pseudoelasticity in NiTi Alloys.” *Le Journal De Physique Colloques*, Vol. 43, 1982. doi:10.1051/jphyscol:1982434.

[19] Shaw, J. A., Churchill, C. B., and Iadicola, M. A. “Tips and Tricks for Characterizing Shape Memory Alloy Wire: Part 1–Differential Scanning Calorimetry and Basic Phenomena.” *Experimental Techniques*, Vol. 32, No. 5, 2008, pp. 55–62. doi:10.1111/j.1747-1567.2008.00410.x.

[20] Otsuka, K., and Wayman, C. M. *Shape Memory Materials*. Cambridge University Press, 1999.

[21] Duerig, T., Pelton, A., and Stöckel, D. “An Overview of Nitinol Medical Applications.” *Materials Science and Engineering: A*, Vol. 273–275, 1999, pp. 149–160. doi:10.1016/S0921-5093(99)00294-4.

[22] Melzer, A., and Stoeckel, D. “Function and Performance of Nitinol Vascular Implants.” *The Open Medical Devices Journal*, Vol. 2, No. 1, 2010.

[23] Petrini, L., and Migliavacca, F. Biomedical Applications of Shape Memory Alloys. *Journal of Metallurgy*. https://www.hindawi.com/journals/jm/2011/501483/. Accessed Mar. 27, 2019.

[24] Lekston, Z., Stróż, D., and Jędrusik-Pawłowska, M. “Preparation and Characterization of Nitinol Bone Staples for Cranio-Maxillofacial Surgery.” *Journal of Materials Engineering and Performance*, Vol. 21, No. 12, 2012, pp. 2650–2656. doi:10.1007/s11665-012-0372-3.

[25] Fox, W. C. Bone Staple, Instrument and Method of Use and Manufacturing, US9017331B2Apr 28, 2015.

[26] Russell, S. M. “Design Considerations for Nitinol Bone Staples.” *Journal of Materials Engineering and Performance*, Vol. 18, No. 5, 2009, pp. 831–835. doi:10.1007/s11665-009-9402-1.

[27] Mereau, T. M., and Ford, T. C. “Nitinol Compression Staples for Bone Fixation in Foot Surgery.” *Journal of the American Podiatric Medical Association*, Vol. 96, No. 2, 2006, pp. 102–106.

[28] Sachdeva, R. C. L., Miyazaki, S., and Farzin-Nia, F. Orthodontic Archwire and Method of Moving Teeth, US5044947ASep 03, 1991.

[29] Suzuki, Y., Miura, F., and Miura, I. Orthodontic Process for Straightening Teeth, US5102333AApr 07, 1992.

[30] Ferreira, M. do A., Luersen, M. A., and Borges, P. C. “Nickel-Titanium Alloys: A Systematic Review.” *Dental Press Journal of Orthodontics*, Vol. 17, No. 3, 2012, pp. 71–82. doi:10.1590/S2176-94512012000300016.

[31] Rossin, P. Eyeglasses and Parts Thereof Made with Specially Processed NiTi Shape Memory Alloy, US6557993B2May 06, 2003.
[32] Rossin, P. Eyeglass Support Temple and Procedure for the Manufacture Thereof, US6511174B1Jan 28, 2003.
[33] Tarnita, D., Bîzdoacă, N., Mîndrilă, I., and Vasilescu, M. M. Properties and Medical Applications of Shape Memory Alloys. *undefined*. /paper/Properties-and-medical-applications-of-shape-memory-Tarnita-B%C3%AEzdoac%C4%83/f5a0367dd665d7074d00f29feebf160698f47a65. Accessed Mar. 28, 2019.
[34] VascuFlex® Peripheral Stent. https://www.bbraun.co.uk/en/products/b50/vascuflex-peripheralstent.html. Accessed Mar. 28, 2019.
[35] Huang, W. "On the Selection of Shape Memory Alloys for Actuators." *Materials & Design*, Vol. 23, No. 1, 2002, pp. 11–19. doi:10.1016/S0261-3069(01)00039-5.
[36] Czechowicz, A., and Langbein, S., Eds. *Shape Memory Alloy Valves: Basics, Potentials, Design*. Springer International Publishing, 2015.
[37] Paik, J. K., Hawkes, E., and Wood, R. J. "A Novel Low-Profile Shape Memory Alloy Torsional Actuator." *Smart Materials and Structures*, Vol. 19, No. 12, 2010, p. 125014. doi:10.1088/0964-1726/19/12/125014.
[38] Stoeckel, D. "Shape Memory Actuators for Automotive Applications." *Materials & Design*, Vol. 11, No. 6, 1990, pp. 302–307. doi:10.1016/0261-3069(90)90013-A.
[39] Jani, J. M., Leary, M., and Subic, A. Shape Memory Alloys in Automotive Applications. *Applied Mechanics and Materials*. https://www.scientific.net/AMM.663.248. Accessed Jun. 19, 2019.
[40] Hartl, D. J., and Lagoudas, D. C. "Aerospace Applications of Shape Memory Alloys." *Proceedings of the Institution of Mechanical Engineers, Part G: Journal of Aerospace Engineering*, Vol. 221, No. 4, 2007, pp. 535–552. doi:10.1243/09544100JAERO211.
[41] McDonald Schetky, L. "Shape Memory Alloy Applications in Space Systems." *Materials & Design*, Vol. 12, No. 1, 1991, pp. 29–32. doi:10.1016/0261-3069(91)90089-M.
[42] Otsuka, K., and Kakeshita, T. "Science and Technology of Shape-Memory Alloys: New Developments." *MRS Bulletin*, Vol. 27, No. 2, 2002, pp. 91–100. doi:10.1557/mrs2002.43.
[43] Fu, Y., Du, H., Huang, W., Zhang, S., and Hu, M. "TiNi-Based Thin Films in MEMS Applications: A Review." *Sensors and Actuators A: Physical*, Vol. 112, No. 2, 2004, pp. 395–408. doi:10.1016/j.sna.2004.02.019.
[44] Kohl, M., Skrobanek, K. D., and Miyazaki, S. "Development of Stress-Optimised Shape Memory Microvalves." *Sensors and Actuators A: Physical*, Vol. 72, No. 3, 1999, pp. 243–250. doi:10.1016/S0924-4247(98)00221-0.
[45] Skrobanek, K. D., Kohl, M., and Miyazaki, S. Stress-Optimised Shape Memory Microvalves. Presented at the Proceedings IEEE The Tenth Annual International Workshop on Micro Electro Mechanical Systems. An Investigation of Micro Structures, Sensors, Actuators, Machines and Robots, 1997.
[46] Xu, D., Wang, L., Ding, G., Zhou, Y., Yu, A., and Cai, B. "Characteristics and Fabrication of NiTi/Si Diaphragm Micropump." *Sensors and Actuators A: Physical*, Vol. 93, No. 1, 2001, pp. 87–92. doi:10.1016/S0924-4247(01)00628-8.
[47] Fu, Y. q., Luo, J. k., Flewitt, A. j., Huang, W. m., Zhang, S., Du, H. j., and Milne, W. i. "Thin Film Shape Memory Alloys and Microactuators." *International Journal of Computational Materials Science and Surface Engineering*, Vol. 2, No. 3–4, 2009, pp. 208–226. doi:10.1504/IJCMSSE.2009.027483.
[48] Kohl, M. *Shape Memory Microactuators*. Springer-Verlag, Berlin Heidelberg, 2004.

[49] Lee, A. P., Ciarlo, D. R., Krulevitch, P. A., Lehew, S., Trevino, J., and Northrup, M. A. "A Practical Microgripper by Fine Alignment, Eutectic Bonding and SMA Actuation." *Sensors and Actuators A: Physical*, Vol. 54, No. 1, 1996, pp. 755–759. doi:10.1016/S0924-4247(97)80052-0.

[50] Takeuchi, S., and Shimoyama, I. "A Three-Dimensional Shape Memory Alloy Microelectrode with Clipping Structure for Insect Neural Recording." *Journal of Microelectromechanical Systems*, Vol. 9, No. 1, 2000, pp. 24–31. doi:10.1109/84.825773.

[51] Gill, J. J., Chang, D. T., Momoda, L. A., and Carman, G. P. "Manufacturing Issues of Thin Film NiTi Microwrapper." *Sensors and Actuators A: Physical*, Vol. 93, No. 2, 2001, pp. 148–156. doi:10.1016/S0924-4247(01)00646-X.

[52] Fu, Y. Q., Luo, J. K., Ong, S. E., Zhang, S., Flewitt, A. J., and Milne, W. I. "A Shape Memory Microcage of TiNi/DLC Films for Biological Applications." *Journal of Micromechanics and Microengineering*, Vol. 18, No. 3, 2008, p. 035026. doi:10.1088/0960-1317/18/3/035026.

[53] Kohl, M., Just, E., Pfleging, W., and Miyazaki, S. "SMA Microgripper with Integrated Antagonism." *Sensors and Actuators A: Physical*, Vol. 83, No. 1, 2000, pp. 208–213. doi:10.1016/S0924-4247(99)00385-4.

[54] Frick, C. P., Lang, T. W., Spark, K., and Gall, K. "Stress-Induced Martensitic Transformations and Shape Memory at Nanometer Scales." *Acta Materialia*, Vol. 54, No. 8, 2006, pp. 2223–2234. doi:10.1016/j.actamat.2006.01.030.

[55] Lahoz, R., and Puértolas, J. A. "Training and Two-Way Shape Memory in NiTi Alloys: Influence on Thermal Parameters." *Journal of Alloys and Compounds*, Vol. 381, No. 1, 2004, pp. 130–136. doi:10.1016/j.jallcom.2004.03.080.

[56] Otsuka, K., and Ren, X. "Physical Metallurgy of Ti–Ni-Based Shape Memory Alloys." *Progress in Materials Science*, Vol. 50, No. 5, 2005, pp. 511–678. doi:10.1016/j.pmatsci.2004.10.001.

[57] Miyazaki, S., Igo, Y., and Otsuka, K. "Effect of Thermal Cycling on the Transformation Temperatures of Ti-Ni Alloys." *Acta Metallurgica*, Vol. 34, No. 10, 1986, pp. 2045–2051. doi:10.1016/0001-6160(86)90263-4.

[58] Thoma, P. E., Blok, A. M., and Kao, M.-Y. "Pushing The Limit to Achieve NiTi SMA Actuating Members That Are Dimensionally Stable and Have High Transformation Temperatures." *MRS Online Proceedings Library Archive*, Vol. 246, 1991. doi:10.1557/PROC-246-321.

[59] Schmidt-Mende, P., and Reiss, H.-G. "Design of Actuating Elements Made of Shape Memory Alloys." *Le Journal de Physique IV*, Vol. 01, No. C4, 1991, pp. C4-175-C4-180. doi:10.1051/jp4:1991427.

[60] Hunter, I. W., Lafontaine, S., Hollerbach, J. M., and Hunter, P. J. Fast Reversible NiTi Fibers for Use in Microrobotics. Presented at the [1991] Proceedings. IEEE Micro Electro Mechanical Systems, 1991.

[61] Otsuka, K., and Ren, X. "Recent Developments in the Research of Shape Memory Alloys." *Intermetallics*, Vol. 7, No. 5, 1999, pp. 511–528. doi:10.1016/S0966-9795(98)00070-3.

[62] Matsumoto, O., Miyazaki, S., Otsuka, K., and Tamura, H. "Crystallography of Martensitic Transformation in Ti–Ni Single Crystals." *Acta Metallurgica*, Vol. 35, No. 8, 1987, pp. 2137–2144. doi:10.1016/0001-6160(87)90042-3.

[63] Miyazaki, S., and Otsuka, K. "Deformation and Transition Behavior Associated with the R-Phase in Ti-Ni Alloys." *Metallurgical Transactions A*, Vol. 17, No. 1, 1986, pp. 53–63. doi:10.1007/BF02644442.

[64] Ren, X., Miura, N., Zhang, J., Otsuka, K., Tanaka, K., Koiwa, M., Suzuki, T., Chumlyakov, Yu. I., and Asai, M. "A Comparative Study of Elastic Constants of Ti–Ni-Based Alloys Prior to Martensitic Transformation." *Materials Science and Engineering: A*, Vol. 312, No. 1, 2001, pp. 196–206. doi:10.1016/S0921-5093(00)01876-1.

[65] Paula, A. S., Canejo, J. P. H. G., Martins, R. M. S., and Braz Fernandes, F. M. "Effect of Thermal Cycling on the Transformation Temperature Ranges of a Ni–Ti Shape Memory Alloy." *Materials Science and Engineering: A*, Vol. 378, No. 1, 2004, pp. 92–96. doi:10.1016/j.msea.2003.11.057.

[66] Saburi, T., Nenno, S., and Fukuda, T. "Crystal Structure and Morphology of the Metastable X Phase in Shape Memory Ti-Ni Alloys." *Journal of the Less Common Metals*, Vol. 125, 1986, pp. 157–166. doi:10.1016/0022-5088(86)90090-1.

[67] Khalil-Allafi, J., Schmahl, W. W., Wagner, M., Sitepu, H., Toebbens, D. M., and Eggeler, G. "The Influence of Temperature on Lattice Parameters of Coexisting Phases in NiTi Shape Memory Alloys—a Neutron Diffraction Study." *Materials Science and Engineering: A*, Vol. 378, No. 1, 2004, pp. 161–164. doi:10.1016/j.msea.2003.11.062.

[68] Kaufman, L., and Cohen, M. "Thermodynamics and Kinetics of Martensitic Transformations." *Progress in Metal Physics*, Vol. 7, 1958, pp. 165–246. doi:10.1016/0502-8205(58)90005-4.

[69] Miyazaki, S., Fu, Y. Q., and Huang, W. M. *Thin Film Shape Memory Alloys: Fundamentals and Device Applications*. Cambridge University Press, New York, NY, USA, 2009.

[70] Wang, F. E., DeSavage, B. F., Buehler, W. J., and Hosler, W. R. "The Irreversible Critical Range in the TiNi Transition." *Journal of Applied Physics*, Vol. 39, No. 5, 1968, pp. 2166–2175. doi:10.1063/1.1656521.

[71] Wang, F. E., Buehler, W. J., and Pickart, S. J. "Crystal Structure and a Unique ``Martensitic'' Transition of TiNi." *Journal of Applied Physics*, Vol. 36, No. 10, 1965, pp. 3232–3239. doi:10.1063/1.1702955.

[72] Sandrock, G. D., Perkins, A. J., and Hehemann, R. F. "The Premartensitic Instability in Near-Equiatomic TiNi." *Metallurgical Transactions*, Vol. 2, No. 10, 1971, pp. 2769–2781. doi:10.1007/BF02813251.

[73] Melton, K. N., and Mercier, O. "The Mechanical Properties of NiTi-Based Shape Memory Alloys." *Acta Metallurgica*, Vol. 29, No. 2, 1981, pp. 393–398. doi:10.1016/0001-6160(81)90165-6.

[74] Khalil-Allafi, J., Dlouhy, A., and Eggeler, G. "Ni4Ti3-Precipitation during Aging of NiTi Shape Memory Alloys and Its Influence on Martensitic Phase Transformations." *Acta Materialia*, Vol. 50, No. 17, 2002, pp. 4255–4274. doi:10.1016/S1359-6454(02)00257-4.

[75] Elahinia, M. H. *Shape Memory Alloy Actuators: Design, Fabrication, and Experimental Evaluation*. Wiley, 2015.

[76] Kockar, B., Karaman, I., Kim, J. I., Chumlyakov, Y. I., Sharp, J., and Yu, C.-J. (Mike). "Thermomechanical Cyclic Response of an Ultrafine-Grained NiTi Shape Memory Alloy." *Acta Materialia*, Vol. 56, No. 14, 2008, pp. 3630–3646. doi:10.1016/j.actamat.2008.04.001.

[77] Cahn, R. W., and Haasen, P., Eds. *Physical Metallurgy*. North Holland, 1996.

[78] Fremond, M., and Miyazaki, S. *Shape Memory Alloys*. Springer, 2014.

[79] Nishida, M., Nishiura, T., Kawano, H., and Inamura, T. "Self-Accommodation of B19′ Martensite in Ti–Ni Shape Memory Alloys – Part I. Morphological and Crystallographic Studies of the Variant Selection Rule." *Philosophical Magazine*, Vol. 92, No. 17, 2012, pp. 2215–2233. doi:10.1080/14786435.2012.669858.

[80] Standard Test Method for Transformation Temperature of Nickel-Titanium Alloys by Thermal Analysis. http://www.astm.org/cgi-bin/resolver.cgi?F2004-05R10. Accessed Jul. 12, 2019.

[81] Todoroki, T., and Tamura, H. "Effect of Heat Treatment after Cold Working on the Phase Transformation in TiNi Alloy." *Transactions of the Japan Institute of Metals*, Vol. 28, No. 2, 1987, pp. 83–94. doi:10.2320/matertrans1960.28.83.

[82] Fan, G., Chen, W., Yang, S., Zhu, J., Ren, X., and Otsuka, K. "Origin of Abnormal Multi-Stage Martensitic Transformation Behavior in Aged Ni-Rich Ti–Ni Shape Memory Alloys." *Acta Materialia*, Vol. 52, No. 14, 2004, pp. 4351–4362. doi:10.1016/j.actamat.2004.06.002.

[83] Baron, M.-P., and Morin, M. "Stress-Induced Transformation and Temperature-Induced Transformation in Cu-Zn-Al Single Crystals." *Le Journal de Physique IV*, Vol. 07, No. C5, 1997, pp. C5-525-C5-530. doi:10.1051/jp4:1997583.

[84] Rao, A., Srinivasa, A. R., and Reddy, J. N. *Design of Shape Memory Alloy (SMA) Actuators*. Springer International Publishing, 2015.

[85] Duerig, T. W. *Engineering Aspects of Shape Memory Alloys*. Butterworth-Heinemann, 1990.

[86] Shaw, J. A., and Kyriakides, S. "Thermomechanical Aspects of NiTi." *Journal of the Mechanics and Physics of Solids*, Vol. 43, No. 8, 1995, pp. 1243–1281. doi:10.1016/0022-5096(95)00024-D.

[87] Lagoudas, D. C., Ed. *Shape Memory Alloys: Modeling and Engineering Applications*. Springer US, 2008.

[88] Daly, S., Ravichandran, G., and Bhattacharya, K. "Stress-Induced Martensitic Phase Transformation in Thin Sheets of Nitinol." *Acta Materialia*, Vol. 55, No. 10, 2007, pp. 3593–3600. doi:10.1016/j.actamat.2007.02.011.

[89] Shaw, J. A., and Kyriakides, S. "On the Nucleation and Propagation of Phase Transformation Fronts in a NiTi Alloy." *Acta Materialia*, Vol. 45, No. 2, 1997, pp. 683–700. doi:10.1016/S1359-6454(96)00189-9.

[90] Truskinovsky, L., and Vainchtein, A. "The Origin of Nucleation Peak in Transformational Plasticity." *Journal of the Mechanics and Physics of Solids*, Vol. 52, No. 6, 2004, pp. 1421–1446. doi:10.1016/j.jmps.2003.09.034.

[91] Wilsdorf, H. G. F. "Apparatus for the Deformation of Foils in an Electron Microscope." *Review of Scientific Instruments*, Vol. 29, No. 4, 1958, pp. 323–324. doi:10.1063/1.1716192.

[92] Hardiman, B., Clark, W. a. T., and Wagoner, R. H. "Automated Jet Polishing of Transmission Electron Microscope Specimens for in Situ Straining." *Journal of Electron Microscopy Technique*, Vol. 5, No. 2, 1987, pp. 199–202. doi:10.1002/jemt.1060050210.

[93] Xu, Y. B., Wang, R. J., and Wang, Z. G. "In-Situ Investigation of Stress-Induced Martensitic Transformation in the Ti-Ni Shape Memory Alloy during Deformation." *Materials Letters*, Vol. 24, No. 6, 1995, pp. 355–358. doi:10.1016/0167-577X(95)00127-1.

[94] Jiang, X., Hida, M., Takemoto, Y., Sakakibara, A., Yasuda, H., and Mori, H. "In Situ Observation of Stress-Induced Martensitic Transformation and Plastic Deformation in TiNi Alloy." *Materials Science and Engineering: A*, Vol. 238, No. 2, 1997, pp. 303–308. doi:10.1016/S0921-5093(97)00422-X.

[95] Tirry, W., and Schryvers, D. "In Situ Transmission Electron Microscopy of Stress-Induced Martensite with Focus on Martensite Twinning." *Materials Science and Engineering: A*, Vol. 481–482, 2008, pp. 420–425. doi:10.1016/j.msea.2006.12.214.

[96] Mao, S. C., Li, H. X., Liu, Y., Deng, Q. S., Wang, L. H., Zhang, Y. F., Zhang, Z., and Han, X. D. “Stress-Induced Martensitic Transformation in Nanometric NiTi Shape Memory Alloy Strips: An in Situ TEM Study of the Thickness/Size Effect.” *Journal of Alloys and Compounds*, Vol. 579, 2013, pp. 100–111. doi:10.1016/j.jallcom.2013.05.054.

[97] Pfetzing-Micklich, J., Wieczorek, N., Simon, T., Maaß, B., and Eggeler, G. “Direct Microstructural Evidence for the Stress Induced Formation of Martensite during Nanonindentation of NiTi.” *Materials Science and Engineering: A*, Vol. 591, 2014, pp. 33–37. doi:10.1016/j.msea.2013.10.035.

[98] Kröger, A., Wernhardt, R., Somsen, Ch., Eggeler, G., and Wieck, A. “In Situ Transmission Electron Microscopy-Investigations on the Strain-Induced B19′-Phase in NiTi Shape Memory Alloys Structured by Focused Ion Beam.” *Materials Science and Engineering: A*, Vol. 438–440, 2006, pp. 513–516. doi:10.1016/j.msea.2006.04.119.

[99] Ball, J. M., and James, R. D. “Fine Phase Mixtures as Minimizers of Energy.” *Archive for Rational Mechanics and Analysis*, Vol. 100, No. 1, 1987, pp. 13–52. doi:10.1007/BF00281246.

[100] Samaee, V., Gatti, R., Devincre, B., Pardoen, T., Schryvers, D., and Idrissi, H. “Dislocation Driven Nanosample Plasticity: New Insights from Quantitative in-Situ TEM Tensile Testing.” *Scientific Reports*, Vol. 8, 2018. doi:10.1038/s41598-018-30639-8.

[101] Treppmann, D., Hornbogen, E., and Wurzel, D. “The Effect of Combined Recrystallization and Precipitation Processes on the Functional and Structural Properties in NiTi Alloys.” *Journal de Physique IV*, Vol. 05, No. C8, 1995, pp. C8-569-C8-574. doi:10.1051/jp4/199558569.

[102] Bataillard, L., Bidaux, J.-E., and Gotthardt, R. “Interaction between Microstructure and Multiple-Step Transformation in Binary NiTi Alloys Using in-Situ Transmission Electron Microscopy Observations.” *Philosophical Magazine A*, Vol. 78, No. 2, 1998, pp. 327–344. doi:10.1080/01418619808241907.

[103] Zhou, N., Shen, C., Wagner, M. F.-X., Eggeler, G., Mills, M. J., and Wang, Y. “Effect of Ni4Ti3 Precipitation on Martensitic Transformation in Ti–Ni.” *Acta Materialia*, Vol. 58, No. 20, 2010, pp. 6685–6694. doi:10.1016/j.actamat.2010.08.033.

[104] Perkins, J. “Lattice Transformations Related to Unique Mechanical Effects.” *Metallurgical Transactions*, Vol. 4, No. 12, 1973, pp. 2709–2721. doi:10.1007/BF02644571.

[105] Wayman, C. M., Cornelis, I., and Shimizu, K. “Transformation Behavior and the Shape Memory in Thermally Cycled TiNi.” *Scripta Metallurgica*, Vol. 6, No. 2, 1972, pp. 115–122. doi:10.1016/0036-9748(72)90261-X.

[106] Matsumoto, H. “Transformation Behaviour of NiTi in Relation to Thermal Cycling and Deformation.” *Physica B: Condensed Matter*, Vol. 190, No. 2, 1993, pp. 115–120. doi:10.1016/0921-4526(93)90454-E.

[107] Matsumoto, H. “Appearance of an Intermediate Phase with Thermal Cycling on the Transformation of NiTi.” *Journal of Materials Science Letters*, Vol. 10, No. 7, 1991, pp. 408–410. doi:10.1007/BF00728048.

[108] Wagner, M. F.-X., Dey, S. R., Gugel, H., Frenzel, J., Somsen, Ch., and Eggeler, G. “Effect of Low-Temperature Precipitation on the Transformation Characteristics of Ni-Rich NiTi Shape Memory Alloys during Thermal Cycling.” *Intermetallics*, Vol. 18, No. 6, 2010, pp. 1172–1179. doi:10.1016/j.intermet.2010.02.048.

[109] Kustov, S., Mas, B., Salas, D., Cesari, E., Raufov, S., Nikolaev, V., and Van Humbeeck, J. “On the Effect of Room Temperature Ageing of Ni-Rich Ni–Ti Alloys.” *Scripta Materialia*, Vol. 103, 2015, pp. 10–13. doi:10.1016/j.scriptamat.2015.02.025.

[110] Wang, X., Van Humbeeck, J., Verlinden, B., and Kustov, S. "Thermal Cycling Induced Room Temperature Aging Effect in Ni-Rich NiTi Shape Memory Alloy." *Scripta Materialia*, Vol. 113, 2016, pp. 206–208. doi:10.1016/j.scriptamat.2015.11.007.

[111] Kim, J. I., and Miyazaki, S. "Effect of Nano-Scaled Precipitates on Shape Memory Behavior of Ti-50.9at.%Ni Alloy." *Acta Materialia*, Vol. 53, No. 17, 2005, pp. 4545–4554. doi:10.1016/j.actamat.2005.06.009.

[112] Wang, X., Kustov, S., Li, K., Schryvers, D., Verlinden, B., and Van Humbeeck, J. "Effect of Nanoprecipitates on the Transformation Behavior and Functional Properties of a Ti–50.8 at.% Ni Alloy with Micron-Sized Grains." *Acta Materialia*, Vol. 82, 2015, pp. 224–233. doi:10.1016/j.actamat.2014.09.018.

[113] Zheng, Y., Jiang, F., Li, L., Yang, H., and Liu, Y. "Effect of Ageing Treatment on the Transformation Behaviour of Ti–50.9 at.% Ni Alloy." *Acta Materialia*, Vol. 56, No. 4, 2008, pp. 736–745. doi:10.1016/j.actamat.2007.10.020.

[114] Karbakhsh Ravari, B., Farjami, S., and Nishida, M. "Effects of Ni Concentration and Aging Conditions on Multistage Martensitic Transformation in Aged Ni-Rich Ti–Ni Alloys." *Acta Materialia*, Vol. 69, 2014, pp. 17–29. doi:10.1016/j.actamat.2014.01.028.

[115] Zhou, Y., Zhang, J., Fan, G., Ding, X., Sun, J., Ren, X., and Otsuka, K. "Origin of 2-Stage R-Phase Transformation in Low-Temperature Aged Ni-Rich Ti–Ni Alloys." *Acta Materialia*, Vol. 53, No. 20, 2005, pp. 5365–5377. doi:10.1016/j.actamat.2005.08.013.

[116] Kompatscher, M., Demé, B., Kostorz, G., Somsen, Ch., and Wassermann, E. F. "Small-Angle Neutron Scattering of Precipitates in Ni–Ti Shape Memory Alloys." *Acta Materialia*, Vol. 50, No. 6, 2002, pp. 1581–1586. doi:10.1016/S1359-6454(02)00019-8.

[117] E Spitalsky. Verfahren, Den Oberflächen von Metallen Und Galvanischen Metallniederschlägen Ein Glänzend Poliertes Aussehen Zu Geben Spitalsky, 225873, 1910.

[118] Jacquet, P. A. "Electrolytic Method for Obtaining Bright Copper Surfaces." *Nature*, Vol. 135, No. 3426, 1935, p. 1076. doi:10.1038/1351076c0.

[119] E. Knuth-Winterfeldt. "Electropolishing with Special Reference to Two Commercial Types of Polishing Apparatus for Metallographic Purposes." *Mikroskopie - Zentralblatt für Mikroskopische Forschung und Methodik*, Vol. 5, 1950, pp. 184–193.

[120] Ayache, J., Beaunier, L., Boumendil, J., Ehret, G., and Laub, D. *Sample Preparation Handbook for Transmission Electron Microscopy: Methodology*. Springer-Verlag, New York, 2010.

[121] Ayache, J., Beaunier, L., Boumendil, J., Ehret, G., and Laub, D. *Sample Preparation Handbook for Transmission Electron Microscopy: Techniques*. Springer-Verlag, New York, 2010.

[122] Wood, W. G., and Surface treating and coating division council. *Metals Handbook. Volume 5, Volume 5,*. American Society for metals, Metals park (Ohio), 1990.

[123] Landolt, D. "Fundamental Aspects of Electropolishing." *Electrochimica Acta*, Vol. 32, No. 1, 1987, pp. 1–11. doi:10.1016/0013-4686(87)87001-9.

[124] Lee, P. J. "Enhanced Control of Electropolishing for the Preparation of Thin Foils for Transmission Electron Microscopy: Artificial and Multiple Phase Micro-Electropolishing." p. 2.

[125] Goodhew, P. J. *Specimen Preparation in Materials Science*. North-Holland, 1972.

[126] Jacquet, P. A. "On the Anodic Behavior of Copper in Aqueous Solutions of Orthophosphoric Acid." *Transactions of The Electrochemical Society*, Vol. 69, No. 1, 1936, pp. 629–655. doi:10.1149/1.3498234.

[127] Geels, K., Fowler, D., Kopp, W.-U., and Rückert, M., Eds. *Metallographic and Materialographic Specimen Preparation, Light Microscopy, Image Analysis and Hardness Testing*. ASTM International, 100 Barr Harbor Drive, PO Box C700, West Conshohocken, PA 19428-2959, 2007.
[128] Yang, G., Wang, B., Tawfiq, K., Wei, H., Zhou, S., and Chen, G. "Electropolishing of Surfaces: Theory and Applications." *Surface Engineering*, Vol. 33, No. 2, 2017, pp. 149–166. doi:10.1080/02670844.2016.1198452.
[129] Heather M. Tomlinson. "An Electro-Polishing Technique for the Preparation of Metal Specimens for Transmission Electron Microscopy." *The Philosophical Magazine: A Journal of Theoretical Experimental and Applied Physics*, Vol. 3, No. 32, 1958, pp. 867–871. doi:10.1080/14786435808237025.
[130] Kirchheim, R., Maier, K., and Tölg, G. "Diffusion and Solid-Film Formation during Electropolishing of Metals." *Journal of The Electrochemical Society*, Vol. 128, No. 5, 1981, pp. 1027–1034. doi:10.1149/1.2127544.
[131] ASTM International. ASTM E1558-09(2014) - Standard Guide for Electrolytic Polishing of Metallographic Specimens. https://webstore.ansi.org/standards/astm/astme1558092014. Accessed Jan. 16, 2019.
[132] Gareth Thomas. *Transmission Electron Microscopy of Metals*. Wiley, 1966.
[133] Heidenreich, R. D. "Electron Microscope and Diffraction Study of Metal Crystal Textures by Means of Thin Sections." *Journal of Applied Physics*, Vol. 20, No. 10, 1949, pp. 993–1010. doi:10.1063/1.1698264.
[134] R. Castaing, and P. Labourie. "Examen Direct Des Métaux Par Transmission Au Microscope Électronique." *Comptes Rendus Académie des Sciences*, Vol. 237, 1953, pp. 1330–1332.
[135] Bollmann, W. "Interference Effects in the Electron Microscopy of Thin Crystal Foils." *Physical Review*, Vol. 103, No. 5, 1956, pp. 1588–1589. doi:10.1103/PhysRev.103.1588.
[136] Nicholson, R. B., Thomas, G., and Nutting, J. "A Technique for Obtaining Thin Foils of Aluminium and Aluminium Alloys for Transmission Electron Metallography." *British Journal of Applied Physics*, Vol. 9, No. 1, 1958, p. 25. doi:10.1088/0508-3443/9/1/305.
[137] Strutt, P. R. "Preparation of Thin Metal Foils from Ordinary Tensile Specimens for Use in Transmission Electron Microscopy." *Review of Scientific Instruments*, Vol. 32, No. 4, 1961, pp. 411–413. doi:10.1063/1.1717390.
[138] Riesz, R. P., and Bjorling, C. G. "Sample Preparation for Transmission Electron Microscopy of Germanium." *Review of Scientific Instruments*, Vol. 32, No. 8, 1961, pp. 889–891. doi:10.1063/1.1717551.
[139] Mirand, P., and Saulnier, A. "Methode Rapide De Preparation De Coupes Metalliques Minces Destinees A Lexamen Direct Dans Le Microscope Electronique." *Comptes rendus hebdomadaires des séances de l'Académie des sciences*, Vol. 246, No. 11, 1958, pp. 1688–1691.
[140] Saulnier, A. "Etude Structurale Du Beryllium Par Micrographie et Microdiffraction Electroniques Sur Coupes Minces." *Journal of Nuclear Materials*, Vol. 2, No. 4, 1960, pp. 299–309. doi:10.1016/0022-3115(60)90002-7.
[141] Phillips, V. A., and Hugo, J. A. "Automatic Polishing Technique for Electro-Thinning Metals for Transmission Electron Microscopy." *Journal of Scientific Instruments*, Vol. 37, No. 6, 1960, p. 216. doi:10.1088/0950-7671/37/6/414.
[142] Booker, G. R., and Stickler, R. "Method of Preparing Si and Ge Specimens for Examination by Transmission Electron Microscopy." *British Journal of Applied Physics*, Vol. 13, No. 9, 1962, p. 446. doi:10.1088/0508-3443/13/9/303.

[143] Hugo, J. A., and Phillips, V. A. “A Versatile Jet Technique for Thinning Metals for Transmission Electron Microscopy.” *Journal of Scientific Instruments*, Vol. 40, No. 4, 1963, p. 202. doi:10.1088/0950-7671/40/4/427.

[144] Wilhelm, F. J. “The Preparation of Beryllium Specimens for Transmission Electron Microscopy by the Knuth System of Electropolishing.” *Journal of Scientific Instruments*, Vol. 41, No. 5, 1964, p. 343. doi:10.1088/0950-7671/41/5/439.

[145] Hugo, J. A., and Phillips, V. A. “A Twin-Jet Technique for Thinning Metals for Transmission Electron Microscopy.” *Journal of Scientific Instruments*, Vol. 42, 1965, pp. 354–355.

[146] Dewey, M. A. P., and Lewis, T. G. “A Holder for the Rapid Electrolytic Preparation of Thin Metal Foils for Transmission Electron Microscopy.” *Journal of Scientific Instruments*, Vol. 40, No. 8, 1963, p. 385. doi:10.1088/0950-7671/40/8/302.

[147] Schoone, R. D., and Fischione, E. A. “Automatic Unit for Thinning Transmission Electron Microscopy Specimens of Metals.” *Review of Scientific Instruments*, Vol. 37, No. 10, 1966, pp. 1351–1353. doi:10.1063/1.1719978.

[148] Ünlü, N. “Preparation of High Quality Al TEM Specimens via a Double-Jet Electropolishing Technique.” *Materials Characterization*, Vol. 59, No. 5, 2008, pp. 547–553. doi:10.1016/j.matchar.2007.04.003.

[149] Goodhew, P. J. “Specimen Preparation for Transmission Electron Microscopy of Metals.” *MRS Online Proceedings Library Archive*, Vol. 115, 1987. doi:10.1557/PROC-115-51.

[150] Luo, Z. *Practical Guide to Transmission Electron Microscopy.* Momentum Press, 2015.

[151] Jacquet, P. A. “Metallography of Aluminum and Its Alloys : Use of Electrolytic Polishing.” 1955.

[152] Witcomb, M. J., and Dahmen, U. “Method for Jet Polishing Two-Phase Materials.” *Microscopy Research and Technique*, Vol. 32, No. 1, 1995, pp. 70–74. doi:10.1002/jemt.1070320107.

[153] Bals, S., Tirry, W., Geurts, R., Yang, Z., and Schryvers, D. “High-Quality Sample Preparation by Low KV FIB Thinning for Analytical TEM Measurements.” *Microscopy and Microanalysis: The Official Journal of Microscopy Society of America, Microbeam Analysis Society, Microscopical Society of Canada*, Vol. 13, No. 2, 2007, pp. 80–86. doi:10.1017/S1431927607070018.

[154] Smallman, R. E., and Bishop, R. J. *Modern Physical Metallurgy and Materials Engineering: Science, Process, Applications.* Butterworth Heinemann, Oxford; Boston, 1999.

[155] Reimer, L., and Kohl, H. *Transmission Electron Microscopy: Physics of Image Formation*. Springer-Verlag, New York, 2008.

[156] Dinda, G. P., Rösner, H., and Wilde, G. “Synthesis of Bulk Nanostructured Ni, Ti and Zr by Repeated Cold-Rolling.” *Scripta Materialia*, Vol. 52, No. 7, 2005, pp. 577–582. doi:10.1016/j.scriptamat.2004.11.034.

[157] Fischione, P. E. “Materials Specimen Preparation for Transmission Electron Microscopy.” p. 10.

[158] Nagasawa, A. “Martensite Transformation and Memory Effect in the NiTi Alloy.” *Journal of the Physical Society of Japan*, Vol. 31, No. 1, 1971, pp. 136–147. doi:10.1143/JPSJ.31.136.

[159] Tirry, W., and Schryvers, D. “Quantitative Determination of Strain Fields around Ni4Ti3 Precipitates in NiTi.” *Acta Materialia*, Vol. 53, No. 4, 2005, pp. 1041–1049. doi:10.1016/j.actamat.2004.10.049.

[160] Świec, P., Zubko, M., Lekston, Z., and Stróż, D. "NiTi Shape Memory Marformed Alloy Studied by Electron Beam Precession TEM Orientation Mapping Method." *Acta Physica Polonica A*, Vol. 131, No. 5, 2017, pp. 1307–1310. doi:10.12693/APhysPolA.131.1307.
[161] Simon, T., Kröger, A., Somsen, Ch., Dlouhy, A., and Eggeler, G. In-Situ TEM Cooling/Heating Experiments on Deformed NiTi Shape Memory Single Crystals. 2009.
[162] Wu, S. K., and Wayman, C. M. "Interstitial Ordering of Hydrogen and Oxygen in TiNi Alloys." *Acta Metallurgica*, Vol. 36, No. 4, 1988, pp. 1005–1013. doi:10.1016/0001-6160(88)90155-1.
[163] Stróż, D., Palka, J., and Lekston, Z. "Nanotexture Studies of NiTi Shape Memory Alloy after Severe Plastic Deformation with the Use of TEM." *Solid State Phenomena*, Vol. 186, 2012, pp. 90–93. doi:10.4028/www.scientific.net/SSP.186.90.
[164] Burow, J., Frenzel, J., Somsen, C., Prokofiev, E., Valiev, R., and Eggeler, G. "Grain Nucleation and Growth in Deformed NiTi Shape Memory Alloys: An In Situ TEM Study." *Shape Memory and Superelasticity*, Vol. 3, No. 4, 2017, pp. 347–360. doi:10.1007/s40830-017-0119-y.
[165] Stróż, D. "TEM Studies of the R-Phase Transformation in a NiTi Shape Memory Alloy after Thermo-Mechanical Treatment." *Materials Chemistry and Physics*, Vol. 81, No. 2, 2003, pp. 460–462. doi:10.1016/S0254-0584(03)00048-8.
[166] Xie, Z., Liu, Y., and Van Humbeeck, J. "Microstructure of NiTi Shape Memory Alloy Due to Tension–Compression Cyclic Deformation." *Acta Materialia*, Vol. 46, No. 6, 1998, pp. 1989–2000. doi:10.1016/S1359-6454(97)00379-0.
[167] Waitz, T., Kazykhanov, V., and Karnthaler, H. P. "Martensitic Phase Transformations in Nanocrystalline NiTi Studied by TEM." *Acta Materialia*, Vol. 52, No. 1, 2004, pp. 137–147. doi:10.1016/j.actamat.2003.08.036.
[168] Liu, Y., Xie, Z., Van Humbeeck, J., and Delaey, L. "Asymmetry of Stress–Strain Curves under Tension and Compression for NiTi Shape Memory Alloys." *Acta Materialia*, Vol. 46, No. 12, 1998, pp. 4325–4338. doi:10.1016/S1359-6454(98)00112-8.
[169] Ewert, J. C., Böhm, I., Peter, R., and Haider, F. "The Role of the Martensite Transformation for the Mechanical Amorphisation of NiTi." *Acta Materialia*, Vol. 45, No. 5, 1997, pp. 2197–2206. doi:10.1016/S1359-6454(96)00322-9.
[170] Grant, D. M., Green, S. M., and Wood, J. V. "The Surface Performance of Shot Peened and Ion Implanted NiTi Shape Memory Alloy." *Acta Metallurgica et Materialia*, Vol. 43, No. 3, 1995, pp. 1045–1051. doi:10.1016/0956-7151(94)00310-E.
[171] Singh, R., Divinski, S. V., Rösner, H., Prokofiev, E. A., Valiev, R. Z., and Wilde, G. "Microstructure Evolution in Nanocrystalline NiTi Alloy Produced by HPT." *Journal of Alloys and Compounds*, Vol. 509, 2011, pp. S290–S293. doi:10.1016/j.jallcom.2011.01.206.
[172] Nemat-Nasser, S., Choi, J.-Y., Guo, W.-G., and Isaacs, J. B. "Very High Strain-Rate Response of a NiTi Shape-Memory Alloy." *Mechanics of Materials*, Vol. 37, No. 2, 2005, pp. 287–298. doi:10.1016/j.mechmat.2004.03.007.
[173] Zhang, Y., Jiang, S., Hu, L., and Liang, Y. "Deformation Mechanism of NiTi Shape Memory Alloy Subjected to Severe Plastic Deformation at Low Temperature." *Materials Science and Engineering: A*, Vol. 559, 2013, pp. 607–614. doi:10.1016/j.msea.2012.08.149.
[174] Gall, K., Tyber, J., Wilkesanders, G., Robertson, S. W., Ritchie, R. O., and Maier, H. J. "Effect of Microstructure on the Fatigue of Hot-Rolled and Cold-Drawn NiTi Shape Memory Alloys." *Materials Science and Engineering: A*, Vol. 486, No. 1, 2008, pp. 389–403. doi:10.1016/j.msea.2007.11.033.

[175] Tirry, W., Schryvers, D., Jorissen, K., and Lamoen, D. “Electron-Diffraction Structure Refinement of Ni4Ti3 Precipitates in Ni52Ti48.” *Acta Crystallographica Section B: Structural Science*, Vol. 62, No. 6, 2006, pp. 966–971. doi:10.1107/S0108768106036457.
[176] Mettler Toledo AE 240 Analytical Balance | Marshall Scientific. *www.MarshallScientific.com*. https://www.MarshallScientific.com/product-p/me-ae240.htm. Accessed Sep. 23, 2019.
[177] Zhang, X., Feng, P., He, Y., Yu, T., and Sun, Q. “Experimental Study on Rate Dependence of Macroscopic Domain and Stress Hysteresis in NiTi Shape Memory Alloy Strips.” *International Journal of Mechanical Sciences*, Vol. 52, No. 12, 2010, pp. 1660–1670. doi:10.1016/j.ijmecsci.2010.08.007.
[178] Product Detail EPO-TEK 353ND. *Epoxy Technology*. https://www.epotek.com/site/component/products/productdetail.html?cid[0]=29. Accessed Jun. 7, 2019.
[179] Luo, Z. *A Practical Guide to Transmission Electron Microscopy: Fundamentals*. 2016.
[180] Williams, D. B., and Carter, C. B. *Transmission Electron Microscopy: A Textbook for Materials Science*. Springer US, 2009.
[181] Fultz, B., and Howe, J. M. *Transmission Electron Microscopy and Diffractometry of Materials*. Springer-Verlag, Berlin Heidelberg, 2013.
[182] Graef, M. D. *Introduction to Conventional Transmission Electron Microscopy*. Cambridge University Press, 2003.
[183] Edington, J. W. Electron Diffraction in the Electron Microscope. In *Electron Diffraction in the Electron Microscope* (J. W. Edington, ed.), Macmillan Education UK, London, pp. 1–77.
[184] Josef Zweck. Focusing Diffraction Patterns and Correct Camera Length Calibration. *Imaging & Microscopy - Research, Development, Production*. https://www.imaging-git.com/science/light-microscopy/focusing-diffraction-patterns-and-correct-camera-length-calibration. Accessed Oct. 2, 2019.
[185] Tecnai On-Line Help Manual -- Options.
[186] Tecnai On-Line Help Manual -- Modes.
[187] Viladot, D., Veron, M., Gemmi, M., Peiro, F., Portillo, J., Estrade, S., Mendoza, J., Llorca-Isern, N., and Nicolopoulos, S. “Orientation and Phase Mapping in the Transmission Electron Microscope Using Precession-Assisted Diffraction Spot Recognition: State-of-the-Art Results.” *Journal of Microscopy*, Vol. 252, No. 1, 2013, pp. 23–34.
[188] Nicolopoulos, S., Rauch, E. F., Véron, M., and Beausir, B. Novel EBSD-TEM like Technique: Texture Analysis, Orientation and Phase Maps on Nanostructured Materials. PRADUA, Italy, 2012.
[189] Vigouroux, M. P., Delaye, V., Bernier, N., Cipro, R., Lafond, D., Audoit, G., Baron, T., Rouvière, J. L., Martin, M., Chenevier, B., and Bertin, F. “Strain Mapping at the Nanoscale Using Precession Electron Diffraction in Transmission Electron Microscope with off Axis Camera.” *Applied Physics Letters*, Vol. 105, No. 19, 2014, p. 191906. doi:10.1063/1.4901435.
[190] Hystiron PI 95 TEM PicoIndenter - Overview. *Bruker.com*. https://www.bruker.com/products/surface-and-dimensional-analysis/nanomechanical-test-instruments/nanomechanical-test-instruments-for-microscopes/pi-95-tem-picoindenter/overview.html. Accessed Sep. 20, 2019.
[191] Samaeeaghmiyoni, V., Idrissi, H., Groten, J., Schwaiger, R., and Schryvers, D. “Quantitative In-Situ TEM Nanotensile Testing of Single Crystal Ni Facilitated by a New

Sample Preparation Approach.” *Micron*, Vol. 94, 2017, pp. 66–73. doi:10.1016/j.micron.2016.12.005.
[192] Idrissi, H., Bollinger, C., Boioli, F., Schryvers, D., and Cordier, P. “Low-Temperature Plasticity of Olivine Revisited with in Situ TEM Nanomechanical Testing.” *Science Advances*, Vol. 2, No. 3, 2016, p. e1501671. doi:10.1126/sciadv.1501671.
[193] Kelly, P. M., Jostsons, A., Blake, R. G., and Napier, J. G. “The Determination of Foil Thickness by Scanning Transmission Electron Microscopy.” *physica status solidi (a)*, Vol. 31, No. 2, 1975, pp. 771–780. doi:10.1002/pssa.2210310251.
[194] Ackermann, I. “Beobachtungen an Dynamischen Interferenzerscheinungen Im Konvergenten Elektronenbündel I.” *Annalen der Physik*, Vol. 437, No. 1–2, 1948, pp. 19–40. doi:10.1002/andp.19484370103.
[195] Ackermann, I. “Beobachtungen an dynamischen Interferenzerscheinungen im konvergenten Elektronenbündel II.” *Annalen der Physik*, Vol. 437, No. 1–2, 1948, pp. 41–54. doi:10.1002/andp.19484370104.
[196] Leapman, R. D., Fiori, C. E., and Swyt, C. R. “Mass Thickness Determination by Electron Energy Loss for Quantitative X-ray Microanalysis in Biology.” *Journal of Microscopy*, Vol. 133, No. 3, 1984, pp. 239–253. doi:10.1111/j.1365-2818.1984.tb00489.x.
[197] Malis, T., Cheng, S. C., and Egerton, R. F. “EELS Log-Ratio Technique for Specimen-Thickness Measurement in the TEM.” *Journal of Electron Microscopy Technique*, Vol. 8, No. 2, 1988, pp. 193–200. doi:10.1002/jemt.1060080206.
[198] van Dyck, D., de Ridder, R., van Tendeloo, G., and Amelinckx, S. “A Cluster Model for the Transition State and Its Study by Means of Electron Diffraction. III. Generalisations of the Theory and Relation to the SRO Parameters.” *physica status solidi (a)*, Vol. 43, No. 2, 1977, pp. 541–552. doi:10.1002/pssa.2210430223.
[199] de Ridder, R., van Tendeloo, G., van Dyck, D., and Amelinckx, S. “A Cluster Model for the Transition State and Its Study by Means of Electron Diffraction I. Theoretical Model.” *physica status solidi (a)*, Vol. 38, No. 2, 1976, pp. 663–674. doi:10.1002/pssa.2210380229.
[200] De Ridder, R., Van Dyck, D., Van Tendeloo, G., and Amelinckx, S. “A Cluster Model for the Transition State and Its Study by Means of Electron Diffraction. II. Application to Some Particular Systems.” *physica status solidi (a)*, Vol. 40, No. 2, 1977, pp. 669–683. doi:10.1002/pssa.2210400235.
[201] van Dyck, D., de Ridder, R., van Tendeloo, G., and Amelinckx, S. “A Cluster Model for the Transition State and Its Study by Means of Electron Diffraction. III. Generalisations of the Theory and Relation to the SRO Parameters.” *physica status solidi (a)*, Vol. 43, No. 2, 1977, pp. 541–552. doi:10.1002/pssa.2210430223.
[202] Van Dyck, D., and Wilkens, M. “Aspects of Electron Diffraction from Radiation-Damaged Crystals.” *Ultramicroscopy*, Vol. 14, No. 3, 1984, pp. 237–251. doi:10.1016/0304-3991(84)90092-5.
[203] Van Torne, L. I., and Thomas, G. “Micro-Electropolishing Transmission Electron Microscopy Specimens.” *Review of Scientific Instruments*, Vol. 36, No. 7, 1965, pp. 1042–1043. doi:10.1063/1.1719756.
[204] Stickler, R., and Engle, R. J. “Microjet Method for Preparation of Wire Samples for Transmission Electron Microscopy.” *Journal of Scientific Instruments*, Vol. 40, No. 11, 1963, p. 518. doi:10.1088/0950-7671/40/11/303.
[205] Kestel, B. J. “Improved Methods and Novel Techniques for Jet Electropolishing of TEM Foils*.” *MRS Online Proceedings Library Archive*, Vol. 199, 1990. doi:10.1557/PROC-199-51.

[206] Samuels, L. E. *Metallographic Polishing by Mechanical Methods*. ASM International, Materials Park, OH, 2003.
[207] Wolf, R. "Electropolishing of Gold and Gold-Rich Alloys." *Micron (1969)*, Vol. 8, No. 3, 1977, pp. 171–172. doi:10.1016/0047-7206(77)90021-8.
[208] Lyles, R. L., Rothman, S. J., and Jäger, W. "A Cyanide-Free Solution for Electropolishing Silver." *Metallography*, Vol. 11, No. 3, 1978, pp. 361–363. doi:10.1016/0026-0800(78)90049-6.
[209] Toušek, J. "Electropolishing of Metals in Alcoholic Solution of Sulphuric Acid." *Electrochimica Acta*, Vol. 22, No. 1, 1977, pp. 47–50. doi:10.1016/0013-4686(77)85052-4.
[210] Product Detail EPO-TEK 377H. *Epoxy Technology*. https://www.epotek.com/site/component/products/productdetail.html?cid[0]=39. Accessed Jun. 7, 2019.
[211] Product Detail EPO-TEK H20E. *Epoxy Technology*. https://www.epotek.com/site/component/products/productdetail.html?cid[0]=84. Accessed Jun. 7, 2019.
[212] Thompson-Russell, K. C., and Edington, J. W. Electron Microscope Specimen Preparation Techniques in Materials Science. In *Electron Microscope Specimen Preparation Techniques in Materials Science* (K. C. Thompson-Russell and J. W. Edington, eds.), Macmillan Education UK, London, pp. 1–136.
[213] Wang, X., Van Humbeeck, J., Verlinden, B., and Kustov, S. "Thermal Cycling Induced Room Temperature Aging Effect in Ni-Rich NiTi Shape Memory Alloy." *Scripta Materialia*, Vol. 113, 2016, pp. 206–208. doi:10.1016/j.scriptamat.2015.11.007.
[214] Schryvers, D., Van Tendeloo, G., and Amelinckx, S. "On the Short Range Order State in Pt3V." *Materials Research Bulletin*, Vol. 20, No. 4, 1985, pp. 361–366. doi:10.1016/0025-5408(85)90001-7.
[215] Schryvers, D., and Amelinckx, S. "Order-Disorder Phenomena in the Platinum Rich Part of the Pt–V Phase Diagram." *Acta Metallurgica*, Vol. 34, No. 1, 1986, pp. 43–54. doi:10.1016/0001-6160(86)90230-0.
[216] Pennycook, S. J., and Jesson, D. E. "High-Resolution Z-Contrast Imaging of Crystals." *Ultramicroscopy*, Vol. 37, No. 1, 1991, pp. 14–38. doi:10.1016/0304-3991(91)90004-P.
[217] Lobato, I., and Van Dyck, D. "MULTEM: A New Multislice Program to Perform Accurate and Fast Electron Diffraction and Imaging Simulations Using Graphics Processing Units with CUDA." *Ultramicroscopy*, Vol. 156, 2015, pp. 9–17. doi:10.1016/j.ultramic.2015.04.016.
[218] Baba-Kishi, K. Z., Welberry, T. R., and Withers, R. L. "An Electron Diffraction and Monte Carlo Simulation Study of Diffuse Scattering in Pb(Zr,Ti)O3." *Journal of Applied Crystallography*, Vol. 41, No. 5, 2008, pp. 930–938. doi:10.1107/S0021889808026253.
[219] Sass, S. L. "Double Diffraction between Bragg Reflections and Planes of Diffuse Intensity Observed with High Energy Electron Diffraction." *Journal of Applied Crystallography*, Vol. 4, No. 3, 1971, pp. 252–254. doi:10.1107/S0021889871006794.
[220] Murakami, Y., and Shindo, D. "Lattice Modulation Preceding to the R-Phase Transformation in a Ti50Ni48Fe2 Alloy Studied by TEM with Energy-Filtering." *Materials Transactions, JIM*, Vol. 40, No. 10, 1999, pp. 1092–1097. doi:10.2320/matertrans1989.40.1092.
[221] Murakami, Y., Shibuya, H., and Shindo, D. "Precursor Effects of Martensitic Transformations in Ti-Based Alloys Studied by Electron Microscopy with Energy Filtering." *Journal of Microscopy*, Vol. 203, No. Pt 1, 2001, pp. 22–33.

[222] Pan, W., Todai, M., and Nakano, T. “β-Phase Instability in Binary Ti–*x*Nb Biomaterial Single Crystals.” *Materials Transactions*, Vol. 54, No. 2, 2013, pp. 156–160. doi:10.2320/matertrans.MC201202.

[223] Kustov, S., Mas, B., Kuskarbaev, Z., Wang, X., and Humbeeck, J. V. “Reply to Comment on: ‘On the Effect of Room Temperature Ageing of Ni-Rich NiTi Alloys.’” *ResearchGate*, Vol. 123, 2016. doi:10.1016/j.scriptamat.2016.06.013.

[224] Morgan, N. B., and Friend, C. M. “A Review of Shape Memory Stability in NiTi Alloys.” *J. Phys. IV*, Vol. 11, 2001, pp. 325–332.

[225] Bhattacharya, K., Conti, S., Zanzotto, G., and Zimmer, J. “Crystal Symmetry and the Reversibility of Martensitic Transformations.” *Nature*, Vol. 428, No. 6978, 2004, pp. 55–59. doi:10.1038/nature02378.

[226] Michutta, J., Somsen, Ch., Yawny, A., Dlouhy, A., and Eggeler, G. “Elementary Martensitic Transformation Processes in Ni-Rich NiTi Single Crystals with Ni4Ti3 Precipitates.” *Acta Materialia*, Vol. 54, No. 13, 2006, pp. 3525–3542. doi:10.1016/j.actamat.2006.03.036.

[227] Chen, Y., Tyc, O., Molnárová, O., Heller, L., and Šittner, P. “Tensile Deformation of Superelastic NiTi Wires in Wide Temperature and Microstructure Ranges.” *Shape Memory and Superelasticity*, Vol. 5, No. 1, 2019, pp. 42–62. doi:10.1007/s40830-018-00205-2.

[228] Sakamoto, H. “Distinction between Thermal and Stress-Induced Martensitic Transformations and Inhomogeneity in Internal Stress.” *MATERIALS TRANSACTIONS*, Vol. 43, No. 9, 2002, pp. 2249–2255. doi:10.2320/matertrans.43.2249.

[229] Miyazaki, S., Otsuka, K., and Suzuki, Y. “Transformation Pseudoelasticity and Deformation Behavior in a Ti-50.6at%Ni Alloy.” *Scripta Metallurgica*, Vol. 15, No. 3, 1981, pp. 287–292. doi:10.1016/0036-9748(81)90346-X.

[230] Yoneyama, T., and Miyazaki, S. *Shape Memory Alloys for Biomedical Applications*. Woodhead Publishing, 2008.

[231] Rauch, E. F., Portillo, J., Nicolopoulos, S., Bultreys, D., Rouvimov, S., and Moeck, P. “Automated Nanocrystal Orientation and Phase Mapping in the Transmission Electron Microscope on the Basis of Precession Electron Diffraction.” *Zeitschrift für Kristallographie International journal for structural, physical, and chemical aspects of crystalline materials*, Vol. 225, No. 2–3, 2010, pp. 103–109. doi:10.1524/zkri.2010.1205.

[232] Laplanche, G., Birk, T., Schneider, S., Frenzel, J., and Eggeler, G. “Effect of Temperature and Texture on the Reorientation of Martensite Variants in NiTi Shape Memory Alloys.” *Acta Materialia*, Vol. 127, 2017, pp. 143–152. doi:10.1016/j.actamat.2017.01.023.

[233] Churchill, C. B., Shaw, J. A., and Iadicola, M. A. “Tips and Tricks for Characterizing Shape Memory Alloy Wire: Part 3–Localization and Propagation Phenomena.” *Experimental Techniques*, Vol. 33, No. 5, 2009, pp. 70–78. doi:10.1111/j.1747-1567.2009.00558.x.

[234] Šittner, P., Heller, L., Sedlák, P., Chen, Y., Tyc, O., Molnárová, O., Kadeřávek, L., and Seiner, H. “B2 ⇒ B19′ ⇒ B2T Martensitic Transformation as a Mechanism of Plastic Deformation of NiTi.” *Shape Memory and Superelasticity*, Vol. 5, No. 4, 2019, pp. 383–396. doi:10.1007/s40830-019-00250-5.

[235] Bei, H., Shim, S., George, E. P., Miller, M. K., Herbert, E. G., and Pharr, G. M. “Compressive Strengths of Molybdenum Alloy Micro-Pillars Prepared Using a New Technique.” *Scripta Materialia*, Vol. 57, No. 5, 2007, pp. 397–400. doi:10.1016/j.scriptamat.2007.05.010.

[236] Lee, S.-W., Mordehai, D., Rabkin, E., and Nix, W. D. "Effects of Focused-Ion-Beam Irradiation and Prestraining on the Mechanical Properties of FCC Au Microparticles on a Sapphire Substrate." *Journal of Materials Research*, Vol. 26, No. 14, 2011, pp. 1653–1661. doi:10.1557/jmr.2011.221.

[237] Sehitoglu, H., Wu, Y., Alkan, S., and Ertekin, E. "Plastic Deformation of B2-NiTi – Is It Slip or Twinning?" *Philosophical Magazine Letters*, Vol. 97, No. 6, 2017, pp. 217–228. doi:10.1080/09500839.2017.1316019.

[238] Gall, K., Tyber, J., Brice, V., Frick, C. P., Maier, H. J., and Morgan, N. "Tensile Deformation of NiTi Wires." *Journal of Biomedical Materials Research Part A*, Vol. 75A, No. 4, 2005, pp. 810–823. doi:10.1002/jbm.a.30464.

[239] Šittner, P., Liu, Y., and Novak, V. "On the Origin of Lüders-like Deformation of NiTi Shape Memory Alloys." *Journal of the Mechanics and Physics of Solids*, Vol. 53, No. 8, 2005, pp. 1719–1746. doi:10.1016/j.jmps.2005.03.005.

[240] Šittner, P., Heller, L., Pilch, J., Curfs, C., Alonso, T., and Favier, D. "Young's Modulus of Austenite and Martensite Phases in Superelastic NiTi Wires." *Journal of Materials Engineering and Performance*, Vol. 23, No. 7, 2014, pp. 2303–2314. doi:10.1007/s11665-014-0976-x.

[241] Wagner, M. F.-X., and Windl, W. "Elastic Anisotropy of Ni4Ti3 from First Principles." *Scripta Materialia*, Vol. 60, No. 4, 2009, pp. 207–210. doi:10.1016/j.scriptamat.2008.09.028.

[242] Sun, Q.-P., and Li, Z.-Q. "Phase Transformation in Superelastic NiTi Polycrystalline Micro-Tubes under Tension and Torsion—from Localization to Homogeneous Deformation." *International Journal of Solids and Structures*, Vol. 39, No. 13, 2002, pp. 3797–3809. doi:10.1016/S0020-7683(02)00182-8.

[243] Miyazaki, S., Imai, T., Otsuka, K., and Suzuki, Y. "Lüders-like Deformation Observed in the Transformation Pseudoelasticity of a Ti□Ni Alloy." *Scripta Metallurgica*, Vol. 15, No. 8, 1981, pp. 853–856. doi:10.1016/0036-9748(81)90265-9.

[244] Shaw, J. A., and Kyriakides, S. "Initiation and Propagation of Localized Deformation in Elasto-Plastic Strips under Uniaxial Tension." *International Journal of Plasticity*, Vol. 13, No. 10, 1997, pp. 837–871. doi:10.1016/S0749-6419(97)00062-4.

[245] Schryvers, D. "Microtwin Sequences in Thermoelastic NixAl100-x Martensite Studied by Conventional and High-Resolution Transmission Electron Microscopy." *Philosophical Magazine A*, Vol. 68, No. 5, 1993, pp. 1017–1032. doi:10.1080/01418619308219383.

[246] Roitburd, A. L. Martensitic Transformation as a Typical Phase Transformation in Solids. In *Solid State Physics* (H. Ehrenreich, F. Seitz, and D. Turnbull, eds.), Academic Press, pp. 317–390.

[247] Kohn, R. V., and Müller, S. "Branching of Twins near an Austenite—Twinned-Martensite Interface." *Philosophical Magazine A*, Vol. 66, No. 5, 1992, pp. 697–715. doi:10.1080/01418619208201585.

[248] Khachaturyan, A. G., and Shatalov, G. A. "Theory of Macroscopic Periodicity for a Phase Transition in the Solid State." *Soviet Journal of Experimental and Theoretical Physics*, Vol. 29, 1969, p. 557.

[249] Šittner, P., Molnárová, O., Kadeřávek, L., Tyc, O., and Heller, L. "Deformation Twinning in Martensite Affecting Functional Behavior of NiTi Shape Memory Alloys." *Materialia*, Vol. 9, 2020, p. 100506. doi:10.1016/j.mtla.2019.100506.

[250] Chen, Y., Molnárová, O., Tyc, O., Kadeřávek, L., Heller, L., and Šittner, P. "Recoverability of Large Strains and Deformation Twinning in Martensite during Tensile

Deformation of NiTi Shape Memory Alloy Polycrystals." *Acta Materialia*, Vol. 180, 2019, pp. 243–259. doi:10.1016/j.actamat.2019.09.012.

List of scientific contributions

Journal articles related to the PhD work

- Pourbabak, S.; Orekhov, A.; Samaee, V.; Verlinden, B.; Van Humbeeck, J.; Schryvers, D. In-Situ TEM Stress Induced Martensitic Transformation in Ni50.8Ti49.2 Microwires. Shap. Mem. Superelasticity 2019, 5 (2), 154–162. https://doi.org/10.1007/s40830-019-00217-6.
- Pourbabak, S.; Wang, X.; van Dyck, D.; Verlinden, B.; Schryvers, D. Ni Cluster Formation in Low Temperature Annealed Ni50.6Ti49.4. Functional Materials Letters 2017, 10, 1740005. https://doi.org/10.1142/S1793604717400057.
- Pourbabak, S.; Orekhov, A.; Schryvers, D. Twin–jet electropolishing for damage–free TEM specimen preparation of metallic microwires. To be submitted.
- Pourbabak, S.; Verlinden, B.; Van Humbeeck, J.; Schryvers, D. Effect of different parameters of DSC cycling on the phase transformation temperatures of micron and submicron grain size $Ni_{50.8}Ti_{49.2}$ micro–wire. To be submitted.

Journal articles not related to the PhD work

- Pourbabak, S.; Montero-Sistiaga, M. L.; Schryvers, D.; Van Humbeeck, J.; Vanmeensel, K. Microscopic Investigation of as Built and Hot Isostatic Pressed Hastelloy X Processed by Selective Laser Melting. Materials Characterization 2019, 153, 366–371. https://doi.org/10.1016/j.matchar.2019.05.024.
- Montero-Sistiaga, M. L.; Pourbabak, S.; Van Humbeeck, J.; Schryvers, D.; Vanmeensel, K. Microstructure and Mechanical Properties of Hastelloy X Produced by HP-SLM (High Power Selective Laser Melting). Materials & Design 2019, 165, 107598. https://doi.org/10.1016/j.matdes.2019.107598.

- Radi, A.; Khalil-Allafi, J.; Etminanfar, M. R.; Pourbabak, S.; Schryvers, D.; Amin-Ahmadi, B. Influence of Stress Aging Process on Variants of Nano-Ni4Ti3 Precipitates and Martensitic Transformation Temperatures in NiTi Shape Memory Alloy. Materials & Design 2018, 142, 93–100. https://doi.org/10.1016/j.matdes.2018.01.024.
- Schryvers, D.; Cao, S.; Pourbabak, S.; Shi, H.; Lu, J. B. Recent EM Investigations on Nano- and Micro-Defect Structures in SMAs. Journal of Alloys and Compounds 2013, 577, S705–S709. https://doi.org/10.1016/j.jallcom.2011.10.112.
- Cao, S.; Pourbabak, S.; Schryvers, D. Quantitative 3-D Morphologic and Distributional Study of Ni4Ti3 Precipitates in a Ni51Ti49 Single Crystal Alloy. Scripta Materialia 2012, 66 (9), 650–653. https://doi.org/10.1016/j.scriptamat.2012.01.045.
- Shi, H.; Pourbabak, S.; Van Humbeeck, J.; Schryvers, D. Electron Microscopy Study of Nb-Rich Nanoprecipitates in Ni–Ti–Nb and Their Influence on the Martensitic Transformation. Scripta Materialia 2012, 67 (12), 939–942. https://doi.org/10.1016/j.scriptamat.2012.08.020.

Conference contributions

- S. Pourbabak, X. Wang, B. Verlinden, J. Van Humbeeck and D. Schryvers "Short-range-order (SRO) in quenched Ni-rich Ni-Ti alloys", The 16th European Microscopy Congress (EMC 2016), Lyon, France, 28 August – 2 September 2016 (oral presentation)
- S. Pourbabak, X. Wang, J. Van Humbeeck, B. Verlinden and D. Schryvers ,"Short range order in low temperature aged and cycled Ni-Ti", International Conference on Martensitic Transformations (ICOMAT 2017), Chicago, Illinois, 9 – 14 July 2017 (oral presentation, presented by Prof. Schryvers)
- S. Pourbabak, X. Wang, D. Van Dyck, J. Van Humbeeck, B. Verlinden and D. Schryvers "Effect of low temperature aging and DSC cycling on the microdomains and microstructures of Ni50.6Ti49.4", European Congress And Exhibition on Advanced Materials and Processes (EUROMAT 2017), Thessaloniki, Greece, 17–22 September 2017 (oral presentation)
- S. Pourbabak, B. Verlinden, J. Van Humbeeck and D. Schryvers "Effect of DSC Cycling on Room Temperature and Low Temperature Aged Nano-Grain Ni-Ti Microwires", European Symposium on Martensitic Transformations (ESOMAT 2018), Metz, France, 27-31 August 2018 (oral presentation)

- S. Pourbabak, A. Orekhov and D. Schryvers "Ni-Ti In-Situ Stress Induced Martensitic Transformation and Strain Mapping in a TEM", European Symposium on Martensitic Transformations (ESOMAT 2018), Metz, France, 27-31 August 2018 (poster)
- S. Pourbabak and D. Schryvers "Twin-jetelectropolishing of Ni-Ti microwires", International Microscopy Congress (IMC 2018), Sydney, Australia, 9 - 14 September 2018 (Mini oral presentation + digital poster, presented by Prof. Schryvers)
- S. Pourbabak, M. L. Montero-Sistiaga, J. Van Humbeeck, K. Vanmeensel and D. Schryvers "TEM investigation of Hastelloy X produced by additive manufacturing", International Microscopy Congress (IMC 2018), Sydney, Australia, 9 - 14 September 2018 (digital poster, presented by Prof. Schryvers)

List of Abbreviations

ACOM	Automated Crystallographic Orientation Mapping
A	Austenite
ADF–STEM	Annular Dark Field Scanning Transmission Electron Microscopy
A_f	Austenite Finish Temperature
A_p	Austenite Peak Temperature
A_s	Austenite Start Temperature
BCC	Body–Centered Cubic
BF–TEM	Bright Field Transmission Electron Microscopy
CBED	Convergent Beam Electron Diffraction
CCD	Charge–Coupled Device
DF–TEM	Dark Field Transmission Electron Microscopy
DIF	Diffuse Intensity Factor
DMA	Dynamic Mechanical Analysis
DSC	Differential Scanning Calorimetry
ED	Electron Diffraction
EELS	Electron Energy Loss Spectroscopy
FCT	Face–Centered Tetragonal
FIB	Focused Ion Beam
GPa	Gigapascal
HAADF	High–Angle Annular Dark Field
HR–STEM	High Resolution Scanning Transmission Electron Microscopy
HR–TEM	High Resolution Transmission Electron Microscopy
IPF	Inverse Pole Figure
LM–STEM	Low Magnification Scanning Transmission Electron Microscopy
LOM	Light Optical Microscope
M	Martensite
MEMS	Micro–Electro–Mechanical System
M_f	Martensite Finish Temperature
M_p	Martensite Peak Temperature
MPa	Megapascal

M_s	Martensite Start Temperature
MT	Martensitic Transformation
ND	Normal Direction
PD	Pulling Direction
PTP	Push–To–Pull
R	R–Phase
R_f	R–Phase Finish Temperature
R_s	R–Phase Start Temperature
RT	Room Temperature
SA	Selected–Area
SAED	Selected–Area Electron Diffraction
SE	Superelasticity
SEM	Scanning Electron Microscopy
SIM	Stress–Induced Martensite
SIMT	Stress–Induced Martensitic Transformation
SMA	Shape Memory Alloys
SME	Shape Memory Effect
STEM	Scanning Transmission Electron Microscopy
TD	Transverse Direction
TEM	Transmission Electron Microscopy
WQ	Water Quenching

Acknowledgement

At the end, I would like to thank everybody who encouraged and supported me over the course of my PhD.

I wish to thank Prof. Dominique Schryvers for giving me the opportunity to carry out this PhD at EMAT. I am grateful to him for being always available and open for my questions and discussions. Besides that, I am thankful for his kindness, understanding and patience.

I thank my co-supervisor Prof. Bert Verlinden for his support and making sure that I have proper access to the lab's instruments at MTM. I also appreciate scientific discussions and comments I received from Prof. Jan Van Humbeeck during these years. I thank my other jury members, Prof. Milorad Milošević, Prof. Wim Wenseleers, Prof. Petr Šittner and Prof. Xiebin Wang for their useful comments and questions on my thesis which led to improve it and my better understanding of some of my results. I specially thank the external jury members, Petr and Xiebin, who traveled long distance to be present at my pre-defense.

I am thankful to Prof. Dirk Van Dyck for his inspiring guides and discussions.

I thank my friends of X.014, Maria, Vahid, Olesia, Thomas and Carolien with whom I had great time in the pre-Titan3 era, when we had our little beautiful world downstairs. I would like to thank the people of X.009 at that time, Niek, Tine and Liesbet, for their friendship and kindness, apart from their technical help to my work. I also thank Miek, Lydia, Christine, Koen, Stijn and Armand for taking care of administrative and technical matters.

I am grateful to Andrey Sergeyevich for being always helpful (and cheerful) when I needed his help. I also thank Nick, Vahid, Hamed and Behnam who taught me how to operate TEM from day 1. And many thanks to my friends in EMAT, specially Robert, Antonis, Nathalie, Andrey, Thais,

Marnik, Vivek, Abner and Mylene, for making an intimate atmosphere. I also thank Alexander for translating my thesis summary.

Many thanks to my officemates and friends in my second university, KU Leuven: Suraj, Maria, Seren, Nur, Bensu, Pierre, Guichuan and Gaurav with whom I had always wonderful time there. Not many people are that lucky to make friends in two universities. I would also like to thank Danny who trained and helped me in the MTM labs.

I wish to thank Maryam, for her unconditional love and patience, for the times that I had no other support but her. I cannot be grateful enough to her for her encouragement during all these years.

I am grateful to my parents who taught me never to give up. They always wanted the best for me, even if that moved me far from them.

I thank my siblings Leila, Zahra and Mohsen, who always supported and encouraged me and shouldered the burden of my absence.

I say hello to Bozorgmehr and Mina, who were small when I left home, and now they are grown adults, and I missed the time in between.

I am in debt with Mr. Bakht–Shirin and Mr. Roshan–Nejad, my science and mathematics teachers in middle school, who opened my eyes to the new science at the time that no computer or internet was there.

And I thank Nima for the ride–sharing to Leuven and nice conversation (and gas station meetings) we had in the way.